

**Tunnel Face Stability
&
New CPT Applications**

Tunnel Face Stability & New CPT Applications

PROEFSCHRIFT

ter verkrijging van de graad van doctor
aan de Technische Universiteit Delft,
op gezag van de Rector Magnificus, prof.ir. K.F. Wakker,
voorzitter van het College voor Promoties,
in het openbaar te verdedigen op maandag 10 september 2001 om 16.00 uur

door Wouter BROERE

civiel ingenieur
geboren te Amsterdam

Dit proefschrift is goedgekeurd door de promotoren:

Prof.ir A.F. van Tol,
Prof.ir E. Horvat

Samenstelling promotie-commissie:

Rector Magnificus,	Technische Universiteit Delft, voorzitter
Prof.ir. A.F. van Tol,	Technische Universiteit Delft, promotor
Prof.ir. E. Horvat,	Technische Universiteit Delft, promotor
Prof.dr.ir. A. Verruijt,	Technische Universiteit Delft
Prof.dr. R.J. Mair,	University of Cambridge, United Kingdom
Dr.-Ing. E.h.S. Babendererde,	Babendererde Ingenieure GmbH, Deutschland
Dr. J.K. van Deen,	GeoDelft
Prof.dr.ir. F.B.J. Barends,	Technische Universiteit Delft

Published and distributed by: DUP Science

DUP Science is an imprint of
Delft University Press
P.O. Box 98
2600 MG Delft
The Netherlands
Telephone: +31 15 27 85 678
Telefax: +31 15 27 85 706
E-mail: DUP@Library.TUdelft.NL

ISBN 90-407-2215-3

Keywords: geotechnics, tunnelling, cone penetration testing

© 2001 by W. Broere

All rights reserved. No part of the material protected by this copyright notice may be reproduced or utilized in any form or by any means, electronic or mechanical, including photocopying, recording or by any information storage and retrieval system, without written consent from the publisher: Delft University Press.

Printed in The Netherlands

Acknowledgements

This research has been conducted at the Geotechnical Laboratory of Delft University of Technology under supervision of Prof. A.F. van Tol and Prof. E. Horvat. Financial support has been obtained from the Chair of Underground Space Technology of Delft University of Technology and the Centrum Ondergronds Bouwen (COB). The foundation of the COB, the execution of their extended research programs and the possibility to interact with the numerous researchers and research institutes involved have been tremendous stimulations during this research.

The pore pressure measurements and background information concerning the Second Heinoord Tunnel have been derived in part from the numerous reports produced by COB committee K100. Further data has been obtained from observations made in person at the building site during the construction works, especially the first passage below 'monitoring field North'. This was made possible by the kind invitation of K100 chairman K.J. Bakker.

The data on the construction of the Botlek Utility Tunnel has been supplied by Gemeentewerken Rotterdam and the Author is thankful for their permission to reproduce the data here. Similar appreciation is extended to NS Railinfrabeheer for their permission to use the measurements made during the construction of the Botlek Rail Tunnel and to B. Grote for his help in obtaining the data.

The high-speed CPTU rig and data acquisition system has been specially designed and constructed by Geomil bv. The pore pressure sensors used were provided by GeoDelft. General support in executing the tests and the design and construction of additional test equipment has been obtained from J. van Leeuwen of the Geotechnical Laboratory. Part of the data used in chapter 3 has been derived from measurements made by B. Bruinsma, K.F.C.M. Benders and K.M.S.K. Kosgoda during their stay at the Laboratory.

Kolla här, min är fan mindre.

Lukas Moodysson: Fucking Åmål

Abstract

During the boring of tunnels with a slurry shield, a bentonite suspension is used to seal the soil at the tunnel face and transfer the support pressure onto the soil skeleton. When excavating, this filter cake is constantly removed by the cutter bits and the slurry infiltrates the soil to rebuild the filter cake. In a foam-conditioned earth-pressure balance shield a similar infiltration process, driven by the foam injections, takes place. This infiltration generates a groundwater flow originating from the face, resulting in excess pore pressures in front of the face. These excess pore pressures lower the stability of the tunnel face and reduce the effectiveness of the support medium. This effect has been incorporated in a limit equilibrium wedge stability calculation for a stratified soil. The resulting model can be used to calculate the minimal required support pressure during excavation.

It has been found that the influence of the infiltration process depends strongly on the permeability of the soil in front of the tunnel and is largest for medium to fine grained sands. In such conditions the required excess support pressure (the difference between the support pressure and the water pressure at rest) can easily be quadrupled. It has also been shown that the same stability model behaves equally well in conditions where infiltration is not a dominant factor and as a result the model can be used for the calculation of the minimal support pressure in a wide range of soil conditions.

From calibration chamber tests on sands with different gradation curves and at different densities it has been found that the cone resistance, obtained from a horizontal cone penetration test, is roughly equal to that obtained from a vertical CPT at low and high densities. At intermediate densities, however, the horizontal cone resistance is approximately 20% higher. The horizontal cone resistance does not show a clear dependence on the gradation of the sand. The sleeve friction, on the other hand, does show a variation with different grain size distributions, but this variation is not linear with grain size distribution. The sleeve friction, however, shows no dependence on the sand density. The results of calibration chamber tests are confirmed by results of model tests and by a simple analytical model of horizontal cone penetration testing. The results indicate that HCPT can be interpreted to the same extent as vertical CPT.

The excess pore pressures generated by the penetration of a piezocone in sand have been measured in calibration chamber tests at penetration rates of 200mm/s. The pore pressures were recorded using the pore pressure transducer at the cone shoulder of a CPTU cone as well as two piezometers installed in the sand bed. In contrast to tests at regular speeds of 20mm/s, excess pore pressures have been measured, although no reliable relation with the density of the sand was found.

The tunnel wound on and on, going fairly but not quite straight into the side of the hill . . . and many little doors opened out of it, first on one side and then on another.

J.R.R. Tolkien: The Hobbit or There and Back Again

Contents

Acknowledgements	v
Abstract	vii
List of Symbols	xi
1 Introduction	1
1.1 Aims of this Research	2
1.2 Outline of this Thesis	3
2 Stability Analysis of the Tunnel Face	5
2.1 Introduction	5
2.1.1 Micro-Stability	6
2.1.2 Global Stability Analyses	8
2.1.3 Loss of Support Medium	17
2.1.4 Laboratory and Field Observations	20
2.2 Wedge Stability Model	27
2.2.1 Multilayered Wedge	28
2.2.2 Vertical Stress Distribution	32
2.2.3 Penetration of Support Medium	37
2.2.4 Model Implementation	46
2.3 Model Sensitivity Analysis	52
2.3.1 Homogeneous System	52
2.3.2 Layered System	60
2.3.3 Safety Factors	64
2.4 Comparison with Field Cases	66
2.4.1 Second Heinenoordtunnel	66
2.4.2 Botlek Utility Tunnel	79
2.4.3 Botlek Rail Tunnel	85
2.5 Further Groundwater Influences	94
2.6 Conclusions	96
3 Horizontal Cone Penetration Testing	101
3.1 Introduction	101
3.2 Interpretation of Cone Penetration Tests	103
3.2.1 Bearing Capacity Models	103
3.2.2 Cavity Expansion Models	104
3.2.3 Steady State Models	105

3.2.4	Finite Element Models	105
3.2.5	Calibration Chamber Testing	106
3.2.6	Empirical Relations	107
3.3	Calibration Chamber Tests on Sand	108
3.3.1	The Calibration Chamber	108
3.3.2	The Sands	110
3.3.3	Overview of Test Series	114
3.3.4	Influence of Relative Density on Horizontal Cone Resistance	119
3.3.5	Influence of Relative Density on Horizontal Sleeve Friction	121
3.3.6	Influence of the Sand Type on Horizontal Cone Resistance	125
3.3.7	Influence of the Sand Type on Horizontal Sleeve Friction	125
3.3.8	Horizontal Stress Measurements	126
3.3.9	Conclusions on Calibration Chamber Tests	128
3.4	Scale Model Tests	128
3.5	Field Tests	131
3.6	Modelling Horizontal Cone Penetration	133
3.6.1	Elastic Cavity Expansion	135
3.6.2	Adapting Existing Theories for HCPT Interpretation	139
3.7	Conclusions	140
4	High-Speed Piezocone Tests in Sands	143
4.1	Introduction	143
4.2	Determination of Liquefaction Potential	145
4.3	Influence of Penetration Speed	148
4.3.1	Influence on Cone Resistance and Sleeve Friction	148
4.3.2	Influence on Excess Pore Pressures	148
4.4	Calibration Chamber Tests	150
4.4.1	Equipment and Test Method	150
4.4.2	Overview of Test Series	151
4.5	Conclusions and Recommendations	157
5	Conclusions and Recommendations	161
	Bibliography	165
	Curriculum Vitae	177
	Samenvatting	179
	Nawoord	183
A	Basic Equations of Groundwater Flow	185
A.1	Semi-confined System of Aquifers	186
A.2	Transient Flow	188
B	Basic Equations of Elasticity	191

List of Symbols

General

c	cohesion
c_u	undrained shear strength
d_{10}, d_{50}	sieve opening at which 10 and 50 mass% of material passes sieve resp.
E	elasticity or Young's modulus
g	acceleration of gravity
i	hydraulic gradient
i_0	stagnation gradient
k	permeability
K, K_y	coefficient of horizontal effective stress
K_a, K_0, K_p	coefficients of active, neutral and passive horizontal effective stress
m_v	compressibility modulus
n	porosity
p	pore water pressure
q_u	unconfined compressive strength
t	time
v	velocity
z	vertical coordinate
β	compressibility of water
γ	soil volumetric weight
γ'	effective soil volumetric weight
$\gamma_{dry}, \gamma_{sat}$	dry and saturated soil volumetric weight resp.
γ_w	water volumetric weight
ϕ	angle of internal friction, hydraulic head
ρ	density
σ	total stress
σ'	effective stress
τ	yield stress
ψ	angle of dilatancy
\times_h	horizontal component
\times_v	vertical component
\times'	effective component

\times_{ij}	$i = j$ normal stress component
	$i \neq j$ shear stress component
$\times_{ij,k}$	derivate of stress component with respect to k ,
	$i, j, k = x, y, z$ cartesian coordinates system
	$i, j, k = r, \theta$ polar coordinates system
	$i, j, k = 1, 2, 3$ principal stress directions
	$k = t$ time derivate

Face Stability

a	soil arching relaxation length
	bentonite infiltration half-time
B	reduced diameter or wedge width
\tilde{c}	hydraulic resistance
C	overburden
d	thickness of aquitard
D	outer diameter of TBM
e	slurry infiltration length
E	resultant earth force
G	effective weight
G_s	overburden force on wedge
G_w	effective weight of wedge
h	water level
h_a	critical air infiltration height
h_c	critical height of a vertical cut
H	thickness of soil layer or aquifer
h_w	Murayama's model parameter
K	resultant friction force on sliding face
l_G, l_p, l_w	Murayama's model parameters
N	stability ratio
N_s, N_γ	Leca & Dormieux load factors
p_0	pore water pressure at rest
P	unsupported face length, excess pore pressure force
q_s	external load at soil surface
q_w	effective load at wedge top
Q	wedge face force
Q_a, Q_b	continuity conditions force on top resp. bottom of wedge segment
r_a, r_d	Murayama's model parameters
r_p	equivalent pore radius
R	radius of TBM, friction force on failure plane
s	support pressure
s_{cutter}	support pressure executed by cutter arms
s_{\min}, s_{\max}	minimal and maximal support pressure resp.
s'	effective support pressure, $s - p$
S	total slurry force

S_s	coefficient of specific storage
t_F	mean infiltration time
T	resultant friction force on wedge side
v	infiltration speed
w	depth of wedge
W	resultant water force
z_h	water table
z_t, z_b	top and bottom of tunnel face resp.
α	slurry infiltration length model parameter
Δp	excess pore pressure
Δs	excess slurry pressure, $s - p_0$
η	safety factor
θ	angle of wedge with horizontal
λ	leakage factor
ν	viscosity
τ_y	static yield strength of the support fluid
\times_a	including the effects of soil arching
\times_{fc}	related to the filter cake
\times_E	related to resultant soil force
\times_F	related to bentonite slurry or support fluid
$\times^{(i)}$	related to wedge segment i
\times_p	related to (excess) pore pressures
\times_{ref}	reference case
\times_W	related to water force

Cone Penetration Testing

D_r	relative density
e	void ratio
f_s	sleeve friction
m	alternative elastic modulus
q_c	cone resistance
q_t	corrected cone resistance
Q_t	normalized corrected cone resistance
r	radius
R_d	ratio of calibration chamber diameter to cone diameter
R_f	friction number
u	measured pore pressure
u_1, u_2, u_3	measured pore pressure at cone tip, cone shoulder resp. behind friction sleeve
W	work per unit volume,
\bar{W}	total work
ε	strain
θ	tangential coordinate

λ	first Lamé constant
μ	second Lamé constant
ν	Poisson constant
ξ	state parameter
\times_0	initial state
\times_a	related to cavity
\times_c	related to cone
\times^H	related to horizontal CPT
\times^V	related to vertical CPT
\times^k	Fourier series component, $k = 1, 2, 3, \dots$

Thus grew the tale of Wonderland:
Thus slowly, one by one,
Its quaint events were hammered out –
And now the tale is done,
And home we steer, a merry crew
Beneath the setting sun.

Lewis Carroll: Alice's Adventures in Wonderland

Chapter 1

Introduction

The use of tunnel boring machines to construct tunnels in soft soils is a relatively new but world-wide fast growing field within civil engineering. This increased interest for soft-ground tunnels falls in step with the growing interest for underground construction as a whole. The growing demand made by consumers on the (limited) available space, combined with higher demands on the quality of newly realised structures, forces decision-makers and engineers to make extended use of the third dimension, and in particular the available subsurface space.

In urbanised areas this trend combines with a desire to improve the living environment by shifting bothersome components of daily life, such as (freight) traffic, away from direct perception and in that way retaining or increasing the amount of space available for scenery and recreation. This desire to reduce interference with the environment also extends to the construction of those underground works themselves.

Tunnels constructed using tunnel boring machines, instead of cut-and-cover methods, seem the optimal solution to meet both the demands made on the final structure and those made on the construction method. As a result construction methods previously used in rocks or soils with large stand-up times have, over the last quarter-century, been adopted and extended in order to use them in soft, heterogeneous and water bearing soils. The techniques are relatively new and furthermore they are constantly adapted to make them suitable for more extreme conditions, where they were previously thought to be inapplicable. As with many progressing technologies, advances in the understanding of the boring process are often made by 'learning through failure'.

The down-side of this still somewhat limited understanding of the various aspects of the boring process, combined with the inherent uncertainties present in any soil stratum, is that there is a high risk of disturbances during the tunnel boring process. Examples of such disturbances are (excessive) settlements of the soil above the tunnel, collapse of the tunnel face, undesired deformation or damage to the tunnel lining and stagnation of the tunnel boring machine. Such disturbances are unwanted, as they may interfere with the surface environment, and for example damage surface structures, or hinder the construction work. In both cases they may increase the overall construction costs, and past experience shows that this can more than double the initial estimated building costs [45, 47].

As a result there are strong technical and economical motives to improve control of the boring process and reduce the amount and extent of the disturbances. This can be attained through an improved understanding of the different parts of the boring process, their interaction with each other and the surrounding soil, and a detailed overview of the soil properties around and above the tunnel.

To gain this overview of the soil properties, in general an extensive soil survey is executed

already in the preliminary stages of the design, and may be further extended before the commencement of the works. A typical site characterisation for a bored tunnel consists of (vertical) sampling and sounding tests at 50 to 100m intervals [68]. This interval is chosen as to obtain an optimum between the reliability of the investigation and the costs involved. However, below current and historical river beds, as found in many delta areas, like the western part of the Netherlands, this frequency may be insufficient to detect local variations of the stratification, such as sand lenses, or detect the presence of obstacles like large boulders [15]. Past tunnelling experiences show that insufficient knowledge of the actual soil conditions or the exact location of layer boundaries can lead to serious disturbances of the boring process, and therefore extra costs [26, 47].

In many cases a more detailed knowledge of the soil conditions would not lead to an altered tunnel alignment. It could however have an impact on the operation of the tunnel boring machine, in order to fine-tune the boring process and in that way minimize the risk of disturbances. Such extra information could well be obtained after the commencement of the actual boring, and it has therefore been suggested to use soil investigation techniques originating from the tunnel boring machine itself. Various techniques have been suggested, amongst which the use of a cone penetration test. Although normally used from the soil surface as a vertical test, in this case it would be rotated by 90° and executed horizontally in front of the tunnel face. Using such a Horizontal Cone Penetration Test, information about the soil up to some 30 metres in front of the tunnel could be obtained.

The properties of the soil influence the amount of deformation that occurs around the tunnel boring machine due to the boring process, and thereby the amount of settlement that occurs at the surface. They also strongly influence the forces needed to support the soil at the tunnel face during the actual excavation. The bandwidth of allowable support forces is limited. If the support force transferred onto the soil is too low, the soil may collapse into the tunnel boring machine, if it is too high the soil may be forced away from the machine or the supporting medium may escape to the surface, an event commonly called a blow-out. In all cases this may lead to stagnation of the boring process or undesired deformation of the surface, and in built-up areas even to damage to surface structures.

In order to reliably establish the allowable bounds of the support pressure, a detailed knowledge of the boring process and the properties of the soil in front and above the tunnel boring machine and a detailed understanding of the possible failure mechanisms is needed. And although a number of different models is presented in literature to calculate the allowable support pressures, there is only a limited understanding of the various aspects that may determine the normative failure mechanism, its dependence on the soil properties and the interaction with the boring process. One of the aspects that has hardly been taken into account is the infiltration of the support medium into the soil and the interaction with the pore water.

The determination of the limits of the support pressure is further complicated in heterogeneous soils, as the presence of different soil types at the tunnel face may influence the governing failure mechanism. This might lead to a situation where the overall stability of the face is undercut by a relatively thin layer with differing properties. An example would be the presence of liquefiable sand lenses at the face.

1.1 Aims of this Research

From the problem areas signalled above, three aspects will be investigated in this thesis. The first is the stability analysis of the face and the interaction of support medium infiltration on

the limits of allowable support pressure. A model will be developed to calculate the minimal required support pressure, which can deal with stratified heterogeneous soils and incorporates the effects of support medium infiltration, but will also be applicable in cases where no infiltration occurs. Using this model, the influence of infiltration will be studied through a parameter analysis as well as by comparison with recent Dutch field cases.

The second part of this study will investigate the possibilities of horizontal cone penetration testing and attempt to find the similarities and differences between horizontal and traditional (vertical) cone penetration. To that end laboratory tests in a calibration chamber will be presented and an analytical model will be derived. For practical reasons the calibration chamber tests will be limited to sands at different densities.

The third part will investigate the possibility of using a piezocone penetration test (CPTU) to determine the liquefaction potential of sands. To this end a number of tests will be performed in a calibration chamber using an adapted sounding installation and a regular piezocone. Again these tests will be limited to clean sands at different densities.

1.2 Outline of this Thesis

Chapter 2 deals with the stability analysis of the tunnel face. Within this chapter the first section gives a short introduction as well as an overview of the state of the art and literature. Section 2.2 forms the central part of the chapter, where the new stability model is described and briefly illustrated. In section 2.3 an extensive parameter analysis is presented, followed in section 2.4 by a comparison with several recent field cases. Section 2.5 subsequently gives a short overview of various influences on the pore pressures around the tunnel boring machine and section 2.6 gives a very concise overview of the model and the main conclusions.

Readers who want to gain a quick understanding of the stability model could start out with these conclusions (section 2.6) and after that refer to the appropriate parts of section 2.2.

Chapter 3 deals with the interpretation of Horizontal Cone Penetration Tests. After a brief introduction, it starts off with a concise overview of the interpretation of regular (vertical) cone penetration tests. Then the various laboratory tests performed, and their results, are discussed in sections 3.3 and 3.4. Section 3.5 briefly lists the available data from field tests on horizontal cone penetration. In section 3.6 a simple analytical model is derived to aid in interpreting the differences between horizontal and vertical cone penetration, followed by conclusions in section 3.7.

The reader who is interested in a quick understanding of horizontal cone penetration might start with the conclusions of this chapter and after that skip back to the results of the laboratory tests, starting in section 3.3.3.

Chapter 4 gives the results from the high-speed piezocone penetration tests. It starts out with a brief introduction, and shortly describes the determination of the liquefaction potential of soils in section 4.2. Then an overview is given of the current literature concerning the influence of the penetration speed on the piezocone test results in section 4.3. Section 4.4 gives an overview of the test conditions and results and is followed by conclusions.

For a quick overview of the test results, and in view of the length of the chapter, the reader might opt to start reading at section 4.4.

The final chapter gives a short overview of the main conclusions and a number of recommendations concerning the optimisation of the tunnel boring process.

I find their colorful adventures fascinating and also mentally stimulating.
– If you ask me, they're about as mentally stimulating as watching
bamboo grow.

Mamasan and kidsan in: The Samurai Pizza Cats

Chapter 2

Stability Analysis of the Tunnel Face

2.1 Introduction

One of the main objectives of the tunnel boring process is to adequately support the soil and to minimize deformations during and after construction. This is especially the case in urban environments, where the influence of a tunnel collapse or extensive deformations can be catastrophic, and even limited soil deformations may damage buildings [112, 126]. To prevent this it is necessary to support soft and non-cohesive soils from the time they are excavated to the moment the final support is installed. Where groundwater is present it is also necessary to prevent a flow towards the tunnel face, as this flow may have an eroding effect on the tunnel face.

When a tunnel boring machine (TBM) is used to excavate the soil, the radial support and watertightness is first ensured by the shield and after that by the tunnel lining. At the face such mechanical support is impractical or impossible to combine with an efficient excavation process, and indirect ways of face support are used. Compressed air or a pressurized slurry may be used in case of a slurry TBM and a mixture of the excavated soil mass and varying additives is used in an earth pressure balance.

Whatever means of support is used, the pressure in the working chamber of the TBM should be kept at such a level that stable working conditions are ensured. It should not be as low as to allow uncontrolled collapse of the soil into the working chamber, nor as high as to lead to large deformations of the soil or to a blow-out and subsequent loss of the support medium.

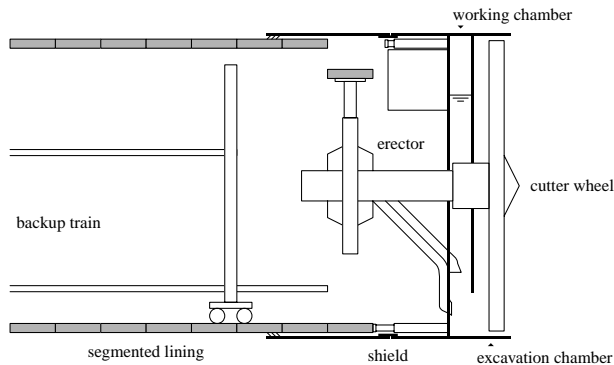


Figure 2.1: Shield tunnel boring machine

The actual range of allowable support pressure for a given tunnel project will depend among other things on the actual soil and groundwater conditions, the excavation method and the size and overburden of the tunnel. To find the minimal and maximal allowable support pressures, a number of models has been proposed in literature over the years to describe different possible failure mechanisms of the tunnel face and to calculate the properties of the support medium necessary to prevent collapse.

These models can be categorised into three main classes based on the type of failure mechanism they describe. Models which describe the behaviour of a group of grains or a single grain at the tunnel face are called internal or micro-stability models. Models which describe a failure mode of a large part of the face or the entire face are called external or global stability models. Some authors further subdivide the external models into local stability models, which do not directly influence the soil surface, and global stability models, which do. Other authors define local instabilities as those external instabilities which influence only part of the tunnel face, regardless of their influence on the soil surface, and that definition will be used in this thesis. Both micro- and local instabilities may well initiate progressive failure and lead to a global collapse of the tunnel face [10]. A third class of models are those which in themselves do not describe the likelihood of occurrence of an instability of the soil around the TBM, but of the loss of the support medium, which in turn of course may lead to a reduction of the support pressure and subsequent collapse of the tunnel face.

In the following sections a brief overview of the different models reported in literature will be given for each of those three categories, as well as a number of field and laboratory observations. A number of effects identified from field cases and laboratory tests is not included in current stability models. Especially the infiltration of the support medium into the soil in front of the TBM and the presence of excess pore pressures may have a profound effect on the stability of the tunnel face. In section 2.2 a stability model will be constructed that does include those effects and the results obtained with this model will be compared with field observations in section 2.4. In section 2.3 the sensitivity of the model to the input parameters is investigated as well as the influence this sensitivity has on the determination of safety factors. Overall conclusions about the use of face stability models and the newly developed model in particular will be presented in section 2.6.

2.1.1 Micro-Stability

Micro-stability, the stability of the single grain or a small group of grains at the tunnel face, is mainly a problem in soils with no or low cohesion and a slurry or air supported tunnel face. In such conditions grains may fall from the soil matrix under gravitational forces. When followed by subsequent grains the face may erode and this can introduce a local or global collapse. To prevent this type of collapse, a minimal pressure difference over the grains is necessary. This has no direct influence on the support pressure, but on the pressure gradient into the soil. As will be shown, this leads to a minimal shear strength requirement for the slurry.

According to Müller-Kirchenbauer [123] a small cohesionless soil element at the tunnel face is subjected to gravity and acted upon by forces from the support medium, $s_F = i_0 \gamma_F$, and the surrounding soil (see figure 2.2). For a given slope α , failure occurs when

$$i_0 \frac{\gamma_F}{\gamma'} \sin \varphi = \sin(\alpha - \varphi), \quad (2.1)$$

with i_0 the stagnation gradient, γ_F the unit weight of the suspension, γ' the effective unit weight

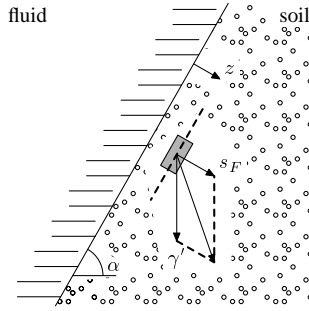


Figure 2.2: Forces included in the micro-stability analysis [123]

of the soil. The stagnation gradient is given by

$$i_0 = \frac{2\tau_F}{r_p \gamma_F}, \quad (2.2)$$

where τ_F the yield strength of the suspension and r_p the equivalent pore radius of the soil capillaries. For the most common case $\alpha = 90^\circ$ this results in a minimum requirement for the yield strength of the support medium

$$\tau_F \geq \frac{r_p \gamma'}{2 \tan \varphi}. \quad (2.3)$$

A number of researchers have made estimates of the equivalent pore radius r_p , resulting in slightly different estimates of τ_F . Kilchert [93] for example uses

$$r_p = 2(1 - n)d_{10} \quad (2.4)$$

which relationship leads to

$$\tau_F \geq \frac{d_{10}(1 - n) \gamma'}{\tan \varphi}. \quad (2.5)$$

Except for its direct influence on the stability of a single grain, the yield strength has a major influence on the infiltration length of the support medium into the soil. This in turn can have a significant effect on the global stability, an effect that will be covered in detail in section 2.2.3.

In cohesive soils the stability of individual particles will generally be secondary to the stability of the entire face. A problem could occur when a pressure gradient towards the working chamber is present. Such a situation could occur in an EPB shield with a support pressure below the hydrostatic pressure [52]. Unfortunately, the stability analysis of an infinite slope, the approach followed by Müller-Kirchenbauer to obtain (2.1), cannot be extended straightforward for a cohesive-frictional material.

Another approach would be to investigate the stability of an unsupported vertical cut ($\alpha = 90^\circ$) in a purely cohesive material subject to a drag force. A simple upper bound analysis assuming a straight failure plane and no drag force [167] leads to a maximum height before failure

$$h_c \leq \frac{4c_u}{\gamma}. \quad (2.6)$$

This is only slightly higher than the best known upper bound solution, which has a factor 3.83 instead of 4 [161]. It is assumed that a seepage flow is present and results in a horizontal drag force $\gamma_w i$ [125]. In that case the maximum height of the cut can be estimated from

$$h_c \leq \frac{4c_u}{\gamma} \frac{1}{f + \sqrt{f^2 + 1}} \quad (2.7)$$

with $f = i\gamma_w/\gamma$ or, inversely, the critical gradient can be determined.

In cases where the groundwater flow towards the face becomes a problem, a closer analysis is warranted. A possible approach would be to choose an arbitrary failure height for the slope, i.e. a reference stress level, and then proceed with a slope stability analysis, e.g. Müller-Kirchenbauer's method, Bishop's method or a fully numerical (FE) solution method [136]. Alternatively one could use a semi-empirical approach as used in the analysis of piping phenomena, but with less stringent safety factors, as the time span over which the slope has to remain stable is significantly shorter [74, 115]. Since cases where the piezometric head within the excavation chamber is lower than outside are not very common and moreover fall outside the scope of this thesis, such analyses will not be made here.

2.1.2 Global Stability Analyses

A number of authors has described external failure mechanisms of the tunnel face and derived formulae to calculate a suitable support pressure by analytical or empirical means. Historically, the first models were upper and lower bound plasticity solutions for an (associated) Tresca material. At later times solutions for non-associated Mohr-Coulomb material and limit equilibrium models were published. The different models will be described briefly in the following paragraphs and an overview is given in table 2.1. In part this table has been adapted from Balthaus [23] and Krause [98].

One of the first models was derived by Broms & Bennermark [48] in 1967. They derive a relationship describing the stability of unsupported vertical openings in an undrained cohesive (Tresca) material, see figure 2.3. With this relationship they define the stability ratio N to be equal to the difference between total overburden stress and support pressure divided by the undrained shear strength,

$$N = \frac{q_s - s}{c_u} + \frac{\gamma}{c_u} (C + R), \quad (2.8)$$

with q_s the surface load, C the overburden, R the tunnel radius and s the support pressure. From observations of collapses in both building pits and tunnel constructions, and from laboratory extrusion tests, they find that an opening in such conditions will become unstable for $N > 6$.

In 1980 Davis et al. [63] investigate the stability of an idealised partially unlined tunnel heading in a Tresca material and introduce the distance P between the face and the point where a stiff support is provided (Figure 2.4). They use the vertical opening as presented by Broms & Bennermark as one of three limit cases for their stability analysis. They further derive upper and lower bound plasticity solutions for the stability of a plane strain unlined cavity (Figure 2.4b) and a plain strain 'long wall mining' problem, obtained by taking $P = \infty$ in figure 2.4a. Their upper and lower bound solutions for the two-dimensional unlined cavity are summarised in figure 2.5.

Of particular relevance to the face stability of a tunnel excavated using a shield machine is the case $P = 0$. Davis et al. derive two lower bound solutions, using a cylindrical and a spherical

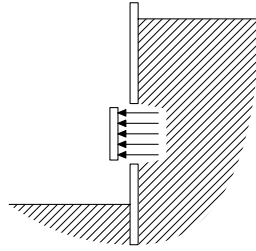


Figure 2.3: Unsupported opening in vertical hold [48]

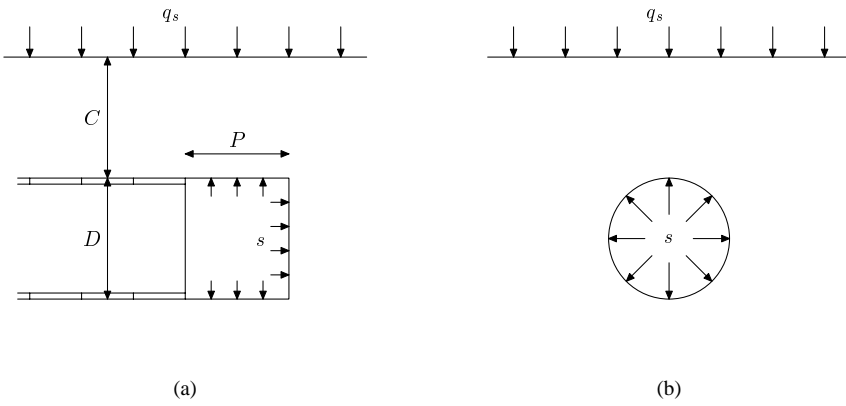


Figure 2.4: Schematisation of partially unlined tunnel [63]

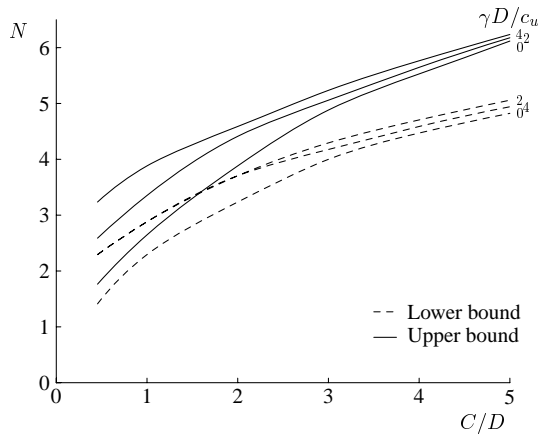


Figure 2.5: Upper and lower bound stability ratios for a plane strain unlined tunnel [63]

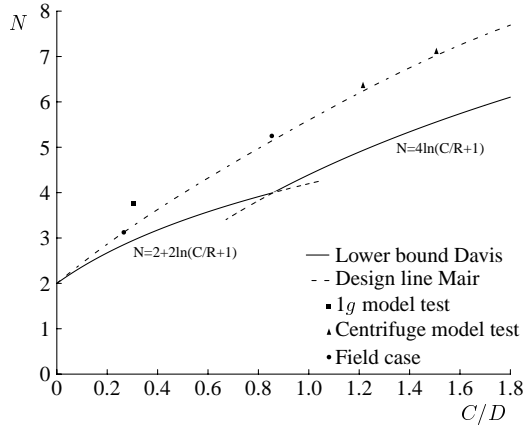


Figure 2.6: Stability ratios for lined tunnels ($P = 0$) in clay [112]

stress field. The corresponding stability ratios are respectively

$$N = 2 + 2 \ln \left(\frac{C}{R} + 1 \right) \quad (2.9)$$

$$N = 4 \ln \left(\frac{C}{R} + 1 \right). \quad (2.10)$$

Figure 2.6 shows that these lower bound solutions correspond well with a number of laboratory tests and field collapses as well as with the stability ratio design line obtained by Kimura & Mair [94] for tunnels in undrained conditions.

A few years earlier, in 1977, Atkinson & Potts [13] derived the minimal support pressure for an unlined cavity in a dry cohesionless material (see figure 2.4b). They differentiate between two limit cases. The first case is a tunnel in a weightless medium with a surface load q_s , the second a tunnel in a medium with $\gamma > 0$ but without surface loading. For this second case they derive two lower bound solutions. For cases where $c > 0$ and $\phi > 0$, which include all practically relevant cases, it can be shown however that of these solutions the overburden independent lower bound solution

$$s_{\min} = \frac{2K_p}{K_p^2 - 1} \gamma R, \quad (2.11)$$

where

$$K_p = \frac{1 + \sin \phi}{1 - \sin \phi}, \quad (2.12)$$

is always normative. As this represents a statically admissible stress field it is a safe estimate for the minimal support pressure. The kinematic upper bound solution on the other hand, which is the inherently unsafe estimate, yields a lower value for the minimal support pressure. It should be noted that both upper and lower bound solutions found by Atkinson & Potts are independent of the relative overburden C/D .

Leca & Dormieux [106] propose a series of conical bodies in 1990 (see figure 2.7). Combined with different stress states, similar to those proposed by Davis et al., they derive lower

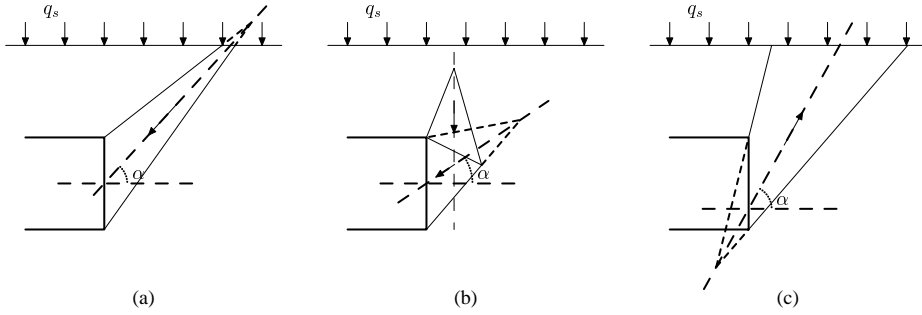


Figure 2.7: Conical failure mechanisms [106]

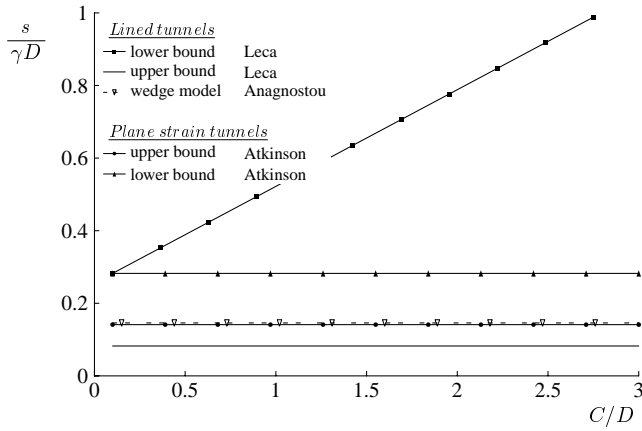


Figure 2.8: Upper and lower bounds of the support pressure for lined ($P = 0$) and unlined ($P = \infty$) tunnels [112]

and upper bound limits for both the minimal and maximal support pressure of a lined tunnel in a dry Mohr-Coulomb material. They present two sets of graphs for the dimensionless load factors N_γ and N_s , one for minimal and one for maximal support pressures. Using these graphs the resulting support pressures can be calculated as

$$s = N_s q_s + N_\gamma \gamma D. \tag{2.13}$$

Their (unsafe) upper bound solution for the minimal support pressure is in good correspondence with the results from laboratory and centrifuge tests on tunnels in sand by Atkinson et al. [12] and centrifuge tests by Chambon & Corté [60], which all fall between the bounds set by Leca's upper bound solution and Atkinson's lower bound solution. The accompanying lower bound solution, however, shows a depth dependence of the support pressure not observed in laboratory tests. These solutions have been plotted in figure 2.8 for the case of $c' = 0, \phi' = 35^\circ$. The upper and lower bound solutions for the maximal support pressure derived by the same authors have not been plotted in this figure as they yield unrealistically high values for all but the shallowest tunnels [37, 112].

The minimal support pressures needed for a semi-circular and spherical limit equilibrium mechanism, which roughly resembles the mechanism used by Broms & Bennermark (see fig-

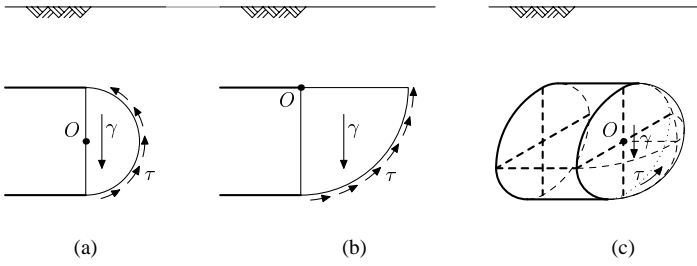


Figure 2.9: Circular and spherical failure mechanisms [98]

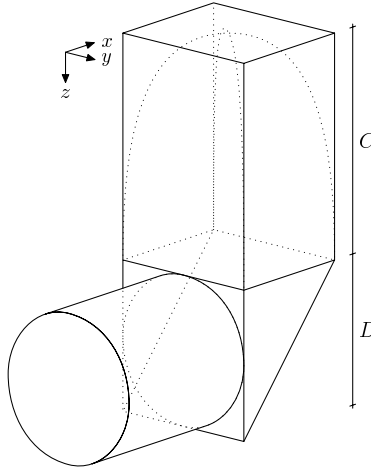


Figure 2.10: Wedge and silo model

ure 2.9) have been calculated by Krause [98] in 1987 in a limit-equilibrium analysis using the shear stresses on the sliding planes. Of the three mechanisms proposed, the quarter circle (Figure 2.9b) will always yield the highest minimal support pressure

$$s_{\min} = \frac{1}{\tan \phi} \left(\frac{1}{3} D \gamma' - \frac{1}{2} \pi c \right). \quad (2.14)$$

As Krause already indicates this may not always be a realistic representation of the actual failure body. In many cases the half-spherical body (Figure 2.9c) will be a better representation. In that case the minimal support pressure can be found from

$$s_{\min} = \frac{1}{\tan \phi} \left(\frac{1}{9} D \gamma' - \frac{1}{2} \pi c \right). \quad (2.15)$$

An often encountered limit equilibrium model is the wedge model, which assumes a sliding wedge loaded by a soil silo. As it is central to the new stability model developed in this thesis, the theoretical background of the wedge model will be covered in more detail in section 2.2. A number of slightly different implementations has been described in literature.

Murayama [92, 98] calculated the minimal support pressure using a two-dimensional log-spiral shaped sliding plane in 1966 (Figure 2.11). Five years before, a three-dimensional model

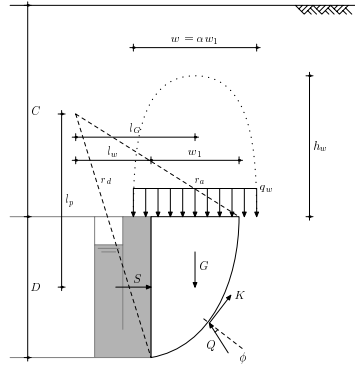


Figure 2.11: Log-spiral shaped sliding wedge, adapted from [98]

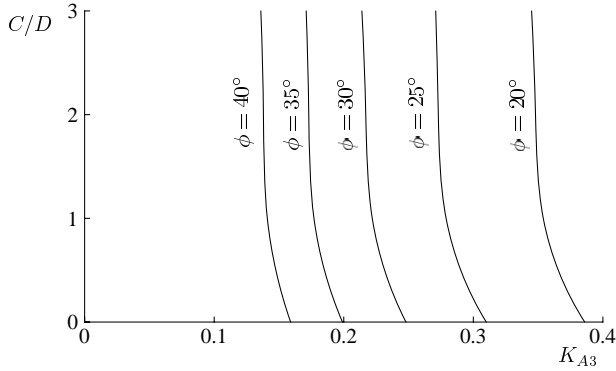


Figure 2.12: Three-dimensional earth pressure coefficient K_{A3} obtained by Jancsecz & Steiner [89]

as sketched in figure 2.10 had already been outlined by Horn [80], using a triangular wedge with a straight instead of log-spiral shaped front. His article offers no practical elaboration and an implementation of this model is first published by Jancsecz & Steiner in 1994 [89]. They incorporate the influence of soil arching above the TBM and present their results in the form of a three-dimensional earth pressure coefficient K_{A3} , represented in figure 2.12 for different values of overburden and angle of internal friction ϕ . These results are valid for a homogeneous soil only and disregard the effect of slurry infiltration.

In the same year Anagnostou & Kovári [6, 8] show the eroding influence of slurry infiltration on face stability using a similar model. Theoretically the bentonite should seal the face like a membrane and the entire support pressure would be transferred to the soil skeleton at this membrane. Especially in coarse soils the slurry will over time infiltrate a certain distance into the soil. Especially during stand-still of the TBM this reduces the effectiveness of the support pressure and undermines the initial stability of the wedge. This effect is illustrated for a 10m diameter tunnel in figure 2.13, where the long term safety factor is compared to the initial or membrane model safety factor for different values of the characteristic grain size d_{10} , the bentonite shear strength τ_F and the excess slurry pressure Δs . It shows that in fine grained soils the factor of safety can be increased by increasing the excess slurry pressure, but that in coarser

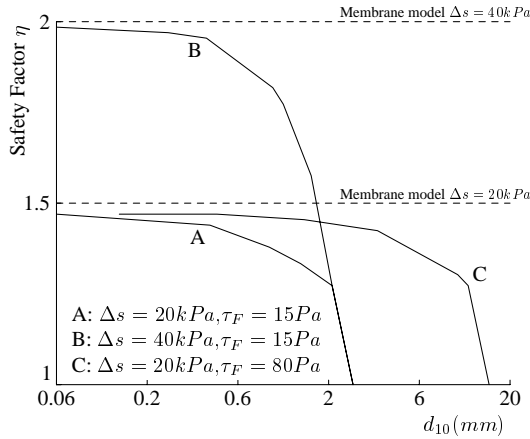


Figure 2.13: Effect of slurry infiltration on the stability safety factor for a 10m diameter slurry shield [8]

soils this has little effect as it will only increase the infiltration depth of the slurry. Increasing the bentonite content and thereby the shear strength of the slurry results in a more effective filter cake and increases the safety factor in such conditions. The effects of slurry infiltration will be covered in more detail in section 2.2.3.

The same authors also use a wedge model for the face stability of earth pressure balance shields. In cases where the piezometric head within the excavation chamber is lower than that of the surrounding soil, a seepage flow will develop in the direction of the tunnel. This seepage force is obtained from a separate three-dimensional finite element seepage-flow calculation and added to the force equilibrium of the wedge model [7]. The results of this study are presented as four dimensionless factors which contain the dependence of the minimal support pressure on tunnel diameter, effective weight of the soil, cohesion and effective support pressure s' .

In 1988 Mohkam [119] already described a limit equilibrium model using a roughly log-spiral shaped wedge which has to be obtained from a variational analysis over the unknown position $w(x,y)$, angle $\theta(x,y)$ and total stress $\sigma(x,y)$ of the failure plane. The model also includes the effect of the reduced effectiveness of the slurry pressure due to infiltration using a non-linear relation between infiltration distance and effective slurry pressure. The large number of unknowns present in the model leads to a highly iterative solution procedure and a rather unwieldy model. The model can be substantially simplified by prescribing the shape of the failure body and the total stress field and in that case it becomes very similar to the other wedge models.

A problem common to all global stability models described above is that they are only suited for homogeneous soil conditions. Heterogeneity of the soil above or in front of the TBM remains a problem. While practical experience shows that the stability of the face is often a problem in heterogeneous soils [47, 112], more so than in homogeneous soils, at the same time it cannot be quantified straightforwardly by any of those models. In such conditions one may attempt to establish upper and lower limits to the support pressure by simplifying the geometry of the problem or using averaged soil properties. There are however no clear methods to make such simplifications or obtain such averages and a certain amount of engineering judgement is necessary. A stability model that deals with layered soils, especially at the face, is clearly

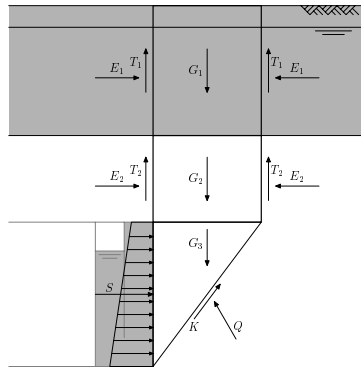


Figure 2.14: Two-dimensional wedge with layered soil column [30]

needed.

To deal with this problem Katzenbach introduces a two-dimensional wedge model, as sketched in figure 2.14, that can include layered soils above the TBM, but not in front of the TBM [30]. It remains unclear from the brief description, however, whether this model includes arching effects of the soil above the tunnel or to what extent these heterogeneities influence the required support pressure. Section 2.2.2 will show that the effect of layered soils above the face can easily be included in Terzaghi's arching formulae and thereby in the wedge models described by Jancsecz & Steiner or Anagnostou & Kovári. The model sketched by Katzenbach is a two-dimensional simplification of such a model.

The global stability models summarized above allow one to approximate the minimal and/or maximal support pressure, mostly by upper and lower bound inclusion, but give no insight in the safety margins present in these calculations or the safety margins that should be applied during the actual execution of the tunnelling works.

The stability ratio N defined by Broms & Bennermark [48] can of course be viewed as a safety factor, but with the somewhat confusing effect that a higher stability ratio corresponds with a lower factor of safety, and the actual margin of safety is not easily established. Table 2.2 gives an indication of the relation between the actual stability number and expected deformations [14]. Romo & Diaz [59, 144] have made a correlation between the stability ratio and the safety factor, but related the concept of safety to the occurrence of settlements at the surface and not to the stability of the face.

Definitions of the (partial) factor of safety specific to a wedge stability model have been made by Jancsecz [88] and Sternath [156]. These will be discussed in section 2.3.3. An often encountered approach of more practical nature is the inclusion of an absolute safety margin, as illustrated in section 2.1.4.

A more precise assessment of the safety margins available under field conditions is hindered by the practical problems as well as the financial consequences of a full scale tunnel face collapse, and most efforts in this direction have been made using laboratory models, as illustrated in section 2.1.4. Establishing a relation between (partial) safety factors and an acceptable risk level for the entire tunnelling project is also complicated by the fact that most stability models have no explicit dependence on time, excavation speed or excavation distance.

Apart from the analytical models described above, a number of numerical models has also been described in literature. The lion's share however are finite element calculations tailored to

Year Publ.	Author	Soil c ϕ	c
1961	Horn	+	+
1966	Murayama	+	+
1967	Broms & Bennermark	-	+
1977	Atkinson & Potts	+	-
1980	Davis et al.	-	+
1987	Krause	+	+
1988	Mohkam	+	+
1990	Leca & Dormieux	+	+
1991	Mori	-	+
1994	Jancsecz & Steiner	+	+
1994	Anagnostou & Kovári	+	+
1999	Belter et al.	+	+

^a Model can/cannot (+/-) deal with: $\phi = 0$
 3D = model includes three-dimensional effects

N	Deformation
< 1	Negligible
1 – 2	Elastic
2 – 4	Elasto-plastic
4 – 6	Plastic
> 6	Collapse

Table 2.2: Relation between stability ratio and deformation

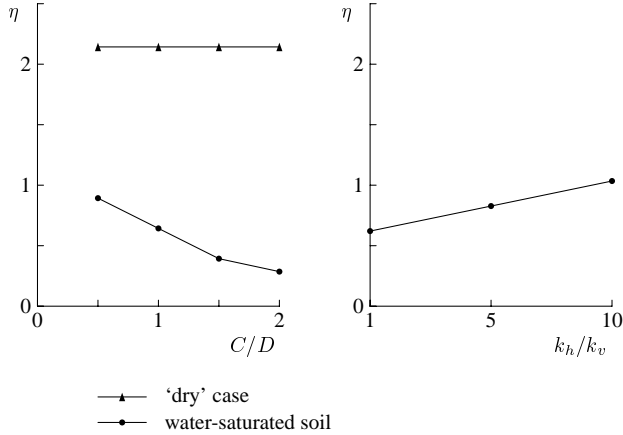


Figure 2.15: Face stability safety factor for an 8m diameter tunnel as function of relative overburden and as function of the ratio of horizontal over vertical permeability [52]

a certain project and are hardly adaptable for general cases. An exception is the model reported by Buhan et al. [52]. They describe the framework for a three-dimensional finite element model of the face of an EPB machine, where the drag forces of seepage flow towards the face have been included. This model is applied to an 8m diameter tunnel, and the influence of varying overburdens on stability has been studied (see figure 2.15). They also find that the stability safety factor depends solely on the ratio of horizontal to vertical permeability k_h/k_v and not on their individual magnitudes.

2.1.3 Loss of Support Medium

When a (sudden) loss of the support medium in the working chamber takes place, and the support medium is not or not adequately replenished, the pressure at the face will drop. If the support pressure decreases, this in turn may lead to active global collapse of the face. The instigation of this kind of failure is a high support pressure. Such failures are often categorised as blow-outs, but encompass the classical blow-out as well as several other mechanisms. These will be listed in the following section.

First we will deal with the classical blow-out, the lifting of a soil body by a high support pressure and the subsequent sudden loss of the support medium. The model which yields the lowest maximal allowable support pressure assumes the lifting of the soil over a fairly large region. This may occur when the support medium infiltrates the soil, for example in a slurry shield when no filter cake is present at the face. In that case friction of the lifted soil body with

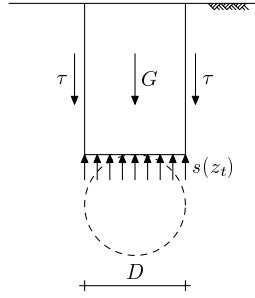


Figure 2.16: Blow-out model including friction at boundaries

its surroundings can be neglected and the blow-out pressure equals the vertical total stress

$$s_{\max} = \sigma_v. \quad (2.16)$$

Other models do take the shear stresses between the moving soil body and its surroundings into account. These shear stresses can be included directly as a shear force along the vertical sides of a two-dimensional rectangular body, as sketched in figure 2.16, which leads to an allowable pressure

$$s_{\max} = C \left[\gamma + \frac{2c + CK_y \gamma' \tan \phi}{D} \right]. \quad (2.17)$$

Another approach is to include a wedge shaped body which is lifted together with the soil column and calculate the allowable support pressure assuming that this entire body must be lifted. Balthaus [24] for example models an inverted truncated pyramid with angles $45^\circ + \phi/2$ (see figure 2.17) and holds that the safety against blow-out η is given by

$$\eta = \frac{G}{S} > \eta_1 = \frac{6(B' + C \cot(45^\circ + \phi/2))}{B' s(z_t)} > \eta_2 = \frac{\gamma C}{s(z_t)} \quad (2.18)$$

and further that it is sufficient to determine η_1 as a conservative estimate of the safety against blow-out. It should of course be ensured that the shear force between the central soil column and the outer wedges is sufficient to lift the wedges. An assumption made in this model is that the support pressure can find no weakened flow channels to the surface, for example due to bore holes [9].

When the face is supported by air, the same estimates of the maximal allowable support pressure hold but another effect has also be taken into account. When the face is not completely sealed, air will leak out of the working chamber and flow into the soil. An air bubble may then form in front of the face, as sketched in figure 2.18. If the assumption is made that the air pressure must be lower than the weight of the overlying layers [62], a critical height h_a above the tunnel can be determined as

$$h_a = \frac{\frac{\gamma}{\gamma_w} C - D}{1 + \frac{\gamma}{\gamma_w}} \quad (2.19)$$

with γ_w the unit weight of water, while the stand-up time before blow-out is given by

$$t = \frac{n}{k} \left[(D + C) \ln \left(1 + \frac{h_a}{D} \right) - h_a \right]. \quad (2.20)$$

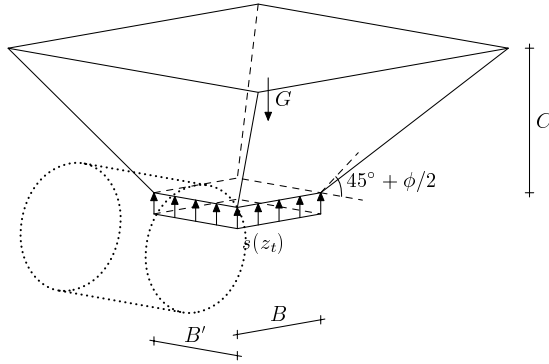


Figure 2.17: Balhaus' model for the safety against blow-out

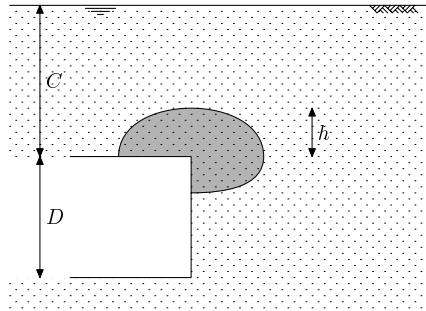


Figure 2.18: Drying of soil due to expanding air bubble

According to Babendererde [16] this type of blow-out is most common in soils with low permeability ($<10^{-5}$ m/s) or with overlying soil layers with low permeability, so that air reserves can build up below ground. In homogeneous soils with high permeability ($>10^{-2}$ m/s) air will escape almost unhindered and erosion of the surface soil and flow channels might occur, but a build-up of air pockets is not likely to occur. He also states that the different combinations of soil permeability and air loss mechanism show different characteristics of air consumption over time, which can be used to assess the safety against blow-out during the actual tunnelling works.

Instead of lifting the soil as a whole, the fluid pressure can be large enough to force individual soil particles apart and form cracks in the soil. The fluid will propagate into the cracks and as the pressure loss along the crack is often negligible, the process will continue to elongate the crack. This process is known as soil fracturing. The flow channel created in this way can be either horizontal or vertical and these channels tends to propagate quickly. Due to its sudden occurrence, speedy propagation and resulting loss of large amounts of support medium, fracturing is difficult to recognize in time and is as hazardous to the boring process as a blow-out.

Mori [121] defines the pressure at which (vertical) fracturing must occur for a normally consolidated soil as

$$s_f = K_0 \sigma'_v + p + q_u \tag{2.21}$$

with q_u the unconfined compressive strength. In general fracturing will occur somewhat earlier,

resulting in an unsafe estimate of the maximal support pressure. For highly overconsolidated soils with $K_0 \geq 1$, the horizontal effective stress may be greater than the vertical, as a result of which horizontal fracturing will occur at a stress significantly lower than determined by (2.21). Bezuijen [35] states a more general formula,

$$s_f = \sigma_3 + \eta_f c_u \quad (2.22)$$

which defaults to (2.21) for $\eta_f = 2$ and normally consolidated soil. Bezuijen holds that when taking $\eta_f = 1$, this expression will yield safe estimates of the maximum allowable support pressure.

Comparing the maximal allowable support pressures resulting from the various models, the frictionless blow-out model in general yields the lowest maximal allowable pressure, followed by the requirements resulting from fracturing, blow-out mechanisms including shear forces and finally global stability analyses for the maximal allowable support pressure.

Another mechanism which has been named as a possible method to create a flow channel from the face to the surface is piping. However, piping is caused by a sufficiently large exit gradient of the support medium at the surface and this gradient is small in a regular boring process. In case a slurry shield is used with no filter cake present at the face, the exit gradients could be expected to be of the magnitude needed to wash out particles at the surface. Then a flow channel could be created by continued erosion, a process which generally takes place on a larger timescale than the boring process. As such it is not deemed a very likely mechanism. Furthermore the support pressures needed to create a large enough pressure gradient are so large that other mechanisms are likely to occur sooner, which further decreases the likelihood of piping occurring as a failure mechanism of the tunnel face.

2.1.4 Laboratory and Field Observations

The validity of the stability models should preferably be backed by field observations. The large number of unknowns often present in field conditions and the high costs resulting from a collapse of the face and subsequent stand-still of the tunnel boring process are major reasons that most researchers have used laboratory tests to investigate the boundaries of allowable support pressures and to support their models. These tests can be broken down into geocentrifuge tests, 1g laboratory tests like extrusion tests and scale model analogs. Examples from all these categories will be given and their applicability to the problem of face stability briefly mentioned.

Furthermore, even where projects are well documented and extensive information on the soil conditions is given in literature, measurements of the actually used support pressures are hardly ever given, and cases where a direct connection is made between support pressure measurements and face instabilities are almost non-existent. A few cases where sufficient information is available will be discussed in section 2.4 and used to validate the stability model developed in section 2.2. Lacking data on actual collapses, one can alternatively use the design guidelines and measured pressures of the regular boring process to establish a range of suitable working pressures. The bounds of this range may give an indication of the minimal and maximal allowable support pressures, especially if the difference between the bounds is reasonably small. To this end we will also look at estimative methods and rough guidelines for the support pressure.

Several authors have reported investigations on the face stability of tunnels using geocentrifuges. These tests can be divided into tests on supported and (partially) unsupported tunnels, or into tests on sandy or clayey soils. Tests in sandy soils are almost without exception made with a supported model tunnel. In these tests the method of face support can differ. In

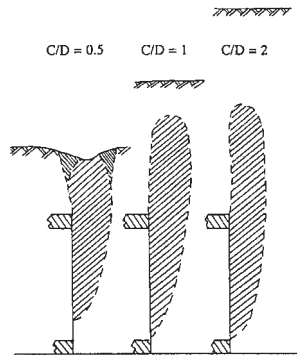


Figure 2.19: Centrifuge experiment results, showing failure bulbs above TBM for different overburdens [60]

the simple case without groundwater the face can be supported by a piston. This mechanical support is slowly removed to simulate a face collapse. These tests mainly give an indication of the shape of the failure mechanism. Another possibility is to use an impermeable membrane supported by air or fluid pressure. In this case the required support pressure can be found by slowly reducing the support pressure behind the membrane and observing deformations. Even in this last setup it is not possible to investigate what influence the infiltration of the support medium into the sand has on the stability of the tunnel face, as the membrane serving as the tunnel face must be impermeable.

Chambon & Corté [60] used a model tunnel sealed by a membrane and embedded in a homogeneous sand layer. They gradually reduced the support pressure and found wedge shaped failure planes loaded by soil silos. Their investigation focussed on the influence of the overburden on the silo formation and shows that a soil silo will form even if only a small overburden is present but that its influence will be limited by the proximity of the soil surface. They further show that a soil silo can develop fully at an overburden equal to the tunnel diameter or larger (see figure 2.19). Similar experiments have been conducted by Hisatake et al. [78] and Atkinson & Potts [11, 13].

Bezuijen & Messemackers-van de Graaf [37] have compared the results from three centrifuge tests on sand and soft clay with postdictions from most of the minimal support pressure models mentioned above. They find that the Anagnostou & Kovári wedge model including a soil silo with an arching relaxation length equal to the inverse of the tunnel radius predicts the collapse pressure within 2%, both for their model tunnels in sand and those in clay, a degree of accuracy not matched by any of the other models. Slurry infiltration was not included in the tests however, as an impermeable membrane was used to simulate the face. In one of the tests in clay, the area surrounding the face which encompassed the failure plane was removed from the sample after the tests. Tomography was then used to establish the three-dimensional shape of the failure plane without further disturbance of the soil, the results of which are shown in figure 2.20.

Tests in clayey soils have been made with an entirely supported face as well as with an unsupported face or even partially unlined tunnel. Such centrifuge tests have been reported by amongst others Mair [112]. These tests show a minimal support pressure that is largely independent of the overburden and can be plotted between the upper and lower bounds derived by Atkinson as shown in figure 2.8. The large deformations of the face that occur after failure

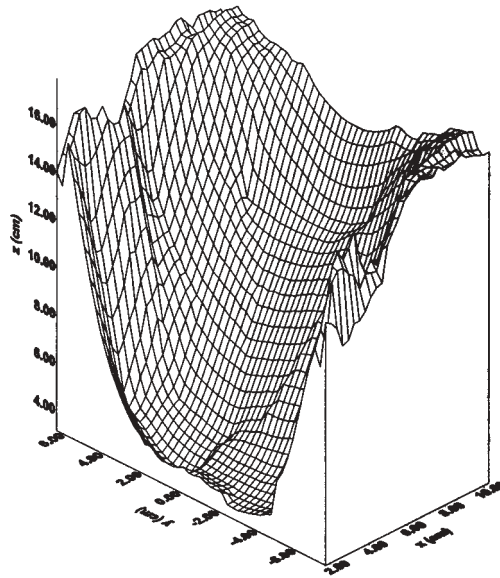


Figure 2.20: Shape of the failure plane in front of tunnel observed in centrifuge test [37]

are shown clearly by Calvello [55].

A different type of laboratory experiment has been performed by Domon [69]. Using a Discrete Element Model, which basically is a two-dimensional tunnel face cross section constructed from small metal cylinders, he shows that large deformations occur in a wedge shaped area at the tunnel face and smaller deformations in the overlying strata (Figure 2.21). As with most centrifuge and other laboratory tests, this type of experiment is primarily suited to show the shape and extent of the deformations around the tunnel face at a progressed state of collapse, but has no direct value for the determination of a suitable support pressure.

From the laboratory tests it can be seen that the geometry of the failure mechanism in sand and in clay is notably different. Tests in sand show a chimney-like failure mechanism, described by the wedge stability models. Centrifuge tests on clay show a much larger and widening zone influenced by the instability (see figure 2.22). This is generally consistent with instabilities observed in the field [112].

Allersma [4] investigated the influence of a clay layer on the failure mechanism in a trap door test. He compared a test on a model simulating 30m of homogeneous dense sand with a model in which a clay layer of 2m thickness is over- and underlain by dense sand. Both tests show the same chimney-like failure mechanism and he concludes that the failure mechanism is not strongly influenced by the presence of the clay layer. This indicates that a similar description of soil arching can be used in heterogeneous layered soils as in homogeneous soils.

As said, insight in the limits of allowable support pressure can be gained not only from laboratory tests but also to a certain extent from the design guidelines based on previous field experiences. These guidelines do not exactly give the minimal or maximal allowable support pressures and often do not claim to do so, but give a suitable working support pressure. As there is a tendency to work with a low support pressure in order to minimize friction and maximize excavation speed [62, 165], the design guidelines for the minimal support pressure are often

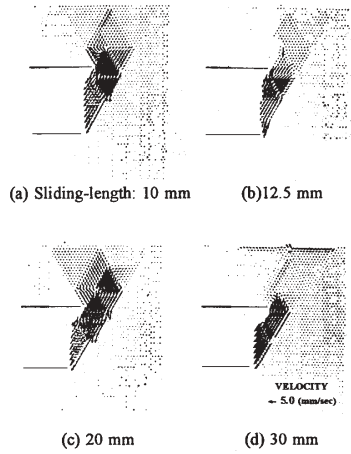


Figure 2.21: Incremental displacement field from discrete element experiment [69]

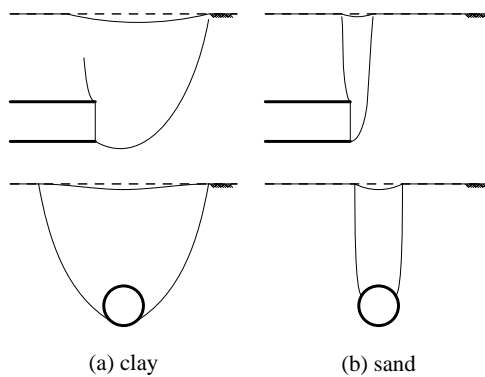


Figure 2.22: Overall shape of the failure mechanism observed in sand and in clay [112]

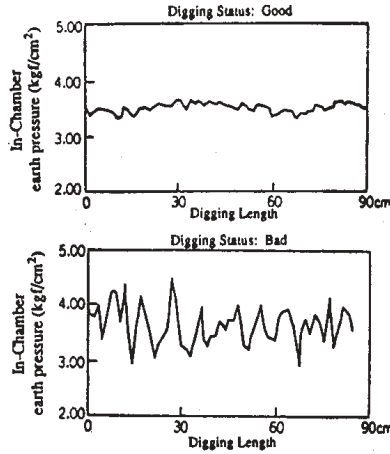


Figure 2.23: Pressure fluctuations [92]

close to the actual allowable minimal support pressure. Care must be taken however to ensure that these design rules are used for the soil conditions they were developed for. An often quoted rule of thumb for the support pressure is [62]

$$s_{\min} = K_a \sigma'_v + p + 20\text{kPa}. \quad (2.23)$$

Kanayasu [92] lists the used support pressure for a number of Japanese tunnelling projects (see table 2.3). For EPB tunnelling projects the earth pressure at rest has often been used to establish the working pressure. Depending on the soil conditions the water pressure and/or a small safety margin is added. For slurry shield tunnelling the support pressure is predominantly based on the water pressure, to which the active earth pressure and/or a small safety margin is added. The safety margin is used to intercept the pressure fluctuations that occur during a normal boring process. From the figures quoted in table 2.3 it can be seen that fluctuations in the order of 20kPa may occur during a regular boring process.

The magnitude of the support pressure fluctuations depends on the quality control of the boring process. Kanayasu illustrates this by two examples, one for a regular boring process and one for a badly controlled boring process (see figure 2.23). In the badly controlled case sudden changes of over 100kPa may occur. Aristaghes [10] suggests that such pressure fluctuations are an indication of local instabilities occurring at the face, which in turn is seen as an indication that the face is near global collapse.

Another estimate for the required support pressure, based on field observations and local practise, has been proposed by Mori [121]. He proposes the difference between the earth pressure at rest and the pressure exerted by the cutter wheel as a suitable working pressure, especially in cohesive soils excavated with a full-face cutting wheel. It is not clear however whether this rule of thumb is limited to earth pressure balance shields or to cases where groundwater flow plays a secondary role.

As noted earlier, the stability of the face is a problem in heterogeneous soils, especially when different soil layers are present at the face. The different layers may well make different or even contradictory demands on the required support pressure. Stratification at the face may

D (m)	Soil type	Support pressure used
7.45	soft silt	earth pressure at rest
8.21	sandy soil, cohesive soil	earth pressure at rest + water pressure + 20kPa
5.54	fine sand	earth pressure at rest + water pressure + fluctuating pressure
4.93	sandy soil, cohesive soil	earth pressure at rest + 30–50kPa
2.48	gravel, bedrock, cohesive soil	earth pressure at rest + water pressure
7.78	gravel, cohesive soil	active earth pressure + water pressure
7.35	soft silt	earth pressure at rest + 10kPa
5.86	soft cohesive soil	earth pressure at rest + 20kPa
6.63	gravel	water pressure + 10–20kPa
7.04	cohesive soil	earth pressure at rest
6.84	soft cohesive soil, diluvial sandy soil	active earth pressure + water pressure + fluctuating pressure (\approx 20kPa)
7.45	sandy soil, cohesive soil, gravel	water pressure + 30kPa
10	sandy soil, cohesive soil, gravel	water pressure + 40–80kPa
7.45	sandy soil	loose earth pressure + water pressure + fluctuating pressure
10.58	sandy soil, cohesive soil	active earth pressure + water pressure + fluctuating pressure (20kPa)
7.25	sandy soil, gravel, soft cohesive soil	water pressure + 30kPa

Table 2.3: Support pressure used in several Japanese tunnelling projects (first part EPB and second part slurry supported) [92]

also lead to occurrence of different (local) instabilities than described by the global stability models or to entirely different failure mechanisms.

For example, where lenses of pressurised water-bearing sands exist in clay layers, it is difficult to ensure face stability with slurry shields, as the water pressure in these lenses tends to neutralize the support system and collapse of the face and large settlements may result [173]. Even when such lenses initially have a pore pressure equal to the surrounding pore pressures, the infiltration of the slurry into the lenses and the inability of this filtrate water to drain off can result in excess pore pressures in the lenses and a resulting loss of stability.

A related problem which is not limited to heterogeneous soils is the infiltration of large amounts of filtrate water from the slurry into the soil. Especially when no filter cake forms or if this filter cake is continuously removed by the cutter wheel, a large influx of water into the soil will take place. Under certain groundwater flow conditions this influx may lead to significant excess pore pressures in front of the TBM, which lower the effective stress and thereby the stability of the face [120]. Kanayasu [92] has identified this problem and states that it may become an important factor in soils with permeabilities $k \approx 10^{-5}$ m/s or larger. Piezometer measurements made at the Second Heinenoordtunnel have recorded excess pore pressures 30 metres in front of the TBM (see figure 2.24). It must be noted that, as the pore pressures are plotted against distance to the face, the downward spikes represent the pressure measurements

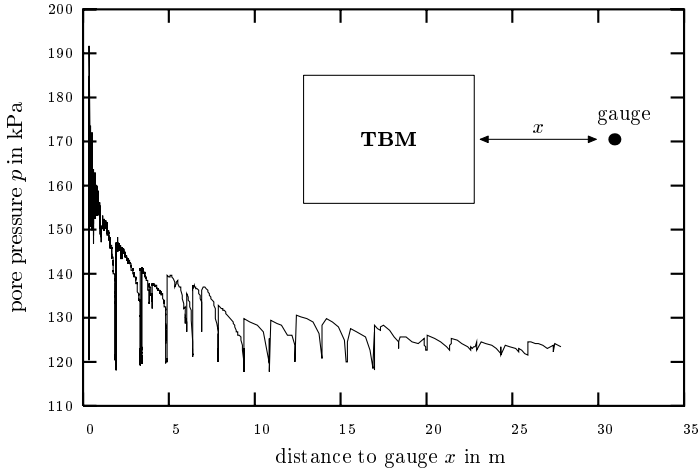


Figure 2.24: Pore pressure measurements in front of TBM at 2nd Heinenoordtunnel [38]

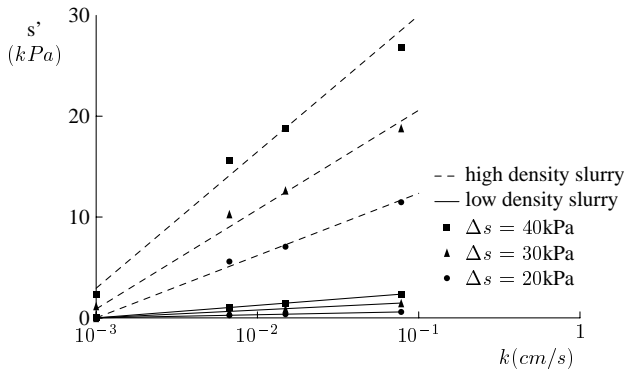


Figure 2.25: Relationship between permeability and effective slurry pressure [120]

during standstill of the TBM and the lowest points of the spikes coincide with the pore pressures at rest. As these measurements will be used in the evaluation of the stability model, they will be discussed in more detail in section 2.4.

Hashimoto et al. [75] report similar measurements from a field case, where excess pore pressures were recorded up to 10m in front of the tunnel face. They show a different pressure distribution with distance from the face for three different slurry types in similar soil conditions, but do not give the actual slurry or soil properties involved. Mori et al. [120] report laboratory tests, numerical modelling as well as field observations on this phenomenon in sandy soils. Field measurements show excess pore pressures up to 40kPa and a visible influence at least 30m in front of the tunnel face. Based on laboratory tests and numerical models they conclude that within the investigated margins a decreasing permeability significantly reduces the effective slurry pressure as excess pore pressures dissipate more slowly. They also conclude that this effect can be countered by using a slurry with a higher fines content. Their results are presented in figure 2.25.

Especially for sandy soils laboratory investigations and field experience have shown that, if

the support pressure is too low, failure occurs within a wedge shaped failure body in front of the face. This wedge is loaded by an arching soil column and the shape of this silo is not strongly influenced by the presence of different soil layers above the TBM. If the soil is permeable and the support medium is able to infiltrate the soil, this may lead to excess pore pressures in front of the face. If these excess pore pressures cannot dissipate quickly enough they will lower the effective support pressure s' well below the excess support pressure Δs used and may lead to instability of the tunnel face. This effect is not included in any of the stability models described in section 2.1.2 but will strongly influence the required minimal support pressure.

2.2 Wedge Stability Model

The basic wedge stability model is a limit equilibrium analysis of a wedge shaped soil body at the tunnel face, loaded by a soil column, as sketched in figure 2.10. This wedge and silo body shows a resemblance to the failure modes observed in e.g. the centrifuge tests performed by Chambon & Corté [60] or actual field collapses [48, 112], which have been described in section 2.1.4. A number of authors has published slightly different implementations of the wedge model over the years, which have been briefly listed in section 2.1.2. As said there, these models differ in which effects are taken into account, for example soil arching or slurry infiltration. The following section will first look at the differences and shortcomings of these models in more detail. Subsequently we will build a wedge stability model that deals with the identified problems.

The most notable problem with the existing wedge stability models is that they are suited for homogeneous soils only. As we will see later, the force equilibrium on the wedge depends among other things on the angle of internal friction of the soil. When different soils are present within the tunnel face, and those soils have different angles of internal friction, the force equilibrium used by the models of Jancsecz & Steiner [89] and Anagnostou & Kovári [6, 7, 8] is not valid and there is no straightforward way to approximate or average the soil properties to obtain the correct support pressure. When the soil boundaries occur only above (or below) the tunnel face and the entire wedge falls within a single homogeneous layer, the force equilibrium equations can be adapted in a reasonably straightforward manner, as illustrated by Katzenbach's model [30].

It has been observed however that heterogeneities or layer boundaries can have a significant effect on the stability of the tunnel face, and a reliable calculation of the minimal support pressure in such conditions is needed to ensure an undisturbed excavation [110]. To this end a stability model is needed that can deal with heterogeneities at the tunnel face in a straightforward and consistent manner. Since the shape of the collapsing body in front of the TBM is very similar to that observed in collapses of slurry-filled trenches, as is the formulation of the equilibrium equations for both cases [93, 164], the experiences gained with slurry-filled trenches in heterogeneous conditions will be used to construct a multi-layer wedge stability model.

A second problem is formed by the transfer of the support force onto the soil skeleton. In the most simple wedge model, as presented by Jancsecz & Steiner, the entire support force at the face acts on the wedge. This implicitly assumes that the face is impermeable to the support medium, or sealed by some kind of membrane. If a bentonite slurry is used to support the face, however, the bentonite will infiltrate the soil skeleton to a certain length before an impermeable filter cake is formed. The support force is transferred onto the soil skeleton over a certain length and, as shown later, this reduces the effective support force somewhat. In fine grained soils the effect is negligible and a membrane wedge model can be reliably used. In coarse, gravelly,

soils with high permeability on the other hand, the slurry will permeate to significant distances, as shown by Steiner [155]. In such cases the reduction of effective support force may become significant, as has been shown by Anagnostou & Kovári.

Anagnostou & Kovári assumed that this effect would be unimportant during actual boring and would only become significant during stand-still. Then the gradual infiltration would undermine the stability of the face over time. They made the implicit assumption, however, that there would be no build-up of excess pore pressures in the soil in front of the TBM due to this infiltration. In soil conditions where excess pore pressures can accumulate in front of the TBM during the excavation, as observed at the Heinenoord site (see section 2.1.4) such a model does not yield a correct minimal support pressure [92]. The interplay between infiltration, excess pore pressures and effective stresses can have a significant influence on the face stability and as such should be included in a stability model explicitly.

A third effect that needs to be included in a wedge stability model to accurately predict the minimal support pressure is soil arching. Centrifuge tests by Bezuijen & Messemackers-van de Graaf [37] for example, combined with postdictions from most stability models, have shown that the support pressure at collapse can be accurately predicted only if the effects of soil arching are included. Neglecting soil arching and presuming a linear stress distribution with depth would lead to much higher minimal support pressures than actually observed. This has also been observed by Jancsecz & Steiner and Anagnostou & Kovári, but seems to have been neglected by Katzenbach.

Now that some of the problem areas related to wedge stability models have been recognised, a stability model will be constructed that can deal explicitly with three of these effects; heterogeneities at the tunnel face, the infiltration of slurry into the soil in front of the TBM and the presence of excess pore pressures, which can of course result from the slurry infiltration, but may also have other origins. The following section will first deal with the formulation of a wedge stability model which can handle heterogeneities in a straightforward manner. Although the model will be formulated in such a way that it is suited to deal with infiltration and excess pore pressures, those effects will not be included directly, but will be introduced in section 2.2.3 and 2.2.3. Before that we will discuss the effects of soil arching and its addition to the stability model in section 2.2.2. The suitability of the resulting model will be illustrated by field cases in section 2.4 and further discussed in section 2.3.

2.2.1 Multilayered Wedge

To construct a wedge stability model, as sketched in figure 2.26, which can handle heterogeneous soil conditions, the horizontal slice model described by Walz [174] for slurry-filled trenches will serve as a starting point. The failure wedge is subdivided in N smaller bodies, see figure 2.27, possibly of different thickness, inside each of which the soil conditions are homogeneous. The soil conditions may vary between these slices, as may the wedge angle $\theta^{(i)}$ between the i 'th slice's slanted failure plane and the horizontal.

Each slice i is loaded by the resulting forces from the slice above ($i - 1$) and below ($i + 1$), $Q_a^{(i)}$ and $Q_b^{(i)}$ respectively, the effective weight of the slice itself $G_w^{(i)}$ and an overburden force $G_s^{(i)}$. At the slanted failure plane there is a cohesive force $K^{(i)}$ acting parallel to the plane, as well as a friction force $R^{(i)}$, which results from the normal force $N^{(i)}$, working perpendicular to the failure plane. The side faces of the wedge are each assumed to be loaded by the shear forces $T^{(i)}$, which act in the same direction as $K^{(i)}$, against the deformation direction of the wedge. Force equilibrium will yield the effective earth force $E^{(i)}$ at the face which, combined with the

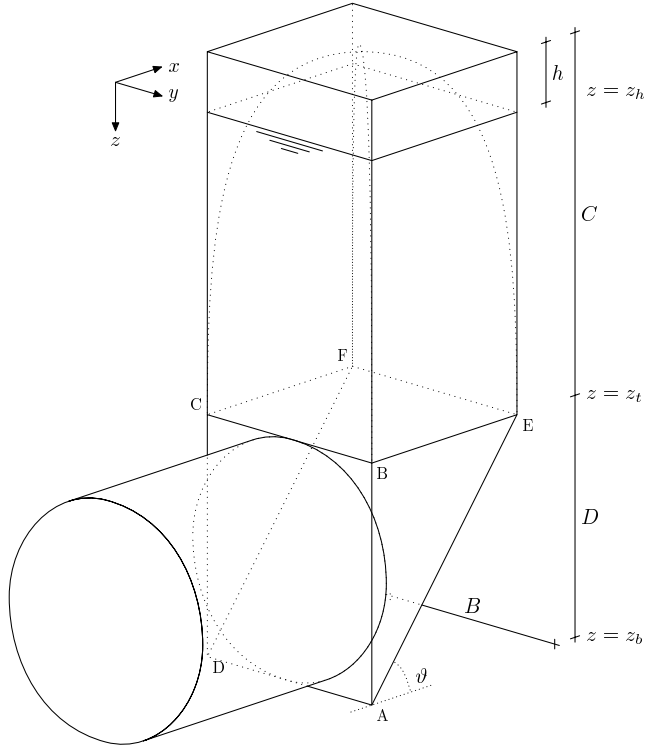


Figure 2.26: Wedge loaded by soil silo

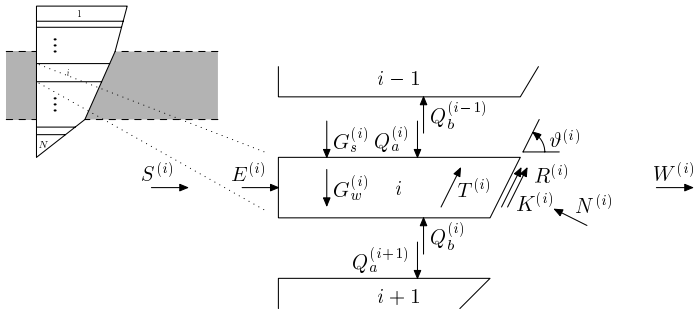


Figure 2.27: Definition of symbols in the multilayered wedge model

water force $W^{(i)}$, is equal to the support force $S^{(i)}$.

The conditions of horizontal and vertical equilibrium lead to

$$E^{(i)} + 2T^{(i)} \cos \theta^{(i)} + (K^{(i)} + R^{(i)}) \cos \theta^{(i)} - N^{(i)} \sin \theta^{(i)} = 0 \quad (2.24)$$

$$Q_a^{(i)} + G_s^{(i)} + G_w^{(i)} - Q_b^{(i)} - 2T^{(i)} \sin \theta^{(i)} - (K^{(i)} + R^{(i)}) \sin \theta^{(i)} - N^{(i)} \cos \theta^{(i)} = 0 \quad (2.25)$$

respectively [174]. Introducing $R^{(i)} = N^{(i)} \tan \varphi^{(i)}$ eliminates $N^{(i)}$ and combining (2.24) and (2.25) makes it possible to eliminate $R^{(i)}$, leading to

$$G_s^{(i)} + G_w^{(i)} + Q_a^{(i)} - Q_b^{(i)} + 2T^{(i)} \frac{1}{\zeta_-^{(i)}} + K^{(i)} \frac{1}{\zeta_-^{(i)}} + E^{(i)} \frac{\zeta_+^{(i)}}{\zeta_-^{(i)}} = 0 \quad (2.26)$$

Here the shorthand notation

$$\zeta_- = \tan \varphi \cos \theta - \sin \theta \quad (2.27)$$

$$\zeta_+ = \tan \varphi \sin \theta + \cos \theta \quad (2.28)$$

has been introduced. Each slice has to satisfy the equilibrium (2.26) as well as the continuity condition

$$Q_a^{(i)} = Q_b^{(i-1)} \quad (2.29)$$

for all i . Boundary conditions are $Q_b^{(N)} = 0$ and $Q_a^{(1)} = 0$. Using the boundary condition for slice N , it can be easily seen that for this slice (2.26) can be transformed to

$$\begin{aligned} Q_a^{(N)} &= Q_b^{(N-1)} \\ &= - \left[G_s^{(N)} + G_w^{(N)} + 2T^{(N)} \frac{1}{\zeta_-^{(N)}} + K^{(N)} \frac{1}{\zeta_-^{(N)}} + E^{(N)} \frac{\zeta_+^{(N)}}{\zeta_-^{(N)}} \right] \end{aligned} \quad (2.30)$$

This result can be combined with the equilibrium relation for slice $N - 1$ to yield

$$\begin{aligned} Q_a^{(N-1)} &= Q_b^{(N-2)} \\ &= - \left[G_s^{(N)} + G_s^{(N-1)} + G_w^{(N)} + G_w^{(N-1)} + 2T^{(N)} \frac{1}{\zeta_-^{(N)}} + 2T^{(N-1)} \frac{1}{\zeta_-^{(N-1)}} \right. \\ &\quad \left. + K^{(N)} \frac{1}{\zeta_-^{(N)}} + K^{(N-1)} \frac{1}{\zeta_-^{(N-1)}} + E^{(N)} \frac{\zeta_+^{(N)}}{\zeta_-^{(N)}} + E^{(N-1)} \frac{\zeta_+^{(N-1)}}{\zeta_-^{(N-1)}} \right] \end{aligned} \quad (2.31)$$

and so on for the slices $N - 2$ to 1 to finally yield

$$\begin{aligned} Q_a^{(1)} &= - \left[\sum_{i=1}^N G_s^{(i)} + \sum_{i=1}^N G_w^{(i)} + 2 \sum_{i=1}^N T^{(i)} \frac{1}{\zeta_-^{(i)}} + \sum_{i=1}^N K^{(i)} \frac{1}{\zeta_-^{(i)}} + \sum_{i=1}^N E^{(i)} \frac{\zeta_+^{(i)}}{\zeta_-^{(i)}} \right] \\ &= 0, \end{aligned} \quad (2.32)$$

where the upper boundary condition has been used.

For the case of a single slice wedge in a homogeneous soil, (2.32) simplifies to

$$G_s + G_w + (2T + K) \frac{1}{\zeta_-} + E \frac{\zeta_+}{\zeta_-} = 0 \quad (2.33)$$

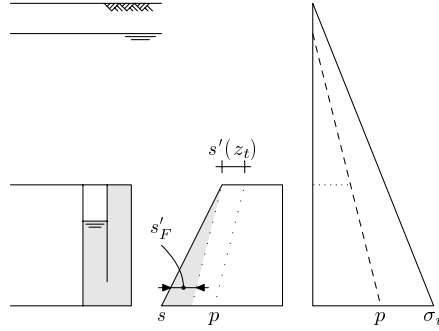


Figure 2.28: Support forces working at the tunnel face

from which E can be solved as

$$E = -\frac{\zeta_- (G_s + G_w) + (K + 2T)}{\zeta_+} \quad (2.34)$$

which corresponds with the result obtained by Walz [174] and Jancsecz [89]. For this simplified case the forces acting on the wedge can be found straightforwardly as

$$G_s = BD \cot \theta \sigma'_v(z_t) \quad (2.35)$$

$$G_w = \frac{BD^2 \cot \theta}{2} \gamma' \quad (2.36)$$

$$K = \frac{BD}{\sin \theta} c \quad (2.37)$$

$$T = \frac{D^2 \cot \theta}{2} (c + K_y \bar{\sigma}'_v \tan \varphi) \quad (2.38)$$

with

$$\bar{\sigma}'_v = \sigma'_v(z_t) + \frac{1}{3} D \gamma' \quad (2.39)$$

and B the wedge width, the influence of which will be discussed in section 2.3. The minimal required support pressure $S = E + W$ can be found by iterating over all θ and maximising E . This is the basic form in which the wedge stability model has also been presented by amongst others Jancsecz & Steiner and Anagnostou & Kovári.

For the construction of a wedge stability model that can deal with heterogeneity as well as infiltration and excess pore pressures, the finite sum representation (2.32) will be converted to an integral representation. Before doing this, a closer look is needed at the distribution of the effective support pressure acting at the tunnel face. As sketched in figure 2.28, the support force can be split into a part depending solely on the effective pressure at $z = z_t$ and a part depending on the effective weight of the support medium. With the effective bentonite pressure

$$s'_F = \int_{z_t}^z \gamma'_F dz \quad (2.40)$$

the deviatoric support force is defined as

$$S'_{\text{dev}} = B \int_{z_t}^{z_b} \frac{\zeta_+}{\zeta_-} s'_F dz \quad (2.41)$$

As $s'(z_t)$ is a constant, it can be easily seen that the integral representing the vertical effective force depending on the effective support pressure can be split into

$$B \int_{z_t}^{z_b} \frac{\zeta_+}{\zeta_-} s' dz = S'_{\text{dev}} + Bs'(z_t) \int_{z_t}^{z_b} \frac{\zeta_+}{\zeta_-} dz \quad (2.42)$$

which will be used to find an explicit relation for the minimal support pressure, given the effective weight of the support medium γ'_F .

Taking $N \rightarrow \infty$ it follows from (2.32) that the minimal support pressure at $z = z_t$ can be calculated from maximising

$$s'(z_t) = - \frac{G_s + G_w + K' + 2T' + S'_{\text{dev}}}{Z} \quad (2.43)$$

over θ , where

$$T' = \int_{z_t}^{z_b} \frac{w}{\zeta_-} [c + K_y \sigma'_v \tan \phi] dz \quad (2.44)$$

$$K' = B \int_{z_t}^{z_b} \frac{c}{\zeta_- \sin \theta} dz \quad (2.45)$$

$$G_s = \frac{BD}{\tan \theta} \sigma'_v(z_t) \quad (2.46)$$

$$G_w = B \int_{z_t}^{z_b} w \gamma' dz \quad (2.47)$$

$$Z = B \int_{z_t}^{z_b} \cot(\phi - \theta) dz \quad (2.48)$$

and $w = (z_b - z) \cot \theta$ for $z_t \leq z \leq z_b$. It should be noted at this point that in general all variables under the integrals are z -dependent, even though this dependence has not been written explicitly.

Having obtained (2.43) makes it possible to determine the required effective support pressure $s'(z_t)$ for a given angle θ and, given the distribution of the effective weight of the support medium γ'_b and the pore water pressures p , the required support pressure on the entire face $s = s' + p$. The desired minimal support pressure can be found by maximising s as function of θ . The angle for which the required support pressure is largest represents the failure mode most likely to occur. This procedure is less straightforward than it may seem, however, as a number of additional effects, like soil arching and excess pore pressures, have to be taken into account.

2.2.2 Vertical Stress Distribution

One of the main effects that has to be taken into account when using a wedge model to accurately estimate the minimal support pressure is soil arching. From centrifuge tests [37, 60] reviewed in section 2.1.4 it can be observed that part of the soil column above the wedge does not act as a load on the wedge, but is carried by the surrounding soil. The effective load acting on top of the wedge G_s is therefore less than the total weight of the soil above the tunnel, as can be visualized from figure 2.19. This arching effect has also been observed by Terzaghi in trap door experiments [161] and later applied by Huder for the calculation of arching effects around slurry-filled trenches [82]. We will follow a similar approach to include this effect in the face stability calculation [138].

Terzaghi modelled a strip of the soil, as sketched in figure 2.29, loaded by the stress $\sigma'_{v,a}$ resulting from the silo above it and its effective weight γ' . Along the sides of the strip of the

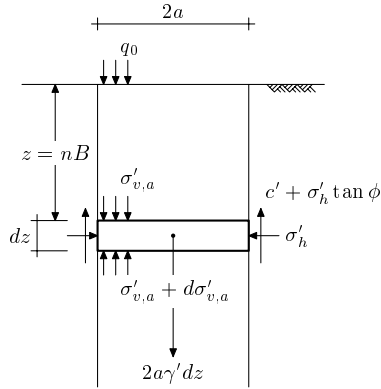


Figure 2.29: Definition of forces acting on a strip of soil in an arching soil column

silo acts a shear force τ , which transports part of the load onto the surrounding soil. Vertical equilibrium for a strip of width $2a$ and unit length demands that

$$2a \sigma'_{v,a} + 2a \gamma' dz - 2\tau dz = 2a (\sigma'_{v,a} + d\sigma'_{v,a}) \quad (2.49)$$

If $\tau = c' + K \sigma'_{v,a} \tan \phi'$ this leads to

$$\frac{d\sigma'_{v,a}}{dz} = \gamma' - \frac{c' + K \sigma'_{v,a} \tan \phi'}{a} \quad (2.50)$$

Solving this equation, using the boundary condition $\sigma'_{v,a} = q_0$ for $z = 0$, with q_0 an arbitrary surface surcharge, leads to

$$\sigma'_{v,a} = \frac{a\gamma' - c'}{K \tan \phi'} \left(1 - e^{-K \tan \phi' \frac{z}{a}} \right) + q_0 e^{-K \tan \phi' \frac{z}{a}} \quad (2.51)$$

In a layered soil, a similar result can be obtained for each separate layer, integrating from top to bottom and using the effective stress at the bottom of the previous layer as the continuity condition for the following layer. For layer i with top $z = t^{(i)}$ it is found that

$$\sigma'_{v,a} = \frac{a\gamma'^{(i)} - c'^{(i)}}{K^{(i)} \tan \phi'^{(i)}} \left(1 - e^{-K^{(i)} \tan \phi'^{(i)} \frac{z}{a}} \right) + \sigma'_{v,a}(t_i) e^{-K^{(i)} \tan \phi'^{(i)} \frac{z}{a}} \quad (2.52)$$

for $t^{(i)} \leq z < t^{(i+1)}$. Again a surcharge can be applied on top of the first layer $i = 1$, so that $\sigma'_{v,a}(0) = q_0$ and the distribution of effective vertical stresses with depth is completely determined.

A point of discussion is the relaxation length a to be used in the calculations. Terzaghi models an infinitely long or two dimensional silo, where the shear stress only acts on two sides of the silo. Jancsecz [89] on the other hand proposes a column of soil with a width equal to the tunnel diameter D and depth equal to the wedge depth at the top, $w(z_t) = D \cot \theta$ (see figure 2.30) and shear stresses acting on all four silo boundaries. Using this approach the relaxation length a in (2.52) is found as the quotient of area over circumference of the silo,

$$a = \frac{A}{O} = \frac{BD \cot \theta}{2(D + B \tan \theta)} \quad (2.53)$$

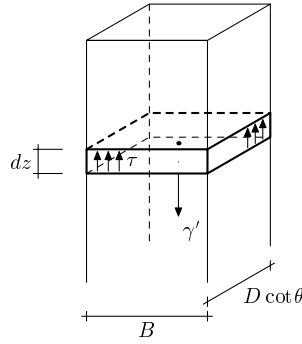


Figure 2.30: Arching soil column with shear forces on all boundaries

Although this seems to take into account the three-dimensional nature of the soil silo, Huder has shown that for slurry trenches the two-dimensional schematisation, where $2a$ is equal to the largest length of the trench, is in good agreement with field observations. The equivalent approximation for the face stability model leads to

$$a = \frac{B}{2} \quad (2.54)$$

This leads to three possible ways to estimate the vertical load on the top of the wedge: (a) without soil arching, (b) with two-dimensional arching or (c) with three-dimensional arching. The results of these model implementations will be compared to a number of centrifuge tests reported in literature. For now the possible influence of the wedge width B will be neglected and it will be assumed that $B = D$. The relaxation length for the different cases can then be simplified to

$$a = \infty, \quad (2.55a)$$

$$a = R, \quad (2.55b)$$

$$a = R \frac{1}{1 + \tan \theta}. \quad (2.55c)$$

The resulting vertical stresses for an example in dry sand ($c' = 0, \phi' = 35^\circ, \gamma = 20 \text{ kN/m}^3$) have been plotted in figure 2.31.

Having established the vertical stress on top of the wedge, a further problem arises with the distribution of vertical stresses along the sides of the wedge and the accompanying horizontal stresses, which contribute to the force T . Again three possible implementations are suggested. The first possibility is to disregard any arching effects when calculating the horizontal stresses at the wedge sides. The second option is to continue the arching stress distribution $\sigma'_{v,a}$ given by (2.52) and derive the horizontal stresses from this. A third option would be to choose the stress on the wedge sides in such a manner that it falls between the first two options, for example to linearly interpolate the vertical stress between the stress including arching at the top of the wedge, $\sigma'_{v,a}(z_t)$, and the vertical stress without arching effects $\sigma'_v(z_b)$ at the bottom of the wedge, as sketched in figure 2.32 [93].

The idea behind this last model is that the soil-arch widens with depth and is caused by deformations at the top of the tunnel only. That would then result in an increase of the total stresses below the top of the tunnel, either proportional to γ or to the stress level without arching

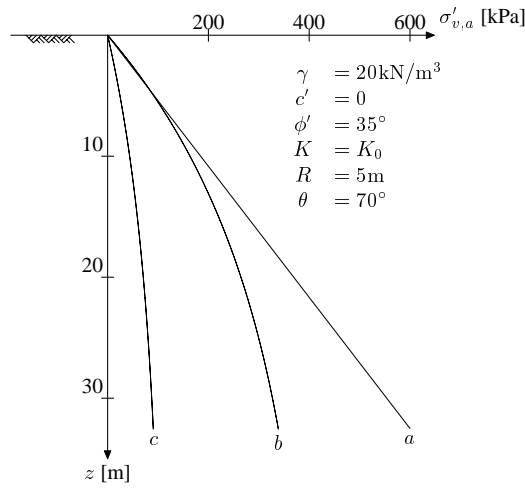


Figure 2.31: Vertical stress distribution for different arching implementations

effects. Deformation occurs over the entire face and not only at the top of the wedge and as such this model is not considered very likely. Furthermore, in slurry-filled trenches it has been observed that an effective stress reduction occurs within the deforming soil body, but also that this body is defined by clear shear bands and that outside these shear bands no stress reduction or even a slight stress increase can be observed. Therefore an intermediate model has not been implemented.

The combined effects of soil arching and the stress distribution on the wedge sides lead to nine possible implementations, which we will refer to as a_1, a_2 , etc. As a_1, a_2 and a_3 are completely identical and, as said above, b_3 and c_3 have not been implemented, this leaves five different possible models. Within each of these models the value of K_y is needed to calculate

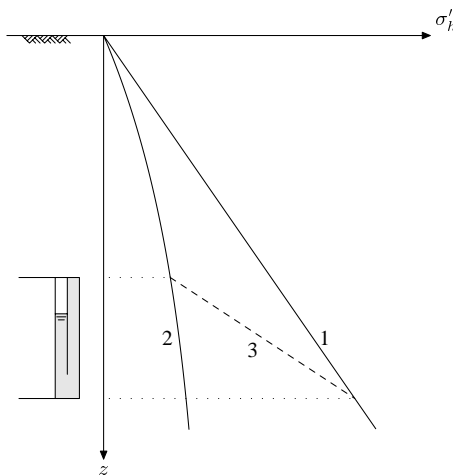


Figure 2.32: Possible horizontal stress distributions along wedge sides

Test ^b	Meas.		Calculated s' divided by Measured s' ^a										Best Result
	s' (kPa)	a_0	a_a	$b_{1,0}$	$b_{1,a}$	$b_{2,0}$	$b_{2,a}$	$c_{1,0}$	$c_{1,a}$	$c_{2,0}$	$c_{2,a}$		
CS0.5/5	3.6	3.65	4.45	3.26	4.20	3.76	4.42	2.54	3.70	3.73	4.31	$c_{1,0}$	
CS0.5/5	3.3	4.00	4.88	3.58	4.61	4.12	4.85	2.79	4.06	4.09	4.73	$c_{1,0}$	
CS1/5	3.5	5.52	6.85	4.08	5.81	5.14	6.33	1.97	4.19	4.48	5.52	$c_{1,0}$	
CS1/5	3.0	6.41	7.95	4.73	6.74	5.97	7.35	2.28	4.87	5.20	6.41	$c_{1,0}$	
CS1/5	3.3	5.79	7.18	4.27	6.09	5.39	6.64	2.06	4.39	4.70	5.79	$c_{1,0}$	
CS1/10	7.4	5.13	6.35	3.77	5.40	4.78	5.89	1.83	3.89	4.15	5.13	$c_{1,0}$	
CS2/5	4.0	7.64	9.60	3.52	6.48	5.78	7.67	0.00	2.88	4.12	5.53	$c_{1,0}, c_{1,a}$	
CS2/10	8.0	7.66	9.63	3.53	6.48	5.79	7.68	0.00	2.88	4.12	5.54	$c_{1,0}, c_{1,a}$	
CS4/10	8.2	13.2	16.8	1.81	6.91	6.82	10.1	0.00	0.12	4.09	5.81	$b_{1,0}$	
CS4/13	13.4	10.9	13.8	1.40	5.58	5.53	8.17	0.00	0.02	3.31	4.70	$b_{1,0}$	
BS0.8/10	6.6	1.76	3.24	1.76	2.91	2.16	2.67	0.98	2.41	1.96	2.41	$c_{1,0}$	
BC0.8/10	17.0	1.30	1.50	1.04	1.29	1.22	1.39	0.67	0.99	1.09	1.25	$b_{1,0}$	
BC0.6/10	11.0	1.69	1.69	1.45	1.51	1.65	1.87	1.07	1.16	1.55	1.75	$c_{1,0}$	

^aFormat is $a_{n,m}$: a = arching model (a = none, b = 2D, c = 3D), n = stress on wedge sides (1 = linear, 2 = incl. arching), m = K -value used (0 = K_0 , a = K_a)

^bFormat is ATn/m: A = Author, T = Type of Test, n = Overburden-Diameter Ratio, m = Diameter in m. Authors: B=Bezuijen [37], C=Chambon [60]. Type: S=Sand, C=Clay.

Table 2.4: Comparison of centrifuge test results with models with different arching implementations

T , and from that E . Two possible values $K_y = K_0$ and $K_y = K_a$ have been implemented and will be referred to as $a_{1,0}$ and $a_{1,a}$, etc. The support pressure calculated with each of these implementations is compared with the results from the centrifuge tests by Bezuijen [37] and Chambon [60] in table 2.4. Here the measured values of s' are listed, as well as the ratio of the calculated value over the measured value.

The comparison between centrifuge test results and calculated support pressures does not yield a definite answer which arching model to use. This is partly due to the limited number of centrifuge tests and the differences between the tests. The tests reported by Chambon & Corté have been performed in dry Fontainebleue sand with a reported $\phi' = 35^\circ$. These tests show a different behaviour with varying overburden. For the tests with low overburden, $C/D \leq 1$, the $c_{1,0}$ model yields the best, and safe, prediction of the required support pressure. For the tests with an overburden 2 times the tunnel diameter, the $c_{1,0}$ model again yields the closest match, but this time it gives an unsafe prediction of the required support pressure and the best safe prediction is obtained with the $c_{1,a}$ model. For the deeper tunnels, with $C/D = 4$, the best prediction is obtained with the $b_{1,0}$ model. In this case both the $c_{1,0}$ and the $c_{1,a}$ model yield an unsafe prediction.

The tests by Bezuijen on the other hand have been done in completely saturated sand ($\phi' = 35.6^\circ$) and soft clay samples ($\phi' = 23^\circ, c' = 1\text{kPa}$) with low overburdens, $C/D = 0.6$ or 0.8 . The results of two tests are best predicted by the $c_{1,0}$ arching model. In one case this a slightly unsafe prediction and the best safe prediction is obtained with the $b_{1,0}$ model. For the third test the $b_{1,0}$ model yields the best safe prediction, although the $c_{1,a}$ and the $c_{2,0}$ models are also very close.

Based on this small number of tests it must be concluded that overall the $c_{1,0}$ model yields the most accurate prediction of the minimal support pressure at which complete failure occurs and the $c_{1,0}$ model will be used in further calculations. This model does however yield an unsafe prediction for several cases, especially the deeper tunnels with $C/D = 4$. In those cases the $b_{1,0}$ model yields a better prediction. That the $c_{1,0}$ model yields the unsafe prediction that the face is stable even without support may be due to an overestimation of the stress reduction caused

by soil arching. Given the fact that the $b_{1,0}$ yields a safe prediction in all cases, this model may be preferable from an engineering point of view. This choice may be further strengthened if it is desired to limit the deformations caused by the excavation process.

The various arching implementations can be roughly associated with the amount of deformation that occurs at the face. The support pressure found from the c models is the pressure at which total failure of the face occurs, at which point large deformations have already occurred. The b models on the other hand seem to yield the support pressure at which only limited deformation of the face occurs. Such limited deformations are needed to initiate the friction forces and are inevitable in the boring process. The a models are equated to a situation where no deformation has occurred and as a result the a model strongly overpredicts the minimal required support pressure. In combination with the effect of slurry infiltration and excess pore pressures as described next, these models would yield extremely high required support pressures, resulting in extremely high overburden requirements, which are not backed by any field experience.

The influence of the choice of the arching model and K_y will be briefly illustrated in section 2.3 for the reference case described there. Based on the limited evidence available, however, all further calculations will be made with the $c_{1,0}$ model in order to best predict the minimal required support pressure. The fact that it may yield unsafe support pressures, possibly due to variations in the soil properties, should be overcome by the use of safety factors. And as is true in all cases where limit equilibrium models are used, the possible occurrence of failure by a different mechanism, in particular micro-stability, must be checked separately.

2.2.3 Penetration of Support Medium

Another effect that has to be taken into account, in particular when boring in permeable soils, is the penetration of the support medium into the soil. This infiltration may in turn lead to excess pore pressures in front of the TBM as well as a reduction of the effective support force.

If a bentonite slurry is used, the bentonite should ideally form a thin impermeable filter cake on top of the face. The entire support force from the slurry is then transported onto the soil skeleton at the face. In reality the slurry will always infiltrate the pores to a certain extent before clogging of the pores occurs and a filter cake is formed. The support pressure is then transported onto the soil skeleton over this infiltration length. This situation is sketched in figure 2.33. In case the soil is very coarse and the pores are very large, the bentonite will fail to form a filter cake, however, and infiltrate the soil to a much larger depth. The support force is then transported onto the soil skeleton by drag forces. Most practical cases will show a mixture of those two effects, type 3 in figure 2.33.

From experiences with slurry-filled trenches [93, 164] it is known that the infiltration of the slurry into the soil reduces the effectiveness of the support. If the slurry infiltrates the soil to such an extent that the infiltration length e is larger than the wedge width w at a certain depth, part of the support force is transferred onto the soil outside the collapsing soil body and thereby does not help to stabilise the tunnel face. Only the pressure drop over the wedge width may be reckoned in the effective support force. If both the infiltration length e and the pressure distribution over this length are known, the effective support force can be found by integrating the remaining slurry pressure $\Delta p(x, z)$ at the wedge face (see figure 2.36 for definitions) over the entire face and subtracting this from the support force S ,

$$S' = S - \int_{z_t}^{z_b} p(w(z), z) dz \quad (2.56)$$

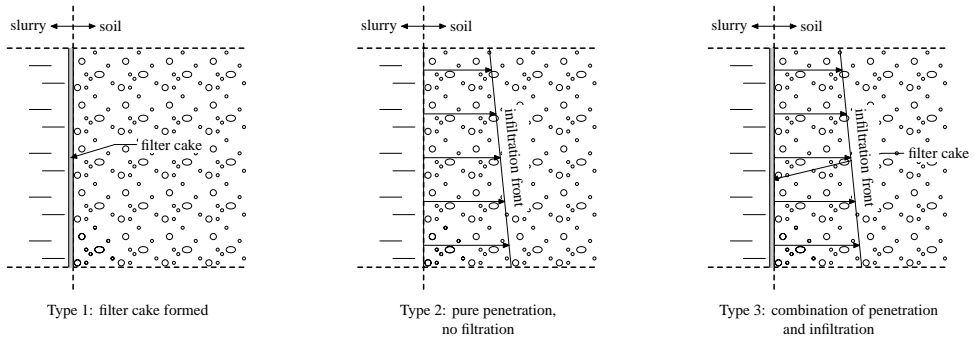


Figure 2.33: Three cases of slurry infiltration: (a) formation of filter cake only; (b) pure penetration, no filtration; (c) combination of filtration and penetration [123]

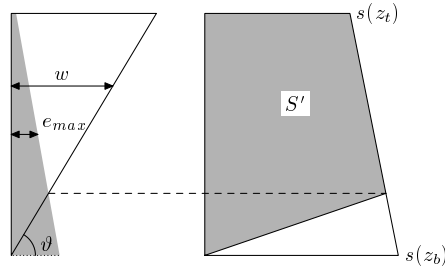


Figure 2.34: Approximative method for the effective support pressure

This effective support force S' should be greater or equal to the effective earth force E to keep the face stable.

If only the infiltration length is known, the effective support force can be approximated. Above the depth z for which it holds that $e_{\max} = w$ the entire support pressure is included. Below this point the support pressure is cut off linearly, as sketched in figure 2.34. A similar approximation method has been used by Anagnostou & Kovári [8] in their wedge stability model. For small infiltration lengths the reduction of the effective support force is small and these approximative methods yield acceptable results.

In a model which includes the effects of excess pore pressures it is necessary to evaluate an integral of the support pressure distribution as a function of distance to the tunnel face and depth, which has the same basic form as (2.56), in order to calculate the effective support force. If we choose to first establish the support pressure distribution $\Delta p(x, z)$ where both slurry infiltration and groundwater flow are taken into account and evaluate this integral irrespectively of the occurrence of excess pore pressures and slurry infiltration and independently of the possibility to use an approximative method, the resulting model will actually be simplified. The problem then has been shifted to establishing the pressure distribution.

From column infiltration tests, Krause [98] has determined that the infiltration length e of the slurry is a hyperbolic function of time,

$$e(t) = \frac{t}{a+t} e_{\max} \quad (2.57)$$

where the maximum infiltration length e_{\max} at which stagnation occurs can be found from an

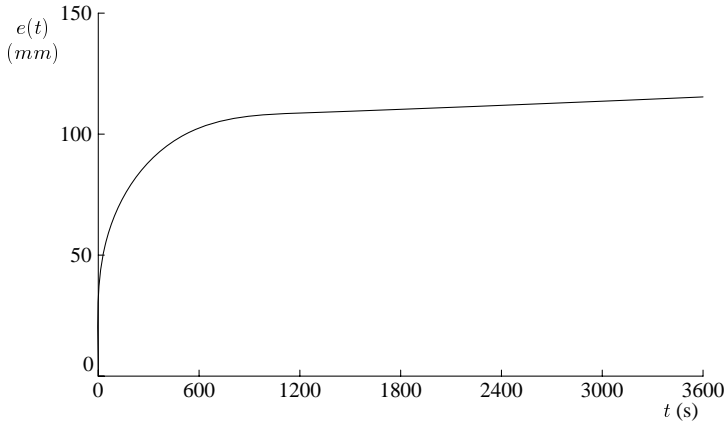


Figure 2.35: Example of slurry infiltration length vs time [98]

empirical relation of the form

$$e_{\max} = \frac{\Delta p d_{10}}{\alpha \tau_F} \quad (2.58)$$

Here Δp is the pressure drop over the filter cake and α and a parameters that should be determined from a column infiltration test. Several authors give differing values for α , but all within the range $\alpha \approx 2-4$ [93, 98, 123].

If one substitutes $t = a$ in (2.57) it can be easily seen that a is the timespan to reach half of the final infiltration length. From experiments by Krause [98], where figure 2.35 gives an example, it can be seen that $a \approx 60 - 180$ s in relatively coarse sand for bentonite suspensions with low τ_F . For finer sands $a \approx 5 - 20$ s or even as low as $a = 1$ s has been reported by Huisman [84]. Although there clearly is a dependence between a on the one hand and d_{10} , τ_F and possibly Δs on the other hand, no relationships are found in literature.

If at $t = 0$ the slurry is applied to the face or the existing filter cake is removed, the slurry will start to infiltrate the soil and at first only a partial filter cake will exist. As the initial infiltration speed is much larger than the speed of the TBM and the speed with which the excavation face moves forward, this speed will be neglected in the description of the infiltration process. Assuming that (2.58) can be inverted for a given infiltration length and combining this with (2.57), an estimate of the pressure drop over this partial filter cake can be obtained from

$$\Delta p_{fc}(t) = \frac{\alpha \tau_F}{d_{10}} e(t) \quad (2.59)$$

If the further assumption is made that the pressure drop within the cake is linear, the pressure within the cake at a certain time is found as

$$p_{fc}(x, t) = s - \frac{\alpha \tau_F}{d_{10}} x \quad x \leq e(t) \quad (2.60)$$

with x the distance from the face and p_0 the pore pressure at rest (see also figure 2.36).

When looking in more detail, the pressure drop within the filter cake is non-linear. This is especially true for small infiltration lengths. Several authors [34, 118] have used a column infiltration test setup to determine the slurry pressure as a function of the distance to the face. A

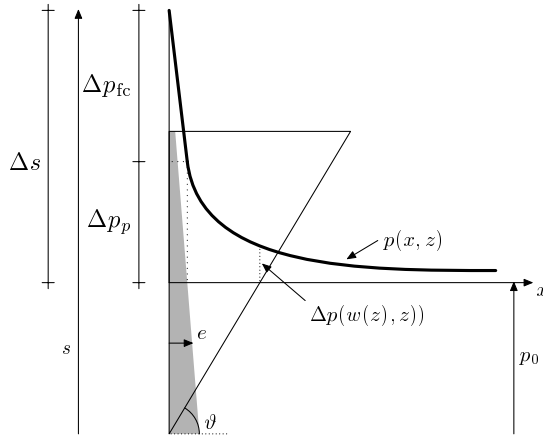


Figure 2.36: Definition of pressure distribution over penetration zone and excess pore pressures

typical result from tests performed by Mohkam is shown in figure 2.37. This non-linear pressure drop within the filter cake will not be included in the stability model. For small infiltration lengths, the non-linear pressure distribution of the groundwater flow, if present, will be dominant and this will be included. For increasing infiltration lengths, the non-linearity decreases and the pressure distribution over the infiltration zone can be reasonably well approximated by a linear relation.

Of course the filter cake is not instantly removed in its entirety, but rather limited zones are excavated by the individual cutter bits. This implies that the infiltration depth of the bentonite, and therefore the pressure drop over the partial filter cake, varies over the face. For the purpose of the stability model a mean pressure drop for the entire face is sufficient, however. If the cutter bits are spaced evenly and non-overlapping over the face, the filter cake will have a timespan t_r , equal to one full rotation of the cutter wheel, to build before it is removed again. Integrating the

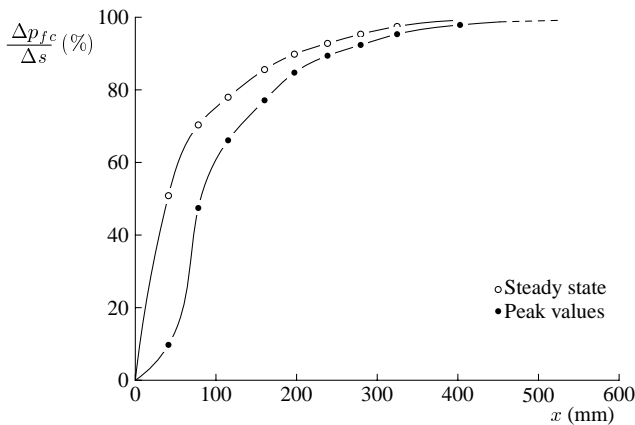


Figure 2.37: Slurry pressure as function of the distance from the face (closed boxes represent peak values, open boxes represent steady state values) [118]

infiltration length $e(t)$ from (2.57) over this timespan and equating this to the infiltration length obtained with a mean infiltration time t_F ,

$$\int_0^{t_r} e(t) dt = \frac{t_F}{a + t_F} e_{\max} t_r \quad (2.61)$$

establishes the mean infiltration time as

$$t_F = \frac{t_r}{\ln(1 + t_r/a)} - a \quad (2.62)$$

and from this an estimate of the mean pressure drop over the entire face is found by setting $t = t_F$ in (2.59).

Having obtained the pressure drop (2.59) the remaining slurry pressure at the far end of the filter cake can be calculated as

$$\Delta p_p = \Delta s - \Delta p_{fc} \quad (2.63)$$

and this value can in turn be used to determine the hydraulic head as input for a groundwater flow calculation (see figure 2.36 for definitions). A description of the groundwater situation around the TBM in full detail will require a time-dependent three-dimensional groundwater model, where heterogeneous soil and possible soil lenses can be included. This implies the use of a full-fledged 3D numerical model, which would make the resulting stability model overly complex and calculations time consuming. To get around this problem we will simplify the groundwater flow problem, preferably to a schematisation that allows an analytical solution. First the simplification of the groundwater flow to a one-dimensional steady-state schematisation will be made, whereby each soil layer will be described as a separate semi-confined aquifer. In homogeneous soils or heterogeneous situations where the schematisation to a one-dimensional semi-confined aquifer is not suitable, some modifications will be made to describe the groundwater flow in front of the TBM more accurately. Later on other possible methods to calculate the excess pore pressures will be taken into account.

The steady state hydrostatic pressure $p(x, z)$ in a semi-confined horizontal aquifer is given by

$$p(x, z) = p_0(z) + \Delta p(z) \exp(-x/\lambda) \quad (2.64)$$

where λ is the leakage factor of the aquifer, which can be computed from the permeability k and height H of the aquifer and the hydraulic resistance \tilde{c} of the overlying aquitard,

$$\lambda = \sqrt{kH\tilde{c}}. \quad (2.65)$$

One is referred to appendix A for the basics of groundwater mechanics and the derivation of (2.64). Equating $\Delta p(z)$ in (2.64) to Δp_p in (2.63) completely establishes the pressure distribution over the wedge,

$$p(x, z, t) = \begin{cases} s - \frac{\alpha \tau_E}{d_{10}} x & 0 \leq x < e(t) \\ p_0 + \Delta s \frac{t}{a+t} \exp(-(x - e(t))/\lambda) & e(t) \leq x \leq w(z) \end{cases} \quad (2.66)$$

if $e(z, t) \leq w(z)$ or simply (2.60) if $e(z, t) > w(z)$. At the same time the excess pore pressure distribution $\Delta p(x, z, t) = p(x, z, t) - p_0(z)$ is established.

Having established (2.66) it is possible to include the influence of the excess pore pressures in the wedge equilibrium. The excess pore pressures at the top of the wedge generate an uplift force which lowers G_s compared to the situation without excess pore pressures. This uplift force is equal to $B \int_0^{w(z_t)} \Delta p(x, z_t, t) dx$ and is already included in (2.46) if excess pore pressures are accounted for in the calculation of σ'_y . The excess pore pressures also lower the shear forces T' on the sides of the wedge, given by (2.44). If these effects are taken into account the wedge equilibrium (2.43) again leads to the required effective support pressure. Another option is of course to neglect the influence of excess pore pressures in the calculation of G_s and T' and calculate those forces from (2.46) and (2.44) using effective pressures obtained with the water pressures at rest, $\sigma' = \sigma - p_0$. The uplift force

$$P_s = B \int_0^{w(z_t)} \Delta p(x, z_t, t) dx \quad (2.67)$$

and shear force reduction

$$P_T = \int_{z_t}^{z_b} \int_0^{w(z)} \frac{1}{\zeta_-} K_y \tan \phi \Delta p(x, z, t) dx dz \quad (2.68)$$

are then explicitly included in the wedge equilibrium, which becomes

$$s'(z_t) = - \frac{G_s - P_s + G_w + K' + 2T' - 2P_T + S'_{dev}}{Z} \quad (2.69)$$

In this formulation special attention must be paid to the fact that both $G'_s = G_s - P_s$ and $T' - P_T$ must be greater or equal to 0 if no tension forces are allowed in the soil. The required support force S can now be found from

$$\begin{aligned} S &= E + W = S' + W \\ &= B \int_{z_t}^{z_b} s'(z, t) dz + B \int_{z_t}^{z_b} p(w(z), z, t) dz. \end{aligned} \quad (2.70)$$

This completes the framework for the basic stability model including excess pore pressures. Section 2.2.4 will deal with the solution scheme and the determination of a number of model parameters, and in sections 2.3 and 2.4 the model will be validated on the basis of field cases and a model sensitivity analysis antirespectively. However, a number of implicit assumptions has been made about the groundwater flow included in the basic model. These deserve closer attention.

Firstly, the excess pore pressure distribution assumes a steady state flow, which will take a certain timespan to develop. This timespan may under certain conditions be longer than the time between subsequent stand-stills of the TBM, when no or only limited infiltration takes place and excess pore pressures can dissipate. To investigate the influence of the excavation and stand-still timespans in relation to the conductivity of the soil, an estimate of the discharge from the excavation chamber and a transient groundwater flow model are needed. The second assumption is that in cases where multiple soil layers are present at the tunnel face, the excess pore pressure distribution in all of these layers is given by (2.66), and the separate layers do not interact. In the model as described this assumption is also used for cases where layers are in fact aquitards or where an interacting system of aquifers exists. A groundwater flow model for coupled aquifers would be needed to investigate the influence of this simplification. The following paragraphs will deal with these assumptions in reverse order.

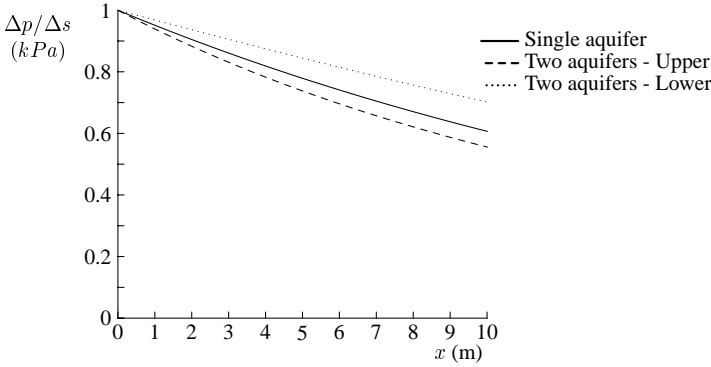


Figure 2.38: Comparison between pressure distribution in a single aquifer and a set of two interacting aquifers

Solving the system of differential equations for a coupled set of interacting semi-confined aquifers is somewhat more intricate than solving a one-dimensional groundwater flow problem. Appendix A outlines the general solution procedure and goes into more detail for a system of two aquifers. Suppose two layers $i = 1, 2$ with k_i , H_i and \tilde{c}_i are subject to an excess pore pressure Δp at the face. The pressure distributions p_i in the aquifers are then given by

$$p_1 = p_0 + \Delta p A^+ e^{-\omega_1 x} + \Delta p A^- e^{-\omega_2 x} \quad (2.71)$$

$$p_2 = p_0 + \Delta p A^+ \alpha_{2,1} e^{-\omega_1 x} + \Delta p A^- \alpha_{2,2} e^{-\omega_2 x} \quad (2.72)$$

with p_0 the hydrostatic pressure and

$$a_{i,j} = \frac{1}{k_i H_i \tilde{c}_j} \quad (2.73)$$

$$A^\pm = \pm \frac{a_{1,1} + a_{1,2} - 3a_{2,2} \pm \sqrt{(a_{1,1} - a_{2,2})^2 + 2(a_{1,1} + a_{2,2})a_{1,2} + a_{1,2}^2}}{2\sqrt{(a_{1,1} - a_{2,2})^2 + 2(a_{1,1} + a_{2,2})a_{1,2} + a_{1,2}^2}} \quad (2.74)$$

$$\alpha_{2,j} = \frac{a_{1,1} + a_{1,2} - \omega_j^2}{a_{2,2}} \quad (2.75)$$

$$\omega_j^2 = \frac{1}{2}(a_{1,1} + a_{1,2} + a_{2,2}) + \frac{1}{2}\sqrt{(a_{1,1} - a_{2,2})^2 + 2(a_{1,1} + a_{2,2})a_{1,2} + a_{1,2}^2} \quad (2.76)$$

Although slightly more complicated, the resulting pressure distributions do not differ much, as can be seen in figure 2.38, where a system of two layers with $H_1 = H_2 = 2\text{m}$, $k_1 = k_2 = 10^{-5}\text{m/s}$, $\tilde{c}_1 = \tilde{c}_2 = 10^7\text{s}$ is compared with a single aquifer $k = 10^{-5}\text{m/s}$, $H = 4\text{m}$, $\tilde{c} = 10^7\text{s}$. For the stability model the pressure distribution over the wedge width, approximately up to $D/2$ from the face, is of main importance. As the pore pressure distribution for the single aquifer differs little from the solution for the two-aquifer case over this interval, the single aquifer has been used for simplicity.

A different case is where there are no confining layers above the tunnel. In this case a solution for unconfined flow conditions would be preferred over semi-confined flow. To simplify the problem, Bezuijen [33] chose a spherical well with radius $r_w = D/2$ centred at the tunnel

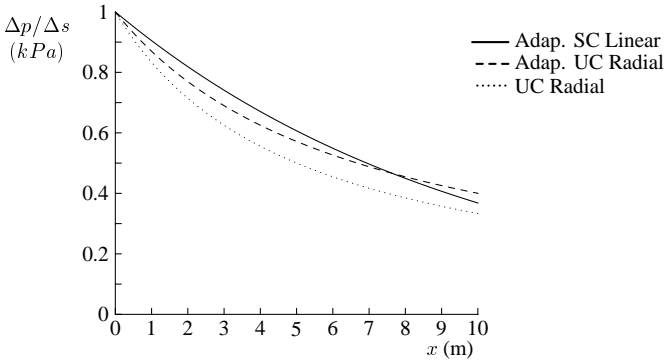


Figure 2.39: Comparison between unconfined radial, adapted unconfined radial and adapted semi-confined linear groundwater flow

face instead of a plane tunnel face and neglected any influence from the surface discontinuity. The resulting pressure distribution is

$$p = p_0 + \Delta p \frac{R}{x + R} \quad (2.77)$$

Bezuijen has shown that the excess pore pressure distribution resulting from a simple radial flow model yields a relatively steep gradient i at the face when compared with three-dimensional numerical groundwater flow calculations [39] or field measurements. As the pore pressure distribution within the failure wedge is of main importance for the stability analysis, he proposes a scaling factor to reduce the gradient within the wedge resulting from a radial flow model. To keep the same difference in hydraulic head this implies scaling the distance from the well with this factor. Another solution to this problem is to use the same exponential distribution as with semi-confined flow, but to choose a suitable value for the leakage length, i.e. $\lambda = D\sqrt{C/D}$.

For a 10m diameter tunnel, $C/D = 1$, in an unconfined aquifer with $k = 10^{-4}$ m/s, and $\Delta s = 35$ kPa, Bezuijen uses three-dimensional numerical investigations to find a scaling factor. Using this value, figure 2.39 shows the pore pressure distribution resulting from unadapted radial flow, scaled radial flow and from semi-confined flow using $\lambda = D\sqrt{C/D}$. It is clear that the difference between the adapted radial and adapted linear flow solutions is minimal over the width of the wedge. For simplicity of further calculations the semi-confined flow distribution has been used even where it is not fully justified.

Secondly, in order to determine the rise of excess pore pressures with time, the discharge from the face will be determined first. There are three straightforward ways of determining this discharge. The first possibility is to use the average infiltration speed of the bentonite infiltration zone, the second is to derive the discharge from the static groundwater flow model and the third is to use laboratory and field experiences.

For the first option, differentiating (2.57) with respect to time yields the infiltration speed

$$v_e = \frac{a}{(a+t)^2} e_{\max} \quad (2.78)$$

which, multiplied by the porosity of the soil, yields a discharge

$$q_e = n v_e \quad (2.79)$$

For the second option we use the semi-confined linear static flow equation (2.64). The discharge follows from (A.1) as

$$q_x = \frac{k \Delta p_p}{\lambda \gamma_w} \exp(-x/\lambda). \quad (2.80)$$

The third option is to use field and laboratory observations. According to Mohkam [117, 118] the amount of water displaced by the penetrating slurry for each full turn of the cutting wheel is equal to the amount of pore water in the excavated soil, so that

$$q_c = \frac{l_{\text{cut}}}{t_{\text{cut}}} n \quad (2.81)$$

where l_{cut} is the cutting depth and t_{cut} the time needed for a full turn of the cutter wheel.

Each of these discharges can be used in a solution for transient flow in a semi-confined aquifer, the derivation of which is given in [49], see appendix A;

$$\varphi = \varphi_0 + \frac{Q\lambda}{4kH} \left[\operatorname{erfc} \left(\frac{xu}{2\sqrt{t}} + \frac{\sqrt{t}}{u\lambda} \right) \exp \left(\frac{x}{\lambda} \right) - \operatorname{erfc} \left(\frac{xu}{2\sqrt{t}} - \frac{\sqrt{t}}{u\lambda} \right) \exp \left(-\frac{x}{\lambda} \right) \right] \quad (2.82)$$

with $u = \sqrt{S_s/k}$ and $S_s = \rho g(m_v + n\beta)$ the coefficient of specific storage. This solution gives the pore pressure distribution in a layer with a constant discharge at $x = 0$ and a constant head $\varphi = \varphi_0$ at $x \rightarrow \infty$. It can be used to estimate the speed at which the excess pore pressure will rise in front of the tunnel face. Note that the flux q in (2.79) to (2.81) is given per unit area of the face, whereas the inflow Q is per unit width of the aquifer, so that q has to be multiplied by the (average) height of the face or layer to obtain Q in (2.82).

When boring is stopped the pressure distribution in the aquifer is initially given by (2.64). Assuming no influx takes place to or from the excavation chamber, i.e. the bentonite membrane is impervious, a transient flow model yields the time-dependent pressure distribution in the aquifer as

$$\varphi = \varphi_0 + \frac{\Delta\varphi}{2} \left[\operatorname{erfc} \left(-\frac{xu}{2\sqrt{t}} + \frac{\sqrt{t}}{u\lambda} \right) \exp \left(-\frac{x}{\lambda} \right) + \operatorname{erfc} \left(\frac{xu}{2\sqrt{t}} + \frac{\sqrt{t}}{u\lambda} \right) \exp \left(\frac{x}{\lambda} \right) \right] \quad (2.83)$$

where $\Delta\varphi = \Delta p/\rho g$ at $t = 0$. This equation can be used to estimate the pressure drop in the aquifer between subsequent excavation periods or to estimate the remaining excess pore pressures at the start of an excavation sequence if the timespan between two subsequent excavation sequences is less than needed to fully dissipate the excess pore pressures.

In all presented calculations the shear strength of the bentonite slurry τ_F has been used without reference to any influence of shear velocity, i.e. implicitly the shear capacity of the slurry has been described by the static yield strength τ_y only, and any influence of the dynamic viscosity ν has been neglected. The parameters for such a simple model can be reliably obtained from a simple Marsh-funnel test [96]. The viscosity has to be determined with a roto-viscometer for example, but to take this into account in the model the infiltration speed v must be known. This infiltration speed can be derived from (2.78). Based on Huisman [84] it can be found that for a Bingham fluid the dynamic shear strength is given by

$$\tau_F = \tau_y + \nu \left(\frac{8v}{d_{10}} \right) \quad (2.84)$$

where the characteristic grain size d_{10} has been equated to the characteristic hydraulic pore diameter for simplicity.

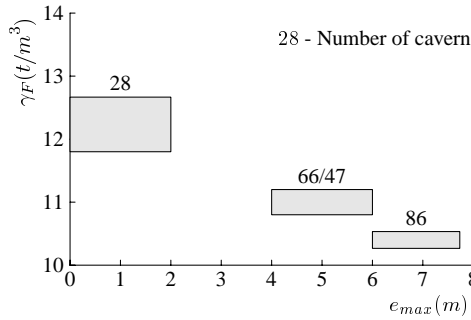


Figure 2.40: Slurry infiltration vs density [155]

Huisman [83] has shown that the dynamic shear strength of a bentonite suspension can be described more accurately over a large infiltration speed interval by a Herschel-Bulkley model than by a Bingham model. In that case

$$\tau_F = \tau_y + K \left(\frac{8v}{d_{10}} \right)^n \quad (2.85)$$

with K the Herschel-Bulkley coefficient and n the Herschel-Bulkley exponent.

Further research [85] has also shown that bentonite suspensions suffer from a significant deterioration in shear strength when subjected to mechanical mixing directly before testing in a roto-viscometer as compared to undisturbed samples. This reduction can be up to 60% of the shear strength τ_y . Slurry is subjected to heavy mechanical mixing for instance in the slurry pumps shortly before injection into the working chamber of the TBM.

On the other hand, when the bentonite suspension is let to rest in the excavation chamber, for example during standstill, gelation will set in and the shear strength will slowly increase over time [85]. As a result the shear strength that can be expected and used in calculations during standstill is higher than that during excavation. A further influence on the effective shear strength of the slurry is the amount and gradation of fines in the slurry. In most cases the properties of the slurry are determined from a clean bentonite suspension, but the excavated clay and sand that is also part of the slurry may well alter the infiltration properties of the slurry. Observations by Steiner [155] (see figure 2.40) show that the density of the slurry, i.e. the amount of excavated material present in the slurry, has a clear influence on the maximum infiltration length e , i.e. an influence on the apparent shear strength of the slurry.

Such influences should be taken into account when determining the shear strength τ_F of the slurry to be used in calculations to obtain e.g. the infiltration length e . Under normal circumstances, however, the influence on the minimal support pressure is limited and as such will be neglected in the remainder of this thesis.

2.2.4 Model Implementation

The model given by (2.70) with pore pressure distribution (2.66) will be referred to as the basic model. As said before this is a multilayered wedge stability model that includes the effects of soil arching, slurry infiltration and excess pore pressures, with the separate layers schematised as independent one-dimensional semi-confined aquifers. In this model the required effective support force S' for a given slip angle θ can be found when the pore pressure distribution $p(x, z, t)$

	Param.	Value		Param.	Value
Tunnel	D	10 m	Slurry	τ_F	5 Pa
	C	15 m		a	180 s
Soil	γ	20 kN/m ³	Aquitard	α	2.5
	c	0		t_F	10 s
	ϕ	30 °		γ_F	10 kN/m ³
	d_{10}	100 μ m		\tilde{c}	10 ⁹ s
	k_h, k_v	10 ⁻⁴ m/s		d_2	2 m
				Aquifer	H_1
			H_2	18 m	

Table 2.5: Parameters for reference tunnel No.1

in front of the face is known. This pressure distribution in turn depends on the excess support pressure Δs , which is a function of the water force W and S' .

This implicit set can be solved iteratively, calculating the support force S from a given pore pressure distribution $p(x, z, t)$ and using the resulting support pressure to update the pore pressures. A suitable starting point for the iterative procedure is the minimal support pressure obtained from a full membrane stability model, e.g. Jancsecz & Steiner [89].

Once the required support force for a given θ has been found, a second iteration over θ is needed in order to find the angle for which S is maximal. The resulting support pressure s is the required minimal support pressure.

For these calculations a number of parameters are needed. First, the general layout of the wedge is given by the tunnel diameter D , overburden C and wedge width B . The wedge width B has been taken as a separate variable, as some sources use $B = \frac{\pi}{4}D$ with the result that the area of the wedge face BD is equal to the area of the circular tunnel face, whereas others use $B = D$. Another possibility is to set $B = 1.8D$ and use the resulting model to estimate the minimal support pressures for a Double-O TBM or other TBMs with non-circular cutting faces.

The stresses in the soil can be obtained from the surface overburden q_s and the pore pressures p_0 , soil unit weight γ , cohesion c and angle of internal friction ϕ for each layer. As the arching length according to (2.53) depends on the wedge angle θ , the vertical stresses need to be recalculated for each wedge angle. To assess the groundwater flow conditions the horizontal and vertical permeabilities k_h, k_v are needed or alternatively the leakage factor λ for the layers in front of the TBM.

To evaluate the slurry infiltration the characteristic grain size d_{10} of the layers in front of the TBM and the shear strength of the bentonite τ_F are needed as well as estimates of the slurry half-infiltration time a and the mean infiltration time t_F . Also, the gradient of the effective slurry density is needed to calculate s'_F , but lacking data on the conditions in the excavation chamber this parameter can be eliminated by taking the slurry density equal to that of water.

In the following paragraphs the results from the basic model will be compared with those from other stability models, described in section 2.1.2, as well as with models with minor variations in model implementation. To this end a reference tunnel has been chosen as sketched in figure 2.41 and parameters from table 2.5. The aquitard differs in conductivity only from the other soil layers, so it simplifies to a homogeneous problem for models that do not include the effects of groundwater flow.

To compare the basic model with the existing wedge stability models, two modifications will be made. The first is to exclude the influence of excess pore pressures by taking an infinite infiltration time $t_F = \infty$, which has the result that the entire support pressure is transferred onto

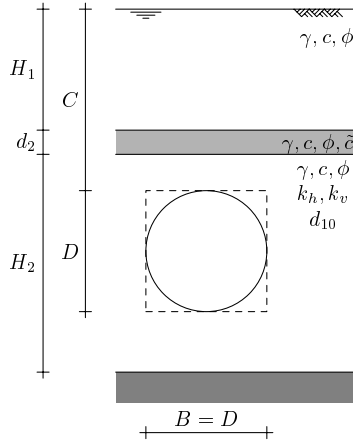


Figure 2.41: Geometry of reference tunnel No.1

Model	s_{\min} (kPa)	Δs_{\min} (kPa)	$\Delta p(w)$ (kPa)
Atkinson & Potts		37.5	
Krause (half sphere)		19.2	
Leca & Dormieux		7.1	
Jancsecz & Steiner	247.3	47.3	
incl. arching	207.2	7.2	
Anagnostou & Kovári	209.8	9.8	
Basic	226.6	26.6	23.8
excl. excess pore pressures	207.4	7.4	0
excl. all infiltration	207.3	7.3	0
Parabolic failure plane	214.9	14.9	12.8
excl. all infiltration	204.0	4.0	0

Table 2.6: Required minimal support pressure at tunnel axis, from different models, for reference tunnel No.1

the soil skeleton by the filter cake and no excess pore pressures are generated by infiltration in the area beyond the filter cake. The resulting model can be compared to the Anagnostou & Kovári model [6]. The second modification will exclude the influence of slurry infiltration and excess pore pressures entirely. This is achieved by choosing infinite yield strength τ_F for the bentonite as well as an infinite τ_F . The result will be an infinitely thin membrane which carries the entire support pressure. The resulting model can be compared with the model by Jancsecz & Steiner [89].

A third modified model includes infiltration effects, but models the wedge with a parabolic failure plane instead of a straight plane. This shape conforms more closely to the actual failure plane observed in centrifuge experiments (see section 2.1.4 and in particular figure 2.20). The basic model can easily be modified in this way by taking $w(z) = \sqrt{D}(z_b - z) \cot\theta$ as the wedge width. The sides of the wedge remain parallel planes. This modification is made to show the influence which the shape of the failure plane may have on the minimal support pressure.

Table 2.6 lists the minimal support pressures at the tunnel axis calculated with the different

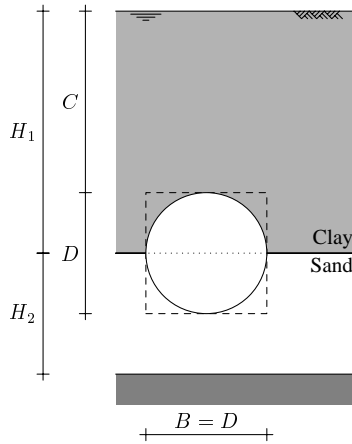


Figure 2.42: Geometry of reference tunnel No.2

	Param.	Value		Param.	Value
Tunnel	D	10 m	Slurry	τ_F	5 Pa
	C	15 m		a	180 s
	H_1	20 m		α	2.5
	H_2	30 m - H_1		t_F	10 s
Sand	γ	20 kN/m ³	Clay	γ_F	10 kN/m ³
	c	0		γ	17 kN/m ³
	ϕ	30 °		c	2 kPa
	d_{10}	100 μ m		ϕ	20 °
	k_h, k_v	10 ⁻⁴ m/s		d_{10}	1 μ m
				k_h, k_v	10 ⁻⁹ m/s

Table 2.7: Parameters for reference tunnel No.2

models. It is clear that the minimal support pressure calculated with the basic model is substantially higher than that calculated with other models. By excluding the influence of excess pore pressures the model yields a lower support pressure than the Anagnostou & Kováři model, as it still includes the drag forces of the slurry, whereas Anagnostou & Kováři exclude those. By further excluding slurry infiltration, the basic model completely reverts to the membrane model as described by Jancsecz & Steiner, including the effects of soil arching. Comparing the parabolic wedge with the other models it can be seen that the influence of the wedge shape is significant and that in this case the linear wedge is normative. This can be expected as the wedge side planes have a relatively larger area, resulting in a larger friction force T , which in this case more than compensates for the increased wedge weight.

Although a confining layer is present above the tunnel in this first reference case, it has properties identical to the rest of the soil except for its hydraulic conductivity. As a result the soil can be considered homogeneous for the purpose of all stability calculations not including excess pore pressures. To illustrate the influence of heterogeneity of the soil and the influence of possible model implementations on the required support pressure, a second reference case is presented in figure 2.42, with soil properties as listed in table 2.7.

For this case the basic model will be compared to the parabolic failure plane and to a model

Model	s_{\min} (kPa)	Δs_{\min} (kPa)	$\Delta p(w)$ (kPa)
Basic	220.2	20.2	13.1
ex. all infiltration	208.6	8.6	
Parabolic failure plane	215.4	15.4	9.2
ex. all infiltration	206.4	6.4	
Multi-sloped failure plane	220.2	20.2	13.2
ex. all infiltration	208.8	8.8	

Table 2.8: Required minimal support pressure at tunnel axis, from different models, for reference tunnel No.2

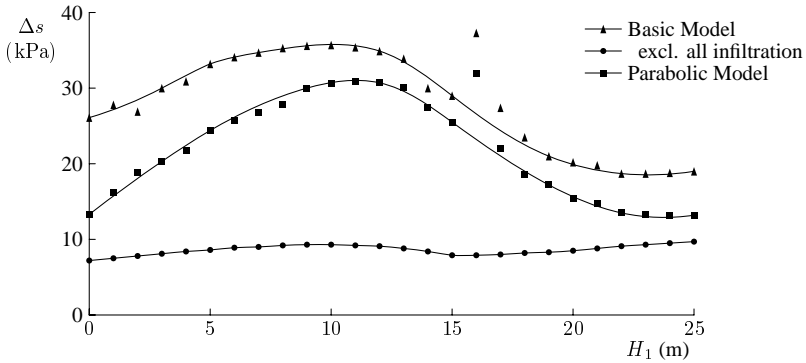


Figure 2.43: Influence of position of layer boundary on minimal support pressures for reference tunnel No.2

that allows a failure plane with different slopes in each soil layer, so that $\theta^{(i)}$ (see figure 2.27) may take a different value for each of the soil layers. This model will be referred to as the multi-slope model. The results of these calculations with $H_1 = 20\text{m}$ are presented in table 2.8. To further show the influence of the position of the boundary between the sand and clay layers, the thickness of the clay layer has been varied and the resulting minimum excess support pressures are presented in figure 2.43.

From the results in table 2.8 it can be seen that the difference between the support pressure calculated with the multi-slope model and the basic model, which can be seen as a simplification of the multi-slope model, is minimal. The calculation time required for the multi-slope model is substantially higher however, so that for further calculations the basic model will be used. The basic model could be extended further, so that a different value of $\theta^{(i)}$ is allowed in each slice of the wedge. The calculation times, resulting from the variational analysis over all possible slope combinations as well as the iterative procedure needed to find the excess pore pressure distribution, for a model with sufficient slices to approximate a failure plane as given in figure 2.20, are so large however that the use of such a model is impractical and will not be discussed any further.

The minimal support pressures calculated for different values of H_1 , presented in figure 2.43, show the strong non-linear influence of the position of the layer boundary on the minimal support pressure. In this graph the points are the calculated values for the three different models for integer values of H_1 , whereas the drawn lines are the trendlines resulting from these models. The model without infiltration effects shows there is a certain influence on the minimal support

pressure from the position of the boundary between sand and clay layers, even if this boundary lies well above the tunnel face. This is due to the difference in effective stress and shear capacity and the resulting change in the overburden force G_s . When the boundary between clay and sand falls within the tunnel face, there is also an influence on the friction forces acting on the wedge. These are minor effects, however, when compared to the non-linear effects present in the basic and parabolic models, which show the strong influence of excess pore pressures on the minimal support pressure and the influence of the thickness of the aquifer on the leakage factor λ .

A point to note is the difference between the trendline and the calculated values when the boundary between sand and clay layers lies slightly below the top of the tunnel ($H_1 > C$). As the infiltration length e and the leakage factor λ are much smaller in clay, the excess pressure found from (2.66) drops considerably faster with distance from the face. As a result, the uplift force P_s at the top of the wedge is strongly reduced, whereas the shear force reduction P_T due to the infiltration in the sand layer is still a strong influence. This results in an increased minimal support pressure (2.69) and coupled to that increased excess pore pressures. The effects can be noted from the difference between calculated minimal support pressures resulting from (2.69) and the trendline for $H_1 = 16\text{m}$. This influence is so strong that for $15\text{m} < H_1 < 15.35\text{m}$ the calculated minimal support pressures are larger than σ_v , which might lead to blow-out according to (2.16). If however a stability analysis is made for a slightly smaller wedge, which has its top just below the boundary between sand and clay layers, a minimal support pressure just below the drawn trendline is found, as expected.

A second point to note is that the calculated values for a wedge face which lies fully within the clay layer do not coincide with those found with the model excluding infiltration, although this might be expected on physical grounds. This is due to the fact that only the boundary position H_1 has been varied and not the characteristics of the slurry infiltration, in particular the infiltration half time a . If these effects had been included, the pressure drop over the filter cake would become equal to the excess support pressure and the calculated minimal support pressure would approach the values found with the model excluding all infiltration effects, in the same manner as illustrated in table 2.6 for tunnel No. 1.

These calculations show the strong influence the slurry infiltration and excess pore pressures have on the minimal support pressure. This influence is even more pronounced in a layered system, where the position of the layer boundary influences the overburden load G_s as well as the leakage factor λ . The result is a strongly non-linear relation between the position of the layer boundary and the soil parameters on the one hand and the (excess) minimal support pressure on the other hand. How this relationship depends on the separate parameters will be investigated in the next section.

The stability model presented in this section is a logical extension of the limit equilibrium models used to investigate the stability of slurry-filled trenches and has been proposed in similar form by other authors. The model presented here differentiates itself as it can deal with heterogeneous soils and takes the effects of slurry infiltration as well as excess pore pressures into consideration. Based on the preliminary analysis presented above, the model behaves as expected, but a more thorough analysis will be made in the following sections. First a parameter analysis of the model will be carried out and then the model results will be compared to field observations from several tunnelling projects in soft, heterogeneous and water-bearing soils.

2.3 Model Sensitivity Analysis

The calculations made with the basic model in the previous section show that the model has a strong non-linear dependence on the variation of the position of the layer boundary and on the resulting variation in soil parameters. It does not show however which individual parameters influence the results most strongly. To that end a more systematic investigation of the sensitivity to the various input parameters and several model choices will be made. First the individual parameters will be investigated, for which Reference Tunnel No. 1 will be used. As it will become clear that several parameters are in reality coupled, a few calculations will be made using sets of coupled parameters, simulating different soil types. Then an analysis will be made of the sensitivity of the model in a heterogeneous, two-layer, system to the parameters that the model is most sensitive to. Finally some remarks regarding the safety philosophy and safety factors will be made.

The results of the calculations are presented as Δs , the difference between the support pressure and the water pressure at rest, i.e. excluding excess pore pressures generated by the boring process. In most cases, except where noted otherwise, the water table used is equal to the soil surface.

2.3.1 Homogeneous System

The first analysis will be made based on reference tunnel No. 1, described on page 48. For each of the parameters a variation interval around the reference value has been chosen (see table 2.9). Within this interval a number of calculations has been made in order to get a reasonable overview of the model's behaviour as a function of the variation of each separate parameter. For most parameters the boundaries of the variation interval have been chosen very wide, to include any reasonable variation that might occur in practice. As the leakage factor λ is the main parameter for the groundwater flow and thereby governs the excess pore pressure distribution, this analysis has been repeated for three different reference values of λ : $\lambda \gg D$, $\lambda \approx D$ and $\lambda \ll D$. The resulting excess minimal support pressures are presented in figure 2.44, with the exception of the influence of the water level z_h which has been presented in figure 2.45. In these graphs the dots indicate the excess minimal support pressure for the reference case. The chosen values of the leakage factor are: (a) $\lambda = 1342\text{m}$, (b) $\lambda = 6\text{m}$ and (c) $\lambda = 0.06\text{m}$. For case (b) the gradient of the excess minimal support pressure around the reference point, as well as the maximal gradient, have also been listed in table 2.10. The same data is also presented in figure 2.46, scaled to the excess support pressure found for the reference case, Δs_{ref} , so the relative influence of the various parameters is shown more clearly, but due to the partial overlap of the lines some information is obscured.

From figure 2.44 it can be seen that the model is most sensitive to changes in the overburden C , diameter D , angle of internal friction φ and the density of the slurry γ_F . It can also be obtained that a simultaneous variation of C and D , such that the ratio C/D remains constant, will have a more limited influence on the support pressure than a change in either D or C separately. This is shown in figure 2.47, where the variation of the excess minimal support pressure is presented as a function of tunnel diameter, for a constant C/D ratio. This graph also shows the strong influence of soil arching for tunnels with large overburden ($C/D > 2$), which leads to a calculated excess minimal support pressure close to nil. That the influence of the diameter is stronger than that of the overburden is to be expected as a result of soil arching. The counter-effect that the support pressure increases with the increase in piezometric head, which goes along with the increase in overburden, has been removed from this data as the excess support

Param.	Min.	Ref.	Max.	
C	5	15	25	m
D	5	10	15	m
γ	11	20	22	kN/m ³
c		0	5	kPa
ϕ	10	30	50	°
d_{10}	1	100	10 ⁴	μm
τ_F	1	5	15	Pa
a	1	180	360	s
α	2	2.5	4	
t_F	1	10	60	s
γ_F		10	12	kN/m ³
λ	$6 \cdot 10^{-2}$	1342	$6 \cdot 10^4$	m
z_h		0	15	m

Table 2.9: Parameters for sensitivity analysis based on Tunnel No. 1

Param.	dΔs (kPa/unit)	dΔs/Δs (%/unit)	Max. dΔs (kPa/unit)	unit
C	-2.3	-15.3	-3.3	m
D	4.5	30.0	5.7	m
γ	1.5	10.0	2.0	kN/m ³
c	-6.3	-72.4	-6.3	kPa
ϕ	-2.1	-14.0	-5.9	°
d_{10}	0.25	1.7	0.34	mm (!)
τ_F	0	0	-0.1	Pa
a	0.01	0	0.3	s
α	0	0	0	
t_F	-0.08	-0.5	-0.08	s
γ_F	-17.2	-160.8	-17.2	kN/m ³
λ	1.26	8.4	1.48	m
z_h	-2.2	-17.2	3.2	m

Table 2.10: Sensitivity of basic model to parameters, Tunnel No. 1(b), $\lambda = 6\text{m}$

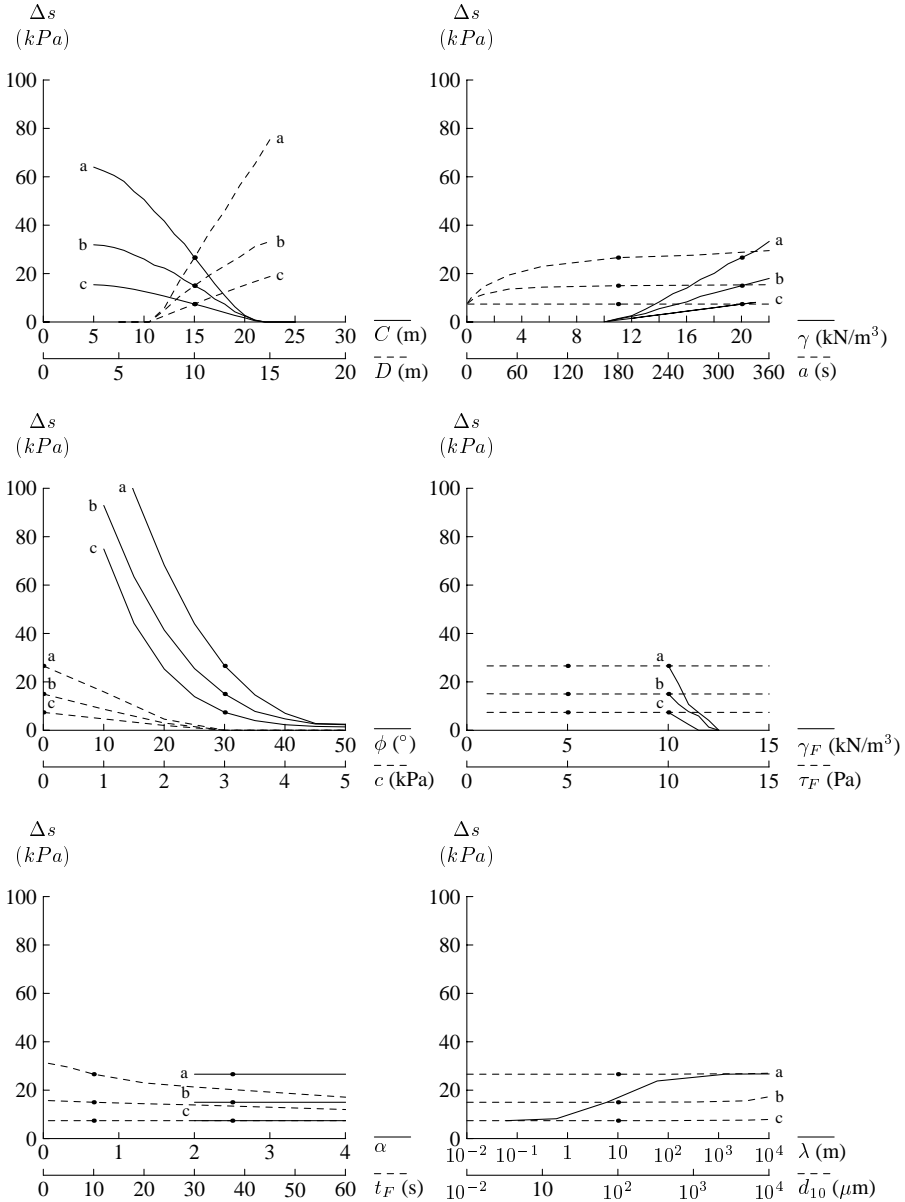


Figure 2.44: Sensitivity analysis No. 1, influence of parameter variation on excess minimal support pressure (Leakage factor: (a) $\lambda = 1342\text{m}$, (b) $\lambda = 6\text{m}$, (c) $\lambda = 0.06\text{m}$)

pressure Δs has been presented.

A further result that follows expectations is that for soils with $\gamma < \gamma_w$ the required excess support pressure is equal to zero, as these soils have no effective weight. The fact that the volumetric weight of the slurry has such a strong influence may be somewhat surprising, as in a full membrane model the support pressure at the axis is independent of γ_F . In such a model the density of the slurry only adds to the support force S in the force equilibrium. In the basic model considered here, however, the gradient of the slurry pressure also influences the excess support pressure at each level of the face. Therefore it influences the excess pore pressure (2.66) and, via the effective stresses, both the friction forces acting on the wedge as well as the effective support pressure s' . And as the triangular side planes of the wedge are not symmetrical in vertical direction with respect to the tunnel axis, this influences the force equilibrium somewhat, resulting in the shown dependence of the basic model on the density of the slurry.

The shear strength of the slurry τ_F , the characteristic grain size d_{10} and the slurry infiltration model parameter α have little or no influence on the support pressure. This can be understood, as these parameters are only used to determine the slurry infiltration length e_{\max} . As sketched in figure 2.36, the excess pressure distribution before point $e(t)$, derived from e_{\max} , is linear and shows an exponential decay after this point. For large values of λ the difference between a linear and exponential pressure distribution is negligible over the depth w of the wedge, and little influence from the actual value of e_{\max} could be expected. For smaller values of λ it might be expected that the value of e_{\max} has an influence on the minimal support pressure. However, for small values of e_{\max} , compared to the wedge depth $w(z_r)$, the reduction of the effective support pressure (figure 2.34) would be small in any case. Only for large values of e_{\max} a significant influence on the minimal support pressure could be expected. The allowable variation in α and τ_F is small, however, and only the variation in d_{10} is sufficient to lead to large enough values of e_{\max} . In the case of a homogeneous face the resulting influence on the minimal support pressure is opposed by the increased uplift force P_s , so hardly any influence remains, as apparent from figure 2.44. Only for soils with $d_{10} > 1\text{mm}$ or multi-layered faces in heterogeneous soils, the increase in the minimal support pressure would be significant. This can be observed from figure 2.46.

Figure 2.45 shows the influence of a lowered water table on the excess minimal support pressure. The increase in effective stress in the soil which results from this lowered water table leads to an increased friction along the sides of the soil column and the side planes of the failure wedge. A result is an increased arching effect in the soil column on top of the wedge. This is counteracted by the load increase due to the higher effective weight of the soil, which is the cause of the increase in effective stress, and this interaction leads to the shown dependence.

As noted before in section 2.2.4, the independent variation of the characteristic grain size d_{10} , the permeability k , the infiltration half time a and the yield strength of the support medium τ_F lead to a somewhat clouded view of the dependence of the minimal support pressure on the soil type. As in practice these parameters are not independent, a variation of the soil type will result in a coupled variation in these parameters, as for example shown in table 2.11. These sets of parameters have been used to give an indication of the sensitivity of the basic model to a change in soil type. The resulting minimal support pressures are presented in figure 2.48.

It can be seen that the highest excess support pressures are needed in sandy soils with permeabilities $10^{-5} < k < 10^{-3}\text{m/s}$. This corresponds with the field observations by Mori [120] that the reduction in effective support pressure due to excess pore pressures can become a major problem in soils with permeabilities within the indicated range.

Reference tunnel No. 1 will be used to show the influence several model choices have on

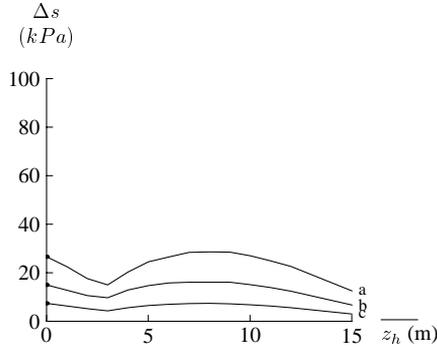


Figure 2.45: Sensitivity analysis No. 1, influence of water level z_h on excess minimal support pressure (Leakage factor: (a) $\lambda = 1342\text{m}$, (b) $\lambda = 6\text{m}$, (c) $\lambda = 0.06\text{m}$)

Type	No.	γ (kN/m^3)	ϕ ($^\circ$)	c (kPa)	k (m/s)	d_{10} (μm)	a (s)	τ_F (Pa)
Clayey	1	16	15	2	10^{-10}	2	1	1
	2	17	17.5	10	10^{-9}	5	1	1
	3	17	17.5	5	10^{-8}	5	5	1
	4	18	22.5	5	10^{-7}	10	10	5
	5	18	27.5	2	10^{-6}	10	60	5
	6	19	30	0	10^{-5}	50	120	5
Sandy	7	20	30	0	10^{-4}	100	180	10
	8	20	32.5	0	10^{-3}	500	120	10
	9	20	35	0	10^{-2}	1000	60	15
	10	20	35	0	10^{-1}	2000	60	20
Gravelly	11	20	40	0	10^0	4000	60	30

Table 2.11: Input parameters for analysis of sensitivity to coupled parameters variation, with parameters indicative for various soil types

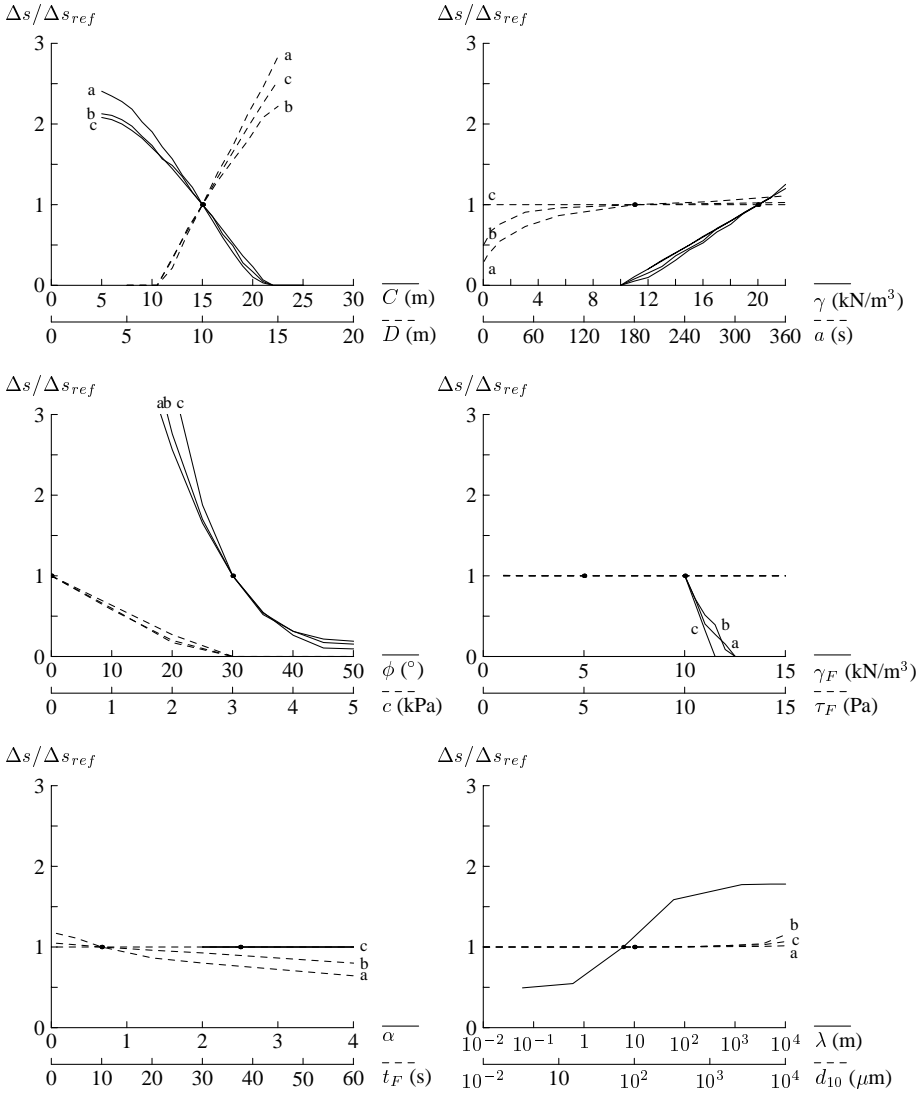


Figure 2.46: Sensitivity analysis No. 1, relative influence of parameter variation on excess minimal support pressure (Leakage factor: (a) $\lambda = 1342\text{m}$, (b) $\lambda = 6\text{m}$, (c) $\lambda = 0.06\text{m}$), with Δs_{ref} the excess support pressure for the reference case)

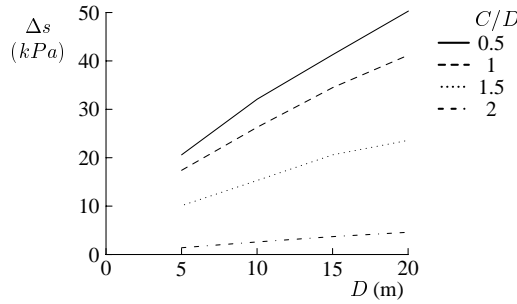


Figure 2.47: Influence of diameter variation on excess minimal support pressure, for constant C/D ($\lambda = 6\text{m}$)

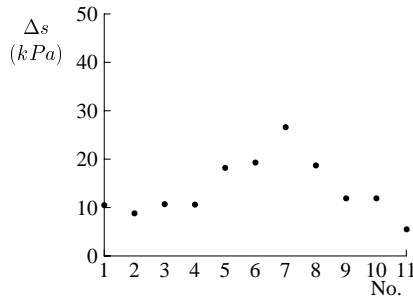


Figure 2.48: Influence of soil type on excess minimal support pressure, based on parameter sets in table 2.11

the minimal support pressure. The arching implementation and the value of the horizontal effective stress coefficient have already been investigated in section 2.2.2 for the wedge model, but without the inclusion of the influence of excess pore pressure in the model. The influence of the wedge width B has not been investigated at all up to this point. Two obvious choices for the value of B are $B = D$ and $B = \frac{\pi}{4}D$. Quite another reason to vary the wedge width is to estimate the minimal support pressure needed for a non-circular shield, such as a double-O shield. In such a case the wedge width is larger than the tunnel diameter, up to twice the diameter, and the relative influence of the soil friction on the side planes of the wedge T is reduced, while the influence of overburden G_s and wedge weight G_w are increased. The influence of these wedge widths as well as intermediate wedge widths has been presented in figure 2.49.

It is clear that for the basic model the wedge width B has a significant influence on s_{\min} , and for $B/D < 0.75$ the calculated excess support pressure is equal to zero. Although table 2.4 suggests that the basic model with $B = D$ may slightly overpredict the minimal support pressure, it also shows that a reduction of the width to $B = \frac{\pi}{4}D$ will yield values well below those obtained from centrifuge tests (see table 2.4). Combined with the shape of the failure wedge observed in figure 2.20, this leads to the conclusion to use B equal to the width of the face in all calculations. This choice is linked to the choice of the arching model and would have to be reviewed if a different arching implementation were chosen.

Figure 2.50 shows the influence of the various possible implementations of soil arching above the tunnel and at the side planes of the wedge, as well as the choice of the horizontal effective stress coefficient. See page 36 for the definition of the different arching implement-

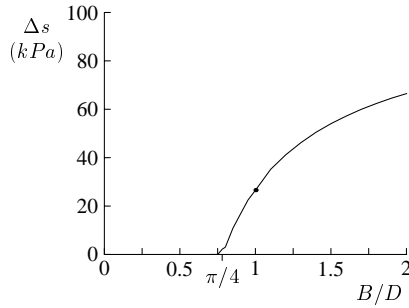


Figure 2.49: Influence of wedge width B on excess minimal support pressure, based on Reference Tunnel No. 1(a)

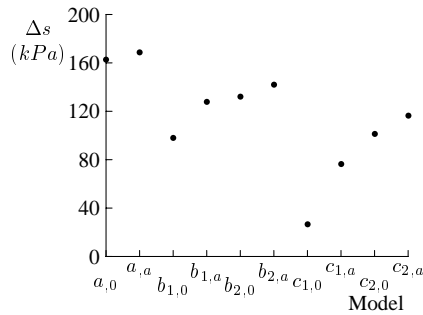


Figure 2.50: Influence of arching model and horizontal effective stress coefficient choices on excess minimal support pressure, based on Reference Tunnel No. 1(a)

ations. From this figure it can be seen that the basic model is highly sensitive to these model choices. Based on the limited amount of data from centrifuge tests, the $c_{1,0}$ model has been chosen in section 2.2.2. This model yields the lowest minimal support pressure. As suggested in section 2.2.2, the $b_{1,0}$ model might be a more conservative model choice, but the influence of infiltration and excess pore pressures had not been taken into account there. From the data presented here it can be seen that the b model yields far higher minimal support pressures, but, as there is a lack of field or centrifuge test data for these theoretical cases, no founded comparison can be made at this point.

For the case studies presented in section 2.4 a similar problem holds, as there is no indication that the support pressures used in these projects are the minimal support pressures. A model could be falsified however in those cases where failure of the face did with certainty not occur and the model predicts minimal support pressures significantly higher than those used, i.e. failure should have occurred with certainty at the pressure used. Extensive laboratory investigations or precise field measurements on the support pressures used at the time of failure are still lacking for cases where excess pore pressures are a factor of importance. The same holds for investigations into the influence of excess pore pressures on soil arching and thereby on the effective overburden load G_s .

A further model choice investigated for Reference Tunnel No. 1 is the model of the dynamic shear strength of the support medium. In all previous calculations the shear strength has been derived for a Bingham fluid, for which the influence of dynamic viscosity is neglected. As

No.	model	τ_y (Pa)	ν (Pa s)	K (Pa s ⁿ)	n	Δs_{\min} (kPa)
1	Bingham	5				26.6
2	Bingham	3	0.03			26.6
3	Herschel-Bulkley	2		0.3	0.55	26.6
4	Herschel-Bulkley	0.5		0.2	0.75	26.7

Table 2.12: Input parameters and excess support pressure for different bentonite shear strength models, Reference Tunnel No. 1(a)

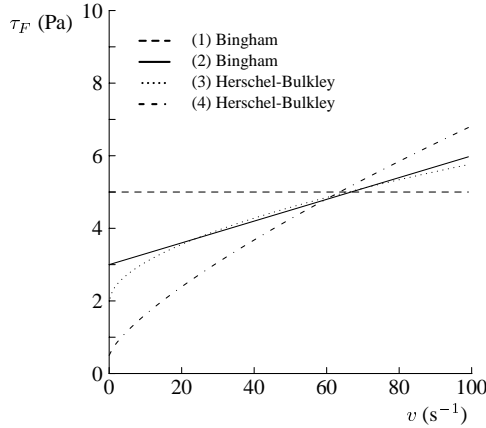


Figure 2.51: Dynamic shear strength derived for different models listed in table 2.12

noted before, according to Huisman [83] the dynamic shear strength of bentonite suspensions in column infiltration tests can be reliably modelled over a large speed interval by the Herschel-Bulkley model. In that case the infiltration speed, found from (2.78), has to be taken into account when deriving the shear strength τ_F of the bentonite from (2.84) or (2.85) and calculating the infiltration length e . As it has already been shown in figure 2.46 that τ_F has hardly any influence on the required minimal support pressure, it should be no surprise that the actual shear strength model has little influence too. This is underlined by the results presented in table 2.12, based on the input values given in the same table. The resulting dynamic shear strengths for these input values have been plotted in figure 2.51.

2.3.2 Layered System

The sensitivity analysis presented in figure 2.44 only shows the influence of individual parameters for a single homogeneous soil layer. The calculations made in section 2.2.4 for Reference Tunnel No. 2 already showed that the basic model has a non-linear dependence on, among other things, the position of the layer boundary in a two-layer system. The same geometry has also been used to study the influence of changes in the parameters of the individual layers. This analysis has been limited to the soil properties that influence the minimal support pressure most strongly: the volumetric weight of the soil and the angle of internal friction, as well as the position of the layer boundary. The results of these calculations are presented in figures 2.52 and 2.53.

The geometry used for the sensitivity analysis presented in figure 2.52 is roughly the same as

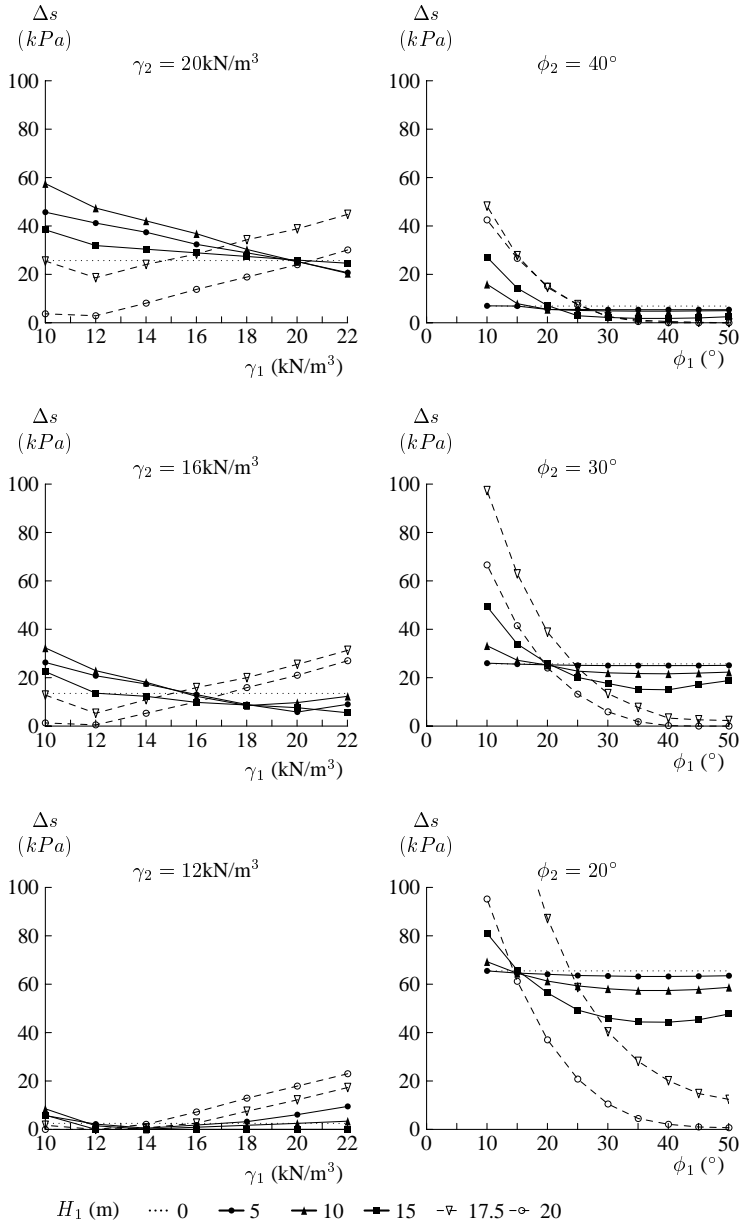


Figure 2.52: Sensitivity analysis No. 2, influence of parameter variation on excess minimal support pressure in a two-layer system for a cohesive upper layer

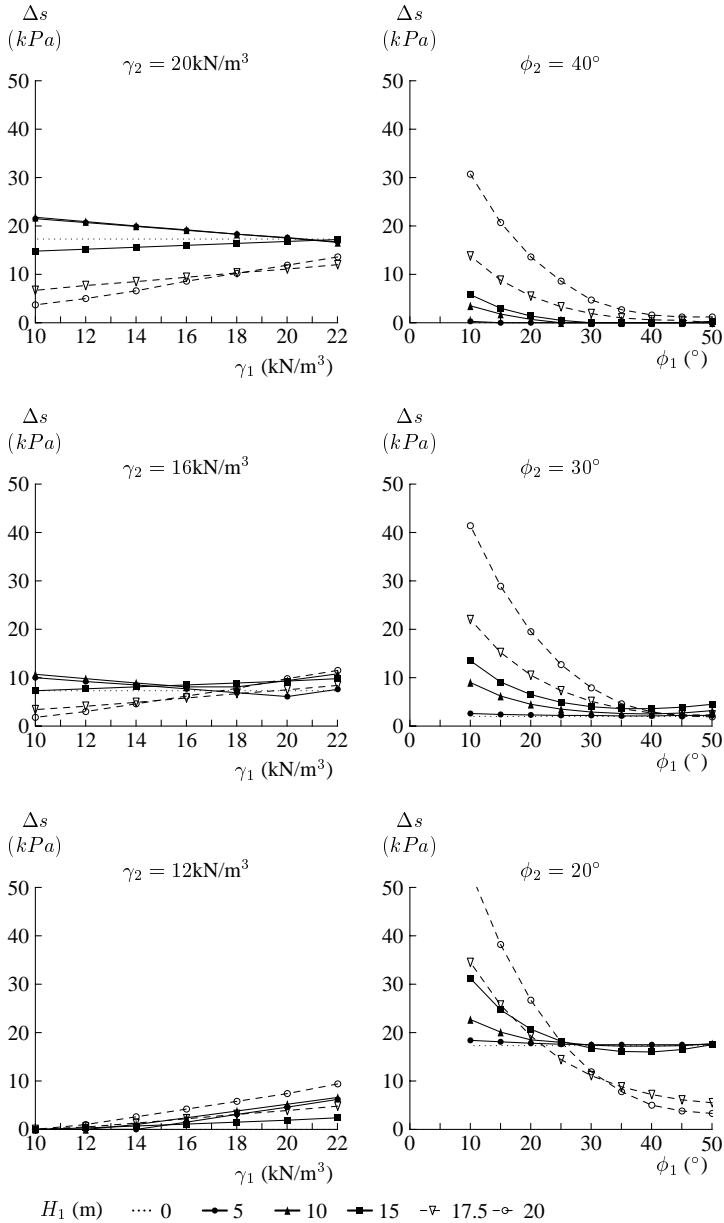


Figure 2.53: Sensitivity analysis No. 2, influence of parameter variation on excess minimal support pressure in a two-layer system for a cohesive lower layer

Reference Tunnel No. 2, a clay layer overlying a sand layer, with a few exceptions. Firstly, the reference value for the volumetric weight of the upper (clay) layer, denoted as γ_1 in these graphs, is taken 20kN/m^3 . Secondly, the leakage length of the sand layer is taken $\lambda = 100\text{m}$, and for the clay layer equal to 0, where needed. Based on this situation, calculations have been made where $H_1 = 5\text{m}$, 10m , 15m , 17.5m and 20m . Only in the last two cases does the boundary between the sand and clay layer fall within the tunnel face. Given these five cases, the volumetric weight of the upper layer has been varied between 10kN/m^3 and 22kN/m^3 . Calculations have also been made for situations where the volumetric weight of the lower layer γ_2 has been chosen 16kN/m^3 and 12kN/m^3 . After that the angle of internal friction of the upper layer φ_1 has been varied between 10° and 50° , and the angle of internal friction of the lower layer has been varied between $\varphi_2 = 20^\circ$ and 40° .

It is immediately clear that the model behaves somewhat differently in case the boundary between the two layers falls within the face, compared to the case with a homogeneous face. The graphs for the variation in volumetric weight show that a reduction of the weight of the wedge, resulting from a reduction in γ_2 , reduces the minimal support pressure. This reduction is greater than the reduction resulting from a lower overburden weight, as the overburden influence is already reduced by soil arching. A lower overburden also influences the vertical effective stress and thereby the friction forces on the wedge planes, so that the overall effect of a reduced overburden is an increase of the minimal required support pressure.

Also visible is the influence of the uplift force P_s , which has been commented on before. When the top of the wedge falls within an aquitard or a layer with a very small leakage length, and the remainder of the wedge falls within a layer with a leakage length of the order of or greater than D , the uplift force is effectively cancelled while the effectiveness of the support is still reduced. The relative influence decreases as more of the wedge falls within the aquitard, since the effectiveness of the support increases. From figure 2.52 it can be seen that this effect is greater as γ_2 is greater. This can be understood, as the maximal influence of the uplift force is to negate the overburden load G_s . If the overburden is effectively cancelled out of the equilibrium, the driving force is formed by the wedge weight and that is greater for greater γ_2 . This leads to an increase in Δs , which is amplified by the non-linearity of the model. It is interesting to note that the difference in Δs between the cases $H_1 = 17.5\text{m}$ and $H_1 = 20\text{m}$ is not influenced by the ratio γ_1/γ_2 but only by the volumetric weight of the lower layer, Gg_2 .

The graphs which show the influence of the angle of internal friction of the upper layer φ_1 (see figure 2.52 again) predominantly show that the friction forces on the wedge are of major importance. If the layer boundary falls within the face, lower values of φ_2 or φ_1 have a strong influence on the required support pressure, as already shown in section 2.3.1. Again this influence is amplified for cases where the layer boundary falls slightly below the top of the failure wedge.

Now the main differences between the upper and lower layer, which have not been varied, are the cohesion of 2kPa of the upper layer and the leakage lengths of 100m for the lower layer and 0m for the upper layer. To show the differences with a system where the upper layer is the permeable non-cohesive layer and the lower layer is the cohesive impermeable layer, a similar set of calculations has been made for a system where the properties of the two layers have been interchanged. Thus for the reference case: $\gamma_1 = 20\text{kN/m}^3$, $\gamma_2 = 20\text{kN/m}^3$, $\varphi_1 = 30^\circ$, $\varphi_2 = 20^\circ$, $c_1 = 0$, $c_2 = 2\text{kPa}$, $\lambda_1 = 100\text{m}$ and $\lambda_2 = 0$. Figure 2.53 shows the results of these calculations. Note that the vertical scale differs from figure 2.52.

The sensitivity analysis for a cohesive lower layer shows the same behaviour of the model as for a non-cohesive lower layer, except for two major points. Firstly, the required support pressures are generally lower than in the non-cohesive case due to the extra support force resulting

from the cohesion. Secondly the effective loss of P_s in case the layer boundary falls slightly below the top of the wedge does not occur, as in this case the lower layer is the impermeable one and the upper layer the aquifer with a leakage length $\lambda = 100\text{m}$. When in this case the layer boundary lies slightly below the top of the wedge, the loss of effective support force due to the generated excess pore pressures is partly compensated by the upward force P_s .

From these analyses it can be concluded that the presence of layer boundaries within the tunnel face has a distinct influence on the behaviour of the model, and also that the presence of light overburden layers or layers with poor frictional properties has an even more significant influence on the required minimal support pressure. The detrimental effects of low volumetric weight or poor frictional capacity will often combine in practical cases and further amplify the required minimal support force. Manifold examples can be found in the western part of the Netherlands, where weak Holocene clay or peat layers are overlying Pleistocene sands.

2.3.3 Safety Factors

Several authors have attempted to implement a safety factor into a (full membrane) wedge stability model and establish acceptable safety factors to be used with that implementation. Jancsecz [89] uses a separate factor of safety on the water pressure and the effective (three-dimensional) soil pressure, so that the total support force is derived from

$$S = \eta_E E + \eta_W W \quad (2.86)$$

and the overall safety factor is then be defined by

$$\eta = \frac{S}{\eta_E E + \eta_W W} \quad (2.87)$$

but no explicit values are given for the partial or overall safety factors. This implementation is somewhat reminiscent of the implementation in DIN4126 [93] of the safety factors used for the wedge stability calculations of slurry-filled trenches.

Sternath [156] on the other hand does take a layered soil above the tunnel into account and defines the safety factor by

$$\eta = \frac{R_2 + R_3}{G_1 - R_1 + W + G_2 + G_3}, \quad (2.88)$$

where G_i are the overburden forces of the separate layers and R_i the resistances mobilized against failure, including the overburden reduction due to soil arching (see figure 2.14). And as R_3 , the resultant of K and S , includes the slurry force as well as soil friction forces, this does not offer a clear safety definition, which is aggravated by Sternath's remark that other distributions of the resisting forces R_i over numerator and denominator are possible. Also, he does not give a recommended minimum value for η .

Returning to (2.86) and the already noted parallel to slurry-filled trenches, the DIN4126 poses two separate requirements. For each level in the trench the slurry pressure must be equal or higher than 1.05 times the water pressure, which could be roughly translated to $\eta_W = 1.05, \eta_E = 0$ for a totally submerged tunnel. And for the total wedge the support force S has to be larger than the water force W and 1.1 or 1.3 times the effective earth force E . Whether the value of $\eta_E = 1.1$ or 1.3 has to be used depends on whether or not there are constructions in the vicinity of the trench. The minimal support pressure at each level is determined by the largest support pressure resulting from these two requirements.

Especially during boring, a major difference between a slurry-filled trench and a tunnel face is of course the required stand-up time. A slurry-filled trench has to be kept stable in the order of hours or even days, whereas during excavation, the tunnel face is constantly removed and the concept of a required stand-up time becomes somewhat obscured. And in a regular boring process the required stand-up time during the ring-building phase of the boring process is in the order of 30 minutes to an hour, but at the end of the excavation phase the support pressure can be adjusted to obtain a higher factor of safety. Such a consideration might indicate that a lower safety factor is required during boring as compared to a slurry-filled trench. During stand-still, when a similar safety factor might be in order, the problem of excess pore pressures does not occur and additional measures can be taken to ensure the stability of the face.

On the other hand, in a fully excavated slurry-filled trench there are no pressure fluctuations due to the excavation process, and the filter cake will be fully established, so that the entire support pressure is transferred onto the soil skeleton, and there is no problem with excess pore pressures. Such considerations would indicate that a higher safety factor is required, as compared to those given in DIN4126.

The opinions given in literature about an acceptable choice for the partial safety factors differ somewhat. Balthaus [24] simply suggests to use $\eta_W = 1.0$ and $\eta_E = 1.1/1.3$. On the other hand, the design calculations for the Second Heinenoord Tunnel [139] prescribe $\eta_W = 1.05$ and $\eta_E = 1.5$, to be used with the full-membrane wedge stability model described by Jancsecz. In a follow-up on his original article Jancsecz [88] advises to use partial factors $\eta_E \geq 1.5 - 1.75$ and $\eta_W = 1.05$ with his full-membrane model. In the same article he advises a safety factor against blow-out $\eta_B = 1.1$, which corresponds with commonly used factors. This suggests that the level of safety recommended by Jancsecz is not extremely high, even though the safety factors are relatively high.

The use of such high partial safety factors to reach an adequate level of safety suggests that the model is highly sensitive to some of its input parameters or that certain important aspects of the physical process to be modelled are not or inadequately captured within the model. The cases presented in sections 2.2.4 and 2.3 suggest that both are true. The full-membrane model does not include the effects of slurry infiltration and excess pore pressures, which significantly increase the minimal support pressure for certain cases. The models presented by e.g. Jancsecz or Anagnostou [7] do not deal with the influence of heterogeneity at the tunnel face, which may also affect the stability of the tunnel face, and the basic model is shown to be highly sensitive to changes of among other things the angle of internal friction, cohesion and permeability of the soil as well as the volumetric weight of the support medium.

A complication arises with the introduction of excess pore pressures in the stability model, as the interaction between excess pore pressures and minimal support pressure precludes the simple use of a (partial) safety factor of the form (2.86). If for a given pore pressure profile $p(x, z)$ the minimal support pressure is found and the excess support pressure Δp is multiplied by a given factor, this will not with certainty yield the desired level of safety. As the excess pore pressures will also increase with an increased support pressure, the effective support pressure may increase less than the desired safety factor, increase not at all, or even lower the level of safety. To circumvent this problem the safety factor has to be applied to the effective support pressure s' derived from a matching pore pressure profile.

Another method is of course to derive material factors for the separate parameters based on a desired safety level [103]. And although a semi-probabilistic safety analysis for a homogeneous soil could be made, based on the data presented in figure 2.44 and a founded choice for a level of safety, the many peculiarities observed in section 2.2.4 and 2.4 for heterogeneous soils warrant the derivation of those material factors from a full probabilistic safety analysis. Such an analysis

falls outside the scope of this thesis. From the sensitivity analyses it is clear, however, that the main influences for which partial factors have to be found are c , ϕ and γ of the soil, γ_F for the slurry and z_h .

Also, in view of the contradicting effects and demands made on the minimal support pressure and the necessary margin between minimal and maximal support pressure, as well as the limited field experience with cases where excess pore pressures play an important role, one would be best advised to use an absolute safety margin between the minimal and maximal allowable support pressure. This margin should serve to compensate for the unavoidable pressure fluctuations that occur during boring as well as the uncertainty in the exact value of the boundaries of the support pressure due to uncertainties and statistical variations of the soil properties, in particular the angle of internal friction and the permeability.

2.4 Comparison with Field Cases

The parameter analysis conducted in section 2.3 gives an overview of the behaviour of the basic model, but does not shed any light on the level of agreement between the results calculated with the model and the conditions observed for actual cases. In order to clarify this agreement, to show the value of the model for engineering practice and to point out the problems that may arise, a number of cases will be analysed in the following section.

First, two slurry tunnelling projects will be described where measurements of the support pressure as well as the excess pore pressures have been made. This will further highlight the importance of the inclusion of excess pore pressures in the wedge stability model and the broad range of geological and geohydrological circumstances in which the basic model yields reliable results. Then a case study will be made to show the similarities between a foam-conditioned EPB machine and a slurry machine and the applicability of the model for such a case.

2.4.1 Second Heinoordtunnel

The Second Heinoord Tunnel is a twin-tube, 8.3m outer diameter, 950m long bored tunnel under the River Oude Maas in the vicinity of Rotterdam, constructed between 1996 and 1999. It is often referred to as the first bored tunnel in the Netherlands and is one of the first large diameter tunnels in soft alluvial soils with high water pressure. The construction site is next to the location of the First Heinoord Tunnel, an immersed tunnel. Due to its status of first bored tunnel and the large number of unknowns involved in the tunnel boring process in soft to very soft soils with high water pressures, the project was designated a pilot project and an extensive monitoring programme was carried out [19, 20].

As part of the measurement program a large number of additional sensors was installed in the TBM, to measure slurry discharges and slurry and earth pressures at the face and in the working and excavation chambers. At the north and south banks of the river two monitoring fields were laid out. These test sites, each approximately 50m by 75m, were financed by the Centrum Ondergronds Bouwen (COB) and housed surface settlement plates, extensometers, inclinometers, piezometers and stress monitoring stations [18]. A third field at the north bank of the river was financed by the Municipality of Amsterdam and consisted of a large number of instrumented wooden and concrete piles, as well as extensometers, settlement plates and stress monitoring stations. The objective of this test site was to measure the influence of the boring process on the bearing capacity and deformation behaviour of the piles [86, 126, 128].

Param	value
D	8.55m
τ_F	5Pa
γ_F	10.2-14kN/m ³
a	100-600s
t_F	6-12s
l_{cut}	5cm

Table 2.13: Operative parameters for Second Heinenoord TBM

In this section the main focus will be on the COB monitoring field North and the piezometers that were installed in the path of the TBM, approximately at the projected axis of the first tube. See figure 2.54 for an overview of the test site North.

The TBM used was a 8.55m Mixshield machine from Herrenknecht, which operated exclusively in slurry mode. The cutter wheel was a slender five spoke wheel carrying 32 cutters (see figure 2.55). Overcutters at two of the spokes are capable of excavating up to 60cm outside the shield. Fresh slurry enters the working chamber by the main inlet or is pumped directly into the excavation chamber by several inlets at the submerged bulkhead around the axis of the cutter wheel. The maximum capacity of the excavation chamber inlets is limited to 20% of the total slurry discharge capacity of the machine [122]. Slurry exits the excavation chamber through a relatively small opening in the submerged bulkhead and passes a grille before reaching the outlet. Obstructions in the outflow of the slurry have been reported, especially when excavating the pleistocene clay layers below the river, most probably due to adhesion of clay lumps, leading to large pressure fluctuations and necessitating manual cleaning of the working chamber [17]. The suboptimal flow of slurry through excavation and pressure chambers led to an accumulation of spoil and a relatively dense slurry staying in the excavation chamber during regular operation, combined with large pressure fluctuations in the working chamber. Normal excavation speed reported was between 1 and 2 rotations per minute at an average cutting speed of 5cm/min. Other operational parameters as obtained from field observations or laboratory measurements and used in calculations in this section are reported in table 2.13 [105, 171].

Figures 2.56 and 2.57 give an overview of the soil stratification for the first tube. The top soil consists of several metres of Holocene deposits overlying Pleistocene sands and clays. The Holocene deposits are made up of fine sand, alluvial clay and peat. The top of the Pleistocene layer consists of sand, giving way to strongly consolidated and slightly sticky clay layers at greater depths. Near the start and end shafts the tunnel lies within the Holocene layers and only touches the sand layers at the invert, but below the river the tunnel lies entirely within the pleistocene layers. Here a considerable part of the face lies within the stiff clay layers. The stratification below the COB monitoring field North is shown in more detail in figure 2.58. This figure also shows the location of two of the piezometers installed in the path of the TBM. For a number of selected profiles the stratification is listed in table 2.14, with the accompanying soil properties listed in table 2.15 [44, 104, 101]. The indices to the soil types used in the latter table correspond to the numbers used in the various stratification overviews.

Both North and South embankments have their water table at 0.0m+NAP. The river Oude Maas has a mean level at 0.0m+NAP and a tidal influence of 0.5m. This tidal influence also manifests itself in the sand layers below the river and beneath both banks with an amplitude of roughly 0.3m.

For these profiles the minimal support pressure at the axis s_{min} and the resulting excess pore pressure Δp_p have been calculated using the basic model, i.e. the model with a straight failure



	8	9	10
0.75	-25.1		
A	38F		
1.0	-26.5		
F	38A		
0.2	-20.4	-21.0	
A	38F	38A	
0.25	-16.5	-21.4	22.5
	32	38F	38A
1.0	-27.1	-27.6	-27.9
	38E	38C	38F
0.6	-22.6	-25.9	-27.0
	38A	38E	38F
0.8	-22.0		
	38A		
1.0	-21.8	-26.0	-28.2
	38A	38E	38F
0.2	-16.8	-24.0	
	32	38A	
0.1	-14.5	-15.4	-22.1
	31	32	38A
0.75	-21.5	-24.5	
	38A	38E	

unnel

Index	Desc.	γ_{dry} (kN/m ³)	γ_{sat} (kN/m ³)	c (kPa)	ϕ (°)	c_u (kPa)	d_{10} (μ m)	k (m/s)
F1	rock fill		18.0	0	40			
OA	mainly sand	16.5	19.5	0	34			$1 \cdot 10^{-5}$
OB	mainly clay	16.0	16.0	3	23	30		$1 \cdot 10^{-7}$
1	clay, silty	16.5	17.2	3	26	40		$1 \cdot 10^{-7}$
2	sand, clay layers	16.0	18.0	0	30			$5 \cdot 10^{-6}$
3	sand, some clay layers	17.0	20.0	0	33			$5 \cdot 10^{-5}$
1-3	clay, sandy	16.5	16.5	4	26	40		$1 \cdot 10^{-7}$
4	peat	11.5	11.5	4	20	25		$5 \cdot 10^{-9}$
15	clay, organic		16.5	7	26	45		$1 \cdot 10^{-7}$
9	peat		14.0	7	25	35		$5 \cdot 10^{-9}$
16	clay, silty		17.0	5	26	40		$1 \cdot 10^{-7}$
17	clay, thin sand layers		18.5	7	30	65		$3 \cdot 10^{-7}$
18	sand		20.5	0	36		140	$1 \cdot 10^{-5}$
18A	sand, thin clay and peat layers		20.5	0	35			$5 \cdot 10^{-5}$
16-18	clay, sandy		18.0	7	29	60		$3 \cdot 10^{-7}$
31	clay, silty, sandy		18.0	4	27.5	75		$1 \cdot 10^{-7}$
32	sand, medium coarse, gravel		20.5	0	36		200	$4 \cdot 10^{-4}$
38A	clay		20.0	7	31	140		$1 \cdot 10^{-6}$
38C	peat		14.0	7	27.5	140		$1 \cdot 10^{-8}$
38D	sand, clay layers		20.0	7	32	140		$1 \cdot 10^{-6}$
38E	sand		20.5	0	37			$1 \cdot 10^{-5}$
38F	sand		20.5	0	37			$3 \cdot 10^{-4}$

Table 2.15: Soil properties for Second Heinenoord Tunnel profiles

No.	p (kPa)	σ_v (kPa)	$s_{min}^{(b_{1,0})}$ (kPa)	$\Delta p(w)$ (kPa)	$s_{min}^{(c_{1,0})}$ (kPa)	$\Delta p(w)$ (kPa)	$s_{min}^{(pred)}$ (kPa)	$s_{max}^{(pred)}$ (kPa)	s (kPa)
N1	124	266	167.1	33.7	135.5	8.3	162.5	225.9	177
N2	128	289	171.2	32.7	138.4	7.5	166.9	248.2	196
N3	144	325	184.1	27.7	150.1	3.8	187.5	280.5	246
170	180	353	230.1	44.0	188.4	6.5	217.3	307.7	254
250	218	337	280.9	56.9	251.1	29.2	250.6	292.0	275
350	230	347	247.7	14.6	237.4	6.1	257.9	303.0	273
R1	221	358	236.7	13.0	225.8	3.2	247.1	293.1	279
380	218	332	237.7	17.1	225.0	5.6	245.9	287.3	265
525	146	258	175.8	26.0	155.3	7.7	179.2	218.6	198
545	136	271	160.4	19.3	142.2	4.6	172.3	231.9	188
S1	120	251	151.8	27.9	128.7	7.2	153.5	215.4	165

Table 2.16: Calculation results for selected profiles of Second Heinenoord Tunnel



Figure 2.55: Front view of Second Heinenoord TBM

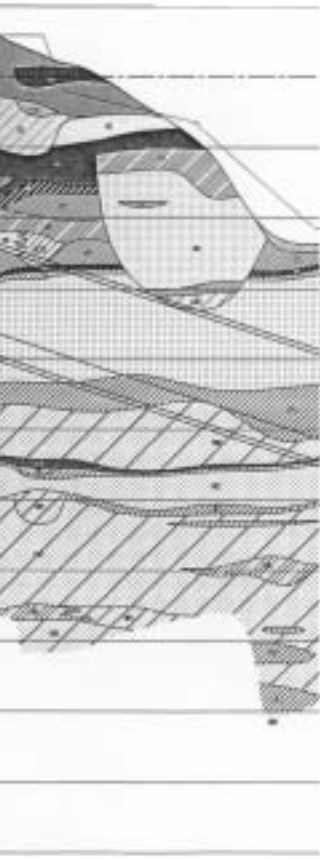
plane and arching model $c_{1,0}$, as well as with a model including the arching model $b_{1,0}$, denoted as $s_{\min}^{(c_{1,0})}$ and $s_{\min}^{(b_{1,0})}$ respectively and similarly for the excess pore pressures, see table 2.16. This table also lists the minimal support pressures calculated with the method prescribed in the design guidelines, $s_{\min}^{(\text{pred})}$ [139]. These design guideline values were derived from a full-membrane model, which did not include three-dimensional arching effects, such as the tabulated values of K_{A3} reported by Jancsecz [89] for non-cohesive layers, and are derived using safety factors $\eta_W = 1.05$ and $\eta_E = 1.5$. As such they can not be directly compared to the s_{\min} values calculated with the other two models, but are included to give an indication of the safety margins used in the design and of the relative position of the design values to the postdicted values of s_{\min} . The maximum support pressure at the top of the face prescribed in these guidelines was equal to σ_v at the top of the face, which has been converted to $s_{\max}^{(\text{pred})}$ at the axis using $\gamma_F = 10\text{kN/m}^3$.

The support pressure s at the axis, back-calculated from the observed pressure in the air-cushion, was 177kPa for profile N1. Back-calculating the support pressure from pressure gauges on the submerged bulkhead or cutter arms (see figure 2.61) leads to a somewhat higher support pressure, 195kPa, but comparing simultaneous measurements from different gauges also indicates that either the density of the slurry varies strongly over the height of the face, reaching values as high as 30kN/m^3 , or that these measurements have not been corrected for certain (unexplained) offsets [17, 162]. Therefore the support pressure backcalculated from the air-cushion pressure has been listed as the used support pressure s in table 2.16.

Comparing the results from the $b_{1,0}$ and $c_{1,0}$ models, it becomes clear that the latter model predicts a relatively small s'_{\min} , whereas most results from the first model lie close to the design values, which included relatively large safety factors. An exception is profile 250, where both the $b_{1,0}$ and $c_{1,0}$ models yield somewhat higher minimal support pressures, since the estimated leakage length for this profile is larger and as a result the aquifer behaves more like a confined



Figure 2.5



outh bank

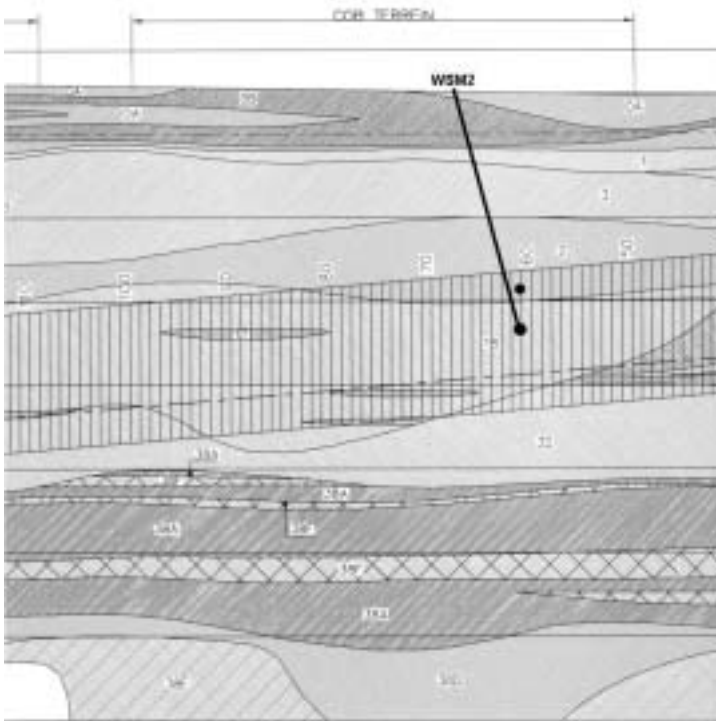


Figure 2.58: Overview of soil stratification at COB monitoring field North and location of piezometers in path of first tube

aquifer, which results in a stronger reaction of the minimal required excess support pressure to the excess pore pressures.

Now the $c_{1,0}$ model, without safety factors, is believed to yield the support pressure at which complete failure of the face has occurred. This is an unsafe estimate of the allowable minimal support pressure. The $b_{1,0}$ model on the other hand should yield an indication of a safe support pressure. It would be more straightforward to choose appropriate safety factors and use the $c_{1,0}$ model to derive a safe estimate of the minimal support pressure. This will not be done for all profiles, but when a safety factor $\eta_E = 1.3$ is implemented for profile N1 this yields $s_{\min} = 156\text{kPa}$. When safety factors $\eta_E = 1.3$ and $\eta_W = 1.05$ are implemented, $s_{\min} = 195\text{kPa}$ is found and when $\eta_E = 1.5$, $\eta_W = 1.05$ are chosen, the resulting $s_{\min} = 300\text{kPa}$ lies well above the allowable maximum support pressure.

From these values it becomes clear that the margin of safety that was thought to be derived from the use of the rather large safety factors in the design guidelines is partly, or completely, eroded if the results from the $b_{1,0}$ model, or a $c_{1,0}$ model using safety factors, are believed to yield the minimal required support pressures. For ring No. 250 the $b_{1,0}$ model yields a minimal support pressure slightly higher than the used pressure and this might indicate that this model overpredicts the minimal support pressure. This slight deviation could, of course, also be accounted for by slight variations in the soil properties.

If, however, the small differences between the observed support pressures and the predictions from the $b_{1,0}$ model are combined with the observed pressure fluctuations, discussed at the

end of this paragraph, it becomes very likely that the $b_{1,0}$ model overpredicts the minimal required support pressure. This model could be used to estimate a safe working pressure, in which case the use of safety factors would not be required. It should be noted, however, that if this approach is taken, the margin between the minimal and maximal allowable support pressure, which was originally intended to serve as a buffer for pressure fluctuations during boring only, will have to compensate for variation in soil properties as well. It is therefore recommended to use a model which predicts failure as closely as possible, and to use safety factors to deal with variations in the soil properties and to use an additional safety margin to counter possible pressure fluctuations. Given the data presented so far, the basic model may be such a model.

A number of pore pressure gauges, installed below COB monitoring field North, gave a unique opportunity to observe the excess pore pressures generated by the boring process and check the validity of the basic model. Figure 2.59 shows the pore pressure measurements from piezometer WSM2, which have been shown previously in figure 2.24. This piezometer was installed in the projected axis of the first tube in a sand layer with overlying Holocene clay layers. The pore pressures were measured with a resolution of 1s. In the figure these pore pressures are given as a function of distance to the face of the TBM instead of time, so that measurements taken during stand-still of the TBM are lumped together and show as vertical downward spikes. Measurements were obtained right up to the instant the gauge was destroyed by the cutter wheel and subsequently hauled to the slurry treatment plant, where it was briefly observed while passing over the sieves.

It can be observed that the pore pressure at rest was approximately 123kPa with a tidal influence of 3kPa, in correspondence with values observed from nearby stand pipes. During boring, however, excess pore pressures were recorded up to 30m in front of the face. When boring stopped, the excess pore pressures dissipated again [38]. The maximum pressure recorded shortly before the gauge was destroyed is somewhat higher than the observed support pressure, but this may be due to local excess pore pressures caused by the cutting process or mechanical contact between the TBM and the pressure gauge. Superimposed on these measurements, using a dashed line, is the excess pore pressure profile calculated with the $b_{1,0}$ model for profile N1. The support pressure calculated by the $b_{1,0}$ is close to the used support pressure. The excess pore pressure distribution in the slurry infiltration zone, which has an length less than 0.5m, has not been plotted, as it would be obfuscated by the large number of spikes, representing pressure fluctuations due to the cutting process, measured over the last metre or so. Except for this last metre, the similarity between the predicted pore pressures using a steady state groundwater flow model and the measured maximum excess pore pressures is remarkable.

Figure 2.60 gives a more detailed look at the dissipation of excess pore pressures with time, starting from the moment the cutter wheel has stopped. The distance between the excavation face and the piezometer at this time was estimated at 60cm [36]. As soon as the removal of the (partial) filter cake is stopped, the bentonite infiltration will not be disturbed any more and a filter cake can form. During this process filtrate water will continue to infiltrate the soil, with resulting excess pore pressure. When, after a certain timespan, the filter cake seals the face, hardly any water will infiltrate the soil and the excess pore pressures will start to dissipate. This behaviour can be observed in figure 2.60. In this graph the dashed line has been calculated using (2.83) with $S_s = 4 \cdot 10^{-5} \text{m}^{-1}$. These measurements substantiate the proposed mechanisms of bentonite infiltration, continuous filter cake removal and the generation of excess pore pressures included in the basic model.

Up to this point the focus has been on the influence of excess pore pressures on the minimal support pressure. The occurrence of an instability while boring below the river Oude Maas in a region with limited overburden gives an opportunity, however, to investigate the allowable

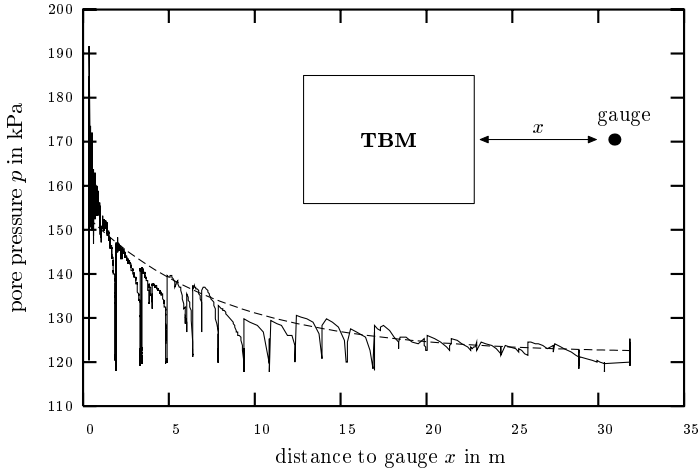


Figure 2.59: Measured excess pore pressure at COB monitoring field North compared with calculated excess pore pressure profile for profile N1 (dashed)

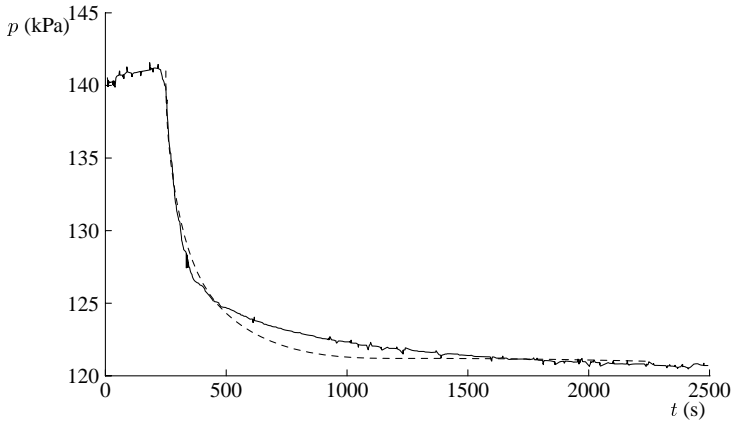


Figure 2.60: Measured excess pore pressure dissipation with time at COB monitoring field North, and calculated dissipation from (2.83) (dashed)

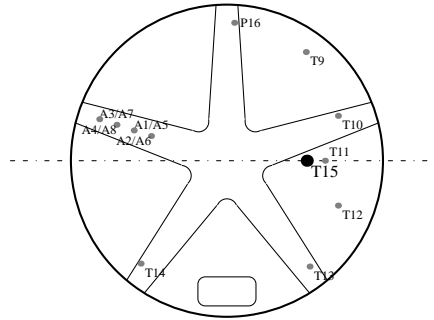


Figure 2.61: Location of pressure gauges on the Second Heinenoord TBM (P16 is located on the pressure bulkhead, T9-T15 are located on the submerged bulkhead, A1-A4 are located on the back of the cutter arm, A5-A8 are located on the front of the cutter arm)

maximum support pressure, as well as the influence of excess pore pressures on the governing failure mechanism [36]. The presence of a number of pressure gauges in the working and pressure chambers of the TBM gives some insight in the realised support pressures.

During boring below the river, the support pressures recorded by pressure gauge T15, located on the submerged bulkhead level with the central axis of the TBM (see figure 2.61) were on average higher than the vertical total stress level and showed a strong variation. They are significantly higher than the support pressure s back-calculated from the air cushion pressure. This difference has been attributed to, among other things, uncorrected offsets, errors in the gauge calibration and direct contact between gauges and clay lumps present in the slurry, but no completely satisfactory explanation has been found. See figure 2.62 for a graph of the recorded support pressures [162]. Indicated are the bounds of the minimum and maximum recorded pressures as well as the averaged pressure over each 1.5m interval. Also indicated are the minimum and maximum allowable support pressures derived from the basic model, the $b_{1,0}$ model, from the predictions using Jancsecz's tabulated values and from the total vertical stress.

At the point indicated in figure 2.62 a flow channel between the excavation chamber and the river bed was created and slurry escaped from the excavation chamber to the river. Attempts were made to counter the loss of support pressure by pumping considerable amounts of slurry, later replaced by pure water and air, to the face. This could not in the end prevent a face collapse, resulting in a blocked excavation chamber [172]. Upon inspection of the river bed, a roughly 6m diameter and several metres deep pit was discovered [140]. Closer inspection of the support pressure measurements at the onset of the loss of support medium shows a sudden drop in the support pressure to the piezometric head of the river (see figure 2.63). This drop occurred at the exact time when, after standstill of the TBM in order to build a new ring, boring was restarted. It is believed that at that time the filter cake was removed and water infiltrated the soil, leading to excess pore pressures in front of the face [36, 162].

This indicates that during stand-still, when a filter cake has formed, the maximum allowable support pressure is significantly higher than the vertical total stress and can be determined from a model that takes three-dimensional dispersion and friction forces into account, such as the model shown in figure 2.17. However, when the filter cake is removed, the maximum allowable support pressure is roughly equal to the vertical total stress. It is reasonable to assume that actual failure occurs at a slightly larger pressure, in the order of the vertical total stress, increased by the undrained shear strength or undrained compressive strength, by way of a fracture-like failure

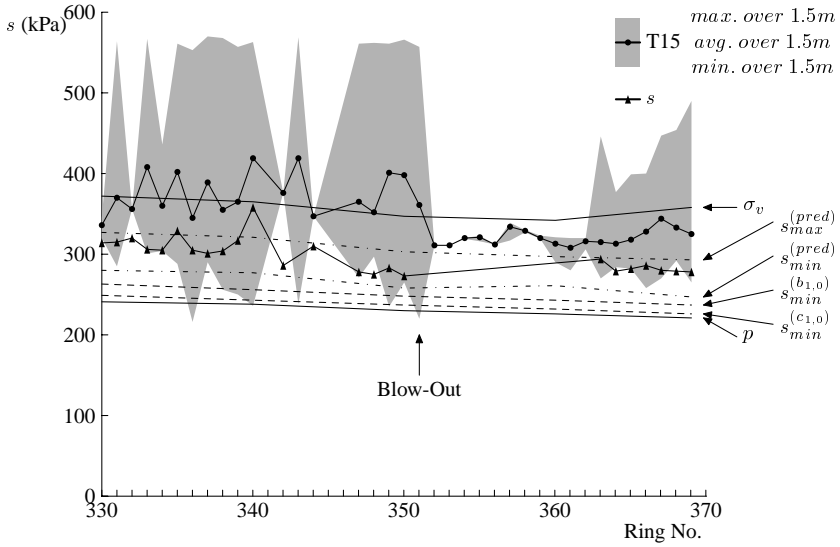


Figure 2.62: Measured support pressures under River Oude Maas at Second Heinoord Tunnel compared with calculated allowable support pressures [162]

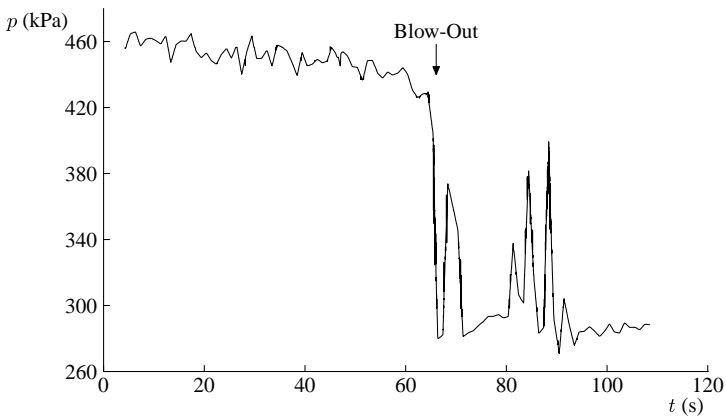


Figure 2.63: Detail of measured support pressures before and during blow-out [162]

mechanism, but the evidence to support this is limited. Therefore it is recommended to limit the maximum support pressure to the vertical total stress [36].

Having established the minimal support pressure derived from the $b_{1,0}$ model on the low end and the vertical total stress on the high end as acceptable bounds for the allowable support pressure, it is interesting to look at the fluctuations in the support pressure shown in figure 2.62. The margin between these bounds is 55kPa, while the difference between the maximum and minimum of registered support pressure over a 1.5m interval is in the order of 330kPa, even excluding the ring where the blow-out took place. Since the various pressure gauges do not show completely similar trends, part of this variation is attributed to direct contact between the pressure gauges and clay lumps present in the slurry, as a combined result of the suboptimal slurry flow conditions and the stickiness of the pleistocene clay layers. But even when a 30s running average is used, the difference remains 48kPa [36]. Although this significantly reduces the severity of the fluctuations, the available margin between minimal and maximal allowable support pressure of 55 kPa was only slightly larger.

The combination of observed pressure fluctuations and the calculated minimal and maximal support pressures indicates that the $b_{1,0}$ model may be somewhat conservative. On several occasions support pressures have been used lower than calculated with the $b_{1,0}$ model. It must be noted, however, that some of the more extreme pressure dips have also exceeded the minimal support pressure calculated with the basic model and that no evidence of total face collapse is found. This might indicate, and is not unreasonable to assume, that short term transgressions of the bounds of allowable support pressure will not immediately lead to a face collapse. The large fluctuations do indicate bad pressure control or frequent local collapses however [10]. Given the data, the basic model is preferred over the $b_{1,0}$ or other models.

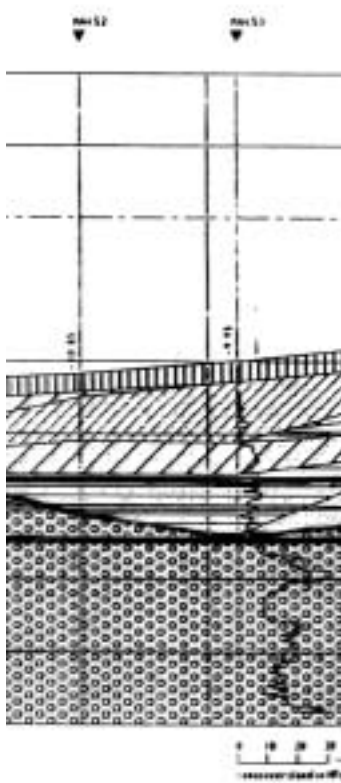
From these measurements it is also clear that the restriction of the maximal allowable support pressure to the vertical stress at the top of the TBM is an overly strict requirement, although the available safety margin is not directly clear. If it is supposed however that fracturing of the aquitard above the TBM (layer 31) is the governing mechanism, the maximal allowable support pressure for ring 350 could be calculated from (2.22) as $s_{\max} \approx 400\text{kPa}$. This is well below the recorded support pressure and indicates that fracturing of this layer may have contributed to the observed blow-out. Given a lack of data, the limitation of the maximal allowable support pressure to the total vertical stress seems warranted, even if overly conservative.

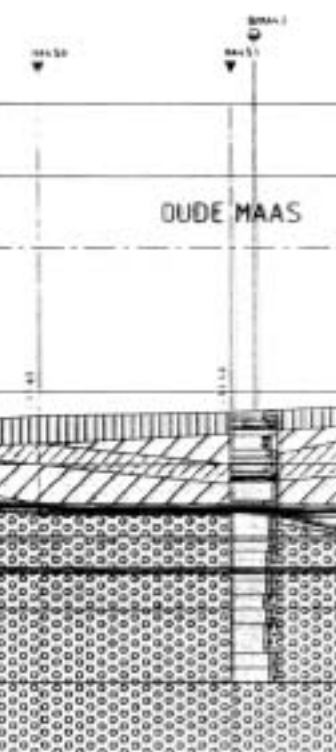
2.4.2 Botlek Utility Tunnel

The Botlek Utility Tunnel is a single 5.14m diameter tunnel bored with a Herrenknecht Hydroshield. Boring started and ended in roughly circular 30m deep and 15m diameter shafts constructed using slurry walls. As the TBM and support train did not fit in the start shaft, a grout body was constructed outside the shaft and excavated to create an artificial cavern. After severe leakage problems with this cavern had been conquered, boring could commence from the north bank in 1998. At the south bank, 5m in front of the arrival cavern, a number of piezometers was installed approximately 2m outside the projected path of the TBM.

The TBM (see figure 2.66) carried a four-spoke wheel equipped with 38 cutters and one central cutter. Regular cutting speeds between 0.5 and 2 rotations per minute have been reported [95].

The soil is characterised by soft Holocene layers, consisting of sand, clay and peat, overlying a Pleistocene sand layer. The tunnel lies within the lowest Holocene layers and the top of the Pleistocene sand layer. See figures 2.64 and 2.65 for an overview of the soil stratification. The position of the profiles in table 2.17 is given relative to the position of the piezometer. Soil





No.	Pos. (m)	Water. Tbl. (m+NAP)
1	-87.5	0.27
1*	-87.5	0.27
2	-60	0.27
2*	-60	0.27
3	-30.5	0.27
3*	-30.5	0.27
4	-2	0.27
4*	-2	0.27



Figure 2.66: Botlek Utility Tunnel TBM

Index	Desc.	γ_{dry} (kN/m ³)	γ_{sat} (kN/m ³)	c (kPa)	ϕ (°)	c_u (kPa)	d_{10} (μm)	k (m/s)
A1	rubble	20	20	0	35	0		
B1	sand	18	20	0	27.5	0		
9a	clay	16.5	16.5	2	22.5	32.5		$2 \cdot 10^{-7}$
9a*	"	16.5	16.5	2	22.5	32.5		$2 \cdot 10^{-8}$
9b	"	16.5	16.5	2	27.5	14		
9c	clay, sandy	16.5	16.5	2	27.5	8		$2 \cdot 10^{-7}$
9c*	"	16.5	16.5	2	27.5	8		$2 \cdot 10^{-6}$
9d	clay	16.5	16.5	2	22.5	14		
10	clay, sand layers	18	18	0	22.5	0		$2 \cdot 10^{-6}$
10*	"	18	18	0	22.5	0		$2 \cdot 10^{-7}$
18a	sand	18	18	0	30	0		
18b	"	18	20	0	32.5	0		
18c	"	18	18	0	32.5	0	67	$2 \cdot 10^{-5}$
18d	"	18	18	0	27.5	0		
20a	sand, clay and peat layers	18	18	0	30	0		$2.61 \cdot 10^{-5}$
20a*	"	18	18	0	30	0		$2 \cdot 10^{-6}$
20b	"	18	18	0	30	0	67	$1.95 \cdot 10^{-5}$
32	sand, medium coarse	18	20	0	35	0	140	$2.61 \cdot 10^{-5}$

Table 2.18: Soil properties for Botlek Utility Tunnel profiles

Param	value
D	5.14m
τ_y	10Pa
ν	0.1Pa s
γ_F	10.5-12.7kN/m ³
a	3s
t_F	10s

Table 2.19: Operative parameters for Botlek Utility TBM

No.	x (m)	z (m +NAP)	p (kPa)	σ_v (kPa)	$s_{\min}^{(b_{1,0})}$ (kPa)	$\Delta p(w)$ (kPa)	s (kPa)	Δp_p (kPa)	$\Delta p(x=0)$ (kPa)
1	87.5	-24.2	244.7	350.6	255.8	2.0	265	4.7	0.0
1*					255.9	2.1			
2	60	-23.4	236.7	343.8	247.5	1.8	263	6.1	0.0
2*					247.6	2.0			
3	30.5	-22.2	224.7	383.6	232.9	1.5	260	8.2	2.9
3*					232.9	1.5			
4	2	-20.9	211.7	460.2	214.6	0,5	260	11.3	7.2
4*					214.7	0.5			

Table 2.20: Calculation results for selected profiles for Botlek Utility Tunnel

properties for the layers in a number of selected profiles are given in table 2.18. Unfortunately the permeability has only been determined for the lower aquifer and not for the aquitards, so that estimated permeabilities for those layers have been used. In order to investigate the sensitivity of the results to these estimated values, additional calculations have been made for all profiles using a different (asterisked) set of parameters.

Table 2.20 lists the predicted minimum support pressures, using the $b_{1,0}$ model, calculated for the profiles listed in table 2.17 as well as the actually used support pressure s , reported by the contractor [46]. It can be seen that the permeability of the overlying aquitards does not strongly influence the minimal support pressure, even though this permeability changes the leakage length λ estimated for the aquifer. It can also be seen that a margin of at least 10kPa has been kept between the used support pressure and the predicted minimal support pressure.

Based on the support pressures reportedly used during construction, the expected excess pore pressure at the end of the filter cake Δp_p and the excess pore pressure that would be measured by the piezometer (at $x=0$) have been calculated. The expected values of the excess pore pressure at the location of the piezometer based on the used support pressures are listed as $\Delta p(x=0)$. Figure 2.67 shows the measurements obtained by the piezometer as a function of the distance between the TBM and the piezometer. The values of $\Delta p(x=0)$ listed in table 2.20 and the calculated excess pore profile have been superimposed in this graph. The uncertainty in the leakage length has a clear influence on the drop of the excess pore pressures with distance x from the face, and therefore on the expected measurements of the excess pore pressure profile. To show this influence both upper and lower bound estimates have been plotted.

From figure 2.67 it is evident that the excess pore pressures measured at the Botlek Utility Tunnel project are significantly smaller than those measured at the Second Heinenoord, but their presence and magnitude have been predicted reasonably well using the same model. Going into further detail it should be noted that, at the Botlek Utility Tunnel project, the piezometer used

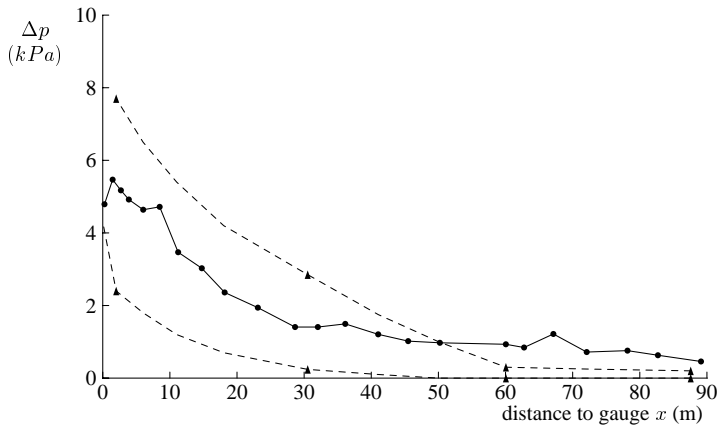


Figure 2.67: Measured excess pore pressures at Botlek Utility Tunnel, with calculated excess pore pressures, upper and lower estimates (dashed lines)

to record the pore pressure was placed 2m outside the path of TBM, whereas at the Second Heinenoord project the piezometers were placed around the projected axis of the tunnel. It is therefore expected that the excess pore pressure distribution measured at Botlek as the TBM nears the piezometer starts to differ from the assumed one-dimensional linear distribution to a greater extent than was the case at the Second Heinenoord.

If it is assumed that the drop of the excess pore pressure is stronger than the assumed distribution (2.66) due to spatial dispersion, this would reduce the difference between the measured and predicted excess pore pressure distribution as sketched in figure 2.67. However, this is only of importance in order to correctly predict the pore pressure distribution and has a lesser bearing on the calculation of the minimal support pressure. Therefore adjustments to (2.66) have not been included in the basic model.

2.4.3 Botlek Rail Tunnel

The Botlek rail tunnel is a 1850m long twin tunnel which runs parallel to the existing rail bridge and the Botlek Utility tunnel. The 9.65m outer diameter tunnel allows double-stack container traffic and is part of the Betuweroute. Like the Second Heinenoord tunnel the Botlek rail tunnel project is a pilot project, on the merits of being the first large diameter tunnel bored with an EPB machine. As such a monitoring programme has been laid out, concentrated in six monitoring crosses MQ1-MQ6 along the alignment as well as a number of sensors in the TBM. The measurement crosses contain inclino- and extensometers as well as piezometers.

The control of the minimal support pressure is often considered not to be an issue with EPB machines. The reasoning behind this is that the excavation chamber of an EPB machine is continuously filled with spoil, so that even at too low support pressures no sudden inflow of material into the excavation chamber could occur. This is not entirely true however, as the control of the volume intake at a too low support pressure is severely hampered and overexcavation becomes very likely. This would in turn lead to increased surface settlements. Furthermore it will be shown that the infiltration of foam into the soil, in case a foam-conditioned EPB machine is used, has similar effects on the required support pressure as the slurry infiltration considered previously, leading to higher required minimal support pressures than derived from

Param	value
D	9.75m
τ_y	5Pa
ν	0.01 Pa s
γ_F	10/14kN m ³
a	300s
t_F	3s

Table 2.21: Operative parameters for Botlek Rail TBM

a full membrane model.

The full-face machine used for the Botlek rail project is equipped with cutter teeth as well as a small central cutter, see figure 2.68. The shield openings are relatively small and visual inspections of the excavation chamber have shown that the central openings clog easily if clay is present at the face and remain effectively closed after that. The tunnel is driven through Holocene clay and peat top layers overlying Holocene and Pleistocene sands, very similar to the stratification at the Utility tunnel. See figures 2.69 and 2.70 for a more detailed overview of the stratification at the locations of the monitoring sites. To deal with the large amount of fine to coarse sand the TBM is equipped with a foaming installation and nozzles in the excavation chamber as well as on the front of the wheel.

Although foam instead of slurry was used to condition the spoil in the excavation chamber, the infiltration length and excess pore pressures will be determined from the same pressure distribution (2.66) as before, only the parameters used will be tailored to reflect the fact that foam is used instead of bentonite. See table 2.21 for the resulting operative parameters. The foam is injected at the face under high pressure and is believed to displace at least part of the pore water that is present. This is supported by the observation that the spoil that exits the screw conveyor is relatively dry and can be easily transported to the surface by a belt conveyor. This displacement of pore water leads to excess pore pressures in front of the face in the same way as if water was injected.

The stratification at the location of MQ1-MQ6 is given in table 2.22, with the soil parameters in table 2.23 [40]. The mean water level in the river is 0.2m+NAP, with an amplitude of 0.4m. This tidal influence also manifests itself in the Pleistocene sand layers as an average piezometric head of 0.2m+NAP with an amplitude of 0.3m. The water level in the Holocene top layers is given in table 2.22. For each of the six test sites the minimal support pressure has been calculated, which is listed in table 2.24. Of special interest are the pore pressure measurements taken at MQ1. They are presented in figure 2.71 as function of time [51].

The first peak in this graph, at the end of day 0, corresponds to the boring of ring 40, the last peak registered corresponds to ring 70. As each ring is 1.5m long this means that excess pore pressures are recorded at least 45m in front of the TBM. The maximum excess pore pressures recorded, 1.25bar, are significantly larger than those measured for the Botlek Utility tunnel.

The representation of the pore pressure measurements as a function of time instead of distance to the face makes it harder to compare with the calculated excess pore pressure distribution according to (2.66). It shows however that the timespan between subsequent excavation periods is less than the time needed for the generated excess pore pressures to fully dissipate. As a result, excess pore pressures resulting from previous excavations remain at the start of subsequent excavation periods. This can be calculated using the transient groundwater model (2.82) for the generation of the excess pore pressures, where the influx (2.81) has been used, and (2.83) for the subsequent dissipation of the generated excess pore pressures. Using $S_y = 7 \cdot 10^{-4} \text{m}^{-1}$ the

	8	9	10
.2	-17.6		
1	32		
.2	-17.6		
1	32		
.8			
.2			
.4	-18.2		
1	32		
.6	-16.3	-17.4	-17.8
1	16	9/31	32
.4			

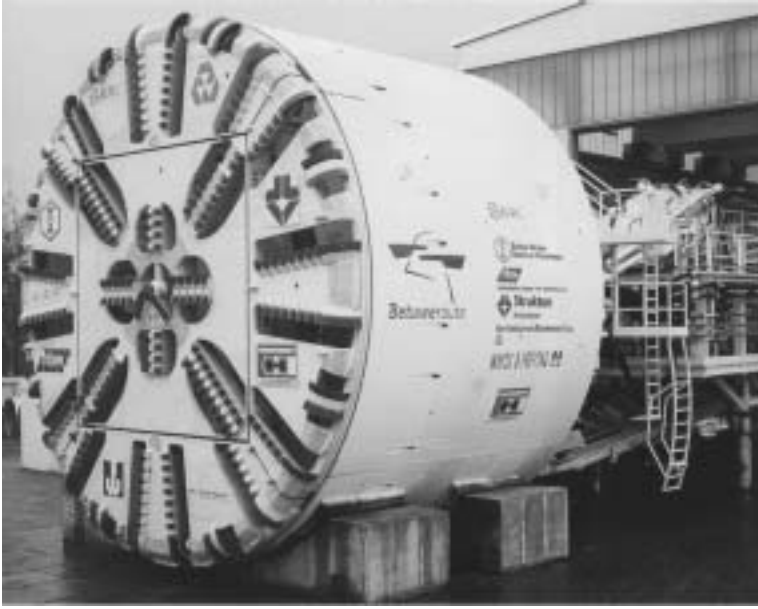
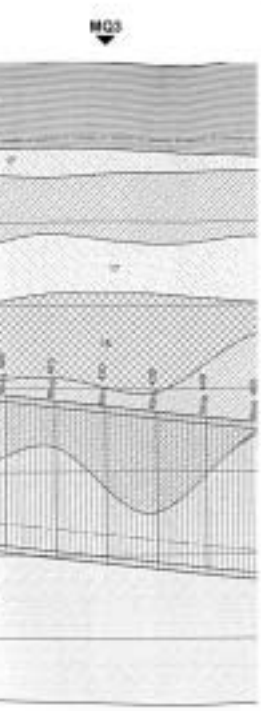


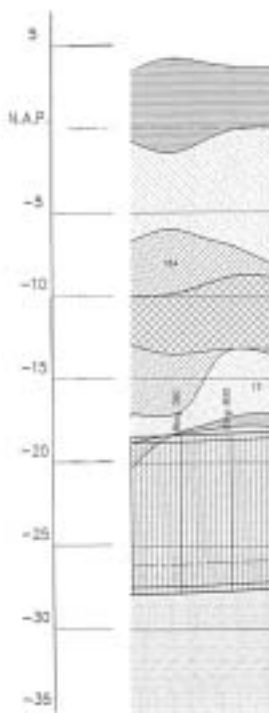
Figure 2.68: Botlek Rail Tunnel TBM

Index	Desc.	γ_{dry} (kN/m ³)	γ_{sat} (kN/m ³)	c (kPa)	ϕ (°)	c_u (kPa)	d_{10} (μm)	k (m/s)
OA	mainly sand	17	19	0	30			
12	clay, silty, sand layers		17	7.5	27.5			
15	clay		15	5	23	60		$7 \cdot 10^{-9}$
16	clay, organic		17	7.5	25			$2 \cdot 10^{-9}$
17	clay, thin sand layers		19	15	27.5			$1 \cdot 10^{-7}$
17*	"		19	0	30			$1 \cdot 10^{-7}$
18	sand, fine		19	0	37		67	$1 \cdot 10^{-5}$
18*	"		19	0	32		67	$1 \cdot 10^{-5}$
18A	sand, fine, thin clay layers		19	0	32.5		67	$1 \cdot 10^{-6}$
18A*	"		19	0	36		67	$1 \cdot 10^{-6}$
9/31	peat, clay, sandy or silty		15	10	25	60		$1 \cdot 10^{-9}$
32	sand, medium-coarse, gravel		20	0	35		140	$3 \cdot 10^{-4}$

Table 2.23: Soil properties for Botlek Rail Tunnel profiles



Q3



Fig

No.	p (kPa)	σ_v (kPa)	$s_{\min}^{(c_{1,0})}$ (kPa)	$\Delta p(w)$ (kPa)	$s_{\min}^{(b_{1,0})}$ (kPa)	$\Delta p(w)$ (kPa)
MQ1	103	226	127.9	20.5	161.8	49.1
MQ1b	117	254	198.2	66.3	261.6	116.7
MQ2	198	414	198.2	0.0	228.3	26.9
MQ3	231	476	231.0	0.0	263.0	13.0
MQ4	253	483	253.0	0.0	329.6	63.4
MQ5	179	334	179.0	0.0	191.9	11.6
MQ6	167	298	167.0	0.0	173.9	3.0

Table 2.24: Calculation results for selected profiles for Botlek Rail Tunnel

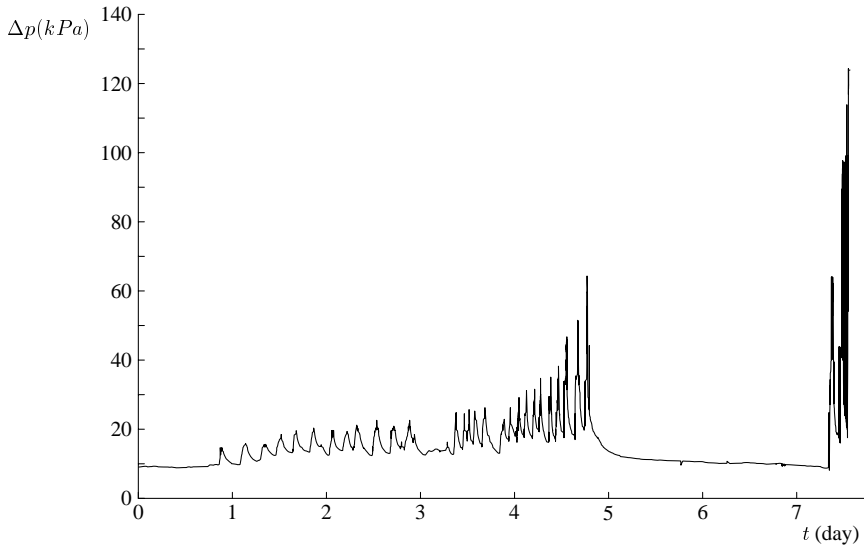


Figure 2.71: Pore pressure measurements for MQ1 as function of time [51]

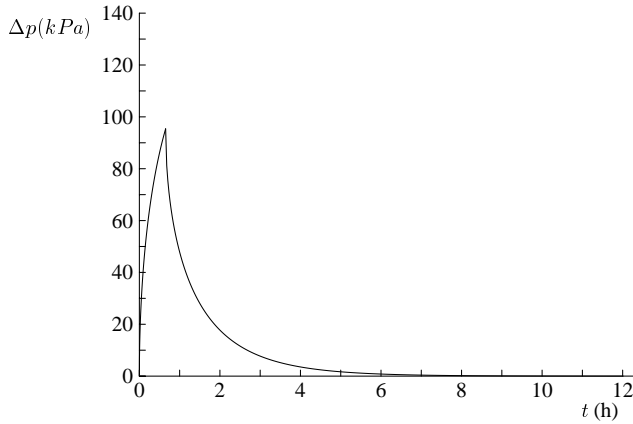


Figure 2.72: Generation and dissipation of excess pore pressures according to (2.81), (2.82) and (2.83) at the tunnel face

resulting time dependent behaviour for a 45min boring sequence followed by standstill has been plotted in figure 2.72. From this figure it can be gained that $1\frac{1}{2}$ to 2 hours after excavating has stopped, the generated excess pore pressures have not dissipated fully and even higher excess pore pressures may be expected at the end of boring of the next ring.

The dissipation of the generated excess pore pressures according to (2.83) for ring 67, when the TBM is still several metres from the piezometer, is compared in figure 2.73 to the measurements made after boring for this ring was complete. This is a more detailed view of the measurements presented in figure 2.71 for $t \approx 114 - 128$ h. It can be seen that a relatively simple groundwater flow model predicts the dissipation of pore pressures reasonably well.

The excess pore pressure profile resulting from (2.66) is compared with the measurements from MQ1 as a function of the distance x between the piezometer and the TBM in figure 2.74. For these calculations an assumed support pressure $s = 200$ kPa has been used. In this figure the excess pore pressures that remain according to (2.83) 1.5h after boring has stopped are also plotted. The latter distribution is an estimate of the remaining excess pore pressures at the beginning of a subsequent excavation. The influence these remaining excess pore pressures may have on the timespan needed to reach the equilibrium distribution (2.66) or on the magnitude of the excess pore pressures reached within an excavation sequence has not been examined here.

It is clear that the infiltration of foam from the EPB machine into the soil and the subsequent driving off of pore water leads to excess pore pressures in roughly the same way as with a slurry machine. The main difference is the pressure with which the foam is injected into the excavation chamber of the TBM. This pressure is a major parameter in the control of the foam quality and as such not directly related to the required support pressure. As a result it is much higher than the slurry pressure in a slurry machine. An undesirable side effect is that higher excess pore pressures are generated, resulting in lower effective stresses, and this in turn leads to higher minimal required support pressures, both due to the loss of friction forces on the wedge and to the loss of effective support force.

Although loss of face stability and the subsequent sudden inflow of soil into the excavation chamber may not be an issue in an EPB machine if the excavation chamber is completely filled, the high support pressures do have a negative influence on the TBM performance. The high excess pore pressure generated is higher than the effective stress level at the top of the face,

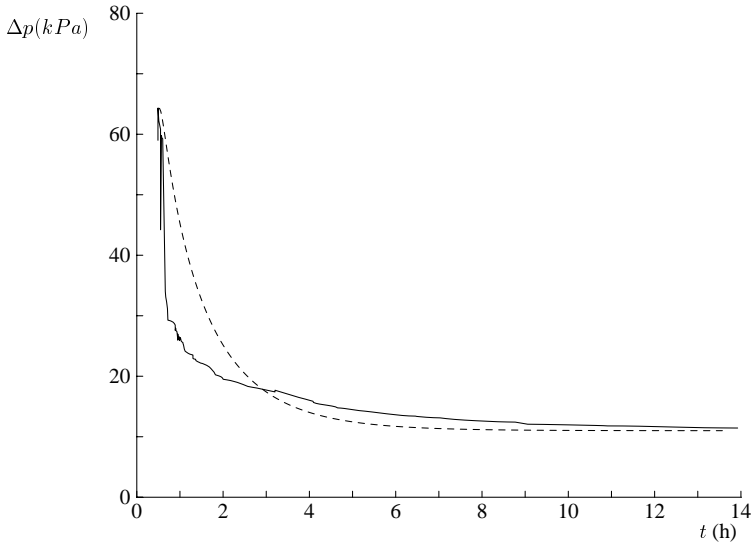


Figure 2.73: Pore pressure measurements for MQ1, ring 67, compared with (2.83) for $x = 4.5\text{m}$

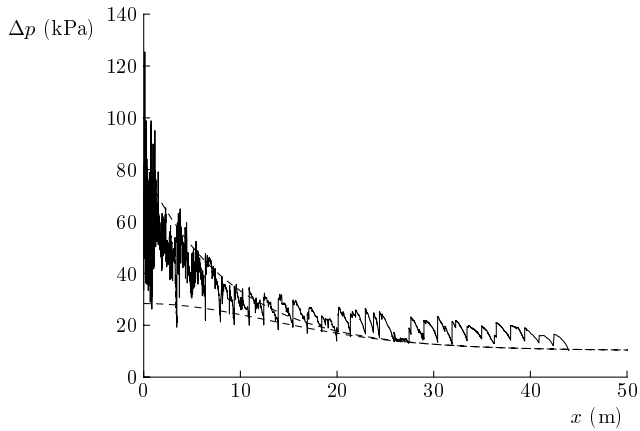


Figure 2.74: Excess pore pressure profiles according to (2.66) and (2.83) for $t = 1.5\text{h}$, compared with measurements for MQ1

as $\sigma'_v(z_a) \approx 119\text{kPa}$ and the measured excess pore pressures indicate that $\Delta s \approx 125\text{kPa}$. This indicates that at the top of the face a limited zone, up to 0.6m from the face, may have liquefied due to the extreme excess pore pressures. As a result the stability of this part of the face and the excavated volume would have been difficult to control, resulting in an overexcavation at the top of the face. This is consistent with the observed large surface deformations at these locations [51].

The pore pressure measurements for the Botlek Rail tunnel show in the first place that there is little difference between foam-conditioned EPB machines and slurry shields, at least where the generation of excess pore pressures and their subsequent influence on the stability of the face are concerned. A difference is of course that the foam does not form a (partial) filter cake and that the pressure drop over the partial filter cake cannot be taken into account. A second difference lies in the demand the foam quality control makes on the foam injection pressure. Since a fixed pressure difference between the foam injection pressure and the pore pressure is required, the foam injection pressure has hardly any relation with the effective support pressure, as is the case in a slurry shield. As it is in fact substantially higher and the foam displaces pore water in a manner very similar to bentonite infiltration, it can lead to much higher excess pore pressures.

Although the foam does not form a filter cake, it does lower the permeability of the soil. As a result support pressures below the hydrostatic pressure can be allowed for short periods even in sandy soils, if the permeability is low enough so that no groundwater flows into the chamber and the foam quality is maintained by regular injections. This effect has been observed in the vicinity of MQ5, where it was possible, during stand-still, to maintain a stable face at support pressures equal to or slightly below the water pressure [51]. This indicates that, barring local and micro-instabilities, the minimal support pressures calculated with the basic model are in all probability close to the actual minimal required support pressure, even in those cases where the model yields a minimal support pressure equal to the hydrostatic pressure.

2.5 Further Groundwater Influences

In the previous sections, only the influence of a simplified pore pressure distribution on the stability of the tunnel face has been taken into account. This does not cover all possible situations encountered in practice. In the following paragraph several remarks will be made about influences of groundwater flow and of excess pore pressures on the stability of the tunnel face that have not been covered before.

In a soft, compressible, impermeable soil the influence of infiltration will be rather limited. Even in such circumstances excess pore pressures may be observed, which have, however, been linked not to the excavation process but to (excessive) grouting at the tail end of the shield. If large volumes of grout are used to compensate the overexcavation of the shield, large displacements may occur, generating excess pore pressures and in time resulting in additional settlements. In such conditions the actual pore pressure distribution around the face also depends on the support force used, which can be obtained from the force in the trust jacks. If the resulting support pressure is greater than the neutral total stress, a further compression of the soil in front of the TBM would add a further excess pore pressure component. In general however the support pressure used in such conditions will be lower than the neutral total stress, and possibly even lower than the active total stress, resulting in a relaxation of the soil and a reduction of the pore pressure.

Akagi [2] has shown that this combined behaviour can be observed in very soft clays, but

also that is difficult to correctly model the combined behaviour using a soil-water coupled finite element analysis. In a more permeable material where infiltration of the support medium plays a role, the situation would be further complicated as the time-dependent infiltration would have to be included. Especially the inclusion of the behaviour of the very thin partial filter cake in a finite element model would pose some problems, as this process occurs at a different scale than the deformations around the TBM.

Buhan [52] has overcome part of these difficulties for the stability of an untreated EPB face, excluding possible influences from the grouting process, by constructing a finite element package specially tailored to include the drag forces on the soil body of a groundwater flow towards the face. As the soil mass in this model is considered homogeneous at the face and inside the working chamber, no problems with differences in permeabilities or scales exist. The model shows the extent to which a drag force towards the TBM lowers the face stability.

As also found in other models of the tunnel face [137], the fact that the soil is continuous and completely homogeneous limits the number of possible failure mechanisms. Micro-instability of the face at low pressure or fracturing of the soil at high pressure will not occur in a finite element model if not specially included in the model by means of discontinuities. Also relatively large moving soil bodies are predicted, as compared to the observations in centrifuge tests, resulting in large areas where friction forces with the surrounding soil are generated. As a result such analyses seem to underestimate the minimal required support pressure and strongly overpredict the actual allowable maximal support pressure. As a result of such modelling issues, the value of finite element analysis for the determination of the limits of allowable support pressure is still rather limited.

Finite element analyses can be used however to investigate partial aspects of the stability problem, such as the three-dimensional dispersion of the excess pore pressures in front of and above the face in a complex heterogeneous soil. In cases where a tunnel is bored in a permeable layer, the excess pore pressures at the top of the aquifer may rise to a significant portion of the excess support pressure. In that case the maximal allowable support pressure could well be determined by the stability of the overlying layers, especially if the effective weight of these layers is low.

Similarly, such analyses could be used in situations where the stability of sand lenses in front of the face is an issue. During excavation the infiltration of support medium into these lenses, combined with their limited storage capacity, will cause a significant rise of the excess pore pressure, with hardly or no spatial dispersion. When the lens is completely full several scenarios can develop. In case of a slurry supported sand lens, the slurry infiltration will cease and the risk of micro-collapses of the lens will increase dramatically. And given a large enough support pressure, the effective stress of the sand could be fully eroded, resulting in a liquefaction of the lens and an unstable face. Even if the effective stress is only partly lowered, liquefaction may be induced by the vibrations of the TBM [127]. For the detailed analysis of such effects a simple wedge stability calculation and one-dimensional groundwater flow model will not suffice and a finite element model can be used to gain a three-dimensional pore pressure distribution as part of the calculation process.

A further point not explicitly covered before is the influence of tidal variations on the limits of allowable support pressure. Although at first glance this only seems to result in a change in the hydrostatic pore pressure, it may also result in a difference in overburden stress and in the limits of allowable effective support pressure. In cases where a partially permeable upper layer is present, a time lapse between the tidal wave and the resulting pressure wave in the subsoil may occur. In such a case the minimal and maximal support pressure should be calculated using different hydrostatic pressures for the different layers. In cases where a limited overburden is

present it may even become necessary to follow the tidal variation with the support pressure to prevent a possible collapse. The construction of the Alte Elbe Tunnel is a well documented case of such a situation and the catastrophe that may follow [109].

2.6 Conclusions

To support the soil and to minimize deformations during the tunnel boring process, a pressurised slurry or foam-conditioned soil mass is often used in soft and water-bearing soils. The objective of this support medium is to transfer the support force from the TBM onto the soil skeleton and in this way ensure the stability of the tunnel face. In a slurry shield the bentonite slurry is used to ensure the micro-stability of individual grains, to seal the tunnel face in order to transfer the support pressure onto the soil skeleton and to prevent sedimentation of soil particles during transport to the spoil treatment plant. To seal the tunnel face the bentonite slurry has to infiltrate the soil and form a filter cake. In an EPB machine, foam or slurry is used to condition the excavated soil mass to improve its plasticity and lower the permeability and water content of the spoil. To reach the latter goal the foam will have to infiltrate the soil and displace the pore water present there.

In this chapter a modified limit equilibrium model has been presented that can be used to calculate the minimal required support pressure, taking the influence of the infiltration processes into consideration. And although the focus lies on the slurry-conditioned boring process, the model can also be used to investigate the stability in a foam-conditioned EPB machine. In this stability model the failure body in front of the TBM is schematised as a wedge loaded by a soil silo. Acting on this wedge are the overburden force resulting from the soil silo and the weight of the wedge itself. Resisting forces are the cohesive-frictional forces on the slanted front plane and triangular side planes of the wedge and the slurry force acting at the tunnel face. This last force is partially counteracted by the force resulting from pore water pressures. Up to this point the model is similar to other wedge stability models described in the literature. The first modification is that the model presented here has been formulated in a manner that can deal with heterogeneous soils above and in front of the tunnel face.

A second modification concerns the infiltration of the support or conditioning medium into the soil. In a slurry tunnelling process the assumption is often made that the bentonite will form a filter cake at the tunnel face, which cake will seal the face and transfer the support force onto the soil skeleton. This assumption is valid to a certain extent during stand-still, but not during the actual excavation process. Each time the cutter bits or roller discs pass over the face, the millimetres or centimeters thick cake is removed along with the excavated soil and infiltration of the support medium into the soil starts to build up a new cake. In this process water infiltrates the soil and generates excess pore pressures in front of the TBM. These excess pore pressures reduce the effective stresses, and thereby the friction forces acting on the wedge, and simultaneously increase the water force counteracting the support force.

To counteract this influence, an increased support pressure is needed, which in turn leads to an increase of the excess pore pressures. The model described in section 2.2 includes these effects and leads to the equilibrium relation

$$s'(z_t) = - \frac{G_s - P_s + G_w + K' + 2T' - 2P_T + S'_{\text{dev}}}{Z} \quad (2.89)$$

which has to be maximised as function of the wedge angle θ . Given the slurry density the total support pressure can then be found by adding the total pore pressure at the far end of the wedge,

i.e.

$$s(z) = s'(z) + p(w(z), z) \quad (2.90)$$

Now the excess support pressure Δs can be defined as the difference between the support pressure and the pore pressure at rest p_0 .

Although different implementations are possible for the distribution of excess pore pressures in front of the face as a function of the excess support pressure and possibly time, in the presented model a one-dimensional static groundwater flow has been assumed. Over the thickness e of the (partial) filter cake the pore pressures are determined from the infiltration relations; beyond that the simple groundwater flow model is used, so that the distribution of pore pressures is given by

$$p(x, z, t) = \begin{cases} s - \frac{\alpha \tau_F}{d_{10}} x & 0 \leq x < e(t) \\ p_0 + \Delta s \frac{t}{a+t} \exp(-(x - e(t)) / \lambda) & e(t) \leq x \leq w(z) \end{cases} \quad (2.91)$$

In this relation the infiltration length e and thereby the pressure drop Δp_{fc} over the filter cake are time dependent. As a result the static groundwater flow model also contains a time-dependence. This results from the fact that the cutter arms do not pass each point of the face at the same time and therefore the build-up of the filter cake varies over the face. To simplify the model, a mean infiltration time t_F has been introduced which models the average filter cake build-up over the face.

A further aspect to be taken into account is the soil arching over the TBM, which reduces the effective load on top of the wedge. In a layered soil the effective stress in an arching soil column in a layer i can be obtained from

$$\sigma'_{v,a}^{(i)} = \frac{\alpha \gamma'^{(i)} - c'^{(i)}}{K^{(i)} \tan \phi^{(i)}} \left(1 - e^{-K^{(i)} \tan \phi^{(i)} \frac{z}{a}} \right) + \sigma'_{v,a}{}^{(i-1)}(t_i) e^{-K^{(i)} \tan \phi^{(i)} \frac{z}{a}} \quad (2.92)$$

Comparing with results from centrifuge tests, the arching relaxation length a which adheres closest to test results is found from

$$a = \frac{R}{1 + \tan \theta} \quad (2.93)$$

And although the overburden load on top of the wedge is obtained from (2.92), the friction forces on the side planes of the wedge have to be derived from the vertical stress linear with depth, using the coefficient of neutral horizontal effective stress K_0 , for a closest match with centrifuge tests with low overburden. For a more conservative implementation, the relaxation length could be chosen as $a = R$, still in combination with K_0 and no relaxation on the side planes. Based on the limited amount of applicable centrifuge tests the second method always yields safe predictions for the minimal required support pressure.

The inclusion of excess pore pressures in the stability calculations has a profound influence on the minimal required support pressure. It has been shown that for a simple reference case of a 10m diameter tunnel in a sandy layer overlain by a clayey impermeable layer, Δs_{\min} can be four times higher than the minimal support pressure found from a model assuming an impermeable filter cake. This is particularly the case in sandy soils with permeabilities $10^{-5} < k < 10^{-3}$ m/s. In clayey soils, with lower permeabilities and finer particles, the infiltration of filtrate water into the soil and the subsequent displacement of pore water does not occur, whereas in gravelly soils

with larger permeability the dissipation of excess pore pressures occurs much faster and as such the loss of effective support pressure is limited.

In cases where the influence of the excess pore pressures is profound, this influence is further amplified as the friction forces on the wedge planes are reduced due to the decrease in effective stress. This loss of stabilising forces is only partially countered by the decrease in overburden load, caused by the uplift force P_s . The end result is that a further increase of the support pressure is needed, not only to counteract the generated excess pore pressures but also due to the reduction of effective stresses and the accompanying reduction of friction forces, which require an increased effective support pressure s' .

A parameter analysis shows that the permeability of the soil, which influences the leakage length λ used in (2.91), is one of the parameters that most strongly affect the minimal support pressure. Others are the angle of internal friction, the volumetric weight and cohesion of the soil as well as the diameter and overburden of the tunnel and the volumetric weight of the slurry. Other parameters, such as the bentonite shear strength, the characteristic grain size, the infiltration half time and the mean infiltration time, are less influential.

This parameter analysis also shows that a low volumetric weight of the layers in front of the TBM has a positive influence, i.e. a decrease of the minimal required support pressure, but that a low volumetric weight of the overburden layers can have a negative effect, as it not only decreases the load on top of the wedge but also the shear forces stabilising the wedge. A decrease of the angle of internal friction of either the overburden layers or the layers at the face always increases the required support pressure. For all these cases it holds that the influence is stronger if the layer or layers at the tunnel face are permeable than if they are impermeable.

The most striking difference between the stability model presented here and classical stability models is the inclusion of the influence of excess pore pressures. At three different tunnelling projects the excess pore pressures in front of the TBM have been recorded by piezometers installed in or close to the path of the TBM. Two of these projects were slurry-shield driven and one was a foam-conditioned EPB machine. All three projects were situated in the western part of the Netherlands and the tunnels were bored in alluvial and diluvial sands overlain by Holocene clay and peat layers. In all three cases, excess pore pressures were recorded up to several decameters before the TBM arrived at the location of the piezometer. The measurements show a very good agreement with the simplified pore pressure distribution assumed in (2.91) and with predictions made for the support pressure and resulting excess pore pressures.

Overall it can be concluded that excess pore pressures have a profound influence on the stability of the tunnel face and on the effectiveness of the support medium. The limit equilibrium model presented here can be reliably used to take these influences into account and although it will generally require some iterative calculations it is less time-consuming than a full three-dimensional coupled soil-water finite element analysis. Furthermore, (partial) safety factors can be implemented straightforwardly in the model to make it suitable for design purposes.

In the basic model presented here a stationary flow has been assumed, and the assumption has been made that the inflow at the face is sufficient to support this stationary flow. Using transient flow models for the excavation period as well as for the stand-still between subsequent excavation periods, the basic model can be adapted to include a time-dependent build-up and dissipation of excess pore pressures in front of the face. Combined with a rough estimate of the discharge from the TBM, this model can be used to predict the excess pore pressures in layered soil conditions exceptionally well.

Questions that were raised but not answered satisfactorily in this chapter concern first of all the description of soil arching over the tunnel and the influence of excess pore pressures on soil arching. Several different models for the soil arching in combination with the friction forces

acting on the wedge have been presented. The model presented here has been chosen based on a small set of centrifuge tests which show a significant amount of scatter. Another grey area concerns the precise behaviour of the filter cake removal and infiltration processes that occur at the tunnel face, which have been roughly approximated and averaged over the entire tunnel face in order to implement them in the stability model. Both are areas which require further study to establish a detailed description but at the same time it is not expected that such study will significantly alter the results of the stability model presented here.

A further point concerns the maximum allowable support pressure. Observations at the Second Heinenoord tunnel indicate that the loss of the support medium along a flow channel between excavation chamber and ground surface, commonly called a blow-out, is the first failure mechanism to occur and ultimately leads to active failure of the face. To prevent such an instability from occurring, in case an inadvertent flow channel to the surface already exists, it is recommended to limit the maximum allowable support pressure at the top of the face to the vertical total stress. It is clear that this is an overly strict requirement, but is unclear how large the safety margin created in this way actually is, as there is (fortunately) a lack of field data to further specify this limit pressure.

And now for something completely different.

Monty Python's Flying Circus

Chapter 3

Horizontal Cone Penetration Testing

3.1 Introduction

The cone penetration test (CPT) is an increasingly used in-situ soil investigation technique for soft soils. This popularity can be attributed to several factors. The CPT offers a relatively cheap and continuous way to determine the soil profile with depth. And although no soil sample is taken, a large number of analytical and empirical relations has been developed based on the CPT readings, not only to classify the soil, but also to estimate a range of soil properties. Since the introduction of the CPT there has been a widespread effort in this field. Further, the CPT offers a way to detect thin layers surpassed only by undisturbed sampling techniques and, due to the ongoing developments of sensors and data acquisition systems, has reached a level where the reproducibility of the test is very good. Also, the possibility to include other sensors such as electric resistivity sensors provides a way to obtain measurements on geo-environmental aspects with a single penetration. All in all the CPT has become the soil investigation technique of choice in soils where penetration is possible, especially in areas with thick, highly stratified layers of soft sediments, as found in the many delta areas over the world.

In recent years there has been a growing number of elongated underground building projects, for example tunnel boring projects, for which a soil characterization is needed over large distances as well as up to large depths. The typical interval between subsequent (vertical) borings or CPTs from the ground surface for such a project lies somewhere in the range of 50 to 100m [68]. This interval should optimally be determined based on the costs involved in the soil investigation, the funds available in the preliminary stages of the project and the need to gain a sufficiently detailed overview of the soil stratification. Experience makes it painfully clear however that, especially in river deltas, this frequency may be insufficient to gain precise knowledge of the variations in stratification and soil properties, needed for an undisturbed tunnel boring process [47].

This need for additional information leads to a demand for additional soil investigations to fill the gaps present in the preliminary soil investigation, which would ultimately lead to a continuous soil profile. Additional vertical soundings and samplings, at for instance 5m intervals, may not always be the optimal solution and other methods have to be considered. Geophysical methods like soil radar or seismological surface wave analysis do give a continuous picture of the subsoil, but have their own disadvantages [64, 73]. They show an inherent trade-off between reach and resolution, and the signal for most methods is strongly dampened by the presence of pore water. As a result they do not provide useful information for all but the shallowest tunnels.

During a tunnel boring project however, the possibility is created to use the tunnel boring machine (TBM) itself as a starting point for soil investigations, instead of the soil surface. This opens the possibility to conduct horizontal cone penetration tests (HCPT), which would give continuous information about the soil directly in front of the TBM. This information could be used to fine-tune the boring process and could be further supplemented by pushing other sensors, such as ground penetrating radar, along with the HCPT [65]. In this manner more detailed information on the soil stratigraphy could be obtained and local anomalies could be detected. Of course this technique is limited, as the data obtained is not available during the design phase but can only be used to fine-tune the boring process.

The use of HCPTs is not limited to obtaining just-in-time information for use in the tunnel boring process, however. Where an underground structure or excavation pit exists next to a building, it is possible to investigate the soil conditions under the building. And combining a cone with a directional drilling rig, it is possible to execute a directionally drilled CPT (DD-CPT) [141], although in this case the focus should be more on additional sensors installed behind the cone, to measure for example the dispersion of pollutants. With a less complicated setup it is already possible to investigate the actual soil properties of embankments, like dikes and mine tailings, or even railroad beds without disturbing the timetable.

A first problem with the use of HCPT lies in the adaptation of equipment in order to make it suitable for use in a TBM. This amounts not so much to adaptations of the rig or cone, as to a need for watertight locks through the TBM's pressure bulkhead [67, 102]. A second problem is posed by the interpretation of the measurements. The models used to interpret CPT all implicitly or explicitly use the radial symmetry in the horizontal plane around the cone, as the horizontal effective stress is believed to be uniform around the cone in this plane. Similarly, the failure mechanism around the cone is assumed to be radially symmetrical. In the case of HCPT this assumption is clearly invalid, as the stress state perpendicular to the cone varies between horizontal and vertical effective stress, and only the pore pressures can be considered uniform.

Not clear, however, is what influence these differences have on the measurements and interpretation of HCPT. In order to establish the relation between horizontal CPT measurements and soil properties, it would be possible to execute a large number of HCPTs and correlate these with known soil properties. This would, however, require a large number of tests and it is far more efficient to establish a relation between the measurements obtained with traditional and horizontal CPT and use this relation to interpretate HCPT using known empirical and analytical models.

To establish the correlation between horizontal and vertical CPT, a number of methods has been used. In the calibration chamber of the Geotechnical Laboratory of Delft University, hereafter simply called the calibration chamber, a number of horizontal and vertical CPTs has been executed. In these test series the influence of relative density and gradation of the sand has been investigated. In parallel, a two-dimensional scale model has been used to visualise the stress paths and failure patterns occurring during horizontal penetration. Furthermore, a simple cavity expansion model has been developed that can deal with the non-uniform stress state around the cone, and this model has been used to investigate the stress-dependence of the ratio between horizontal and vertical cone resistance.

Prior to the start of this research, only a single reference to the horizontal use of a cone was made, by Santoyo [149], who described using a cone and rods to detect the presence of boulders in front of a tunnel face. Parallel to this research a research project has been conducted by the Centrum Ondergronds Bouwen (COB) in cooperation with GeoDelft. This project focussed on the development of a HCPT installation for use in a TBM and the selection of additional sensors

to be installed behind the cone. Within the framework of this research a number of HCPTs has been made, which will be reviewed in section 3.5.

This chapter will start off with a brief overview of empirical and analytical interpretations of traditional, vertical, CPT. Then the test setup of the calibration chamber will be described, followed by the results obtained with tests in the calibration chamber. Additional laboratory and field experiments will be described next. This in turn will be followed by the derivation of a cavity expansion model used to interpret HCPTs and a discussion of the possibilities to interpret HCPT using conventional vertical CPT models.

The abbreviation CPT will be used in the classical sense, to refer to vertical cone penetration testing, as well as to refer to the combined field of vertical, horizontal and slanted cone penetration testing. In those cases where confusion might arise when a statement is made exclusively about vertical CPT, the abbreviation VCPT will be used.

3.2 Interpretation of Cone Penetration Tests

A large number of different approaches to interpreting the CPT has been presented in literature over the years. An excellent overview is given by Yu & Mitchell [116, 178]. They divide the models into bearing capacity, cavity expansion, steady state deformation, finite-element and calibration chamber models. Only a concise overview of the different categories will be given here. All these models can be used to predict the cone resistance given the soil properties, but can tackle the inverse problem of predicting the soil properties from CPT measurements with varying success. Apart from those analytical and calibration chamber interpretations, there are also empirical relations with different soil types and properties. As the mainstay of tests analysed in this chapter are tests on sand, the focus will be strongly on methods dealing with cohesionless soils.

3.2.1 Bearing Capacity Models

Historically, the first models to analyse cone penetration were bearing capacity models. These models assume the cone resistance q_c to be equal to the collapse load of a deep circular foundation. This collapse load can be determined using a limit equilibrium or slip-line analysis. The limit equilibrium approach is the most popular and a large number of different failure mechanisms has been proposed, including plane strain wedge penetration models as well as circular footing bearing models. Figure 3.1 shows two different mechanisms, proposed by Terzaghi [161] and de Beer [28, 70] respectively. In most cases the bearing capacity calculated for the assumed failure mechanism is converted to a cone resistance using some kind of shape factor. The slip-line approach is somewhat more rigorous, as it satisfies not only the equilibrium equations, but also a given yield criterium everywhere in the slip-line network. The first solutions of this type were given by Sokolovskii [153] for cohesionless materials.

For either approach the resulting bearing capacity is most often presented as cone factor N_c or N_q , for cohesive or non-cohesive materials respectively, where after the usual simplifications

$$q_c = N_c c + \sigma_v \quad (3.1)$$

$$q_c = N_q \sigma_v \quad (3.2)$$

The cone factor N_c often depends on the cone shape and roughness only, and as a result depends on the stress level only as far as the cohesion is stress dependent. N_q resulting from models for

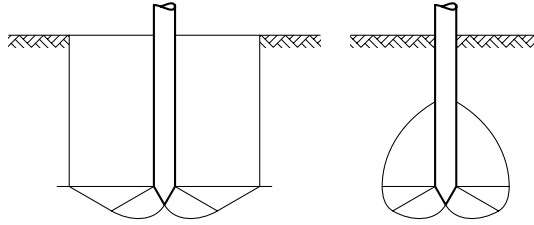


Figure 3.1: Bearing capacity models, after Terzaghi (left) and De Beer (right)

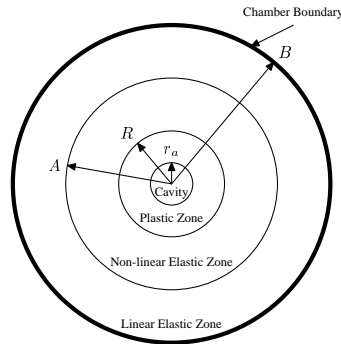


Figure 3.2: Cavity expansion model, after Salgado [146]

frictional material on the other hand depends mainly on the friction angle or relative density, but may also depend on the stress level directly or indirectly through the coefficient of effective horizontal stress or over-consolidation ratio. Some models, such as Sokolovskii's model, further depend on the friction angle at the soil-cone interface or the cone roughness factor.

The radial symmetry inherent in all these models as well as the connection to the surrounding undisturbed stress field at the outer edge of the failing body disallow a simple adaptation of an existing model to one suited for the interpretation of HCPT, requiring in essence the development of an entirely new model. The comparison by Yu [178] further shows that the results and agreement with field and calibration chamber observations depend strongly on the failure mechanism chosen. As such these models will be disregarded when trying to adapt existing models for the interpretation of HCPT.

3.2.2 Cavity Expansion Models

A different approach is the use of cavity expansion solutions to predict the cone resistance. Following Bishop's axiom that the pressure required to produce a hole in an elastic-plastic medium is proportional to the pressure needed to expand a cavity of the same size, there has been a sizeable effort to find the limit pressure for cavity expansion in soils. Over the years increasingly realistic stress-strain models, including effects as stress rotation and dilatancy, have been used, resulting in increasingly complex models, up to the point that, for practical purposes, computers have to be used to evaluate the results [146, 170].

The model presented by Salgado et al. [147] is probably the most interesting when dealing with calibration chamber tests, as they investigate the theoretical influence of the chamber

boundaries on the test results. The model assumes a full plastic zone around the cone, in turn surrounded by a non-linear zone, surrounded by a linear elastic zone bounded by the chamber wall. Unfortunately the focus lies on boundary conditions of constant stress in the horizontal plane (i.e. BC1 & BC4, see section 3.2.5 and table 3.1), for which conditions the ratio of measured over theoretical free-field cone resistance is given. The q_c value calculated for a very large elastic radius B (approximating field conditions) is higher than the value calculated for or measured in a calibration chamber, due to the assumptions that during penetration in a flexible wall chamber the stress at the horizontal boundary is constant and all deformations are radial. Both conditions are difficult to obtain in reality. Salgado further states that in a rigid wall chamber this relation between measured and theoretical values would be exactly opposite. [146, 147].

Due to the possibility of including strain-dependent soil properties, large deformations and stress rotation theory in the model the cavity expansion model is deemed a more promising method of describing CPT than bearing capacity theory [178]. Especially when modelling CPT in frictional material more progress has been made here than with steady-state or finite element models. Combined with the possibility of including a non-uniform initial stress state around the cone, this makes a cavity expansion model the most promising candidate for an accurate model of HCPT.

3.2.3 Steady State Models

The steady state model describes the flow of soil around a fixed body representing the cone tip. Introducing constitutive relations the stress field can be calculated from the assumed strain field. One of the first flow fields, defined by Baligh, often referred to as the simple pile model, resembles the flow around a cone with a rounded tip [21]. Later Levadoux & Baligh improved a similar model, the simple cone model, which closer represents the shape of the cone tip, by including the effect of consolidation [22, 107]. The results from both models hardly differ, however [32]. Recent improvements have been made by using finite element or finite difference methods to obtain the stress fields [160, 177]. Although a promising method, results have been limited to undrained cohesive soils so far.

3.2.4 Finite Element Models

The finite element method has been used at first, in a small strain formulation, by de Borst to calculate the collapse load of a cone in a cohesive soil [41, 42]. As the penetrometer is placed in an undisturbed stress state in this approach, and the build-up of stresses due to penetration and displacement of the soil is not included, the resulting cone factors are lower than resulting from bearing capacity theory. Several researchers have attempted to overcome this problem by using a large strain updated mesh analysis [43, 178]. Especially the mesh updating routines introduce possible numerical problems, however.

Some of these limitations have been overcome by van den Berg using a Lagrange-Euler model [32]. In this model the soil flows through a fixed element mesh similar to the steady state models. A major difference is the possibility to calculate the cone resistance variation at the transition of different soil layers as well as the possibility to use frictional soil models and purely cohesive ones. As such this method offers a significant improvement over analytical or small strain FE methods. However, the significant numerical differences between several reference calculations and analytically known solutions suggest that more effort is needed in this area before a reliable prediction of penetration resistance is obtained.

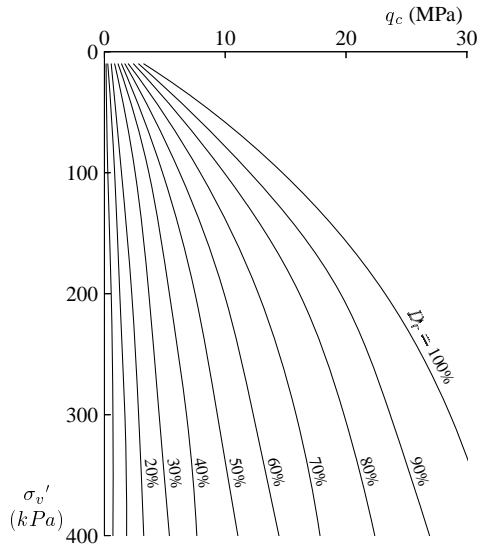


Figure 3.3: Cone resistance vs vertical stress as function of relative density, for normally consolidated sands [150]

3.2.5 Calibration Chamber Testing

Since there are limitations on the use of analytical models to interpret CPT, and correlations from field measurements are difficult to obtain with a high degree of accuracy, as the soil properties are often not known with certainty, large calibration chambers have been used over the years to correlate between relatively well established soil properties and cone resistance. Due to the time and labour consuming procedures to obtain large clay samples, most test series have been performed on sand samples. Within each series the sand used is often the same, whereas the radial and vertical confining pressures as well as the density are varied. The resulting correlations are therefore between the (normalised) cone resistance, the stress level and the density, represented by relative density D_r or state parameter ξ , or sometimes indirectly by the friction angle ϕ . A comparison of test series made in different laboratories shows that the results also depend on the sand type used [81, 90, 134].

Of special interest is the graph presented by Schmertmann [150] showing a relation between cone resistance and vertical effective stress σ'_v for different relative densities (see figure 3.3). This clearly shows that for very low relative densities the cone resistance hardly depends on the effective stress level.

Also of interest are the well controlled experiments by Houlsby & Hitchmann for different stress levels and K -values [81]. From their results they conclude that the cone resistance correlates very well with horizontal effective stress, much more so than with vertical effective stress. Their results can be fitted by a power law of the form

$$\frac{q_c}{p_a} = A \left(\frac{\sigma'_h}{p_a} \right)^{0.6} \quad (3.3)$$

where p_a is a reference pressure equal to atmospheric pressure, in order to make the expressions dimensionless, and A a factor depending on the density of the sand. The conclusion that VCPT

Type	Boundary Conditions
B1	σ_v, σ_h constant
B2	$\varepsilon_v = \varepsilon_h = 0$
B3	σ_v constant, $\varepsilon_h = 0$
B4	σ_h constant, $\varepsilon_v = 0$

Table 3.1: Definition of calibration chamber types based on boundary conditions [134]

is controlled mainly by horizontal effective stress, i.e. the initial stress state perpendicular to the penetration direction, is quite important to the research at hand. After all, in HCPT the stress state perpendicular to the cone varies between vertical and horizontal effective stress, so that a more complex relation between (mean) effective stress and cone resistance will exist.

Although many aspects of the tested soil sample can be controlled in calibration chamber tests, the test setup itself influences the measurements, as is the case with many laboratory experiments. Parkin has given an overview of such influences in calibration chamber testing and concludes that, apart from the preparation method of the sample, the boundary conditions resulting from the chamber design are most influential. See table 3.1 for the common definition of the different chamber types. Most chambers use pressurised membranes at the lateral boundaries (BC1 & 4), which allow a certain control over the lateral stress, but tend to lead to lower cone resistances than would be measured in the field. In a rigid wall chamber the opposite will hold. In both cases the extent of the boundary influence depends on the ratio of the diameter of the chamber to the diameter of the cone, R_d .

3.2.6 Empirical Relations

The results from calibration chamber tests, analytical relations as well as field experiences have been used extensively to construct soil identification charts as a means to solve the inverse problem of deriving soil properties from CPT measurements. Following Begemann [29], most of these charts use the cone resistance q_c and sleeve friction f_s or friction ratio $R_f = f_s/q_c$ as the main indicators of the soil type. Others include further information on the stress level or the pore pressure u to derive correlations for the density or liquefaction potential of the soil [56, 61, 108]. In most cases the normalized corrected cone resistance and friction ratio proposed by Wroth [176] as

$$Q_t = \frac{q_t - \sigma_v}{\sigma'_v} \quad (3.4)$$

and

$$R_f = \frac{f_s}{q_t - \sigma_v} \quad (3.5)$$

are used as entries to the graphs. The corrected cone resistance q_t is derived from the measured cone resistance q_c and pore pressure measurement at the shoulder of the cone u_2 as

$$q_t = q_c + (1 - a)u_2 \quad (3.6)$$

with a an area factor depending on the layout of the cone [108]. Of course this correction can only be made properly if a piezocone test (CPTU) has been performed. It must be noted that Wroth proposed these dimensionless entities for CPTs in clayey soils only, and that for sand

a correlation with the state parameter ξ or horizontal effective stress was suggested [27, 176]. Similarly, for pore pressure readings the factor

$$B_q = \frac{\Delta u}{q_t - \sigma_v} \quad (3.7)$$

was proposed, where the excess pore pressure Δu should be derived from the pore pressure measurement at the shoulder of the cone u_2 if at all possible [175, 176]. The normalisation uses vertical stress for practical engineering purposes, although Wroth already noted the importance of horizontal effective stress as a controlling quantity in penetration resistance.

Except for direct correlations between CPT measurements and soil types, other correlations have been proposed relating the measurements to soil properties for certain soil types. Most common are the correlations with density or friction angle, but correlations with the Young's modulus are also known. The majority of these relations is either limited to a specific soil type or even location or indicative at best. They have hardly any bearing on the interpretation of HCPT and will be disregarded here.

3.3 Calibration Chamber Tests on Sand

In the following section an overview will be given of the test setup used to establish an experimental relationship between HCPT and VCPT measurements. These tests have been performed in a calibration chamber. First an overview of the calibration chamber and the sand bed preparation method will be given. Also an overview of the different sand types is given, along with their main characteristics. This is followed directly by several remarks concerning (possible) problems with the test setup that affect the results.

Then an overview of the different test series performed will be given, followed by an interpretation of the results. As the density of the sand is a known major influence on the cone resistance, the focus lies on the influence of the relative density of the sand bed on the ratios of horizontal over vertical cone resistance as well as sleeve friction. From calibration chamber tests on different sand types it is known, however, that the sand type used may well influence the cone resistance measurements. A number of test series performed in differently graded sands will therefore be used to investigate the influence that gradation or grain size may have on the results.

3.3.1 The Calibration Chamber

The calibration chamber of the Geotechnical Laboratory is 1.9m diameter rigid wall calibration chamber, as sketched in figure 3.4. It is filled with a sand bed with an approximate height of 1.5m. At the bottom of the chamber a number of drains are embedded in a filter bed and connected to a pumping installation. This can be used to saturate the sand bed from below and fluidise the sand. The same installation can alternatively be used to sprinkle water on top of the sand bed and percolate the sand bed, although this option is not used in these test series [79].

After the sand bed is fluidised, a couple of vibrators, affixed to the sides of the tank, can be used to densify the sand while draining the water. Installed are two Wacker AR 06/380 vibrators, each listed as yielding an effective 16kN centrifugal force. Vibration times used are between 0 and 16 minutes. Table 3.2 gives an indication of the relation between vibration time and obtained overall density of the sand bed. After vibrating, the remaining water can either be drained to create an unsaturated sand bed, or the sand sample can be kept (partially) saturated.

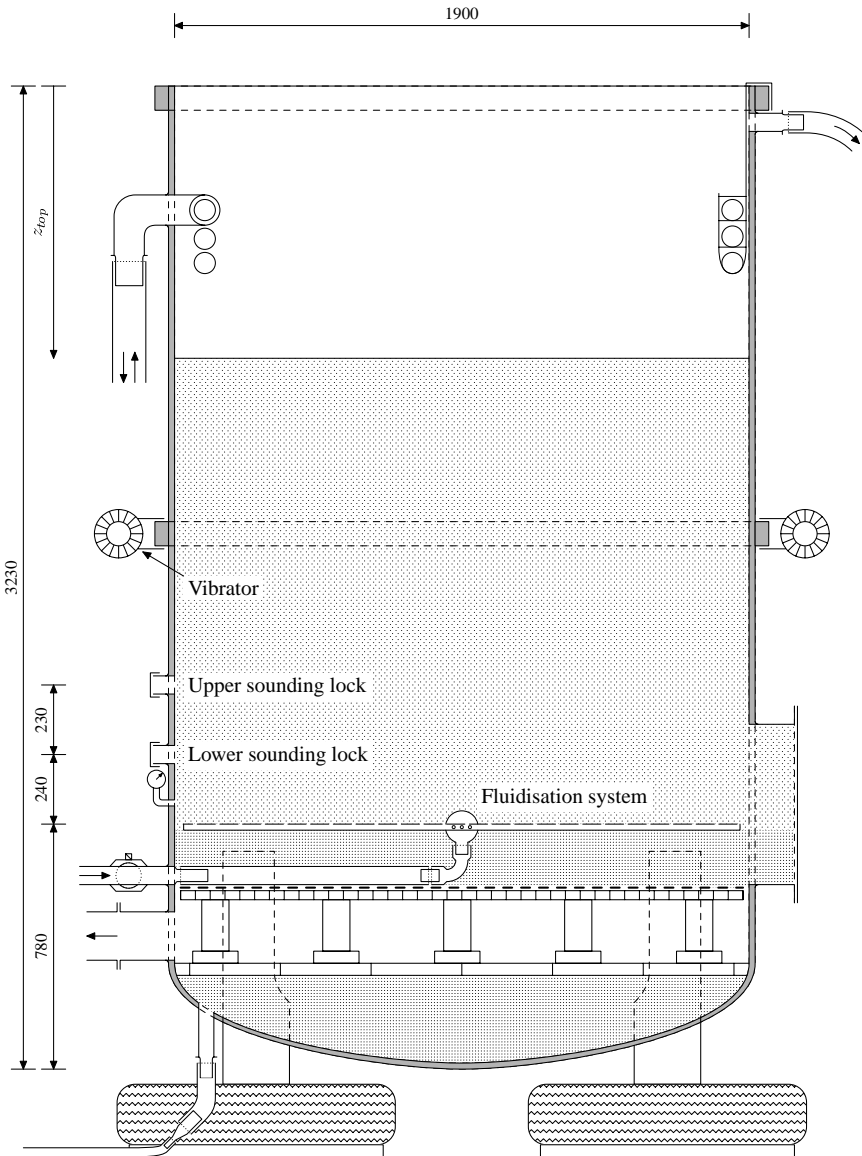


Figure 3.4: Overview of the calibration chamber

Vibration time (s)	Relative density
0	0.182
30	0.311
60	0.376
120	0.444
180	0.578
300	0.687

Table 3.2: Indication of obtained overall density for several compaction times, sand type 1

As the amount of sand in the tank is fixed within a series of experiments, the overall density of the sand can easily be established by measuring the height of the sand bed after densification. Given a reference density e_{ref} and accompanying sand bed height h_{ref} the actual density e of the sand can easily be established if the top level of the sand bed z_{top} , relative to the top of the tank, is measured and the height of the sand bed h calculated;

$$e = (1 + e_{\text{ref}}) \frac{h}{h_{\text{ref}}} - 1. \quad (3.8)$$

This overall density will be used to correlate the test results with the relative density of the sample.

Given the setup of the calibration chamber, it does not adhere to one of the four boundary condition categories established [135, 147], but strictly spoken falls somewhere between BC2 and BC3. It has rigid lateral boundaries and a rigid although badly defined lower boundary. The top boundary is free and has not been loaded in any of the tests. As such it is believed that the chamber is closer to the BC3 category than to BC2.

The chamber differs from most calibration chambers used worldwide on several points. First and most notable is the fact that it is a rigid wall calibration chamber. The severity of the problems normally associated with rigid wall chambers are offset somewhat by the large chamber-to-cone ratio, $R_d = 56$. Furthermore the construction of a true flexible wall chamber allowing simultaneous horizontal and vertical penetration is deemed a technical feat not worth the effort, in view of the likely return in improved test conditions. Secondly, the sand bed is not prepared by the often used pluviation method, but by the above described method of fluidisation and vibration. This leads to less uniformly densified samples, as will be discussed later, but greatly reduces the time and manpower needed to prepare a sample.

3.3.2 The Sands

The experiments in the calibration chamber have been conducted on different sands. The mainstay of the tests has been conducted using a uniformly distributed fine sand, with a $d_{50} = 180\mu\text{m}$. A distribution curve for this sand type is given in figure 3.5. This sand, hereafter named type 1, had been used previously in the same calibration chamber for different tests [76, 79]. As a result of the repeated fluidisation process and limited permeability of the filter drains for fines, the fines that were originally present in the sand had effectively been washed out. It can be seen from the gradation curve that no silt particles remain in the sample.

After a first test series an amount of sand roughly equal to one-quarter of the existing volume was added from a previously unused batch of the same sand. This sand contained a small amount of fines and was mixed thoroughly with the sand already in the calibration chamber,

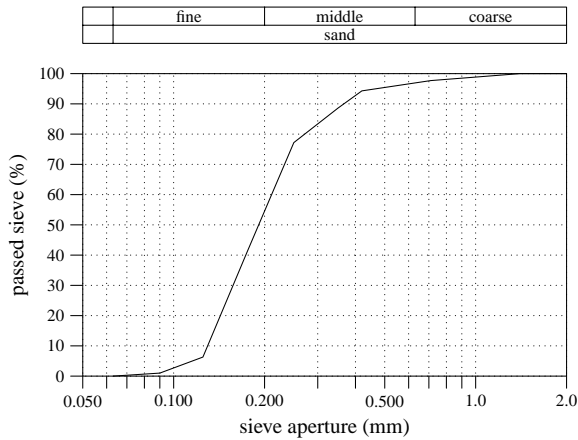


Figure 3.5: Sieve curve, sand type 1

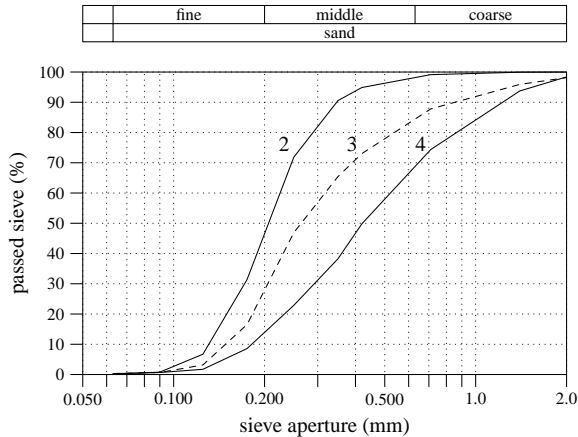


Figure 3.6: Sieve curves, sand types 2, 3 & 4

creating a slightly different sand, type 2, and slightly different test conditions. In subsequent tests roughly one-third of the sand in the calibration chamber was replaced by a more coarsely grained washed river sand, in effect creating two different sand types, type 3 and 4, with differing gradation curves. Figure 3.6 gives indicative gradation curves for the three sand types, as well as the gradation of the river sand used. As the river sand had a low to non-existent fines fraction, the resulting sands also contained hardly any fines.

Although sand type 1 & 2 are similar to each other in most respects, sand types 3 & 4 differ in a number of ways. First of all these sands have different values for the minimal and maximal densities that can be obtained, as can be gained from table 3.3. This table lists the minimal and maximal densities, obtained for each sand type by pouring dry sand through a funnel and extended vibrating and compacting of a moist sample respectively [31, 50, 76, 97].

Secondly, in contrast to sands 1 & 2, the artificial sands 3 & 4 show some segregation over the height of the tank. This is illustrated by figures 3.7 to 3.9, which show the gradation curves

Type	e_{\min}	e_{\max}
1	0.470	0.818
2	0.498	0.801
3	0.454	0.749
4	0.431	0.746

Table 3.3: Minimal and maximal densities for different sands

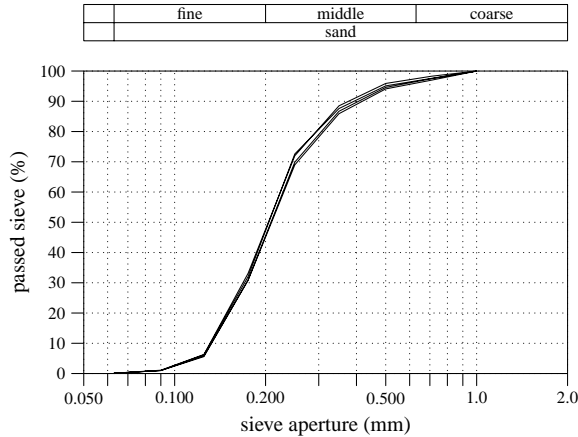


Figure 3.7: Sieve curves, sand type 1, at 0, 0.25, 0.5, 0.75 & 1.0 m below top of sand level

for the different sand types based on samples taken from different depths in the tank. The depth indicated is relative to the top of the tank, not relative to the top of the sand bed. Sand types 1 and 2 show no significant segregation over the height of the tank. Sand type 3 consists of an upper layer that is very similar to the original sand 1 and a lower layer that consists of a coarser material. All HCPTs have been executed well within this lower coarse layer, and the sand at that depth is considered to have a consistent gradation over at least the lower metre. Similarly, sand 4 also shows a differently graded upper layer, although in this case both upper and lower layer differ clearly from the original sand 1.

As the sand at the depth where the horizontal CPTs were executed is not segregated and only the measurements at this depth from the VCPTs are taken into account, the upper layers mainly constitute an overburden weight. Except for a transitional zone where the different properties of the upper layer influence the cone resistance of the lower layer [108, 148], there is no influence of the observed segregation on the measurements in the lower layer, and this transitional zone lies well above the level of the HCPT measurements.

A different but related problem is the observed density variation over the tank. Due to the preparation method of the sand bed and the segregation of the sand, it may be expected that the obtained density in the tank is not uniform over the volume of the tank. An indication of the variation over the height of the tank can be obtained from VCPTs on sand 1 or 2, as these sands show hardly any segregation. See figure 3.10 for three vertical measurements of the cone resistance over the height of the tank and the accompanying horizontal measurement over the width of the tank. From this graph it is clear that below $z \approx 2\text{m}$ the cone resistance increases more rapidly than would be expected, whereas directly above that depth there exists a zone where it even decreases slightly. This indicates a likewise variation of the density in these areas.

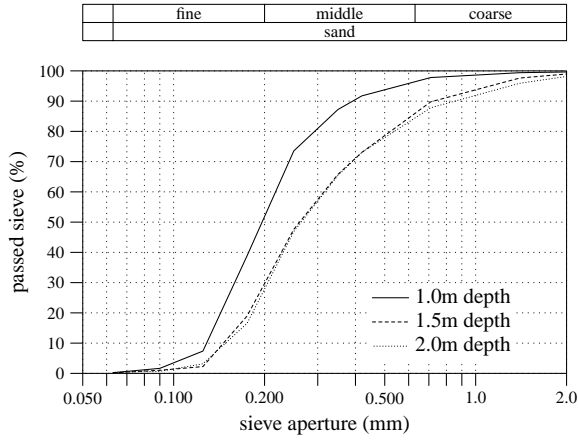


Figure 3.8: Sieve curves, sand type 3, for different depths

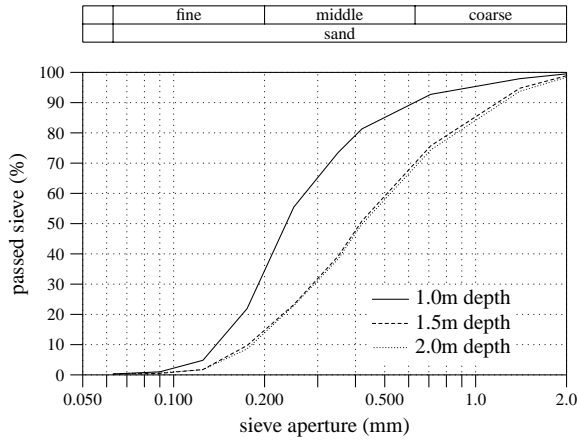


Figure 3.9: Sieve curves, sand type 4, for different depths

Depth (m)	Void ratio		
	Sand 2	Sand 3	Sand 4
1.0	0.686(41)	0.684(14)	0.692(25)
1.5	0.68(14)	0.643(19)	0.562(3)
2.0	0.662(2)	0.610(3)	0.624(3)

Table 3.4: Density for sand type 2,3 & 4, for different depths

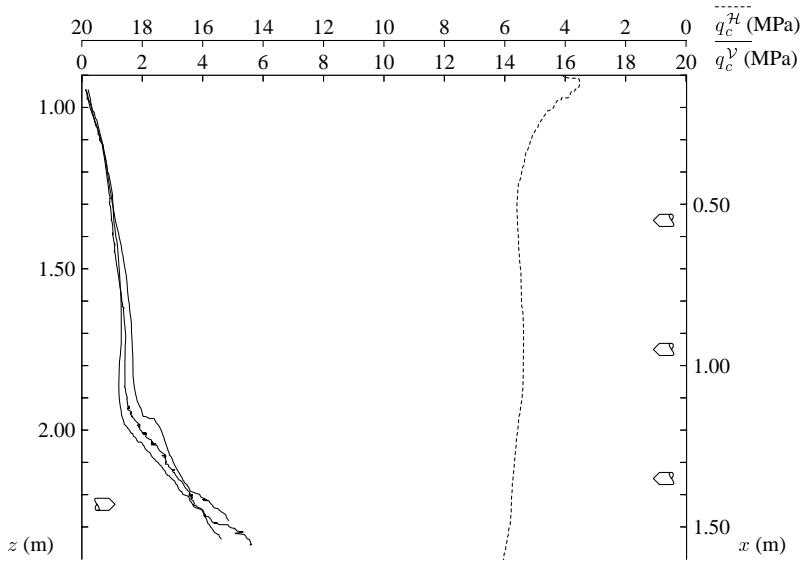


Figure 3.10: Cone resistance variation over the height and width of the tank

The horizontal cone resistance is more or less constant over the width of the tank and shows no indication of significant density variations.

For sands 2, 3 & 4 the void ratio has been determined from undisturbed samples obtained at different depths in the tank [97]. The results are summarized in table 3.4. From these figures it is clear that significant density variations occur over the height of the tank as well as between the different samples taken at the same level. Although the average density for sand 2 is reasonably constant over the height, the deviation between the individual samples is quite large. Almost the opposite holds for sand 3 & 4. In these cases there is a clear density zonation over the height, whereas the different samples taken at the same height have almost the same density. This makes it difficult to reliably establish the local density at the depth where the HCPTs are executed on the basis of the global density only. This problem is mitigated somewhat by the fact that the density at this depth shows little (spatial) variation (see table 3.4).

Overall it can be concluded that the influence of the density variations will result in an uncertainty in the relative density in the order of 10% or less. Although larger than the 5% error often associated with pluviated sand samples [27, 147], the overall severity is not that great, as the main objective will be to correlate between measurements made at the same depth z in the tank in the same sample.

3.3.3 Overview of Test Series

In total 69 horizontal and 151 vertical CPTs were executed, which have been divided in 6 test series. These series differ in the stress level at which the HCPT was executed and the type of sand in the tank.

All tests were executed using two identical standard 10cm² electrical cones equipped with friction sleeves, constructed by A.P. van den Berg Machinefabriek. Cone resistance and sleeve friction were recorded on a Watanabe pen recorder. To allow fluidisation of the sand bed as



Figure 3.11: Overview of HCPT installation mounted on calibration chamber

well as execution of the horizontal CPT below the water table without spilling sand or water, a watertight lock was needed in combination with smooth rods. Due to the limited piezometric head, a simple ball valve and several rubber o-seals were sufficient for this purpose.

As sketched in figure 3.4, there are two positions on the tank where the lock can be installed. These have centres at $z=1.98$ and 2.21 m from the top of the tank, the reference level in all tests. To facilitate the horizontal installation of a hand driven ram, a steel frame with mounting points has been welded to the tank wall, resulting in the setup shown in figure 3.11.

Given the known position of the rams, the location of the cones at the final sounding depth or length can easily be established if it is assumed that the rods do not deflect over the maximal 2m sounding distance. Given the stiffness of the rods this is a valid assumption. For tests on sand 1, up to three vertical soundings were made in each sample as opposed to one horizontal, as sketched in figure 3.12. The positions of the three vertical soundings are situated on a line which has a slight angle to the horizontal sounding. From these measurements three combinations of horizontal and vertical measurements were obtained at the locations shown in figure 3.13. See figure 3.10 for an example of vertical and horizontal cone resistance recordings. For a limited number of tests on sand 1 only a single vertical sounding was made, at position d, for each horizontal test. In the other test series only two vertical tests were executed in each sand sample, at the locations a and c in figure 3.13.

The tests can be categorised by the location of the horizontal ram and the sand type as $n.l.x$. Here the first position (n) denotes the sand type used, i.e. 1 to 4. and the second (l) denotes the location of the horizontal ram, with 1 is lower position and 2 is upper position. The final

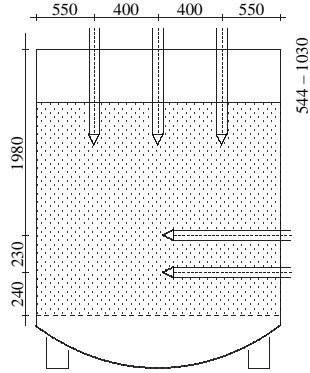


Figure 3.12: Schematic overview of location of CPTs

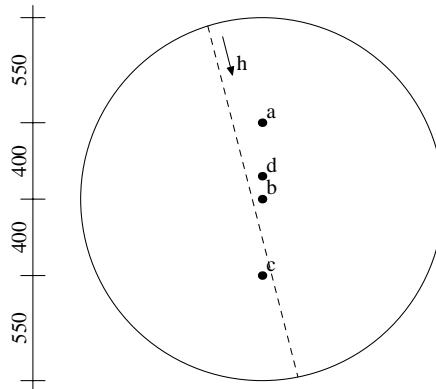


Figure 3.13: Top view of location of horizontal and vertical soundings

Tests	Locations	z_{ref} (mm)	e_{ref}
1.1.01 – 1.1.16	a,b,c	855	0.423
1.1.17 – 1.1.29	d	855	0.423
1.2.01 – 1.2.10	a,b,c	855	0.423
2.2.01 – 2.2.10	a,c	587	0.678
3.2.01 – 3.2.10	a,c	691	0.645
4.2.01 – 4.2.10	a,c	719	0.626

Table 3.5: Overview of test series and test conditions

position (x) codes for the individual sand sample in which the test was executed and the location of the sounding, a, b or c for vertical and h for horizontal.

An overview of all tests is given in table 3.5. From these tests 145 combinations of horizontal (q_c^H) and vertical cone resistance (q_c^V) measurements at the same depth and under the same conditions were obtained. These combinations are shown in figure 3.14, normalised by the (estimated) vertical effective stress. As all tests were made in unsaturated conditions this is equal to the vertical total stress. The normalisation by vertical effective stress has been chosen instead of the horizontal stress because the horizontal stress in the tank is not externally controlled and attempts to measure the horizontal stress state in the tank have resulted in somewhat ambiguous results [31, 50]. For the same reason a normalisation by the mean stress state has been rejected. The sleeve friction measurements for the same tests are plotted in figure 3.15. These measurements are also normalised by the vertical effective stress. In both graphs the line $q_c^H : q_c^V$ respectively $f_s^H : f_s^V = 1 : 1$ is plotted.

From the graphs 3.14 and 3.15 it is clear that the measurements show some dispersion, but this dispersion is not dissimilar to that in many other (vertical) calibration chamber tests [81]. There is however a clear bias, in that the horizontal cone resistance seems on average higher than the vertical, in contrast to the horizontal sleeve friction, which is lower than its vertical counterpart. As might be expected this bias is even clearer in a plot of horizontal vs vertical friction number (see figure 3.16).

The observation that the horizontal cone resistance is higher than the vertical, whereas the sleeve friction or friction number is lower, would warrant a recalibration of the calibration charts for the interpretation of horizontal instead of vertical penetration testing. This observation will be investigated further in the following sections. The reliability of the measurements and the possibility that the observed relation must be ascribed to measuring errors will also be investigated.

First the effects of the density of the sand on the ratio of horizontal over vertical cone resistance will be investigated in more detail. To eliminate possible influences from the grain distribution, only measurements made in sand type 1 will be taken into account. Secondly the effect of the density on the sleeve friction will be investigated. Then the results from tests in sands 2 to 4 will be compared with each other to study the effects of sand type and gradation curve on the cone resistance and sleeve friction ratios.

In the light of possible measurement and interpretation errors, the reading of the cone resistances from the recorder output deserves attention. As the objective is to correlate the horizontal and vertical cone resistance at the same stress level and under similar conditions, these cone resistances should be obtained from positions as close together as possible, i.e. the locations where the horizontal and vertical paths of the soundings cross each other within 10cm distance. This would eliminate some of the ambiguities normally associated with the determination of a suitable reference point and the interpretation of calibration chamber tests [135].

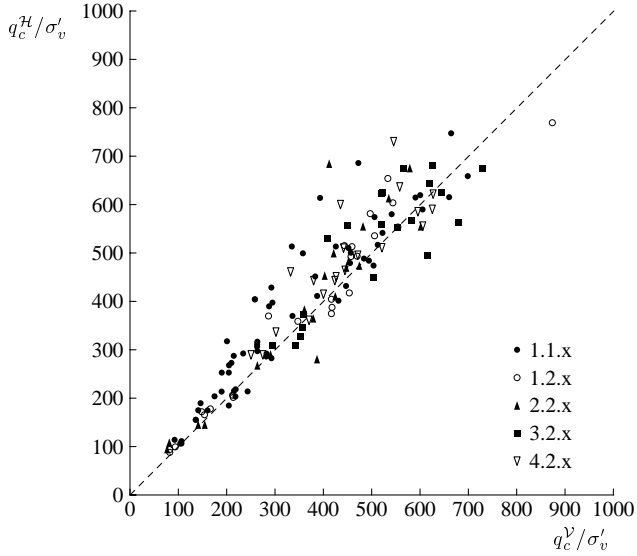


Figure 3.14: Normalised horizontal vs vertical cone resistance

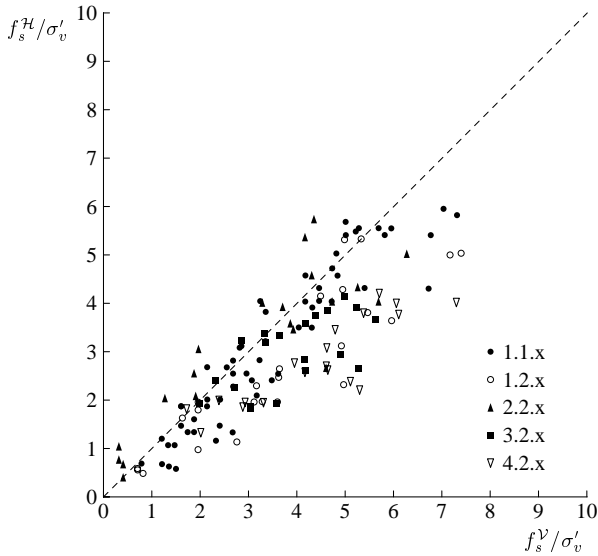


Figure 3.15: Normalised horizontal vs vertical sleeve friction

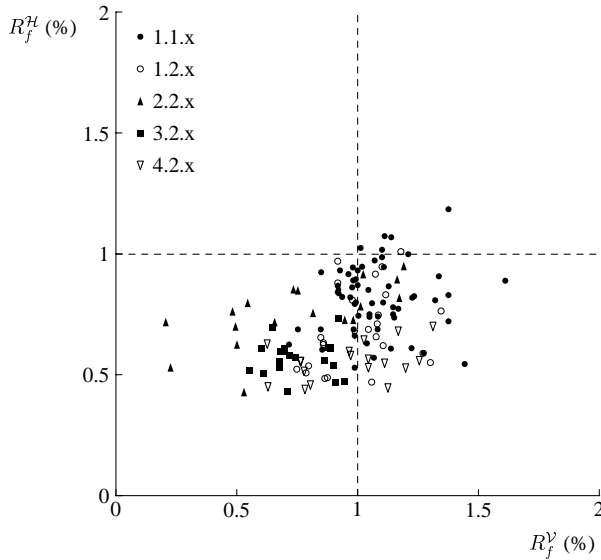


Figure 3.16: Horizontal vs vertical friction number

However, as the vertical CPTs have to be made first, followed by the horizontal or vice versa, in the same sand sample, a certain degree of relaxation can be observed in some cases in the set of measurements that is last made in the vicinity of this point of closest passage. This relaxation is attributed to the cavities left behind after retracting the rods from the earlier set of soundings. It is not present in all measurements and when present it is hardly noticeable at lower densities and more pronounced at higher densities. See the results of a vertical sounding in figure 3.17. This sounding has been made after the horizontal sounding, and a local reduction of the cone resistance at the level of the horizontal sounding ($z = 2.21\text{m}$) can be observed. From the same graph it can also be gained that the effect is less pronounced in the registration of sleeve friction.

To ensure that this interference does not influence the correlations, a couple of measures were taken. First of all, the horizontal sounding for most of the tests was executed after all vertical soundings were completed. The expectation after all is that the horizontal sounding shows no or limited stress dependence and is more or less constant, except for boundary influences. Therefore the interference from the previous soundings is relatively easy to discern. Observations indicate that the interference is also less pronounced in the horizontal soundings. It follows that it is acceptable to make the reading of horizontal cone resistance at a position outside the relaxation zone, where no interference can be detected. This method has been adopted in the determination of horizontal cone resistance and sleeve friction.

3.3.4 Influence of Relative Density on Horizontal Cone Resistance

To investigate the influence of the relative density on the horizontal cone resistance, the ratio of horizontal over vertical cone resistance,

$$q_c^H / V = \frac{q_c^H}{q_c^V} \quad (3.9)$$

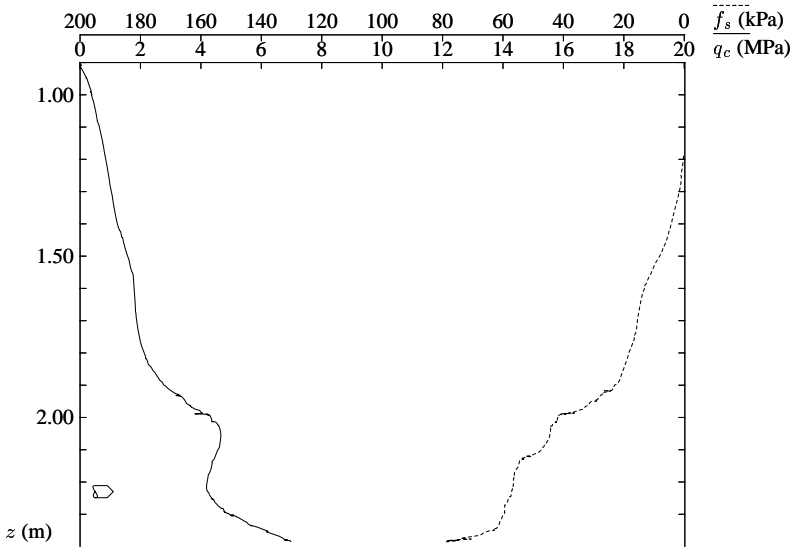


Figure 3.17: Example of cone resistance recording with local reduction

has been plotted against the relative density in figure 3.18. This figure shows clearly that for intermediate densities the ratio of horizontal over vertical cone resistance is larger than unity. For low relative densities the ratio as well as the spread in the data averages to unity, whereas for high densities the trend is less clear but on average lies closer to unity than is the case for medium densities.

These trends for low and high densities can be understood on physical grounds, as will be investigated in more detail later. As said, the obvious difference between horizontal and vertical cone penetration is the stress state perpendicular to the cone. For low densities the calibration chamber tests by Schmertmann, reproduced in figure 3.3, show that cone resistance is hardly dependent on the stress level, so it may be expected that there is little difference between horizontal and vertical CPT. For high densities the vibration process used in densifying the tank not only increases the density but also increases the coefficient of effective horizontal stress K of the sample, slightly overconsolidating the sample. The effect of an increasing K -value will be investigated in more detail in section 3.6.1, but it is easily understood that for $K = 1$ there is no difference in the stress state for either orientation, and equal values for VCPT and HCPT are expected.

Based on these observations a trendline, which represents the mean of the data, is also plotted in figure 3.18. This trendline has been determined using a least squares fit for an assumed relation which fits the constraints mentioned above: a gaussian distribution curve with an offset of 1. Given this assumption the mean of all data points has been fitted as

$$\frac{H}{V} \frac{q_c}{q_c} = 1 + 0.191 e^{-13.6(D_r - 0.497)^2} \quad (3.10)$$

If there is indeed such a unique relationship between horizontal and vertical cone resistance, it is clear from the dispersion in the data that a significant error must be present in the measurements. The question may even be raised whether this error is solely responsible for the observed trend, and whether the relation between the two is simply linear. To answer these questions a closer investigation of the error sources and their magnitude has been made.

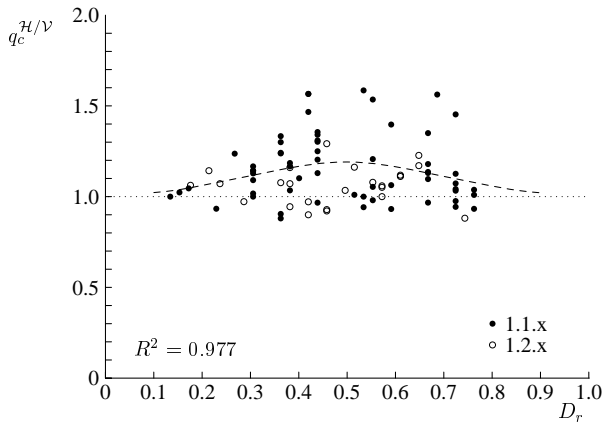


Figure 3.18: Ratio of horizontal over vertical cone resistance vs relative density

The most obvious and most influential errors derive from the inhomogeneities in the tank and the fact that the horizontal and vertical measurements are not executed at exactly the same position in the tank. And as neither the vertical nor horizontal cone resistance or sleeve friction is completely constant over the entire tank, this might lead to errors in the correlated measurements. This can further be combined with positional inaccuracies of the rods due to deflection, an error in the recorded start position of the sounding and errors originating from the manual reading of data from the pen recorder output. As the exact magnitude of these errors is not known, the cone resistance 50mm in front and behind the theoretical position has also been determined and is considered as an indication of the overall error of these influences. The error determined in this way is dominant over all other error sources.

Other errors sources are the accuracies of the cone and recorder, which have a listed 1% error. A further possible error source is the determination of the overall density of the sand, which is determined from a measurement of the sand level z_{top} , with a maximal error of 5mm, and from the density of an undisturbed sample. The reference level and density for each sand type are listed in table 3.5. As this overall density is a factor in calculating the effective stress in the tank, it also influences the calculation of the normalised cone resistance and sleeve friction.

Taking all these errors into account, a plot can be made of the horizontal vs vertical cone resistance for series 1.x.x and also a plot of $q_c^{H/V}$ vs relative density including error bars (see figures 3.19 and 3.20). From these figures it is clear that both the horizontal and vertical cone resistances contain significant errors, up to 23%. Nevertheless they are distributed in such a way that a simple linear relation between $q_c^{H/V}$ and D_r is unlikely and the observation that $q_c^{H/V}$ is approximately 1.2 for intermediate densities remains unchanged.

3.3.5 Influence of Relative Density on Horizontal Sleeve Friction

It has already been noted that the horizontal sleeve friction is lower than the vertical and that this trend is amplified for the friction ratios. In view of the observed relation between cone resistance ratio $q_c^{H/V}$ and relative density, the question arises whether the sleeve friction ratio $f_s^{H/V}$ also depends on the density of the sample. To answer that question, the ratio of horizontal over vertical sleeve friction and the horizontal over vertical friction number are plotted against relative density in figures 3.21 and 3.22 in a similar manner as the cone resistances.

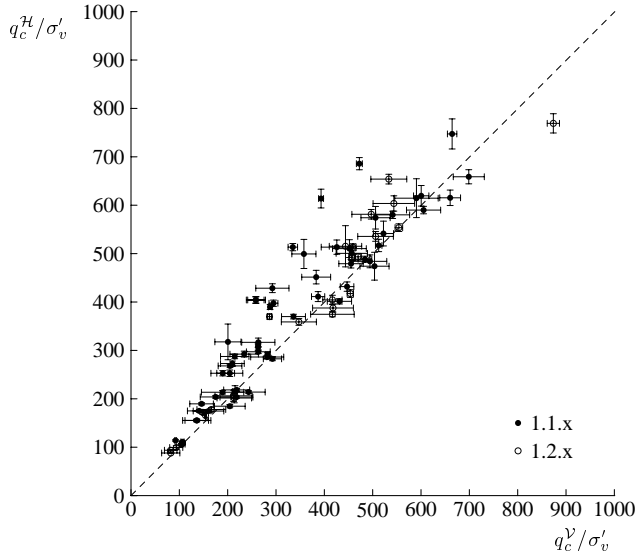


Figure 3.19: Indication of error in cone resistance readings for series 1.x.x

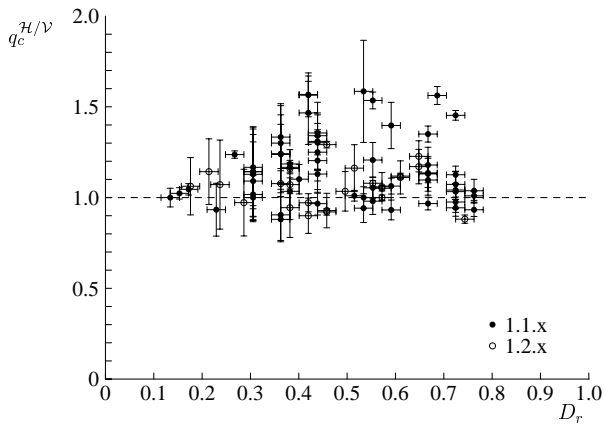


Figure 3.20: Indication of error in cone resistance ratios for series 1.x.x

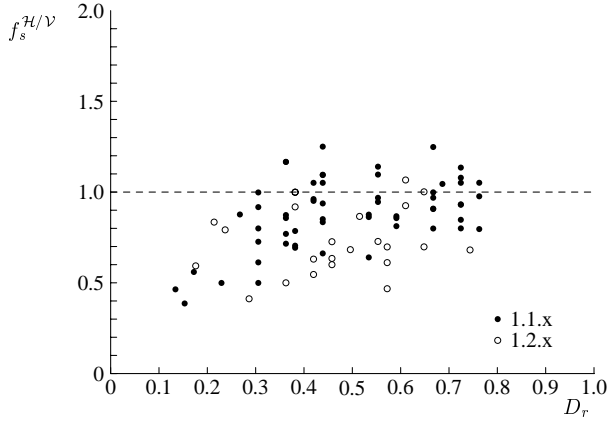


Figure 3.21: Ratio of horizontal over vertical sleeve friction vs relative density

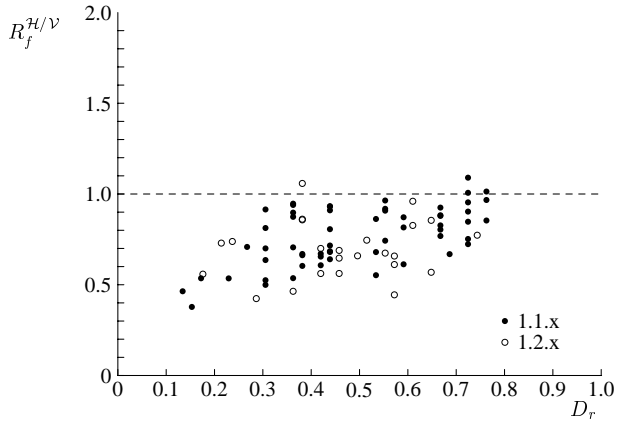


Figure 3.22: Ratio of horizontal over vertical friction ratio vs relative density

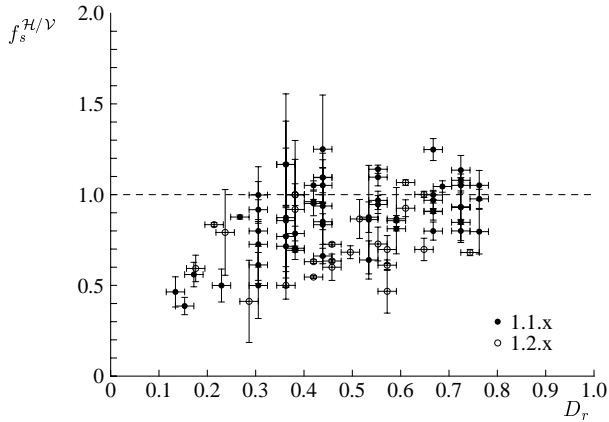


Figure 3.23: Indication of error in sleeve friction ratios for series 1.x.x

From this figures there is no clear relation between sleeve friction and relative density. With some effort a linear trend may be observed where $f_s^{H/V}$ varies between 0.6 for low relative densities to 1.0 for high relative densities observed, but this trend is not clear and depends mainly on the data averaging technique used. The overall mean of $f_s^{H/V}$ is 0.81 and the mean $R_f^{H/V}$ is 0.72. A plot of the sleeve friction ratio vs relative density, including the error bars calculated in the same manner as for cone resistance in the previous section, is given in figure 3.23. And although the largest errors occur at low to intermediate densities and the magnitude of the largest error is, at 43%, larger than the largest error in the cone resistance measurements, this plot gives no grounds to propose a relation between sleeve friction ratio $f_s^{H/V}$ and relative density.

Other (vertical) tests at low stress levels, for example by Smits, in a similar sand and similarly sized chamber, have also shown friction ratios lower than 1% at low stress levels for sands that have friction ratios equal to 1% at higher stress levels [151]. Normally this could be attributed to a slight offset in the recording equipment or to an inherent stiffness of the sleeve, its bearings and its sealing construction. Especially the rubber rings present in modern cones to prevent soil from getting inside the sleeve would be a probable cause. Now a lower sleeve friction is observed in these tests in the upper layers, as can be observed in figure 3.17, but not at the depth of the horizontal sounding. This is also clear from the plot of vertical friction ratios in figure 3.16, which are distributed evenly around 1%. If the stiffness of the system were the cause of a lower than expected friction ratio, it should occur in the same manner in both the horizontal and vertical measurements, which is not the case.

A remaining explanation would be that in the case of a horizontal sounding the slight imbalance in the loading of the friction sleeve, due to the stress difference at the top and bottom of the sleeve, causes an increased friction between the sleeve and other parts of the cone inside the cone, which effectively lowers the registered sleeve friction. This imbalance would not occur in a vertical sounding, which is in theory symmetrically loaded. There is no conclusive evidence in the measurements however to support this claim, and the straightforward way of investigating this possibility by executing the tests at a higher stress level is not possible in the current test setup.

Overall it must be concluded that no trend similar to the one observed for horizontal cone resistance can be deduced from the measurements of sleeve friction and that there is no evidence

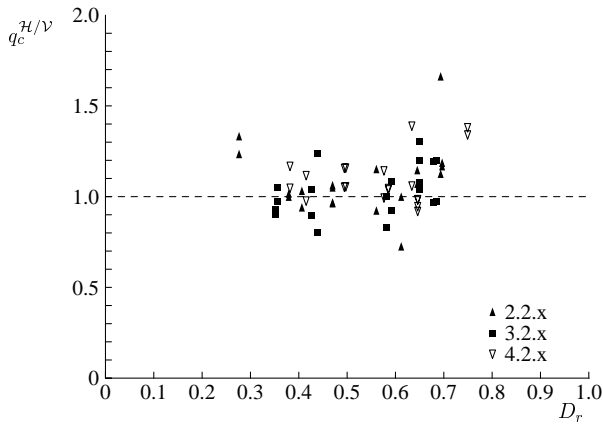


Figure 3.24: Ratio of horizontal over vertical cone resistance vs relative density

that the different stress state around the sleeve influences the horizontal sleeve friction.

3.3.6 Influence of the Sand Type on Horizontal Cone Resistance

As stated before, a number of tests (2.2.1 to 4.2.10) has been executed in differently graded sands to investigate what effects the sand type and gradation has on the horizontal cone resistance and sleeve friction. The results from these tests have not been included in the analysis in the previous two sections, to exclude any possible influence from the sand type and gradation, and are analysed separately in this section.

In a plot of horizontal vs vertical cone resistance (figure 3.14) these three data sets do not clearly stand out from the other data. The scatter in the data at higher cone resistances is somewhat larger compared to series 1.x.x, but overall there is no clear influence of the sand type here. The only noticeable difference lies in the fact that in series 2.2.x lower cone resistances have been measured and that overall the average cone resistance in this series is lower.

When a plot is made of the ratio of cone resistances vs relative density (see figure 3.24) series 4.2.x seems to stand out with a slightly higher average $q_c^H/V \approx 1.1$ than the other two sets, although not significantly so. At low density the two data points from series 2.2.x stand out clearly, but when these are ignored no clear trend between horizontal cone resistance and density shows.

This lack of any discernable influence of the sand type becomes even clearer when the data is plotted together with series 1.x.x (see figure 3.25). The dispersion at higher densities is not much different than that of the remaining data and the same even holds for the points from series 2.2.x at low density. The quality of the previously proposed fit (3.10) is only slightly reduced, to $R^2 = 0.972$.

3.3.7 Influence of the Sand Type on Horizontal Sleeve Friction

In contrast to the cone resistance, the horizontal sleeve friction and friction ratio do change with a change in the sand type. See figures 3.26 and 3.27 for plots of the sleeve friction and friction ratio ratios vs relative density. Although the dispersion is reasonably large, especially for series 2.2.x, there is a significant decrease of f_s^H/V with increasing characteristic grain size d_{50} . The

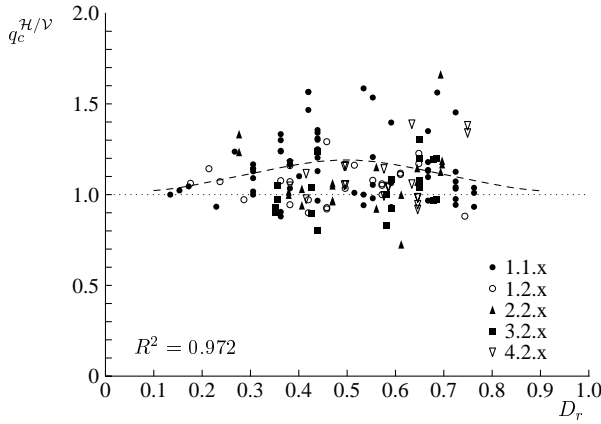


Figure 3.25: Ratio of horizontal over vertical cone resistance vs relative density

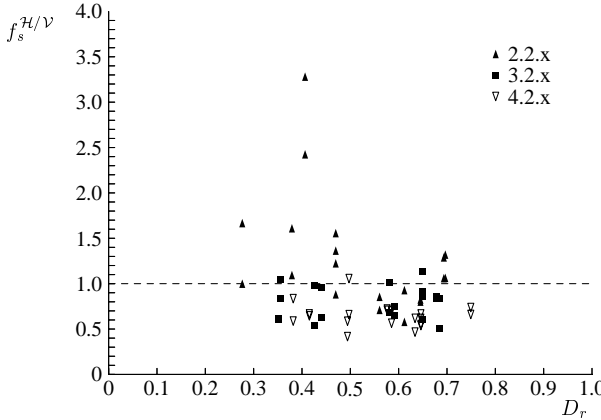


Figure 3.26: Ratio of horizontal over vertical sleeve friction vs relative density

overall mean of f_s^H/V is equal to 1.28 for sand 2, 0.79 for sand 3 and 0.65 for sand 4. The corresponding R_f^H/V are 1.20, 0.77 and 0.60 respectively.

A closer inspection shows that the decrease in R_f^H/V is due to a concurrent rise of the R_f^V and a decrease of the R_f^H . The same holds for the sleeve frictions, notwithstanding the fact that the average and range of cone resistances attained vary somewhat between the three test series.

3.3.8 Horizontal Stress Measurements

Attempts have been made to measure the horizontal stress in the tank. These tests have resulted in somewhat ambiguous results, as shown in figure 3.28. This figure shows the horizontal effective stress coefficient K derived from these measurements for various relative densities in sand 1. These measurements were obtained with a pressure gauge installed in the fluidised sand bed before compaction and vibration of the sand [50]. This method was selected in order to circumvent the standard problem in obtaining in-situ horizontal stress measurements, i.e. that the installation of the measuring device introduces a stress change in the soil, which is difficult

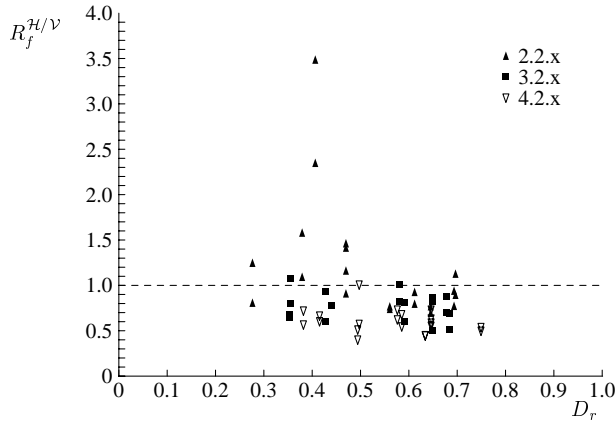


Figure 3.27: Ratio of horizontal over vertical friction ratio vs relative density

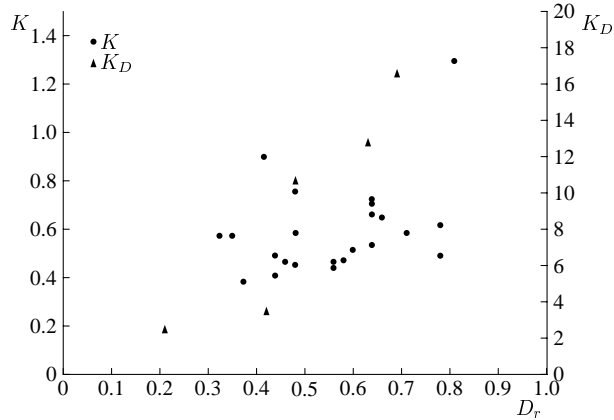


Figure 3.28: Measurements of the coefficient of horizontal effective stress K and dilatometer value K_D

to correct for.

The method followed here does not solve the problem of disturbing the in-situ stresses, however, as during vibration stress concentrations around the gauge may occur and the soil may flow around the gauge, resulting in a local stress release. As a result of such problems, the quality of the data is poor. It can be surmised with difficulty that the average coefficient increases slightly with increasing density and at the same time the values of both the smallest and largest measurement increase.

Apart from measurements with this pre-installed stress gauge, a number of Marchetti Dilatometer Tests (DMT) were performed. The resulting K_D values from these tests are also shown in figure 3.28. These K_D values have not been converted to K values, using the method described by Marchetti [113], as Marchetti's correlation is calibrated only for uncemented clays, and even for these soils the correlation is rather sensitive [159]. The measured K_D values in themselves nevertheless already show a trend of increasing horizontal stress with increasing density. That this implies an increase in K_0 can be derived from the observation by Marchetti [114] that an

increase in K_0 causes a similar increase in K_D , although the ratio between the two stress coefficients may remain unclear.

This trend of increasing horizontal stress with increasing density, caused by the vibration of the tank during densification, has been used in the interpretation of the HCPT results.

3.3.9 Conclusions on Calibration Chamber Tests

From the combined data of all test series it can be concluded that the average horizontal cone resistance is somewhat higher than the vertical cone resistance. When plotted against the relative density a trend shows where the average ratio of horizontal over vertical cone resistance q_c^H/V is approximately 1.2 for intermediate densities and approaches 1.0 for low or high densities. Equation (3.10) has been proposed as a fit of the mean of q_c^H/V as a function of relative density. There is no visible influence of a variation of the gradation and characteristic grain size of the sand however.

The horizontal sleeve friction shows no clear relation with density, but is overall lower than its vertical counterpart, which results in an average $f_s^H/V = 0.81$. The average friction ratio R_f^H/V is even lower at 0.72. Tests on differently graded sands show that the horizontal sleeve friction decreases with increasing characteristic grain size, and increases with increasing fines fraction, and that it does so more strongly than the vertical sleeve friction. The combined result is a decrease of the ratio of horizontal over vertical sleeve friction with an increase in d_{50} for the sands tested.

3.4 Scale Model Tests

A two-dimensional scale model has been used to visualise the failure patterns around a model cone. The scale model consists of a rectangular box with glass side panes, with dimensions $270 \times 270 \times 55\text{mm}$, filled with sand, as shown in figure 3.29. During preparation of the sand sample, the sand was interspersed with thin horizontal stripes of sand with a contrasting colour. An opening at one of the sides as well as at the top of the box allowed a 5mm thick and 55mm wide strip with a 60° cone to be pushed into the sand at a constant speed of approximately 0.5ms^{-1} .

During penetration of the model cone, images were obtained using a digital camera. The deformation pattern around the cone was subsequently visualised by calculating the difference between subsequent images. The equipment and method used have been described extensively by Allersma [5]. Figures 3.30 and 3.31 show typical examples of the deformation pattern obtained with this method. Both tests were executed at a depth of $z/D \approx 35$, which corresponds to the relative depth at which the HCPTs were executed in the full-size calibration chamber.

In these figures the medium grey background indicates zones where no deformation occurred and two subsequent images are identical. Regions that did deform between the instants the exposures were taken show up with roughly horizontal light and dark lines. The thickness of these lines is an indication of the deformation that occurred, and where these lines are abruptly cut off this is an indication of a shear band. The shear bands are most prominent in the horizontal scale test shown in figure 3.31. Shear bands are also present in the vertical scale model test but not as sharply defined. There is on the other hand a clear compression zone visible below the model cone in figure 3.30 whereas there is hardly any compression visible in front of and below the horizontal model cone. Also clearly visible in the vertical test is the

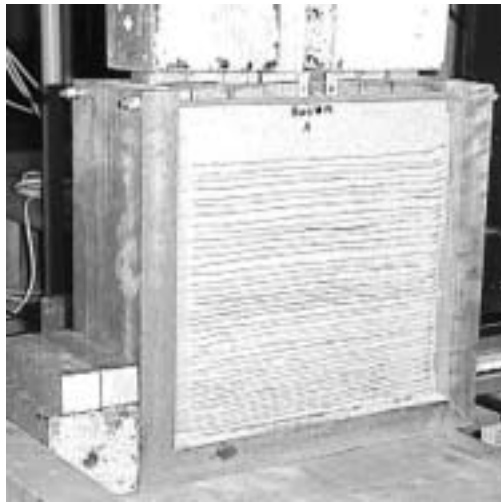


Figure 3.29: Scale model test setup

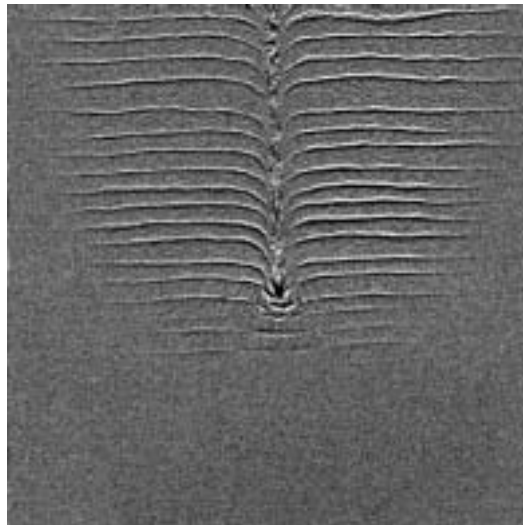


Figure 3.30: Deformation pattern in vertical CPT scale model test

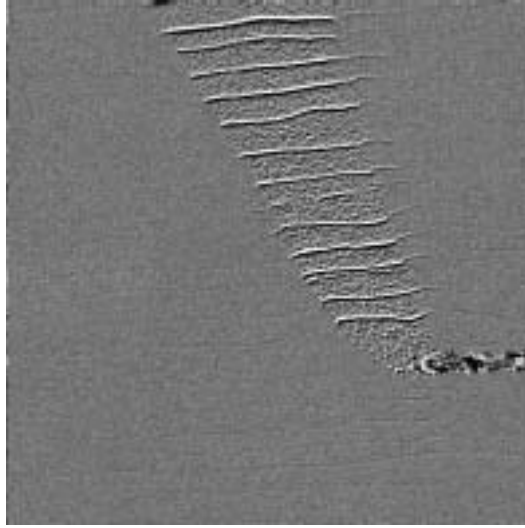


Figure 3.31: Deformation pattern in horizontal CPT scale model test

deformation of the initially horizontal lines near the cone due to the combined effect of shear and compaction.

Based on these model tests it can be concluded that the failure mechanism in HCPT differs from that in VCPT. In vertical penetration two shear lobes develop, one at each side of the cone, whereas in horizontal penetration a soil wedge bounded by two shear bands is lifted. The mechanism observed in the vertical scale tests is similar to the mechanism proposed by Terzaghi (see figure 3.1) or Durgunoglu [70, 178]. The mechanism that occurs in front and above the horizontal model cone on the other hand shows great similarities to the mechanism used by Leca & Dormieux to calculate the maximal support as sketched in figure 2.7. Use of their formulas, however, would yield a depth-dependent horizontal cone factor N_q^H at least ten times greater than the vertical cone factor, which does not correspond to observations. A different model is needed to derive the horizontal cone factor.

That significant differences exist between HCPT and vertical CPT can also be obtained from the stress field around the cone. This stress field was measured using the photo-elastic properties of crushed glass. Once again a two-dimensional scale model was constructed, this time filled with crushed glass, submerged in a fluid with an index of refraction close to that of the glass. At two sides the model was contained within glass panes; the other sides consisted of a stiff framework with a single opening at one side (see figure 3.32). Plates at top and bottom allowed the glass to be compressed, simulating a vertical stress. The direction of the major principal stress could then be observed in circularly polarised light, as described by Allersma [3].

After the glass was loaded, the cone was slowly inserted into the sample. The resulting stress field was determined using a digital camera (see figure 3.33). In this picture the direction of the filaments indicates the direction of the largest principle stress. The intensity is determined by the difference between the two principal stress components in this plane. As one of the perpendicular components of the circularly polarised light is retarded relative to the other due to the stresses in the glass, the light becomes elliptically polarised. At 420 separate points the intensity and orientation of the light was determined; see Allersma [3] for a full explanation

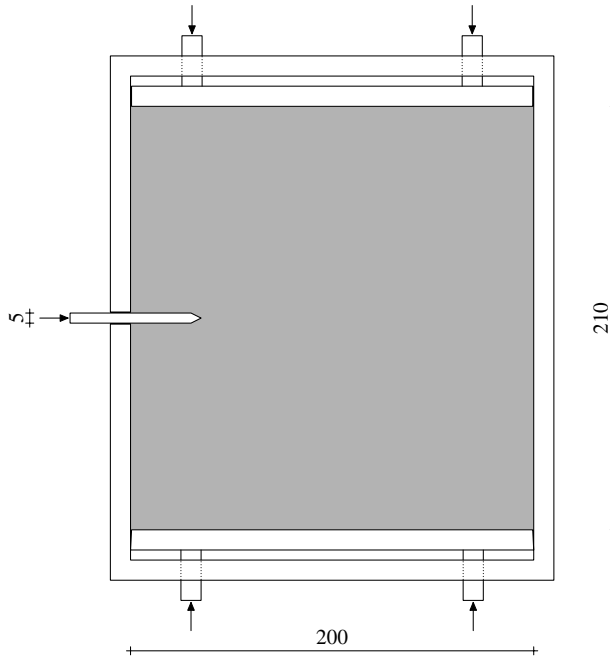


Figure 3.32: Model of HCPT used in photoelastic investigation

of the test equipment involved. From these measurements a plot of the stress trajectories was made (see figure 3.34).

When this plot of the principal stress trajectories is compared to a similar plot for vertical CPT (figure 3.35), obtained by Allersma, the differences between the stress trajectories in HCPT and VCPT are immediately clear. Most obvious is the fact that in the VCPT two isotropic stress points are visible at the level of the cone, indicated by the empty regions where the plotted lines end inside the plotted region. In the HCPT only a single isotropic stress point is visible, directly in front of the cone. Also, in VCPT the stress trajectories starting at the cone shoulder tend to curve back to the shaft, whereas in HCPT they extend to the surface. Although it is clear that significant differences exist in the soil behaviour around horizontal and vertical cones, these differences cannot be directly quantified and incorporated into a model of HCPT.

3.5 Field Tests

As stated in the introduction, mention of a horizontal penetration was made only once prior to the start of this investigation [149]. In parallel there has, however, been a research project financed by the COB to investigate the feasibility of implementing a HCPT installation in a TBM. A number of horizontal penetrations made within the framework of this research have been reported in literature [102, 64, 66, 68].

A number of soundings have been made from a 3m outer diameter pipe jacking in Antwerp. This field test showed the feasibility of executing horizontal CPTs from a small TBM using an adapted CPT rig and demonstrated the added value of the HCPT measurements to the boring process. A direct correlation with vertical CPT data was not possible due to the limited amount

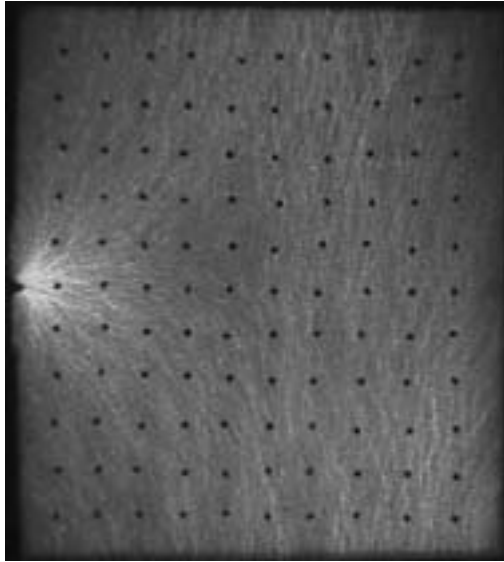


Figure 3.33: Photograph of HCPT in crushed glass, viewed in circularly polarised light

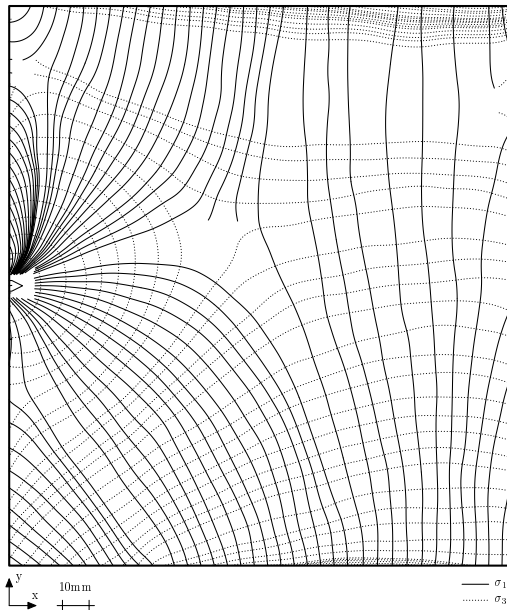


Figure 3.34: Plot of the principal stress trajectories in HCPT shown in figure 3.33

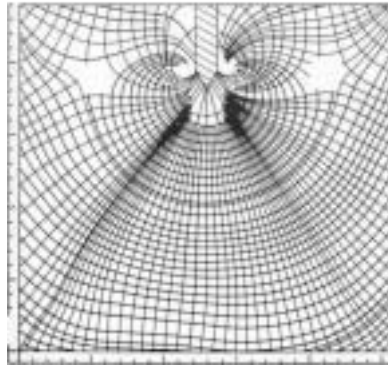


Figure 3.35: Plot of the principal stress trajectories in VCPT, from [3]

Soil type	Number of meas.	$q_c^{H/V}$ avg. (range)	$f_s^{H/V}$ avg. (range)	$R_f^{H/V}$ avg. (range)	$u^{H/V}$ avg. (range)
peat	2	1.6 (0.6-2.5)	1.0 (1.0-1.0)	1.1 (0.4-1.8)	0.9 (0.9)
clay	5	2.0 (1.0-3.0)	0.7 (0.5-1.0)	0.6 (0.2-1.1)	1.0 (0.4-1.6)
sand	1	1.8	1.8	1.0	-

Table 3.6: Ratios of HCPT over VCPT measurements from excavation pit Amsterdam [68]

of vertical penetration data available at the construction site.

In order to correlate HCPT and VCPT measurements, a more interesting set of field measurements has been executed from an excavation pit in Amsterdam. This test consisted of two vertical reference CPTs, three horizontal CPTs and one slanted CPT. They were executed in Holocene clay, peat and sand layers up to a depth of 8m and up to 15m from the sheet pile wall. From the slanted CPT (figure 3.36b) it can be seen that the slanted measurements show a similar but stretched profile compared to the vertical CPT. Comparison of the measurements at the points where the HCPTs and VCPTs cross shows that the ratio q_c^H/q_c^V is larger than unity with a significant amount of scatter (see table 3.6).

Although only one set of measurements was obtained in a sandy soil the overall results of these tests corroborate the trend observed in the laboratory tests that the ratio of horizontal over vertical cone resistance is larger than one while the ratio of friction ratios is less than one.

3.6 Modelling Horizontal Cone Penetration

To establish a relation between soil properties and vertical CPT measurements a large number of models has been developed over the years, as described in section 3.2. All these models use the (implicit) assumption that the stress state in a plane perpendicular to the penetration direction is radially symmetrical. As said before this is not the case in HCPT. Nevertheless it should be theoretically possible to use the same modelling techniques to develop a model for horizontal cone penetration, with the difference that extra difficulties may arise stemming from the fact that the initial stress state around the cone is more complicated. Such a model could then be

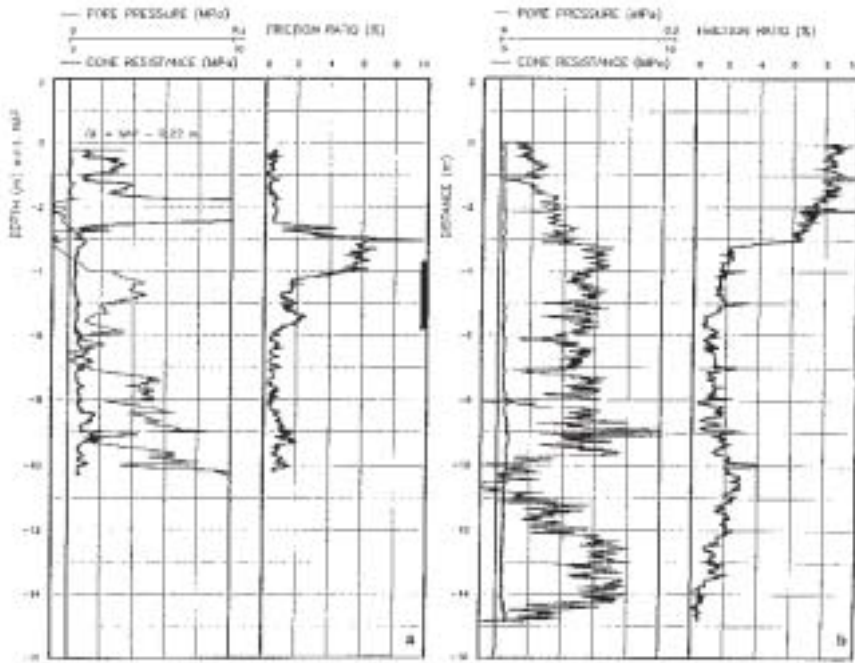


Figure 3.36: Vertical CPT (a) and slanted CPT (b). The slanted CPT starts at -3.7m and extends to -5.7m, the range indicated in (a) [68]

used to relate soil properties to horizontal cone resistance as well as to vertical cone resistance and in this way establish a relation between horizontal and vertical CPT measurements.

In practice this method is complicated by the fact that none of the existing models describes vertical penetration adequately enough to reliably predict cone resistances, and certainly not over a wide range of soil properties. This problem can be overcome in part by using a set of models, one for vertical and one for horizontal penetration, to directly establish the ratio between horizontal and vertical cone resistance. In order to straightforwardly do so, the two models should be derived from the same analytical base, using, as much as possible, the same assumptions and simplifications. As the cavity expansion model is both the most promising method to predict vertical cone resistance and most suited to implement the difference in stress state around the cone, a cavity expansion model has been used to correlate between horizontal and vertical cone resistances.

The basic difference between the two models is, as said, the fact that in horizontal penetration the initial stress state in a plane perpendicular to the penetration resistance differs from the vertical penetration case and moreover is not radially uniform. In vertical penetration the radial stress component in this plane is after all equal to the horizontal effective stress,

$$\sigma_{rr}^V = -\sigma'_h. \quad (3.11)$$

For the horizontal penetration the radial stress varies between the horizontal and vertical effect-

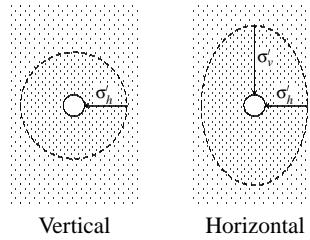


Figure 3.37: Stress state around cone for vertical and horizontal CPT

ive stress, as sketched in figure 3.37. This stress state can be approximated by

$$\sigma_{rr}^H = -\frac{\sigma'_v + \sigma'_h}{2} - \frac{\sigma'_v - \sigma'_h}{2} \cos 2\theta \equiv -\sigma^{(0)} - \sigma^{(2)} \cos 2\theta, \quad (3.12)$$

neglecting stress differences over the cone due to gravity. $\theta = 0$ is the downward vertical direction, as defined in figure B.1.

This non-uniform stress state cannot be implemented directly in any of the existing models, so it is necessary to adapt an existing model or develop a new one. Another difficulty that arises in adapting an existing model lies in the fact that most of these cavity expansion models are based on a spherical cavity expansion. The limit pressure calculated from a cylindrical cavity is lower than that calculated from a spherical cavity and would in most models lead to penetration resistances lower than those observed [58, 170]. In those spherical analyses however, the penetration resistance q_c is governed by initial mean stress, which is equal in both vertical and horizontal penetration. Use of this assumption would immediately lead to the conclusion that horizontal and vertical cone resistances are equal.

Calibration chamber tests on dry sand by Houlsby and Hitchman [81] have shown, however, that there is a strong correlation between q_c and the lateral stress σ_h and almost no correlation with the mean or vertical stresses. This correlation leads amongst others Salgado [146] to propose a cylindrical cavity expansion model for the interpretation of cone penetration. This assumption will be followed here in that a plane strain cavity expansion with the initial stress state given by either (3.11) or (3.12) will be used.

The main differences between the simple model developed here and the state-of-the-art models described by e.g. Salgado [146] are that a linear elastic material model is used instead of an elasto-plastic one and that effects of stress rotations and stress dependent material behaviour are ignored. Furthermore, in this model it is not the limit pressure of the cavity expansion that is desired but the work needed to create a cavity with radius r equal to the cone radius.

3.6.1 Elastic Cavity Expansion

To describe the expansion of a circular cavity with radius r_a in an elastic plane, the governing relations from the theory of elasticity are most conveniently expressed in polar coordinates, as given in appendix B or e.g. Muskhelishvili [124]. Timoshenko [163] gives a general class of solutions to these equations as

$$u_r^{(k)} = r^n \cos k\theta \quad (3.13)$$

$$u_\theta^{(k)} = \alpha r^n \sin k\theta \quad (3.14)$$

where for given order k the values of n and α are determined by

$$n = \pm(k+1) \quad \vee \quad n = \pm(k-1) \quad (3.15)$$

$$\alpha = \frac{(m+1)(n^2-1) - k^2}{k(m+2-mn)} \quad (3.16)$$

This can be easily checked by substitution of (3.13) and (3.14) into (B.13) and (B.14), as demonstrated by Verruijt [168]. As the initial stress state given by (3.12) only contains terms proportional to $\cos 2\theta$ and constant terms, the general solution for the cavity expansion of horizontal penetration can be limited to the terms of order $k=0$ and $k=2$. For an overview of the resulting formulation of the stresses and strains see appendix B.

Hill [77] gives the external work dW per unit volume performed on an element during strain $d\epsilon_{ij}$ as $\sigma_{ij}d\epsilon_{ij}$. Note that use is made of the summation convention. It follows that the total work per unit volume is

$$W = \int \sigma_{ij}d\epsilon_{ij} \quad (3.17)$$

with the integral taken over the actual strain path. To calculate the total work W performed in expanding the cavity from $r_a = 0$ to $r_a = r_c$, with r_c the radius of the cone, the work W per unit volume has to be integrated over the entire plane outside the cavity and over the expansion from $r_a = 0$ to $r_a = r_c$,

$$W = \int \int \int \sigma_{ij}d\epsilon_{ij}r d\theta dr \quad (3.18)$$

taking care that the correct strain path is followed.

First the cavity expansion for the case of vertical penetration will be solved. A cavity with radius a is located in a plane with the initial stress state according to (3.11). This cavity will be expanded by an additional fraction δa . The boundary conditions for this problem can be written as

$$r = \infty : \quad \sigma_{rr} = -\sigma_h \quad (3.19)$$

$$r = r_a : \quad u_r = \delta r_a \quad (3.20)$$

Substituting these boundary conditions into (B.21) and (B.27), the unknown constants $A^{(0)}$ and $B^{(0)}$ can be solved as

$$A^{(0)} = -\frac{\sigma_h}{2m\mu} \quad (3.21)$$

$$B^{(0)} = r_a^2 \left(\frac{\sigma_h}{2m\mu} + \frac{\delta r_a}{r_a} \right) \quad (3.22)$$

and the resulting stresses and strains can be written as

$$\sigma_{rr}^V = \sigma_h - 2\mu \frac{r_a^2}{r^2} \left(\frac{\sigma_h}{2m\mu} + \frac{\delta r_a}{r_a} \right) \quad (3.23)$$

$$\epsilon_{rr}^V = -\frac{\sigma_h}{2m\mu} - \frac{r_a^2}{r^2} \left(\frac{\sigma_h}{2m\mu} + \frac{\delta r_a}{r_a} \right) \quad (3.24)$$

$$\sigma_{\theta\theta}^V = -\sigma_h + 2\mu \frac{r_a^2}{r^2} \left(\frac{\sigma_h}{2m\mu} + \frac{\delta r_a}{r_a} \right) \quad (3.25)$$

$$\varepsilon_{rr}^V = -\frac{\sigma_h}{2m\mu} + \frac{r_a^2}{r^2} \left(\frac{\sigma_h}{2m\mu} + \frac{\delta r_a}{r_a} \right) \quad (3.26)$$

$$\sigma_{r\theta}^V = 0 \quad (3.27)$$

$$\varepsilon_{r\theta}^V = 0 \quad (3.28)$$

The stress state around a given cavity of radius r_a is now found by substituting $\delta r_a = 0$ into (3.22). The component of the strain due to the expansion of the cavity is defined as the difference $\varepsilon_{ij} - \varepsilon_{ij}|_{\delta r_a=0}$. The incremental work per unit volume can then be calculated from

$$dW^V = \frac{2\sigma_h r_a^3 \delta r_a}{m r^4} \quad (3.29)$$

which in turn leads by straightforward integration over r , θ and r_a to the total work

$$W^V = \frac{2\pi}{m} \sigma_h r_c^2 \quad (3.30)$$

In the same manner the total work done in a horizontal cavity expansion will be derived. In this case the initial stress state in the plane perpendicular to the penetration direction is given by (3.12), and has a dependence on $\cos 2\theta$ which was not present in the boundary conditions for the vertical case. Again uniformly expanding the cavity by a fraction δr_a , the boundary conditions can be written as

$$r = \infty : \quad \sigma_{rr}^{(0)} = -\sigma^{(0)} \quad (3.31)$$

$$\sigma_{rr}^{(2)} = -\sigma^{(2)} \cos 2\theta \quad (3.32)$$

$$\sigma_{\theta\theta}^{(2)} = \sigma^{(2)} \cos 2\theta \quad (3.33)$$

$$r = r_a : \quad u_r^{(0)} = \delta r_a \quad (3.34)$$

$$u_r^{(2)} = 0 \quad (3.35)$$

$$\sigma_{r\theta}^{(2)} = 0 \quad (3.36)$$

These boundary conditions result in constants

$$A^{(0)} = -\frac{\sigma^{(0)}}{2m\mu} \quad (3.37)$$

$$B^{(0)} = r_a^2 \left(\frac{\sigma^{(0)}}{2m\mu} + \frac{\delta r_a}{r_a} \right) \quad (3.38)$$

$$A^{(2)} = -\frac{\sigma^{(2)}}{2\mu} \quad (3.39)$$

$$B^{(2)} = \frac{\sigma^{(2)} r_a^2}{2\mu} \frac{2m+2}{2m+3} \quad (3.40)$$

$$C^{(2)} = 0 \quad (3.41)$$

$$D^{(2)} = \frac{\sigma^{(2)} r_a^4}{2\mu} \frac{1}{2m+3} \quad (3.42)$$

and the resulting stresses and strains around the cavity are

$$\sigma_{rr}^H = -\sigma^{(0)} - 2\mu \frac{r_a^2}{r^2} \left(\frac{\sigma^{(0)}}{2m\mu} + \frac{\delta r_a}{r_a} \right) - \sigma^{(2)} \left(1 + \frac{4m}{2m+3} \frac{r_a^2}{r^2} + \frac{3}{2m+3} \frac{r_a^4}{r^4} \right) \cos 2\theta \quad (3.43)$$

$$\varepsilon_{rr}^H = -\frac{\sigma^{(0)}}{2m\mu} - \frac{r_a^2}{r^2} \left(\frac{\sigma^{(0)}}{2m\mu} + \frac{\delta r_a}{r_a} \right) - \frac{\sigma^{(2)}}{2\mu} \left(1 + \frac{2(m+1)}{2m+3} \frac{r_a^2}{r^2} + \frac{3}{2m+3} \frac{r_a^4}{r^4} \right) \cos 2\theta \quad (3.44)$$

$$\sigma_{\theta\theta}^H = -\sigma^{(0)} + 2\mu \frac{r_a^2}{r^2} \left(\frac{\sigma^{(0)}}{2m\mu} + \frac{\delta r_a}{r_a} \right) + \sigma^{(2)} \left(1 + \frac{3}{2m+3} \frac{r_a^4}{r^4} \right) \cos 2\theta \quad (3.45)$$

$$\varepsilon_{\theta\theta}^H = -\frac{\sigma^{(0)}}{2m\mu} + \frac{r_a^2}{r^2} \left(\frac{\sigma^{(0)}}{2m\mu} + \frac{\delta r_a}{r_a} \right) + \frac{\sigma^{(2)}}{2\mu} \left(1 + \frac{2(m-1)}{2m+3} \frac{r_a^2}{r^2} + \frac{3}{2m+3} \frac{r_a^4}{r^4} \right) \cos 2\theta \quad (3.46)$$

$$\sigma_{r\theta}^H = \sigma^{(2)} \left(1 - \frac{2m}{2m+3} \frac{r_a^2}{r^2} - \frac{3}{2m+3} \frac{r_a^4}{r^4} \right) \sin 2\theta \quad (3.47)$$

$$\varepsilon_{r\theta}^H = \frac{\sigma^{(2)}}{2\mu} \left(1 - \frac{2m}{2m+3} \frac{r_a^2}{r^2} - \frac{3}{2m+3} \frac{r_a^4}{r^4} \right) \sin 2\theta \quad (3.48)$$

Now it follows directly that the incremental work per unit volume due to the expansion of the cavity is given by

$$dW^H = \frac{r_a \delta r_a}{r^2} \left[2 \frac{\sigma^{(0)}}{m} \frac{r_a^2}{r^2} + \sigma^{(2)} \left(2 + \frac{4m}{2m+3} \frac{r_a^2}{r^2} + \frac{6}{2m+3} \frac{r_a^4}{r^4} \right) \cos 2\theta \right] \quad (3.49)$$

and as integration over the plane outside the cavity cancels all contributions depending on 2θ the result is simply

$$W^H = \frac{2\pi}{m} \sigma^{(0)} r_c^2 \quad (3.50)$$

This result is remarkably similar to (3.30), with the horizontal stress σ_h replaced by the mean stress $\sigma^{(0)}$.

The calculation of cone resistances from the expressions (3.30) and (3.50) would at least involve the inclusion of a shape factor to account for the shape of the cone, but undoubtedly the resulting relations would not yield a very accurate prediction of measured cone resistances. This is mainly due to the strong simplification made in selecting an elastic medium as the base of the model. There is however no indication that this shape factor differs significantly between horizontal and vertical penetration so that even without precise knowledge of this shape factor the ratio of work done in horizontal penetration to vertical penetration can be calculated as

$$W^{H/V} = \frac{W^H}{W^V} = \frac{\sigma^{(0)}}{\sigma_h} = \frac{1+K}{2K} \quad (3.51)$$

with K the coefficient of effective horizontal stress. This function is equated to the ratio of horizontal over vertical cone resistance, and has been plotted in figure 3.38.

This plot shows clearly that for normally consolidated soils, with $K < 1$, the ratio q_c^H/V is larger than one and that this ratio decreases with increasing overconsolidation. As expected the difference between HCPT and VCPT disappears if $K = 1$. As argued before, when describing the calibration chamber tests, there is a relation between an increase of the density of the sample

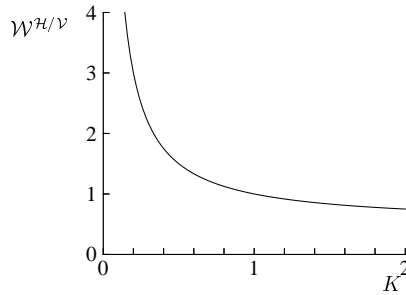


Figure 3.38: Theoretical ratio of horizontal over vertical total work, equated to the ratio of horizontal over vertical cone resistance, vs earth pressure coefficient, resulting from (3.51)

and an increasing K -value due to the preparation method of the sample. Low to intermediate densities correspond roughly with $K = 0.5$ whereas K increases rapidly to 1 at high densities. Combined with the theoretical behaviour derived in (3.51) it could therefore be expected that the horizontal cone resistance is up to 1.5 times the vertical for low to intermediate densities and that the ratio decreases to unity for high to very high relative densities.

3.6.2 Adapting Existing Theories for HCPT Interpretation

The main problem with adapting existing CPT theories to suit HCPT lies in the already stated fact that they assume the initial stress state in a plane perpendicular to the cone to be uniform, i.e. equal to the horizontal effective stress. In the same manner the stress in the direction of penetration is always equal to the vertical effective stress. These theories cannot deal with a radially non-uniform stress distribution around the cone, as is the case in HCPT. A method to adapt these theories would be to determine a radially uniform stress to take the role of σ'_h in horizontal penetration theories.

In the cavity expansion model for horizontal penetration, derived in section 3.6.1, the mean stress $\sigma^{(0)}$ was introduced. Effectively this mean stress took the role of the horizontal effective stress in VCPT theory and as such is a reasonable choice for the replacement stress. Of course this does not say that it is the only possible choice and it is certainly a somewhat arbitrary one, but the same could be said for other choices.

In the same line of thought the vertical effective stress in VCPT theories could be replaced by the initial stress that acts in the direction of penetration in HCPT, which is the horizontal effective stress. The idea is then to replace all instances of σ'_h in an existing VCPT theory by $\sigma^{(0)}$ and all instances of σ'_v by σ'_h , while keeping all other parameters unchanged. Best suited would of course be a theory that separately contains both stresses.

A suitable candidate is the empirical relation given by Jamiolkowski [87] based on calibration chamber tests on different sands

$$q_c^V = C_0 \sigma_v^{C_1} \sigma_h^{C_2} \exp(C_3 D_r) \quad (3.52)$$

with parameters for different sands given in table 3.7. This theory explicitly contains both initial stresses and has been derived for dry sands, so that the total stresses are equal to the effective stresses.

The relation for the horizontal sounding, derived from (3.52) according to the scheme

Sand Type	C_0	C_1	C_2	C_3
Ticino	220	0.065	0.440	2.93
Hokksund	165	0.140	0.400	3.38

Table 3.7: Parameters for different sand types for use in 3.52, [87]

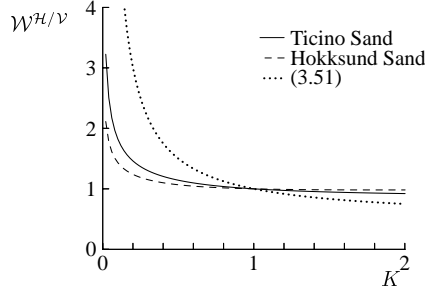


Figure 3.39: Theoretical ratio of horizontal over vertical cone resistance vs earth pressure coefficient based on adapted VCPT model

sketched above, is

$$q_c^H = C_0 \sigma_h^{C_1} \sigma^{(0)C_2} \exp(C_3 D_r) \quad (3.53)$$

resulting in a ratio of horizontal over vertical cone resistance

$$q_c^H / V = K^{C_1} \left[\frac{1+K}{2K} \right]^{C_2} \quad (3.54)$$

For the parameters given in table 3.7 the resulting ratio of horizontal over vertical cone resistance is sketched in figure 3.39 and compared with the result from (3.51). It shows the same trend of higher horizontal than vertical cone resistance at low K -values, only less strongly. For example at $K = 0.5$ the horizontal cone resistance is 50% greater than the vertical according to (3.51), but no more than 15% according to (3.54).

The same approximation of the stress state can of course be applied to other theories. This would lead to slight changes in the numerical results, but not to a fundamentally different behaviour, as this is mostly determined by the assumptions made in equating σ'_h in vertical penetration with $\sigma^{(0)}$ in horizontal penetration. The conclusion already drawn in the previous section that horizontal cone resistance is expected to be higher than vertical cone resistance would remain unchanged.

3.7 Conclusions

The cone penetration test is highly suited for the in-situ determination of the soil characteristics in soft soils. The interpretation of soil characteristics based on the test's main results, the cone resistance q_c and sleeve friction f_s measurements, leans strongly on empirical relations. A number of different analytical models exists but these can only predict cone resistances for a limited range of soil types and can tackle the inverse problem of determining soil properties from CPT measurements with varying success only.

This lack of reliable analytical models for vertical CPT limits the possibilities to adapt a model to horizontal cone penetration. The primary method to establish a correlation between horizontal and vertical cone resistances is therefore to perform both tests in a soil sample under identical conditions. The calibration chamber offers this possibility as it allows the conditioning of sand at various densities. The DUT rigid wall calibration chamber further offers the possibility to successively execute vertical and horizontal CPTs in the same soil sample. In that way any variation in the soil properties due to different sample preparations is eliminated.

In order to obtain a correlation between HCPT and VCPT measurements, a series of calibration chamber tests has been executed in four differently graded sands at different densities. These tests show that measurements obtained in horizontal cone penetration tests in sand differ from those resulting from vertical tests.

Firstly, the horizontal over vertical cone resistance ratio $q_c^{H/V}$ is larger than 1 for sands at intermediate densities, with an average value of 1.2. For low and high densities this ratio tends towards unity. Although the scatter in the data is significant, the average of the data can be described by

$$q_c^{H/V} = 1 + 0.191 e^{-13.6(D_r - 0.497)^2} \quad (3.55)$$

This behaviour of the cone resistance ratio can be understood if the assumption is made that the undisturbed lateral stress is governing the cone resistance. In vertical CPT this is the horizontal stress, whereas in horizontal CPT this stress state varies between the horizontal and vertical stress along the circumference of the cone.

Given the test setup of the calibration chamber and the preparation of the sand by fluidisation and vibration, a relation is established between density and horizontal stress, in that higher densities are accompanied by higher horizontal stresses. For higher densities the coefficient of effective horizontal stress tends towards unity, so that no difference between horizontal and vertical stress exists and as a result no difference in the stress state perpendicular to the penetration direction. This explains the fact that the measured cone resistance ratio tends towards one for high densities.

For loose packed sands the stress state is known to have little influence on the cone resistance, as has been established for example in calibration chamber tests by Jamiolkowski. As a result it may be surmised that also a different stress state between HCPT and VCPT has little influence on the cone resistances and therefore on the cone resistance ratio $q_c^{H/V}$.

For intermediate densities the relation is somewhat more complex. An elastic cavity expansion model has been presented in which the work needed to create a cavity in a medium with a uniform radial stress has been compared with the work needed to create a cavity in a medium with a non-uniform stress state. The first model models vertical CPT, the second horizontal. Although both models are rather simple compared to existing CPT models and are not directly suited to interpret CPT measurements, the ratio of the works resulting from these models gives a reliable estimate of the ratio of cone resistances. This ratio is

$$W^{H/V} = \frac{1+K}{2K} \quad (3.56)$$

with K the coefficient of horizontal stress. This ratio is approximately 1.5 for normally consolidated sands and gives an upper bound estimate for the ratio of cone resistances. This simple model agrees well with the calibration chamber measurements.

This behaviour of the cone resistance ratio as a function of the density is roughly identical for the four differently graded sands that have been tested, and no discernible influence of the grain size distribution is found.

In those respects the sleeve friction ratio f_s^H/V shows a different behaviour. First of all the ratio of sleeve frictions shows no clear dependence on the density of the sand. There is only a slight hint of an increase with relative density, but this is not significant. This ratio does show a clear change with a change in the gradation of the sand, however. The average ratio f_s^H/V varies between 1.28 and 0.65 depending on the sand used. It seems that the horizontal sleeve friction is on average lower than the vertical, but reacts more strongly to changes in the average grain size and the amount of fines. When the changes in the horizontal and vertical friction ratios are looked at in detail, it can be observed that the changes in f_s^H/V , and subsequently in R_f^H/V , must be attributed to simultaneous changes in both friction ratios. Those changes in R_f^H and R_f^V are highly non-linear with respect to the gradation of the sand however.

Interpretation of this behaviour of the friction ratios is complicated as no well-established model for the interpretation of sleeve friction measurements is available at present, neither from vertical nor from horizontal CPT. The somewhat unpredictable behaviour, in which sands with the same vertical friction ratio show clearly different horizontal friction ratios and vice versa, is reason however to use the calibration charts developed from vertical CPT with utmost care, if used in the interpretation of horizontal CPT. A need has been shown for the development of adapted correlation graphs for horizontal CPT, but the current field and laboratory experiences are not extensive enough to make this adaptation with enough confidence. To this end further tests are needed. In laboratory conditions further tests on different sands at various densities and stress levels should be performed, but there is also a need to obtain data in different soil types. For these soils, field tests are more practical even though interpretation problems will arise.

When further calibration chamber tests are executed the design of the current tank should be slightly adapted in order to allow an excess pressure to be applied to the top of the sand, while at the same time keeping the possibility to prepare the sand by the time-efficient method of fluidisation.

Kind of slippery, aren't ye.

Walt Disney: Bambi

Chapter 4

High-Speed Piezocone Tests in Sands

4.1 Introduction

One of the many applications of soil investigation techniques, and one which has received considerable attention in recent years, is the in-situ determination of the liquefaction potential of soils. The 1995 Kobe earthquake has demonstrated once again the devastating effect cyclic loading induced soil liquefaction may have. But also gravity induced flow liquefaction can cause extensive damage to (soil) structures, mainly because it has the potential to extend itself without limit, as the driving force remains unchanged. In this respect flow liquefaction clearly differs from cyclic liquefaction, as in the latter case the generation of excess pore pressure and deformation of the soil will end almost as soon as the driving force ends.

The increased need for underground infrastructure, the simultaneous demand that the construction of this infrastructure causes no disturbances for the environment and the resulting use of tunnel boring techniques whenever deemed possible, have caused an ongoing extension of the range of soil types deemed suitable for tunnel boring. As a result, large diameter tunnels are now proposed at locations where loose packed fine sands are present, which may be susceptible to liquefaction. During the construction of the tunnel the interesting but somewhat disturbing possibility is created that both types of liquefaction, flow and cyclic loading induced, occur at the same time. After all the TBM creates a large partially supported opening in the soil and thereby opens the possibility of flow liquefaction of susceptible soil layers in front of the TBM. At the same time the TBM generates a significant amount of vibrations, which may induce liquefaction by themselves [127, 152]. The combination of both mechanisms which can now occur is a relatively new and hardly studied phenomenon however. In cases where infiltration of the support medium of the TBM into the soil occurs and generates excess pore pressures, the situation is further aggravated by the reduction of the effective stresses and the increased liquefaction potential resulting from this.

Since the introduction of pore pressure measurements during the penetration of a CPT cone in the early 1970's, the piezocone test (CPTU) has been more or less standardized and has found a wide range of application. The test offers a number of advantages over regular CPT, such as the ability to detect thin impermeable layers within a larger permeable stratum, the ability to assess the flow and consolidation characteristics of the soil and the possibility to correct the cone and friction readings for the effects of pore pressures acting on the inside of the instrument [56].

The piezocone test also allows a more detailed and precise evaluation of the soil properties, as for example demonstrated by Campanella & Robertson's classification charts using cone resistance q_c , friction ratio R_f as well as pore pressure ratio B_q [56]. These charts and similar soil

characterisation methods primarily yield a soil classification, but may also give a first indication of other properties like fines content, sensitivity, overconsolidation ratio (OCR) or relative density. Other correlations have been published which yield a more precise determination of soil properties like relative density based on CPT or CPTU measurements, but most are valid only for a limited range of soils [108].

Of those soil properties the relative density, fines content and stress state are of major importance in determining the liquefaction potential of a soil layer. In the case of flow liquefaction, the main parameter is the density of the soil in relation to the critical density, which is used as an indication whether or not the soil is contractant. In the case of cyclic liquefaction, the fines content and stress state are also needed to make a correct assessment of the cyclic resistance ratio (CRR), either indirectly by correlating with the individual parameters or directly by using q_c -CRR correlations. The cyclic resistance ratio is defined as the cyclic stress ratio (CSR) $= \tau/Gs'_v$, at which liquefaction occurs and the determination of the CRR is currently made mainly through the q_c -CSR correlation charts based on the database of field cases compiled by Stark & Olson [154], complemented with data from Suzuki et al. [142].

This method does not directly use the friction and excess pore pressure measurements, although corrections on the effective q_c used as index to the charts can be made. The CRR further depends strongly on the number of stress cycles N applied to the soil. Correlations between N and CRR exist, but these do not generally extend to a single load cycle and as such the extension to flow liquefaction of these methods is not possible, besides the fact that this extension would be somewhat speculative. Furthermore these methods remain indirect and empirical and as a result cannot easily incorporate the effects of a combined static and dynamic load, as in combined flow and cyclic stress liquefaction. Considerable effort is applied nowadays to new techniques to measure in-situ, in a wide range of soils, the CRR in a more direct way, using probes containing vibrating elements and/or using shear wave response of the soil [143, 133].

When attention is limited to contractant soils however, which under saturated conditions should generate excess pore pressures during shear deformation and contraction, and which are therefore susceptible to flow liquefaction and are generally highly susceptible to cyclic liquefaction, it should be theoretically possible to measure these excess pore pressures when in an in-situ test a shear deformation is applied to the soil. Of those contractant soils, loose packed clean sands containing few to no fines are most susceptible to liquefaction.

During cone penetration testing the soil around the cone is subjected to a combined compression and shear deformation and excess pore pressures are generally generated. Whether these excess pore pressures are detected by a piezometer at the shoulder of the cone (see figure 4.1) depends mainly on the permeability of the soil. In soils with a permeability less than 10^{-7} m/s, fully undrained conditions may be expected and the full excess pore pressures generated should be measured in CPTU. In the interval $10^{-7} < k < 10^{-4}$ m/s partially drained conditions may be expected, whereas above 10^{-4} m/s fully drained conditions are most likely. Now the loose sands with low fines content that are of particular interest exhibit such large permeabilities that at regular penetration speed no excess pore pressures are measured at the cone shoulder during regular CPTU, even if they are generated by the shear deformation.

If the penetration speed is increased, however, the dissipation time between the generation of the excess pore pressures and the observation by the piezometer is shortened. This might create the possibility to observe excess pore pressure in contractant soils before they dissipate completely. If so, this would create a more direct observation of the contractancy of the soil and therefore a means to identify liquefiable soils. Using a specially designed miniature cone in a large triaxial cell this behaviour has been observed by Canou et al. at very high speeds [57].

To test whether this behaviour can also be measured using a regular CPTU cone, a number of

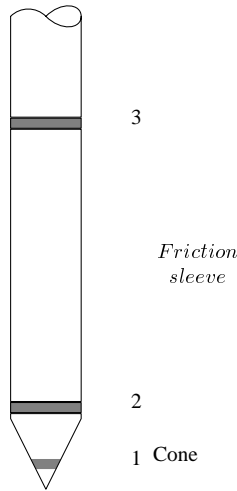


Figure 4.1: Location of filter elements and excess pore pressure measurement in different cone designs and their numbering

tests has been executed in the calibration chamber at the Geotechnical Laboratory, at the regular 2cm/s speed as well as higher speeds. During these tests pore pressures have been measured. The possibility to determine the liquefaction potential using such a method has been compared with methods based on correlation charts using q_c from regular CPT.

First the determination of liquefaction potential based on correlation charts will be described. Then the possible influences of the penetration speed on CPT and CPTU results will be investigated, followed by an overview of the various tests that have been executed in the calibration chamber and their results.

4.2 Determination of Liquefaction Potential

The method of determining the liquefaction potential of the soil as described by Robertson & Fear [142] can be summarized as follows. First the normalized cone resistance q_{c1} is determined as

$$q_{c1} = \frac{q_c}{p_a} \left(\frac{p_a}{\sigma'_v} \right)^{0.5} \quad (4.1)$$

where p_a , the atmospheric pressure, is used as a reference pressure. q_{c1} is subsequently used as an index to a database of field cases. The dividing line between liquefied and non-liquefied sites, for a magnitude $M=7.5$ reference earthquake, and for clean sands with less than 5% fines, defines the CRR. For q_{c1} between 30 and 160 it is defined as

$$CRR = 93 \left(\frac{q_{c1}}{1000} \right)^3 + 0.08 \quad (4.2)$$

This relation is valid for clean sands only. For sands with a fines content higher than 5% a correction can be made to the q_{c1} value [108, 142].

R_f	Soil type	n
<0.6	coarse sand	0.55
0.6 – 0.8	medium coarse sand	0.58
0.8 – 1.1	fine sand	0.61
1.1 – 1.4	silty sand	0.78
>1.4	clayey sand	1

Table 4.1: Soil characterisation and exponent n according to Olsen [132]

This method does not directly take the friction ratio into account, in contrast to the method described by Olsen [132], which differs in two respects. First, the exponent in the cone resistance normalisation is not always equal to 0.5, but depends on the soil type, cone resistance and friction ratio. Secondly the CRR is defined by the cyclic stress ratio to achieve 5% shear strain within 15 stress cycles. In this method, first the soil type is determined, based on friction ratio. From that an estimate of the exponent n can be derived (see table 4.1).

Using this n -value the corrected cone resistance and corrected friction ratio R_{f1} can be determined as

$$q_{c1} = \frac{q_c}{(\sigma'_v)^n} \quad (4.3)$$

$$R_{f1} = \frac{f_s}{q_c} \frac{1}{(\sigma'_v)^{1-n}} 100\% \quad (4.4)$$

The effective stress level can be determined using the measured pore pressures, assuming fully drained penetration, if a CPTU cone is used, or estimated otherwise. The corrected cone resistance and friction ratio are used in turn to determine the value of n from a nomograph (figure 4.2) which leads to an iterative procedure. The resulting q_{c1} and R_{f1} are subsequently used as indices to determine the CRR, where it is assumed that liquefaction will only be a problem at CRR below 0.3. Note that these relations are valid only if all pressures are entered in terms of tsf.

It is known that the cyclic resistance ratio also depends on the number of stress cycles applied to the soil. The CRR given by Olsen is valid for 15 equal load cycles, the CRR defined by Robertson is based on the conditions during a reference M=7.5 earthquake, which is believed to be equal to 15 load cycles at $0.65\tau_{\max}$, with τ_{\max} the maximum shear stress occurring during the earthquake. De Alba et al. give a relation between the CRR and the number of stress cycles N needed to reach initial liquefaction, shown in figure 4.3 [133]. This shows that for a limited number of stress cycles the CRR is significantly higher than for a large number of stress cycles. The influence of a combined static and cyclic load is not clear however and may also depend on the ratio between the static and dynamic load.

It is clear that both methods to determine liquefaction potential do not take the excess pore pressure reading into account. This is not surprising as it is to be expected that in the clean sands for which the method is applicable, at the regular penetration speed of 20mm/s, no excess pore pressures will be measured, as these will have dissipated before the piezometer passes.

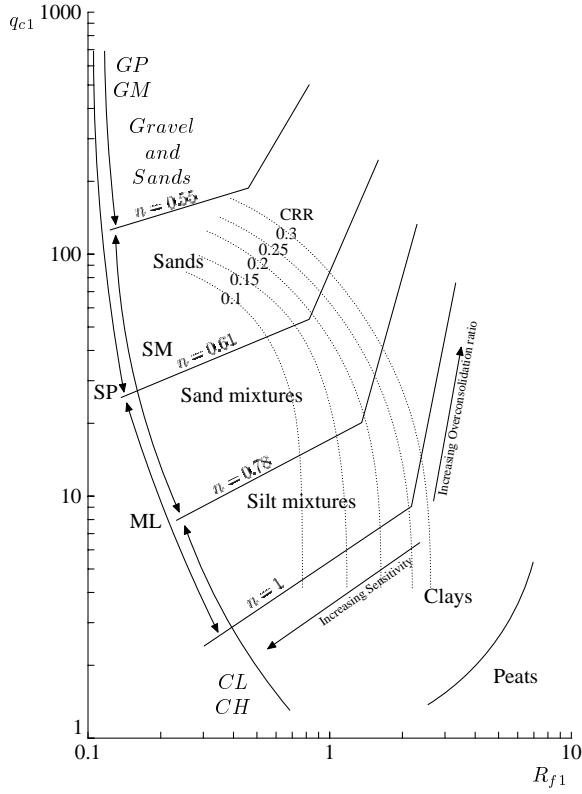


Figure 4.2: Determination of n -value from normalised cone resistance and friction ratio (all terms in tsf) and CRR at 5% shear strain, after [132]

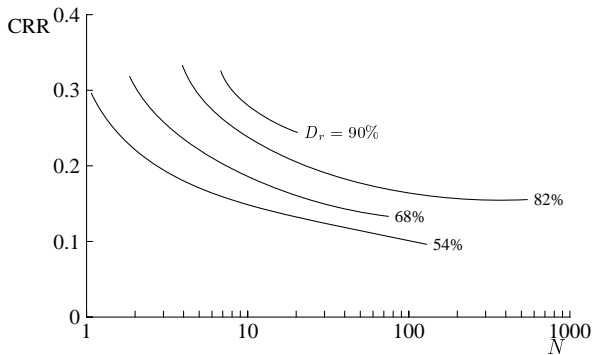


Figure 4.3: Dependence of CRR on number of stress cycles N and relative density [133]

4.3 Influence of Penetration Speed

4.3.1 Influence on Cone Resistance and Sleeve Friction

When the penetration speed is increased, two speed related effects may be encountered. The first is a possible strain rate dependent change in the cone resistance and sleeve friction measurements. The second is a change in the generated excess pore pressures and their dissipation behaviour. The combined influence of these effects on the readings of cone resistance and sleeve friction will be covered in this section; the effects on excess pore pressure readings will be dealt with in section 4.3.2.

Although several researchers have investigated the influence of the penetration speed on the CPT measurements, this research has focussed mainly on the influence of speeds slower than the prescribed regular speed of 20mm/s. However, te Kamp [91] reports a number of tests in saturated conditions at speeds up to 100mm/s, as well as tests at lower than normal speeds. These tests show a roughly logarithmic dependence of the cone resistance on the penetration speed. Based on this observation and the data given by te Kamp it is expected that the cone resistance at a penetration speed of 200mm/s is 5 to 10% higher than at a regular speed. In the same way a 10 to 15% higher sleeve friction can be expected.

4.3.2 Influence on Excess Pore Pressures

In their contribution to ISOPT-1 Campanella & Robertson [56] state that a plausible upper limit to soil permeability for which CPTU at regular speed is performed in undrained conditions is in the order of 10^{-7} m/s. Between 10^{-4} and 10^{-7} m/s a partially drained response may be observed, whereas for permeabilities greater than 10^{-4} m/s a drained response is most likely. And although changes in the penetration rate could be made to change the apparent dissipation behaviour of the soil, the enormous speed difference needed to yield acceptable results are deemed impractical and would introduce additional strain rate effects. This last conjecture is indeed confirmed by the tests performed by te Kamp summarised in the previous section.

The influence of the penetration rate, on the other hand, has been investigated by Canou et al. [57]. They have used a specially constructed miniature piezocone with a cone area of 1cm^2 in a 180mm diameter triaxial cell at penetration rates between 0.1 and 100mm/s and observe excess pore pressures in fine loose sands which depend on the relative density as well as the penetration rate. See figures 4.4 and 4.5 for the results in a fine very uniform Hostun sand.

From the presented test results it remains unclear how well drained the triaxial cell was during the tests and to what extent excess pore pressures were generated due to a hindered dissipation around the cone. Also, there is limited evidence that the generated excess pore pressures are lower at lower confining stress levels, but this effect is not very strong. The miniature cone itself and the data acquisition system used have been specially designed to measure the excess pore pressures generated in these tests, which are small and short-lived in comparison to the excess pore pressures generated in impermeable clays in the field. Compared to regular CPTU cones the minicone has a high sensitivity but limited measuring range and a high data sampling rate. Due to this combination of effects it remains unclear how the boundary conditions imposed by the triaxial cell and the use of the specially designed miniature cone influence the test results in comparison to tests performed under field conditions using regular CPTU cones, and whether or not these measurements can also be obtained with equipment suited to perform field measurements.

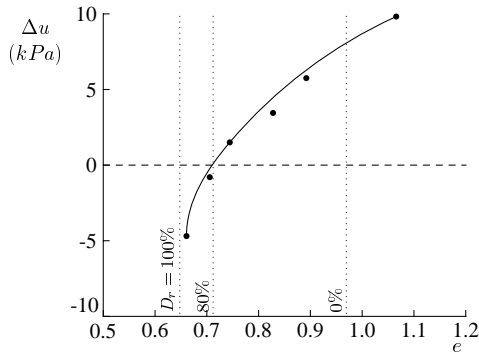


Figure 4.4: Influence of density on excess pore pressure in M-CPTU ($v = 20\text{mm/s}$) [57]

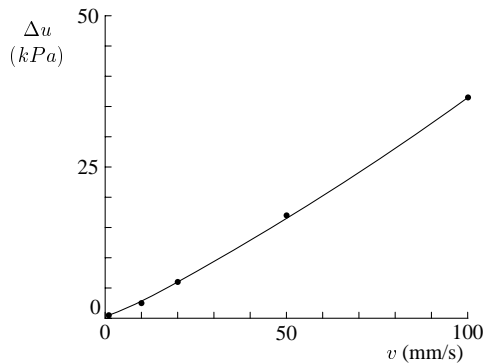


Figure 4.5: Influence of penetration rate v on excess pore pressure in M-CPTU [57]

This could in theory be determined from a cone penetration model including the generation and dissipation of excess pore pressures. Unfortunately most models either assume that penetration (in sand) is fully drained, or that penetration (in clay) is fully undrained up to the instant the piezometer passes and can subsequently be described as simple consolidation problem. That this last assumption does not hold in reality has for example been indicated by Campanella [56]. The excess pore pressures generated on the face (filter position 1) of the cone are caused by compression of the soil by the cone, whereas behind the cone (positions 2 and 3) also a localised shear deformation occurs, generally lowering the apparent excess pore pressures. The interaction of these effects depends among other things on the stress state of the soil, the dissipation rate and excess pore pressure distribution, as indicated by the analytical analyses of e.g. Sully et al. [158] or Burns & Mayne [53, 54], as well as on the dilatancy of the shear zone around the cone shaft, as shown by the finite element analysis of Abu-Farsakh et al. [1].

However, none of these models can analyse the partly drained generation and dissipation of excess pore pressures during penetration in a permeable material like sand, especially as the influence of shear dilatancy around the shaft has to be taken into account.

4.4 Calibration Chamber Tests

To investigate the influence of the density of a sand bed on the excess pore pressures generated during penetration and the possibilities to detect these excess pore pressures using a CPTU cone, a number of tests has been executed in the DUT calibration chamber on sands at different relative densities. These tests have been performed using a regular CPTU cone and an adapted rig, which was able to obtain penetration speeds over 200mm/s, as well as the regular 20mm/s. In order to determine the excess pore pressures, use was made of the piezometer installed in the cone as well as separate piezometers installed in the sand bed.

The objective of these tests was to determine whether the speed difference between 20 and 200mm/s has a detectable influence on the CPTU results and whether these differences can be used to determine the liquefaction potential of the sand bed. This last objective should of course be seen in relation to the possibilities to determine liquefaction potential from a regular CPT or CPTU, for example using the method described by Olson (see section 4.2).

4.4.1 Equipment and Test Method

For an overview of the calibration chamber and the preparation method of the sand the reader is referred to section 3.3. The sand used in this test series was sand No. 2, a uniform fine sand, for which the grain size distribution is given in figure 3.6. Minimum and maximum void ratio are 0.498 and 0.801 respectively.

In contrast to the HCPT tests only one sounding was made in each sand sample in this test series, at position b, see figure 3.13. This was done to eliminate any influence of multiple tests in the same sample on the liquefaction potential and to eliminate any influence of a different position with respect to the boundaries of the tank on the dissipation behaviour around the cone. Although performing only a single test per sample eliminates the possible influence of a densification imposed by a previous penetration and the associated change in the liquefaction potential, it generates a variation between the individual tests due to variations in the preparation of the sand bed.

A further difference with the tests described in the previous chapter is that the sand bed was kept fully saturated in these tests. In all tests the water level was adjusted to within 10cm from the top of the sand bed, which was the accuracy that could be obtained. From this level the pore pressure was assumed hydrostatic with depth for the interpretation of the test results. This leaves, however, an estimated 1kPa variation in the pore pressures between the various tests. These variations in the density of the sample and the water level between the various samples are the main sources of errors when comparing different tests at similar densities.

To measure the excess pore pressures generated by the cone independently from the CPTU cone, two piezometers were installed in the sand bed, at locations approximately 5 and 10cm from the projected path of the cone, as sketched in figure 4.6. The pressure transducers used had a 70kPa operating range and a reported $\pm 0.1\%$ maximal relative error. Calibration of the transducers at low stress levels has indeed shown a maximal error slightly less than 70Pa. The signals from the piezometers were recorded using a pen recorder.

The piezocone used was a 10cm² CPTU cone, designed by Geomil Equipment bv, with reported measuring ranges and accuracies given in table 4.2. Given the measuring range and accuracy of the pore pressure transducer, an error up to 8kPa could be expected, especially at low pore pressures where the effects of non-linearity and hysteresis are most notable. All channels of the CPTU cone were recorded using a Geomil GME400 digital recorder. The combination of cone and data acquisition system forms a CPTU measuring system suited for

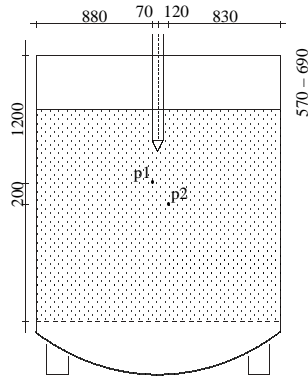


Figure 4.6: Location of piezometers installed in the sand bed

Channel	Range	Accuracy
Cone	50MPa	0.2%
Sleeve	500kPa	0.2%
Pore Pressure	2MPa	0.4%
Inclinometer	15°	2°

Table 4.2: Measuring range and accuracy of the CPTU cone

regular field conditions and satisfying the conditions in most (international) soil investigation codes [108].

The hydraulic rig used to drive the cones (see figure 4.7) was specially designed by Geomil, based on a standard 100kN rig, but with an adapted hydraulic circuit, including a high capacity hydraulic pump and valves. Although this system is capable of maintaining the regular penetration speed of 20mm/s, it also allows penetration speeds up to 300mm/s, depending on the force required to drive the cone. If the total friction on the system increases, the penetration speed reduces, as can be seen in figure 4.8. The required penetration speed of 200mm/s can be maintained up to approximately 40kN, far exceeding the forces required in the calibration chamber.

4.4.2 Overview of Test Series

A total of 16 samples was prepared in which as many tests were performed, 4 soundings at the regular 20mm/s speed and 12 at speeds approximately 200mm/s or more. During 8 of those 12 tests the (excess) pore pressures were also recorded using the piezometers installed in the sand bed. The sand samples were prepared at different densities by means of fluidisation and vibration, as described in the previous chapter. Table 4.3 gives an overview of the test conditions and some indicative values of the test results, which will be explained and discussed in the following paragraphs.

These tests can be logically divided into two subseries of eight tests each. The first set can be used to investigate the influence of the penetration rate v on the measurements. Figure 4.9 shows the results from tests 1, 2 & 4 plotted in the same graph. It is immediately clear that the high-speed sounding results in a far coarser picture of the soil properties, as the data acquisition system completes only two samplings per second, resulting in approximately 10 data points per



Figure 4.7: High-speed penetration rig

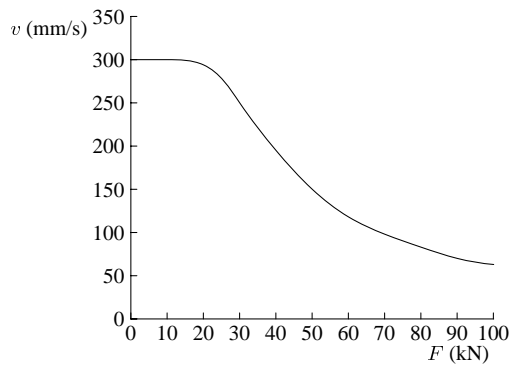


Figure 4.8: Driving force vs maximal penetration speed for adapted CPT rig

No.	D_r	v (mm/s)	Piezo. 1 & 2	q_c (MPa)	min. Δu (kPa)	max. Δu (kPa)	CRR
1	0.23	20		0.52	-3.3	0.5	< 0.1
2	0.24	200		0.33	0	7.8	< 0.1
3	0.35	20		0.34	0	0.6	< 0.1
4	0.35	200		0.41	0	10.2	< 0.1
5	0.32	20		3.57	-0.4	1.1	0.3
6	0.41	200		4.28	-5.0	0.6	> 0.3
7	0.62	20		4.88	-3.5	0.8	> 0.3
8	0.62	200		4.36	-5.9	0.2	> 0.3
9	0.47	200	x	0.59	-2.5	6.8	0.25
10	0.32	200	x	<0.1	-	-	< 0.1
11	0.44	200	x	0.44	-2.3	3.3	0.15
12	0.53	200	x	2.14	-5.0	7.1	< 0.1
13	0.56	200	x	1.62	-4.5	0.3	0.1
14	0.62	200	x	7.44	-16.5	4.4	> 0.3
15	0.62	200	x	5.56	-7.0	0	> 0.3
16	0.80	200	x	9.86	-24.5	4.0	> 0.3

Table 4.3: Overview of regular and high-speed CPTU tests; q_c at $z = 1.3\text{m}$, min & max Δu are minimal and maximal calculated values of Δu over the sounding length

metre of sounding. This is only approximate since the pulse wheel driven depth registration system has problems keeping up with the high speeds and as a result fails to register the entire sounding length. The lost sounding length is relatively easy to correct for, however, as in the calibration chamber the final sounding depth can be established easily. The peaks present in the cone resistance measurements at each 1m interval give additional depth information. Using this information the sounding depth can be corrected in all measurements and this correction has been applied to the data presented in figure 4.9 and all other figures and tables. A remaining uncertainty in the depth registration of approximately 10cm cannot be excluded however.

After this depth correction has been applied, the cone resistance q_c can be established. Apart from the error in the depth registration, the cone resistance has an absolute error of 0.1MPa. The cone resistance has not been normalised by the estimated effective stress, as this would introduce an additional error of over 10%, mainly due to the uncertainty in the depth registration. A further uncertainty is formed by the exact measuring depth, even setting aside the depth registration problems. As only a single measurement per second is made, i.e. a single sampling per 10cm, it is uncertain exactly at which point within this 10cm interval the measurement is made. The result is a further 5cm error in the positioning of the measurement.

The excess pore pressure Δu on the other hand has to be derived from the measured pore pressure u_2 and the hydrostatic pore pressure u_0 . The first one has been measured by the cone, the second one is taken linear with depth from the top of the sand bed. In this calculation the depth uncertainty has a strong influence, as it directly influences the estimated hydrostatic pore pressure. The error resulting from the uncertainty in the water table, the depth registration as well as the sampling depth adds up to 2kPa at the top of the sand bed to approximately 4kPa at the bottom. This is excluding the 8kPa error resulting from the reported accuracy (see table 4.2).

In order to summarise the test results, table 4.3 lists the cone resistance at $z = 1.3\text{m}$ as well as the minimal and maximal derived values for the excess pore pressure Δu . Together with error bars, resulting from the uncertainties in the water table and depth registration, but excluding

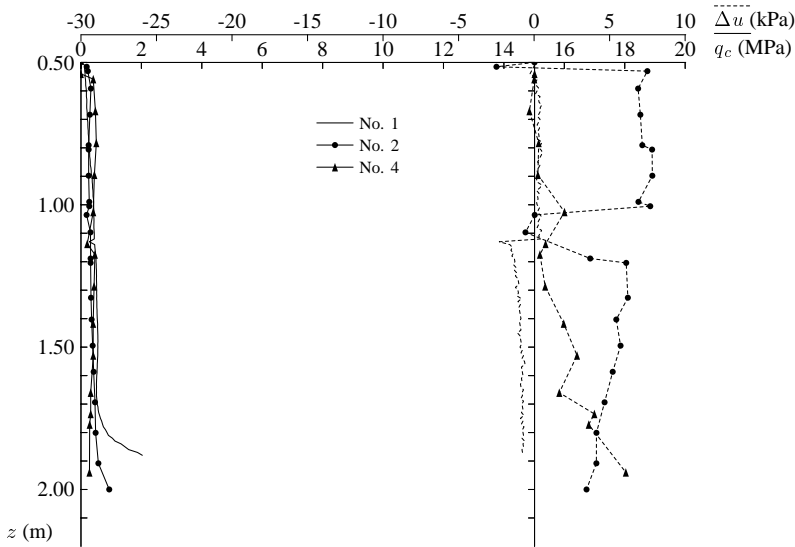


Figure 4.9: Comparison of regular and high-speed CPTU

the 8kPa error resulting from the accuracy of the CPTU pore pressure transducer, the range of excess pore pressures resulting from those minimal and maximal excess pore pressures is plotted against relative density in figure 4.10.

From this figure it is clear that, although larger excess pore pressure occur and are measured at higher than regular penetration speed, there is no correlation with relative density other than that at high densities greater negative excess pore pressures occur. As such the occurrence of great negative excess pore pressures could be an indication of high relative density. A positive excess pore pressure, however, does not yield any definite information on the density of the sand, as positive excess pore pressures manifest themselves more or less similarly for all densities.

Even at similar densities the behaviour of the excess pore pressure with depth can be rather dissimilar, as can be seen from tests 2 and 4, plotted in figure 4.9. Test 2 shows a relatively large positive excess pore pressure, decreasing with depth at the lower end of the sounding, whereas test 4 exhibits no excess pore pressure at the upper part of the sounding and increasing positive excess pore pressures at the lower end.

The comparison of these tests is of course hampered, as there might be a zero-shift (up to 8kPa) between the tests resulting from the (reported) accuracy of the CPTU pore pressure transducer. That hysteresis effects do occur can be inferred from the shift in excess pore pressure at the $z = 1.1\text{m}$ level in sounding no. 1, at which level the rods were extended. In order to exclude such effects, a second series of tests has been performed, with the addition of two high-precision piezometers installed in the sand bed at depths 20cm apart.

As an example from this test series, figure 4.11 shows the cone resistance and excess pore pressure measured at the cone in test no. 9, while figure 4.12 shows the excess pore pressures registered by the two piezometers. The time scale used in this last graph, t_{rel} , has been shifted in the time domain so that for both piezometers $t_{rel} = 0$ corresponds with the time the cone tip passes the depth at which the piezometer is installed. As there is a depth difference of 20cm between the two piezometers, this roughly corresponds with a time difference of 1s.

For tests 9 to 16 the excess pore pressure calculated at the depth of the two piezometers as

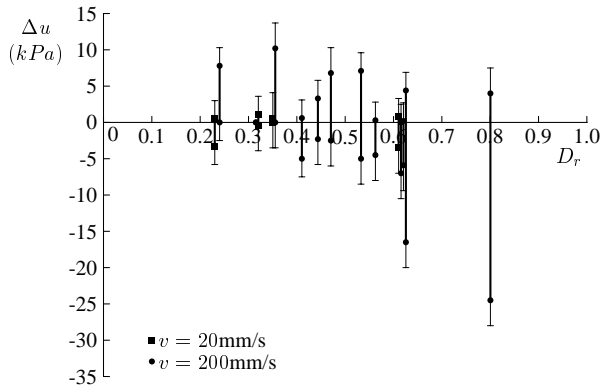


Figure 4.10: Range of excess pore pressures (thick lines) and estimated error due to depth and hydrostatic pore pressure uncertainties (thin lines) vs relative density for regular (boxes) and high-speed (circles) tests

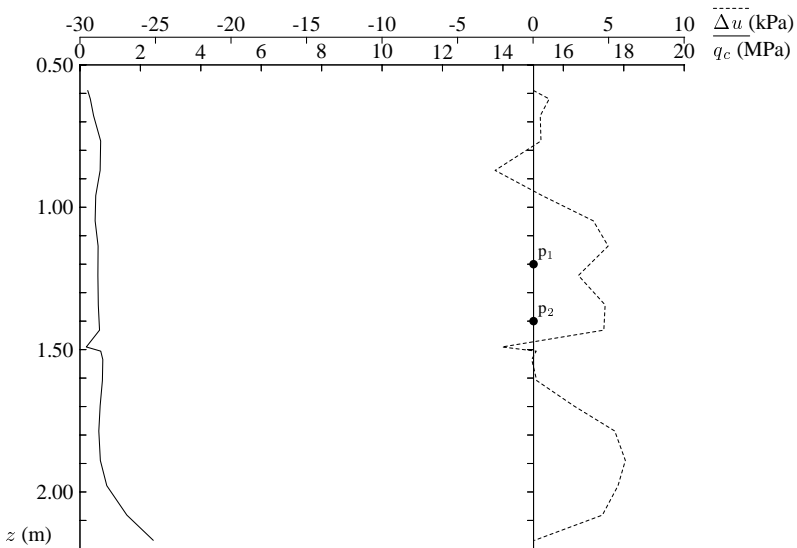


Figure 4.11: Cone resistance and excess pore pressure measured with high-speed CPTU (No. 9), with indicated depth of piezometers p_1 and p_2

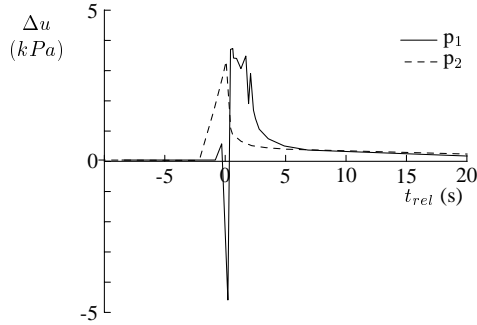


Figure 4.12: Measured excess pore pressures at piezometers p_1 and p_2 for test No. 9 vs t_{rel} ($t_{rel} = 0$ as cone tip passes the piezometer)

No.	D_r	Cone		p_1		p_2	
		$\Delta u(p_1)$ (kPa)	$\Delta u(p_2)$ (kPa)	Δu_{min} (kPa)	Δu_{max} (kPa)	Δu_{min} (kPa)	Δu_{max} (kPa)
9	0.47	3.26	4.94	-4.62	3.63	0	3.25
10	0.32	0	0	0	0.88	0	0.75
11	0.44	0	-2.10	-0.25	4.38	0	2.88
12	0.53	6.00	-4.35	0	3.25	-1.75	1.50
13	0.56	0.27	-0.66	-0.50	0.75	-1.50	0.25
14	0.62	-14.9	-14.8	-4.25	0.88	0	1.50
15	0.62	0	0	-0.38	0.13	-0.88	0.50
16	0.80	-17.1	-20.9	-7.75	0	-3.13	0

Table 4.4: Comparison of excess pore pressures measured behind cone tip and at piezometers p_1 and p_2 , with $\Delta u(p_i)$ the excess pore pressure measured at the depth of piezometer i

well as the extreme excess pore pressures registered by the piezometers are listed in table 4.4. From these tests no. 10 stands out as it met so little resistance that the cone and rods already entered the soil propelled by their own weight only. As a result, the data-acquisition system was not triggered and no pore pressures were measured by the cone, but the test has been included as the piezometers in the sand functioned normally.

From figure 4.12 the general behaviour of the piezometers in loose sand can be observed. As the cone nears the piezometer the pore pressure starts to rise slightly, but for the closest piezometer this behaviour is interrupted by a sharp negative peak. Subsequently the excess pore pressure jumps again to a large positive value and when the cone has passed, a time dependent pore pressure decay starts until after some 20s the excess pore pressures have dissipated.

The original increase in the pore pressure is attributed in part to the contraction of the loose sand as the cone radially deforms the soil and in part to the pore water displaced by the cone. The sharp negative peak on the other hand is attributed to the contractant behaviour associated with the shear deformation that takes place along the shaft after the cone has passed [1, 141]. Next the sand will most probably reach a critical state, so effectively no more deformation takes place, and consolidation starts, as well as a redistribution and dissipation of the excess pore pressures.

At intermediate and high relative densities, the generation of positive excess pore pressures

is less strong, but only completely absent in the $D_r = 80\%$ test. In this test only a sharp negative peak is observed, followed by a slow increase of pore pressures over time, until they reach hydrostatic pressure again. If a sharp negative pressure peak associated with shear behaviour is observed in these tests, it is less prominent than in the tests on loose sand. It must also be noted that, although in figure 4.12 piezometer 2, the outer of the two piezometers, does not show a negative pressure peak as the cone passes, this is not a general behaviour, as in several other tests small negative peaks were recorded.

Comparing the measurements from the piezometers to the CPTU measurements at the same depth it must be noted that, although the measurements made with the piezometers in the sand bed have a high resolution and a small error margin and as such are reliable, they do not correspond well with the measurements made at the cone shoulder and the measured extremes show no clear relation with the density of the sand. When looking in more detail at the piezometer data it could be surmised that large negative shear-related pore pressures followed by positive excess pore pressures are an indication of low density; that the total absence of positive excess pore pressure is an indication of very high densities; and that the absence of large pressure fluctuations is an indication of intermediate densities. Given the small number of tests this is somewhat speculative however. Furthermore, these results do not correspond with the measurements from the CPTU cone and can hardly form the basis for a practical method to investigate the liquefaction potential of the soil.

A point still unaddressed concerns the liquefaction potential of the prepared sand samples. In order to quantify the susceptibility of the samples other than by their overall relative density, the CRR has been calculated using the measured cone resistance and sleeve friction using the method presented by Olson (see section 4.2). The resulting CRRs are listed in table 4.3. A CRR below 0.15 indicates a highly susceptible layer, a CRR over 0.3 indicates a layer that is unlikely to liquefy. It can be seen that a number of highly susceptible samples have been prepared. This was further demonstrated since in two samples with $CRR < 0.1$ the shock generated by the sounding ram as it reached the end of the hydraulic jacks and was suddenly halted, was enough to trigger liquefaction of the uppermost layer, resulting in a clearly visible depression of the sand surface. It remains unclear to which depth this liquefaction occurred, as no evidence of the effect has been observed in either the CPTU or the piezometer measurements.

4.5 Conclusions and Recommendations

When loose sand samples, below the critical density, are subjected to shear deformation they contract and, if saturated, generate positive excess pore pressures. Dense contractant samples generate negative excess pore pressures, on the other hand. During regular piezocone penetration testing in sand, any excess pore pressures generated by the cone dissipate so quickly, however, that they can hardly be detected by a pressure transducer located at the shoulder of the cone. If the penetration rate, normally 20mm/s, were increased, the generated excess pore pressures would have less time to dissipate, resulting in an apparent decrease of the soil permeability as well as a speedier arrival of the pressure transducer.

In order to investigate whether a CPTU installation can be used to detect these excess pore pressures if the penetration rate is increased, a high-speed penetration rig has been developed, capable of sounding speeds up to 300mm/s. Using this rig and a regular CPTU cone, a number of tests was conducted at the regular speed of 20mm/s, as well as a speed of 200mm/s, and in sand samples of different densities.

These tests show that at regular speeds excess pore pressures between -4 and 1kPa are

recorded, with an error up to 1kPa due to uncertainties in the hydrostatic pore pressure and a reported 8kPa error due to the accuracy of the pressure transducer. Taking these errors into account, the magnitude of the measured excess pore pressures becomes unclear, but a steady 0.5 to 1kPa increase of the calculated excess pore pressure is seen in all tests over at least half a metre of sounding length.

The high-speed soundings show a greater variability in the recorded pore pressure and, as a result, in the calculated excess pore pressure. As a result of uncertainties in the depth registration during high-speed soundings, the error margin, excluding the accuracy of the transducer, is raised to 4kPa. At low densities a positive excess pore pressure up to 10kPa can be recorded, but also a 5kPa negative excess pore pressure. At high densities the calculated excess pore pressure fluctuates between 5 and -25kPa, which last value represents a substantial decrease of the pore pressure. Consequently, although a large decrease of the hydrostatic pore pressure during high-speed penetration can be equated to a high density of the sand, a measured increase of the pore pressure does not yield any information on the density of the sand, as such a measurement can be observed in the same manner in low and high density samples.

Given the large inherent error in the pressure transducer of the CPTU cone, as well as the error resulting from the depth registration and uncertainties in the hydrostatic pore pressure, a number of tests were executed with the addition of two high-precision piezometers installed in the sand bed, at points close to projected path of the CPTU cone. During penetration the excess pore pressure generated at these points, 5 and 10cm from the cone, were recorded and compared to the CPTU measurement. At low densities these piezometers show a slight increase of the pore pressure shortly before the passage of the cone with a superimposed sudden pressure drop at the passage of the cone, attributed to the contraction due to the penetration of the cone and the shear deformation of the compressed material at the cone sleeve respectively. At high densities a more or less constant decrease of the pore pressure is recorded without a sudden shear related pressure drop. In both cases the dissipation of the excess pore pressure starts almost as soon as the cone has passed, which indicates that no further effective deformation of the sand (due to skin friction) takes place, which in turn is consistent with sand in a critical state.

Although the measurements from the separate piezometers show a clear difference in behaviour at the extremes of density, the correlation with the CPTU pore pressure measurements is less clear. First of all the characteristic sudden pressure drop seen in loose sands due to shear deformation is of course completely absent from the CPTU measurement, which takes an observation at a constant time lapse relative to the passage of the cone tip. Secondly, the measurement at the cone is not always larger than that of the piezometer, especially when positive excess pore pressures are generated. The large negative excess pore pressures recorded by the cone are not seen by the piezometers on the other hand. Given the poor correspondence between the CPTU pressure transducer recording and the piezometer measurements, the piezometers have not been used to further calibrate the CPTU measurements and reduce the 8kPa error margin, which is attributed to zero-shifts and hysteresis effects.

However, even without this error the value of a high-speed CPTU sounding in order to determine the density or liquefaction potential of a sand bed remains questionable. An approximately 4kPa error remains, due to uncertainties in the depth registration and hydrostatic pore pressure. Even when the first cause could be eliminated, the second would remain, especially in field conditions. Given the magnitude of the observed excess pore pressures at intermediate densities, where a precise determination of the liquefaction potential would be of most value, an overall precision of 2kPa or better would be required. At low or high densities the determination of CRR from a regular CPT, using one of the methods described in literature, would be accurate enough for engineering purposes and little extra information would be required.

This estimated 2kPa error margin should then include the zero-shift and hysteresis effects of the pressure transducer, the uncertainty in the hydrostatic pore pressure of the investigated layer as well as the error in the depth registration resulting from the deviations of the cone from the straight vertical, to name but a few. Without additional measurements of the hydrostatic pore pressure a 1kPa or 10cm water column error in the piezometric head seems difficult to exclude in field conditions. Similar arguments can be found for the other error sources, given the accuracies of current CPTU cones, resulting in a 4kPa or worse expected error margin at best, given regular sounding equipment.

Given this observation, the continuation of similar research should first focus on the development of a measuring device with high enough precision and an in-built measurement of the hydrostatic pore pressure. The calibration of such a device in laboratory conditions would then possibly require calibration chamber tests at far better controlled densities and at higher stress levels. In case a calibration chamber with a pressurised top boundary is used for this purpose, care must be taken that the boundary conditions do not influence the measurements, in particular where it concerns the dissipation behaviour of the excess pore pressure.

Overall, it can be concluded that the generally accepted view of the penetration process, i.e. first the soil is compressed by the penetration of the cone, resulting in excess pore pressures in the displaced material, thenSubsequqnel the soil directly around the shaft is subjected to a localised shear deformation, resulting in general in a negative excess pore pressure until the critical state is reached, shows up in these test results. However, given the inherent errors in the CPTU measurement and the fact that his measurement is made at a fixed location (i.e. time span) after the passage of the cone tip, no meaningful determination of the density of the sand or its liquefaction potential can be made.

There was a point to this story, but it has temporarily escaped the chronicler's mind.

Douglas Adams: So Long, and Thanks for All the Fish

Chapter 5

Conclusions and Recommendations

For a well-controlled tunnel boring process it is first necessary to establish reliable minimal and maximal allowable support pressures at the face and secondly not to exceed those limits. If either of these requirements is not met, an instability of the face may occur, leading to disturbances of the tunnel boring process and (increased) deformation of the soil. This in turn can lead to cost increases or damage to surface structures.

In a slurry-shield tunnelling method a bentonite slurry is used to condition the face and transfer the support pressure onto the soil skeleton. To this end the slurry infiltrates the soil. In an earth-pressure-balance shield foam or other additives may be used in order to lower the permeability and water content of the soil. To reach this goal the foam must infiltrate the soil in front of the TBM and displace the pore water present there. In both cases this infiltration will cause excess pore pressures and a groundwater flow in front of the tunnel face. This infiltration process and the resulting excess pore pressures lower the stability of the face and increase the minimal required support pressure.

A face stability model has been developed which takes the effects of slurry or foam infiltration, groundwater flow and excess pore pressures into account. This model has been based on a wedge stability limit equilibrium model, in which a number of aspects have been included:

- The soil above and in front of the face may be heterogeneous, schematised as horizontal layers. For each layer separate properties can be taken into the calculation, although only the support force for the entire wedge is calculated.
- The load acting on top of the wedge is less than the full weight of the overburden, as part of this load is transferred by friction forces to the surrounding soil. This soil arching effect is modelled using Terzaghi's arching formulae for a full three-dimensional soil silo, resulting in an arching relaxation length $a = R/(1 + \tan\theta)$.
- The friction forces on the triangular side planes of the wedge are calculated from the effective vertical stress, without arching effects, using a coefficient of neutral effective stress K_0 for the best correspondence with results from centrifuge tests. The minimal support pressure calculated in this way indicates the pressure at which total failure has occurred.
- For a more conservative estimate of the minimal support pressure, at which only limited deformation is believed to take place, the arching relaxation length $a = R$ is implemented. This model yields higher minimal required support pressures and comparison with centrifuge and field measurements shows that at these support pressures collapse of the face does not occur, excluding cases where it is triggered by different mechanisms.

- During excavation the filter cake that forms at the face is constantly removed by the cutter bits of the TBM and directly after it is removed starts to build up again. This results in a continuous infiltration process which has been averaged over the face. Over the average infiltration length calculated in this way, part of the support pressure is transferred onto the soil skeleton. The remaining pressure is used as input for a groundwater flow calculation, modelling the tunnel face as a source.
- The resulting excess pore pressures in front of the face lower the effective stresses and thereby lower the friction forces acting on the wedge. The excess pore pressures also lift the soil on top of the wedge, reducing the load on top of the wedge.
- As a result of the excess pore pressure in front of the wedge, the pore water pressure to be countered by the support pressure increases or, alternatively, the effective support pressure decreases. To counter this effect an increased support pressure may be needed.

Using this model a parameter study has been executed. The results have been compared to measurements obtained at several recent tunnel boring projects in the Netherlands, as well as to calculations made with a stability model which does not include the effects of infiltration and excess pore pressures. This study shows that the excess support pressure, the difference between the support pressure and the pore pressure in rest, calculated with the new model including infiltration, can easily be four times higher than calculated with a model not including infiltration effects. This can in part explain the relatively large (partial) safety factors used in current engineering practice for the calculation of minimal support pressures.

This study also shows that the severity of the infiltration depends strongly on the leakage length or permeability of the soil, which parameters are related to each other, and that the influence is strongest for sandy soils with permeabilities $10^{-5} < k < 10^{-3}$ m/s. Outside this range the effects of infiltration and groundwater flow are reduced or partly cancel each other, reducing the overall impact on the minimal support pressure. The stability model, as formulated here, automatically deals with these effects, and as a result can be used equally well in situations where infiltration is a dominant influence as in situations where it is negligible.

Stationary and transient groundwater calculations, using the excess pore pressures calculated with the stability model as input, can be used to predict the generation of excess pore pressures in the vicinity of the TBM. The pore pressures measured using piezometers installed in the ground in front of the TBM at several locations show a very good correspondence with these predictions. Such measurements give a clear indication of the infiltration effect and, in combination with a measurement of the support pressure in the working chamber of the TBM, of the pressure drop over the filter cake at the excavation face. This is an indication for the thickness and quality of the filter cake and can be used as an indication of the quality of the control over the boring process.

The determination of the maximal allowable support pressure, in case the support medium infiltrates the soil and causes excess pore pressures, is less clear than the determination of the minimal support pressure. To limit the maximal allowable support pressure to the vertical total stress (at the top of the TBM) seems a safe, although overly conservative, estimate under normal conditions. It is clear that a large safety margin remains, but there (fortunately) is not enough field data to establish a more reliable upper bound to the allowable support pressures.

During the boring process, additional information about the soil in front of the TBM can be obtained, using sensors fixed on or originating from the TBM. This information may be used to fine-tune the boring process, for example in order to reduce settlements. One of the suggested

techniques is the use of a cone penetration test in a horizontal direction, named Horizontal Cone Penetration Testing (HCPT).

The main difference between normal (vertical) CPT and HCPT lies in the stress states perpendicular and parallel to the penetration direction of the cone. In vertical penetration the undisturbed stress acting in the penetration direction is the vertical effective stress. A uniform radial stress equal to the horizontal effective stress acts in the plane perpendicular to the penetration direction. In horizontal penetration the parallel stress is equal to the horizontal effective stress, whereas the perpendicular stress is not radially uniform, but varies between the horizontal and vertical effective stress.

Models for the interpretation of cone penetration testing cannot or at best approximately deal with this non-radially-uniform perpendicular stress state and, as a result, are not suitable for the interpretation of HCPT. It is also unclear how the penetration direction may influence the failure mechanism occurring around the cone. To this end a number of laboratory tests was performed.

In a 2m diameter calibration chamber a number of tests were performed on sand samples at different densities and with differently graded sands. In all cases one horizontal and one or more vertical tests were performed in the same sample. The cone resistance and sleeve friction measured at the depth of the horizontal sounding in the vertical sounding were compared to those of the horizontal sounding. From these tests it follows that the ratio of horizontal over vertical cone resistance depends on the relative density of the sand, and that for low or high densities the ratio is approximately equal to one, whereas for intermediate densities it rises to 1.2. The grain size distribution of the sand does not seem to influence this ratio.

The ratio of horizontal over vertical sleeve friction on the other hand is not dependent on the density of the sample, but does vary significantly when sands with different grain size distributions are used. For different sands, ratios between 1.3 and 0.65 are found, but there is no clear relation with the characteristic grain size of the sand. On average the horizontal sleeve friction is lower than the vertical, but it reacts more strongly to changes in the grain size distribution and fines content. The changes are not linear however, and no simple relation with grain size has been found. It also remains unclear how different soil types will influence the horizontal sleeve friction.

To further investigate the differences between horizontal and vertical CPT, a number of model tests were performed, showing the qualitative differences in the failure mechanisms and stress states around the cone for both sounding directions. Also a simple analytical model has been derived, based on elastic cavity expansion theory, to calculate the ratio of horizontal over vertical cone resistance. This model predicts that horizontal cone resistance is larger than vertical for normally consolidated soils.

As the laboratory tests are restricted to tests in sand samples and the amount of field experience with HCPT is limited, there is insufficient data to establish a correlation between horizontal and vertical CPT results for all soil types, or directly between HCPT results and soil properties. Given the limited differences it is clear however, that HCPT can be interpreted with the same reliability as vertical CPT, given enough data from different soil types.

During a cone penetration test not only the cone resistance and sleeve friction can be measured, but if a piezocone is used, the pore pressures around the cone can also be measured. In soils with low permeability the excess pore pressures generated by the penetration process are measured in this way. In permeable sand layers no excess pore pressures are detected, even though they are initially generated, as they dissipate too quickly.

If however the penetration rate of the CPTU is increased, it should be possible to detect

excess pore pressures under these conditions before they have fully dissipated. Also, in loose, contractant, sands positive excess pore pressures may be expected due to the penetration of the cone, whereas in dense, dilatant, sands negative excess pore pressure are to be expected. In this way the high-speed CPTU may be used to measure the sand density and to get an indication of the liquefaction potential of the sand.

In order to test this hypothesis, high-speed CPTU tests were performed in the 2m diameter calibration chamber on sands at different densities. The excess pore pressures measured by the piezocone were compared to measurements obtained by two piezometers installed in the sand bed close to the path of the cone. These tests show that the variation in the excess pore pressures measured at the cone shoulder is large. Although large negative excess pore pressures at the cone are only measured in dense sands, positive excess pore pressures, as well as small negative excess pore pressures, are measured at this location for all densities investigated, and may fluctuate strongly. No clear relation between the measured excess pore pressure and the sand density is found.

The measurements from the piezometers installed in the sand bed show that this may in part be caused by the large negative pore pressures generated in the shear band surrounding the cone and rods, dominating the pore pressures generated in loose sands. The measurements are also complicated by the fact that the errors resulting from uncertainties in the hydrostatic pore pressure, the depth registration and the accuracy of the piezocone pressure transducer, are of the same order as the measurements. The overall result of these complications is that no meaningful determination of the sand density can be made using a high-speed CPTU and that the liquefaction potential should be determined using a q_c -CRR correlation.

'Read it?' Good God. It's bad enough to write such a thing.

R.A. Heinlein: Stranger in a Strange Land

Bibliography

- [1] M.Y. Abu-Farsakh, G.Z. Voyiadjis, and M.T. Tumay. Numerical analysis of the miniature piezocone penetration tests (PCPT) in cohesive soils. *International Journal for Numerical and Analytical Methods in Geomechanics*, 22:791–818, 1998.
- [2] H. Akagi and K. Komiya. Finite element simulation of shield tunneling processes in soft ground. In Mair and Taylor [111], pages 447–452.
- [3] H.G.B. Allersma. *Optical Analysis of Stress and Strain in Photoelastic Particle Assemblies*. PhD thesis, Delft University of Technology, 1987.
- [4] H.G.B. Allersma. Simulation of the trap-door problem in a geotechnical centrifuge. In *Mechanics of Jointed and Vaulted Rock*, pages 521–526, Rotterdam, 1995. Balkema.
- [5] H.G.B. Allersma. Using imaging technologies in experimental geotechnics. In *Imaging Technologies*, pages 1–9. ASCE, 1997.
- [6] G. Anagnostou and K. Kovári. The face stability of slurry-shield-driven tunnels. *Tunneling and Underground Space Technology*, 9(2):165–174, 1994.
- [7] G. Anagnostou and K. Kovári. Face stability conditions earth-pressure-balanced shields. *Tunneling and Underground Space Technology*, 11(2):165–173, 1996.
- [8] G. Anagnostou and K. Kovári. Face stability in slurry and EPB shield tunneling. In Mair and Taylor [111], pages 453–458.
- [9] L. Anheuser. Tunnelvortriebsanlagen mit flüssigkeitsgestützter Ortsbrust. *Bautechnik*, 64(11), November 1987.
- [10] P. Aristaghes, F. Berbet, and P. Michelon. CATSBY: Collapse real-time prevention system for slurry tunnel boring machines in soft ground. In Mair and Taylor [111], pages 245–250.
- [11] J.H. Atkinson, E.T. Brown, and D.M. Potts. Ground movements near shallow model tunnels in sand. In Geddes [72], pages 372–386.
- [12] J.H. Atkinson, T.L.L. Orr, and D.M. Potts. Research studies into the behaviour of tunnels and tunnel linings in soft ground. Technical Report 176 UC, Transport and Road Research Laboratory, 1975.
- [13] J.H. Atkinson and D.M. Potts. Stability of a shallow circular tunnel in cohesionless soil. *Géotechnique*, 27(2):203–215, 1977.

- [14] P.B. Attewell. Ground movements caused by tunneling in soil. In Geddes [72], pages 812–948.
- [15] S. Babendererde. Tunnelvortrieb bei partiell schwierigem Gebirgsverhalten. Ereignis und Bewältigung auf Baustellen mit Tunnelbohrmaschinen und Schilden. In *Tunnelvortrieb bei partiell schwierigem Gebirgsverhalten*, pages 139–150. Ruhr-Universität Bochum, June 1987.
- [16] S. Babendererde and J. Holzhäuser. Ondersteuning van het boorfront door verhoogde luchtdruk bij het vloeistofschild. *Geotechniek*, 4(2):36–43, April 2000.
- [17] M. Backus. Tunnel face stability in Dutch soil. Master's thesis, Delft University of Technology, 1998.
- [18] K.J. Bakker, F. de Boer, and J.B.M. Admiraal. Monitoring the Second Heinenoord tunnel and the Botlek Rail tunnel, two independent research programs on bored tunneling in soft soil. In Kusakabe et al. [100], pages 191–196.
- [19] K.J. Bakker, F. de Boer, and J.C. Kuiper. Extensive independent research programs on Second Heinenoord tunnel and Botlek Rail tunnel. In Barends et al. [25], pages 1969–1978.
- [20] K.J. Bakker, W. van Scheldt, and J.W. Plekkenpol. Predictions and a monitoring scheme with respect to the boring of the Second Heinenoord tunnel. In Mair and Taylor [111], pages 459–464.
- [21] M.M. Baligh. Strain path method. *ASCE Journal of Geotechnical Engineering*, 111(9):1108–1136, September 1985.
- [22] M.M. Baligh and J.N. Levaudoux. Consolidation after undrained penetration. II: Interpretation. *ASCE Journal of Geotechnical Engineering*, 112(7):727–745, July 1986.
- [23] H. Balthaus. Standsicherheit der flüssigkeitsgestützten Ortsbrust bei schildvorgetriebenen Tunneln. In J. Scheer, H. Ahrens, H.J. Bargstädt, and H. Duddeck, editors, *Festschrift Heinz Duddeck*, pages 477–492, Braunschweig, 1988. Institut für Statik, TU Braunschweig.
- [24] H. Balthaus. Tunnel face stability in slurry shield tunneling. In of XII ICSMF [130], pages 775–778.
- [25] F.B.J. Barends, J. Lindenberg, H.J. Luger, L. de Quelerij, and A. Verruijt, editors. *Geotechnical Engineering for Transportation Infrastructure*, Rotterdam, 1999. Balkema.
- [26] C. Becker. Galleria Aurelia Roma – Europe's largest hydroshield. In M. Legrand, editor, *Le Creusement des Tunnels en Terrains Meubles et Aquifères*, pages 69–72, Rotterdam, 1985. Balkema.
- [27] K. Been, J.H.A. Crooks, and L. Rothenburg. A critical appraisal of CPT calibration chamber tests. In Ruiter [145], pages 651–660.
- [28] E.E. de Beer. Données concernant la résistance au cisaillement déduites des essais de pénétration en profondeur. *Géotechnique*, 1(1):22–39, June 1948.

- [29] H.K.S.Ph. Begemann. The Dutch Static Penetration Test with the adhesion jacket cone. *LGM Mededelingen*, XII(4):69–100, April 1969.
- [30] B. Belter, W. Heiermann, R. Katzenbach, B. Maidl, H. Quick, and W. Wittke. NBS Köln-Rhein/Main - Neue Wege bei der Umsetzung von Verkehrsprojekten. *Bauingenieur*, 74(1):1–7, January 1999.
- [31] K.F.C.M. Benders. De dilatoconus. Master's thesis, Delft University of Technology, 1999.
- [32] P. van den Berg. *Analysis of Soil Penetration*. PhD thesis, Delft University of Technology, 1994.
- [33] A. Bezuijen. Waterspanningen voor boorfront. Technical Report CO-372590/146, Delft Geotechnics, 1998.
- [34] A. Bezuijen and M. Huisman. Afpleistering en mudspurt tijdens boren. Technical Report 27, Boren Tunnels en Leidingen, 1997.
- [35] A. Bezuijen, M. Huisman, and D.R. Mastbergen. Verdringingsprocessen bij gestuurd boren. Technical Report 17, Boren Tunnels en Leidingen, 1996.
- [36] A. Bezuijen and P.P.T. Litjens. Eerste orde evaluatie K100 BT-A boorfrontstabiliteit. Technical Report CO-384780/19, Delft Geotechnics, 1999.
- [37] A. Bezuijen and C.A. Messemaeckers-van de Graaf. Stabiliteit van het graaffront bij vloeistofondersteuning. Technical Report 33, Boren Tunnels en Leidingen, 1997.
- [38] A. Bezuijen, P.E.L. Schamine, and J.A. Kleinjan. Additive testing for earth pressure balance shields. In Barends et al. [25], pages 1991–1996.
- [39] A. Bezuijen, S.J.M. van Eekelen, and B. Berkhout. Stabiliteit afpleistering. Technical Report 26, Boren Tunnels en Leidingen, 1997.
- [40] R.P. Boeije. K300 geotechniek basis parameterset. Technical Report K300-W-005, Centrum Ondergronds Bouwen, April 1999.
- [41] R. de Borst. Calculation of collapse loads using higher order elements. In *Proc. IUTAM Conf. on Deformation and Failure of Granular Materials, Delft*, pages 503–513. Balkema, 1982.
- [42] R. de Borst and P.A. Vermeer. Finite element analysis of static penetration tests. In Verruijt et al. [169], pages 457–462.
- [43] R. de Borst and P.A. Vermeer. Possibilities and limitations of finite elements for limit analysis. *Géotechnique*, 34(2):199–210, 1984.
- [44] Centrum Ondergronds Bouwen. Parameterset voor de predicties. Technical Report K100-W-004, Centrum Ondergronds Bouwen, 1996.
- [45] O. Braach. Risiken und Chancen beim mechanisierten Tunnelbau. In *Forschung + Praxis 34: Tunnelbau - Neue Chancen aus europäischen Impulsen*, pages 41–45, Düsseldorf, 1992. STUVA, Alba.

- [46] W. Broere. Berekeningen waterspanningen voor boorfront Leidingentunnel onder de Oude Maas, Rotterdam. Technical report, Delft University of Technology, May 1999.
- [47] W. Broere and B. Polen. Risico's en storingen bij geboorde tunnels. Technical Report 02, Delft University of Technology/Centrum Ondergronds Bouwen, 1996.
- [48] B.B. Broms and H. Bennermark. Stability of clay at vertical openings. *Journal of the Soil Mechanics and Foundations Division*, 93(1):71–94, January 1967.
- [49] G.A. Bruggeman. *Analytical Solutions in Geohydrological Problems*. Elsevier, 1999.
- [50] B. Bruinsma. Horizontaal sonderen. Master's thesis, Delft University of Technology, 1997.
- [51] BTC/NS-RIB. Waterspanningsmeting MQ1, 2000. Personal Communication.
- [52] P. de Buhan, A. Cuvillier, L. Dormieux, and S. Maghous. Face stability of shallow circular tunnels driven under the water table: A numerical analysis. *International Journal for Numerical and Analytical Methods in Geomechanics*, 23:79–95, 1999.
- [53] S.E. Burns and P.W. Mayne. Monotonic and dilatatory pore-pressure decay during piezocone tests in clay. *Canadian Geotechnical Journal*, 35:1063–1073, 1998.
- [54] S.E. Burns and P.W. Mayne. Pore pressure dissipation behaviour surrounding driven piles and cone penetrometers. *Transportation Research Record*, 1675:17–23, 1999.
- [55] M. Calvello and R.N. Taylor. Centrifuge modelling of a spile-reinforced tunnel heading. In Kusakabe et al. [100], pages 345–350.
- [56] R.G. Campanella and P.K. Robertson. Current status of the piezocone test. In Ruiter [145], pages 93–116.
- [57] J. Canou, M. El Hachem, A. Kattan, and I. Juran. Mini piezocone (M-CPTU) investigation related to sand liquefaction analysis. In Ruiter [145], pages 699–706.
- [58] J.P. Carter, J.R. Booker, and S.K. Yeung. Cavity expansion in cohesive frictional soils. *Géotechnique*, 36(3):349–358, 1986.
- [59] C. Cassinis, P. Nisio, and V. Capata. Settlement and face stability boring a large tunnel. In Publications Committee of XI ICSMF, editor, *Proceedings of the Eleventh International Conference on Soil Mechanics and Foundation Engineering*, pages 2057–2062, Rotterdam, 1985. Balkema.
- [60] P. Chambon and J.F. Corté. Shallow tunnels in cohesionless soil: Stability of tunnel face. *ASCE Journal of Geotechnical Engineering*, 120:1148–1165, 1994.
- [61] Z. Cheng-Hou, G. Greeuw, J. Jekel, and W. Rosenbrand. A new classification chart for soft soils using the piezocone test. *Engineering Geology*, 29:31–47, 1990.
- [62] COB Commissie L510. Inventarisatie ontwerpmethoden boortunnels voor weg- en railverbindingen. Technical Report L510-01, COB, 1996.
- [63] E.H. Davis, M.J. Gunn, R.J. Mair, and H.N. Seneviratne. The stability of shallow tunnels and underground openings in cohesive material. *Géotechnique*, 30(4):397–416, 1980.

- [64] J.K. van Deen. Zoeken naar obstakels in de bodem. *Land+Water*, pages 20–21, 1995.
- [65] J.K. van Deen. De ondergrond doorzien. *COB Nieuws*, pages 9–11, December 1997.
- [66] J.K. van Deen. Deelproject L320 horizontaal wegdrukken en sonderen, deelactiviteit 2.1 fase 1. Technical Report CO-371940/15, Delft Geotechnics, April 1997.
- [67] J.K. van Deen. Grondonderzoek ondergronds: De prikneus en speurneus. *COB Nieuws*, 1(27):8–9, March 1999.
- [68] J.K. van Deen, G. Greeuw, R. van den Hondel, M.Th. van Staveren, F.J.M. Hoefsloot, and B. Vanhout. Horizontal CPTs for reconnaissance before the TBM front. In Barends et al. [25], pages 2023–2030.
- [69] T. Domon, T. Konda, K. Nishimura, and M. Matsui. Model tests on face stability of tunnels in granular material. In Negro Jr. and Ferreira, editors, *Tunnels and Metropolises*, pages 229–234, Rotterdam, 1998. Balkema.
- [70] H.T. Durgunoglu and J.K. Mitchell. Static penetration resistance of soils: I — Analysis. In N.N., editor, *In Situ Measurement of Soil Properties*, pages 151–189. A.S.C.E., June 1975.
- [71] K. Fujita and Kusakabe, editors. *Underground Construction in Soft Ground*, Rotterdam, 1995. Balkema.
- [72] J.D. Geddes, editor. *Large Ground Movements and Structures*, London, 1978. Pentech Press.
- [73] J. Greenhouse, P. Pehme, D. Coulter, and Q. Yarie. Trends in geophysical site characterization. In Robertson and Mayne [143], pages 23–34.
- [74] D.J. Hagerty. Piping/sapping erosion. II: Identification-diagnosis. *Journal of Hydraulic Engineering*, 117(8):1009–1025, 1991.
- [75] T. Hashimoto, K. Hayakawa, K. Kurihara, T. Nomoto, M. Ohtsuka, and T. Yamazaki. Some aspects of ground movement during shield tunneling in Japan. In Mair and Taylor [111], pages 683–688.
- [76] F.R.O. Hekman. De verhouding tussen de schachtwrijving van een gedrukte en een getrokken paal. Master's thesis, Delft University of Technology, 1995.
- [77] R. Hill. *The Mathematical Theory of Plasticity*. Oxford University Press, Oxford, 1950.
- [78] M. Hisatake, T. Eto, and T. Murakami. Stability and failure mechanisms of a tunnel face with a shallow depth. In T. Fujii, editor, *Proceedings of the 8th Congress of the International Society for Rock Mechanics*, pages 587–591. International Society for Rock Mechanics, 1995.
- [79] L. van Hoogevest. Verdichting van losgepakt zand door doorstroming met water. Master's thesis, Delft University of Technology, February 1985.
- [80] N. Horn. Horizontaler Erddruck auf senkrechte Abschlussflächen von Tunnelröhren. In *Landeskongress der Ungarischen Tiefbauindustrie*, pages 7–16, November 1961.

- [81] G.T. Houlsby and R. Hitchman. Calibration chamber tests of a cone penetrometer in sand. *Géotechnique*, 38(1):39–44, 1988.
- [82] J. Huder. Stability of bentonite slurry trenches with some experiences in Swiss practice. In *Fifth ECSMFE, Madrid*, volume 1, pages 517–522, 1972.
- [83] M. Huisman. Meetrapport consistentie boorvloeistof. Technical Report 18, Boren Tunnels en Leidingen, 1996.
- [84] M. Huisman. Theorie en proeven statische afpleistering. Technical Report 34, Boren Tunnels en Leidingen, 1998.
- [85] M. Huisman and A.M. Talmon. Verandering consistentie boorvloeistof. Technical Report 30, Boren Tunnels en Leidingen, 1997.
- [86] M. Hutteman and E.A.H. Teunissen. Palenproef. *COB Nieuwsbrief*, 1(2), July 1997.
- [87] M. Jamiolkowski, V.N. Ghionna, R. Lancelotta, and E. Pasqualini. New correlations of penetration tests for design practice. In Ruiter [145], pages 263–296.
- [88] S. Jancsecz. Modern shield tunneling in the view of geotechnical engineering: A reappraisal of experience. In of XIV ICSMFE [131], pages 1415–1420.
- [89] S. Jancsecz and W. Steiner. Face support for a large mix-shield in heterogenous ground conditions. In *Tunneling '94*, London, 1994. Institution of Mining and Metallurgy.
- [90] K. Joustra and J.G. de Gijt. Results and interpretation of cone penetration tests in soils of different mineralogic composition. In Verruijt et al. [169], pages 615–626.
- [91] W.G.B. te Kamp. The influence of the rate of penetration on the cone resistance ' q_c ' in sand. In *Proceedings of the Second European Symposium on Penetration Testing*, pages 627–633, Rotterdam, 1982. Balkema.
- [92] S. Kanayasu, I. Kubota, and N. Shikibu. Stability of face during shield tunneling – A survey of Japanese shield tunneling. In Fujita and Kusakabe [71], pages 337–343.
- [93] M. Kilchert and J. Karstedt. *Schlitzwände als Trag- und Dichtungswände, Band 2, Stand-sicherheitberechnung von Schlitzwänden*, pages 28–34. DIN, Berlin, 1984.
- [94] T. Kimura and R.J. Mair. Centrifugal testing of model tunnels in soft clay. In of X. ICSMFE [129], pages 319–322.
- [95] J.A. Kleinjan. Leidingentunnel Oude Maas. Resultaten kennisproject. Technical Report 98-052/A, Gemeentewerken Rotterdam, 1999.
- [96] F. Kleist and T. Strobl. Die Fließgrenze von Schmalwandsuspensionen und die Auslaufzeit aus dem Marsh-Trichter. *Geotechnik*, 21(2):97–102, 1998.
- [97] K.M.S.K. Kosgoda. Horizontal soil investigation using cone penetration test (HCPT) in sandy soil. Master's thesis, International Institute for Hydraulics and Environmental Engineering, Delft, February 2000.
- [98] T. Krause. *Schildvortrieb mit flüssigkeits- und erdgestützter Ortsbrust*. PhD thesis, Technischen Universität Carolo-Wilhelmina, Braunschweig, 1987.

- [99] E. Kreyszig. *Advanced Engineering Mathematics*. John Wiley & Sons, 1993.
- [100] O. Kusakabe, K. Fujita, and Y. Miyazaki, editors. *Geotechnical Aspects of Underground Construction in Soft Ground*. Balkema, 2000.
- [101] E.A. Kwast and J.W. Plekkenpol. Deformaties van de grond, spanningsveranderingen in de omgeving en gronddrukken op de tunnelling. Interim report K100-W-002, Bouwdienst Rijkswaterstaat: Projectbureau Boortunnels, November 1995.
- [102] COB L320. Horizontaal sonderen met de prikneus, Europaterminal Antwerpen. Technical Report L320-05, Centrum Ondergronds Bouwen, 1999.
- [103] COB L500. L500 toetsingsrichtlijn voor het ontwerp van boortunnels voor weg- en railinfrastructuur. Technical report, Centrum Ondergronds Bouwen, 2000.
- [104] G. de Lange. Additioneel grondonderzoek Tweede Heinenoordtunnel. Technical Report K100-W-006, Centrum Ondergronds Bouwen, 1995.
- [105] G. de Lange, J.K. Haasnoot, and F.W.J. van Vliet. Additioneel grondonderzoek II. Boorvloeistof, Tweede Heinenoordtunnel. Final report K100-W-027, Delft Geotechnics, March 1996.
- [106] E. Leca and L. Dormieux. Upper and lower bound solutions for the face stability of shallow circular tunnels in frictional material. *Géotechnique*, 40(4):581–606, 1990.
- [107] J.N. Levaux and M.M. Baligh. Consolidation after undrained piezocone penetration. I: Prediction. *ASCE Journal of Geotechnical Engineering*, 112(7):707–726, July 1986.
- [108] T. Lunne, P.K. Robertson, and J.J.M. Powell. *Cone Penetration Testing in Geotechnical Practice*. Blackie, London, 1997.
- [109] B. Maidl, M. Herrenknecht, and L. Anheuser. *Mechanised Shield Tunnelling*. Ernst, Berlin, 1996.
- [110] R.J. Mair. Design and construction of tunnels in soft ground. In Barends et al. [25], pages 1915–1921.
- [111] R.J. Mair and R.N. Taylor, editors. *Geotechnical Aspects of Underground Construction in Soft Ground*, Rotterdam, 1996. Balkema.
- [112] R.J. Mair and R.N. Taylor. Theme lecture: Bored tunnelling in the urban environment. In of XIV ICSMFE [131], pages 2353–2385.
- [113] S. Marchetti. In situ tests by flat dilatometer. *ASCE Journal of Geotechnical and Environmental Engineering*, 109:299–321, March 1980.
- [114] S. Marchetti. Detection of liquefiable sand layers by means of quasi-static penetration tests. In Verruijt et al. [169], pages 689–695.
- [115] W. Meyer, R.L. Schuster, and M.A. Sabot. Potential for seepage erosion of landslide dam. *ASCE Journal of Geotechnical Engineering*, 120(7):1211–1229, 1994.
- [116] J.K. Mitchell and T.L. Brandon. Analysis and use of CPT in earthquake and environmental engineering. In Robertson and Mayne [143], pages 69–97.

- [117] M. Mohkam and C. Bouyat. Le soutènement liquide - dispositif de simulation d'un bouclier à pression de boue. In *International Congress AFTES*, pages 85–95, 1984.
- [118] M. Mohkam and C. Bouyat. Research studies for slurry shield tunneling. In *4th International Conference of the Institution of Mining and Metallurgy*, pages 235–241, 1985.
- [119] M. Mohkam and Y.W. Wong. Three dimensional stability analysis of the tunnel face under fluid pressure. In G. Swoboda, editor, *Numerical Methods in Geomechanics*, pages 2271–2278, Rotterdam, 1989. Balkema.
- [120] A. Mori, K. Kurihara, and H. Mori. A study on face stability during slurry type shield tunneling. In Fujita and Kusakabe [71], pages 261–264.
- [121] A. Mori, M. Tamura, K. Kurihara, and H. Shibata. A suitable slurry pressure in slurry-type shield tunneling. In G.E. Pearse, editor, *Tunneling '91*, pages 361–369, London, 1991. Institution of Mining and Metallurgy.
- [122] F.J.H. Mouwen. Mixing in the slurry chamber of a hydrosshield. Master's thesis, Delft University of Technology, March 1997. Fac. of Mech. Eng., Dep. of Dredging Tech.
- [123] H. Müller-Kirchenbauer. Stability of slurry trenches in inhomogeneous subsoil. In N.N., editor, *9th International Conference on Soil Mechanics and Foundation Engineering*, pages 125–132, 1977.
- [124] N.I. Muskhelishvili. *Some Basic Problems of the Mathematical Theory of Elasticity*. Noordhof, Leiden, 4th edition, 1954.
- [125] N. Nanninga. Foundation engineering. Technical report, Delft University of Technology, ca. 1970.
- [126] H. Netzel and F.J. Kaalberg. Numerical damage risk assessment studies on masonry structures due to TBM-tunneling in Amsterdam. In Kusakabe et al. [100]. preprints pp. 235–244.
- [127] R.E.P. de Nijs. Verweking van grond aan het boorfront. Master's thesis, Delft University of Technology, 1996.
- [128] Adviesbureau Noord/Zuidlijn. Palenproef. *COB Nieuws*, 1(18), April 1998.
- [129] Publications Committee of X. ICSMFE, editor. *Proceedings of the 10th International Conference on Soil Mechanics and Foundation Engineering*, Stockholm, Rotterdam, 1981. Balkema.
- [130] Publications Committee of XII ICSMFE, editor. *Proceedings of the 12th International Conference on Soil Mechanics and Foundation Engineering*, Sao Paolo, 1989.
- [131] Publications Committee of XIV ICSMFE, editor. *Proceedings of the Fourteenth International Conference on Soil Mechanics and Foundation Engineering*, Rotterdam, 1997. Balkema.
- [132] R.S. Olsen. Using the CPT for dynamic site response characterization. In J.L. Von Thun, editor, *Earthquake Engineering and Soil Dynamics II – Recent Advances in Ground-Motion Evaluation*, number 20 in Geotechnical Special Publication, pages 374–388. ASCE, 1988.

- [133] Committee on Earthquake Engineering. Liquefaction of soils during earthquakes. Technical report, National Research Council, 1985.
- [134] A.K. Parkin. The calibration of cone penetrometers. In Ruiters [145], pages 221–243.
- [135] A.K. Parkin and T. Lunne. Boundary effects in the laboratory calibration of a cone penetrometer for sand. In Verruijt et al. [169], pages 761–768.
- [136] F. Pellet, F. Descoedres, and P. Egger. The effect of water seepage forces on the face stability of an experimental microtunnel. *Canadian Geotechnical Journal*, 30:363–369, 1993.
- [137] R. Peters. Boorfrontstabiliteit van een DOT-tunnel in slappe grond. Master's thesis, Delft University of Technology, 1999.
- [138] E.G. Prater. Die Gewölbewirkung der Schlitzwände. *Der Bauingenieur*, 48:125–131, 1973.
- [139] J.L. van der Put. Samenvatting berekeningen boortunnel 2e-Heinenoord. Technical Report 1933-T-962150, Rijkswaterstaat, 1996.
- [140] J.L. van der Put. Evaluatie boorfrontstabiliteit. *COB Nieuwsbrief*, 1(4), May 1998.
- [141] P.K. Robertson. Personal communication, 1998.
- [142] P.K. Robertson and C.E. Fear. Liquefaction of sands and its evaluation. In K. Ishihara, editor, *Earthquake Geotechnical Engineering*, pages 153–1289. Balkema, November 1995.
- [143] P.K. Robertson and P.W. Mayne, editors. *Geotechnical Site Characterization*. Balkema, 1998.
- [144] M.P. Romo and C. Diaz. Face stability and ground settlement in shield tunneling. In of X. ICSMFE [129], pages 357–360.
- [145] J. de Ruiters, editor. *Penetration Testing 1988*, Rotterdam, 1988. Balkema.
- [146] R. Salgado, J.K. Mitchell, and M. Jamiolkowski. Cavity expansion and penetration resistance in sand. *ASCE Journal of Geotechnical and Geoenvironmental Engineering*, pages 344–354, April 1997.
- [147] R. Salgado, J.K. Mitchell, and M. Jamiolkowski. Calibration chamber size effects on penetration resistance in sand. *ASCE Journal of Geotechnical and Geoenvironmental Engineering*, 124:878–888, September 1998.
- [148] G. Sanglerat. *The Penetrometer and Soil Exploration*. Elsevier, Amsterdam, 1972.
- [149] E. Santoyo. Use of a static penetrometer in a softground tunnel. In *Penetration Testing*, pages 835–839, Rotterdam, 1982. Balkema.
- [150] J.H. Schmertmann. Measurement of in situ shear strength. In *ASCE Specialty Conference on In Situ Measurements of Soil Properties*, volume II, pages 57–138, New York, 1975. ASCE.
- [151] F.P. Smits. Cone penetration tests in dry sand. In Verruijt et al. [169], pages 877–881.

- [152] M.Th.J.H. Smits and B. de Ruiter. Hoe schadelijk zijn trillingen door (ondergrondse) bouwactiviteiten? *Geotechniek*, 2(2):11–17, April 1998.
- [153] V.V. Sokolovskii. *Statics of Granular Media*. Pergamon Press, London, 1965.
- [154] T.D. Stark and S.M. Olson. Liquefaction resistance using CPT and field case histories. *ASCE Journal of Geotechnical and Geoenvironmental Engineering*, 121(12):856–869, December 1995.
- [155] W. Steiner. Slurry penetration into coarse grained soils and settlements from large slurry shield tunnel. In Mair and Taylor [111], pages 329–333.
- [156] R. Sternath and Th. Baumann. Face support for tunnels in loose ground. In J. Golser, W.J. Hinkel, and W. Shubert, editors, *Tunnels for People*, pages 317–323, Rotterdam, 1997. Balkema.
- [157] O.D.L. Strack. *Groundwater Mechanics*. Prentice Hall, 1989.
- [158] J.P. Sully, P.K. Robertson, R.G. Campanella, and D.J. Woeller. An approach to evaluation of field CPTU dissipation data in overconsolidated fine-grained soils. *Canadian Geotechnical Journal*, 36:369–381, 1999.
- [159] A. Tanaka and G.E. Bauer. Dilatometer tests in a Leda clay crust. In Robertson and Mayne [143], pages 877–882.
- [160] C.I. Teh and G.T. Houlsby. An analytical study of the cone penetration test in clay. *Géotechnique*, 41(1):17–34, 1991.
- [161] K. Terzaghi. *Theoretical Soil Mechanics*. John Wiley & Sons, 1951.
- [162] E. Teunissen. Metingen en postdicties boorfrontdrukken buis 1. Technical report, Centrum Ondergronds Bouwen, 1999.
- [163] S.P. Timoshenko and J.N. Goodier. *Theory of Elasticity*. McGraw-Hill, New York, 2nd edition, 1951.
- [164] A.F. van Tol. Stabiliteit van diepwandsleuven. In *Funderingstechniek II, S&E Publicatie No. 20*, pages 107–139, Gouda, 1987. Betonvereniging.
- [165] A.O. Uriel and C. Sagaseta. General report: Selection of design parameters for underground construction. In of XII ICSMFE [130], pages 2521–2551.
- [166] A. Verruijt. *Theory of Groundwater Flow*. Macmillan, London, 1970.
- [167] A. Verruijt. *Grondmechanica*. DUM, Delft, 1990.
- [168] A. Verruijt. Stresses in tunnel linings. Private Communications, 1996.
- [169] A. Verruijt, F.L. Beringen, and E.H. de Leeuw, editors. *Proceedings of the Second European Symposium on Penetration Testing*. Balkema, May 1982.
- [170] A.S. Vesić. Expansion of cavities in infinite soil mass. *Journal of the Soil Mechanics and Foundations Division*, 98(3):265–290, March 1972.

- [171] F.W.J. van Vliet, W.G.M. van Kesteren, and D.R. Mastbergen. Stromingsprocessen in mengkamer TBM. Interim report K100-W-034, WL/Delft Hydraulics, May 1996.
- [172] S. van Vliet and F.J. Wermer. Boorproces Tweede Heinenoordtunnel weer hervat na vertraging door instabiliteit graaffront. *COB Nieuwsbrief*, 1(3), November 1997.
- [173] S. Wallis. Redesigned hydroshield gives boulders short drift. *Tunnels & Tunneling*, pages 41–42, June 1990.
- [174] B. Walz, J. Gerlach, and M. Pulsfort. Schlitzwandbauweise, Konstruktion, Berechnung und Ausführung. Technical report, Bergische Universität Gesamthochschule Wuppertal, 1983.
- [175] C.P. Wroth. The interpretation of in situ soil tests. *Géotechnique*, 34(4):449–489, December 1984.
- [176] C.P. Wroth. Penetration testing — A more rigorous approach to interpretation. In Ruiter [145], pages 303–311.
- [177] H.S. Yu, L.R. Hermann, and R.W. Boulanger. Analysis of steady cone penetration in clay. *ASCE Journal of Geotechnical and Geoenvironmental Engineering*, 126(7):594–605, July 2000.
- [178] H.S. Yu and J.K. Mitchell. Analysis of cone resistance: Review of methods. *ASCE Journal of Geotechnical and Geoenvironmental Engineering*, pages 140–149, February 1998.

As the Lecturer in Recent Runes put it: 'He called me in and asked me what I did, exactly. Have you ever heard of such a thing? What sort of question is that? This is a *university!*'

Terry Pratchett: The Last Continent

Curriculum Vitae

Wout Broere was born on the 17th of April 1971 in Amsterdam. After attending the Vossius Gymnasium he started a Civil Engineering study at Delft University of Technology in August 1989. He graduated in February 1995 at the chair of Foundation Engineering on the subject of 'risks and disturbances during the boring of tunnels' and obtained a M.Sc. degree. In October 1993 he also started a study of Astrophysics at the University of Amsterdam, for which he obtained a propaedeutic exam in February 1995.

In May 1995 he started as a research assistant at the Geotechnical Laboratory under joint supervision of the chairs of Foundation Engineering and Underground Constructions. His research topic was the 'Optimisation of the Tunnel Boring Process with a Focus on Geotechnical Aspects' and the research resulted in this thesis.

During the past five years he wrote several papers for international conferences as well as national journals. He also acted as thesis advisor for numerous graduation students and has worked in collaboration with other research institutes and geotechnical consultants.

In 1997 he participated in the Competition to Calculate Settlements at the Haarajoki Test Embankment, organised by the Finnish National Road Administration (FINNRA), together with Mr. D.A. Kort and Prof. A.F. van Tol. They were awarded a second prize for the most accurate prediction, and a first prize for the best presentation format.

Zwaarwichtig neemt de machine zijn balen kennis op;
knarsend, piepend, steunend komt zijn produkt naar
buiten: kleine wolkjes bijtende veelkleurige stoom.

Jack Vance: De Duivelsprinsen

Samenvatting

Graaffrontstabiliteit & Nieuwe Sondeertoepassingen

Ondanks enorme technische vooruitgang in de laatste decennia zijn de risico's bij het boren van tunnels in slappe gronden groter dan bij andere ondergrondse werken. Tijdens het boren treden storingen op in het boorproces welke voor vertragingen en kostenverhogingen kunnen zorgen en deformaties en schade aan de omgeving kunnen veroorzaken. Gedeeltelijk zijn deze storingen terug te voeren op een beperkte kennis van het grondgedrag en de grondgesteldheid rondom de tunnelboormachine. Een beter inzicht in het grondgedrag voor de machine tijdens het boorproces zou dan ook kunnen bijdragen aan betere beheersing van de projectkosten.

In slappe, heterogene en watervoerende gronden, die kenmerkend zijn voor deltagebieden, is het noodzakelijk om tijdens het boren de zojuist ontgraven opening te ondersteunen om instorten te voorkomen. In vloeistof- of gronddrukbalansschilden wordt daarom aan het graaffront een steundruk toegepast, door middel van een vloeistof respectievelijk grondbrij. De steundruk dient zo gekozen te worden dat geen bezwijken van het graaffront optreedt, en bij voorkeur zodanig dat de deformatie van de omgeving minimaal is. Hiertoe dient de steundruk te allen tijde tussen de minimaal benodigde en de maximaal toelaatbare steundruk te blijven.

In een vloeistofschild wordt een bentonietsuspensie gebruikt om aan het graaffront een filtercake op te bouwen, welke de poriën in de grond afdicht. Door deze filtercake wordt de steundruk op het korrelskelet overgebracht. Tijdens het boren schrapen de snijtanden op het graafwiel echter voortdurend de opgebouwde filtercake af, waarna de bentonietsuspensie opnieuw in het massief zal infiltreren om een nieuwe filtercake op te bouwen. Tijdens dit infiltratieproces ontstaan wateroverspanningen in de grond voor de tunnelboormachine, waardoor de stabiliteit van de grond en de effectiviteit van het steunmedium verlaagd worden.

In een gronddrukbalansschild worden regelmatig schuim of andere conditioneringsmiddelen toegepast om de consistentie van de grondbrij in de mengkamer te verbeteren. Een deel van de werking van het schuim berust op het feit dat tijdens de injectie van schuim in de grond het daar aanwezige grondwater wordt verdrongen. Hierdoor ontstaan wateroverspanningen voor het boorfront. Ook in dit geval wordt de stabiliteit van de grond voor de machine verlaagd.

Dit effect van wateroverspanningen voor het boorfront is in een stabiliteitsmodel ingebouwd. Dit model houdt tevens rekening met gelaagdheid van de grond, zowel voor als boven het graaffront, en met boogwerking in de grondlagen boven de machine. Berekeningen die met dit model zijn uitgevoerd laten zien dat onder invloed van wateroverspanningen een aanzienlijke verhoging van de minimale steundruk nodig kan zijn, ten opzichte van de minimale steundruk die berekend is met een model dat geen rekening houdt met dit effect. Het sterkst blijkt de invloed zich te laten gelden in zandgronden met een doorlatendheid tussen de 10^{-5} en 10^{-3} m/s.

Aan de hand van de berekende steundrukken en de gebruikte (eenvoudige) grondwaterstromingsmodelleringen is tevens voor een aantal projecten berekend welke wateroverspanningen

voor de tunnelboormachine verwacht kunnen worden. De resultaten van veldmetingen komen goed met deze berekeningen overeen.

Daarnaast is aandacht besteed aan de bepaling van de maximaal toelaatbare steundruk. Duidelijk is dat voor de bepaling van de maximaal toelaatbare steundruk het verlies van het steunmedium door een blow-out of scheurvorming van de grond maatgevender is dan de deformatie van (de grond voor) het graaffront. Voor de exacte bepaling van de daaruit voortvloeiende maximale steundruk zijn echter onvoldoende gegevens beschikbaar. Beperken van de toelaatbare steundruk tot de totaalspanning aan de bovenzijde van de tunnelboormachine blijft in de meeste omstandigheden een voor de hand liggende keuze, ook al is deze keuze zeer conservatief.

Tijdens het boren kan aanvullende informatie over de grondgesteldheid voor het front verkregen worden met sensoren op of vanuit de machine. Deze informatie kan gebruikt worden om onzekerheden in het bestaande grondonderzoek te verkleinen of het boorproces nauwkeurig te controleren, bijvoorbeeld teneinde de zettingen te minimaliseren. Een van de mogelijke technieken is horizontaal sonderen.

Een belangrijk verschil tussen horizontaal sonderen en (traditioneel) verticaal sonderen, is de initiële spanningstoestand rond de conus. Tijdens verticaal sonderen is de spanning loodrecht op de sondeerrichting overal de horizontale totaalspanning, tijdens horizontaal sonderen varieert deze echter rondom de conus tussen de horizontale en verticale totaalspanning. Deze niet uniforme spanningsverdeling loodrecht op de conus kan in bestaande modellen (voor verticaal sonderen) niet meegenomen worden. Daardoor is niet a priori duidelijk wat de verschillen tussen horizontaal en verticaal sonderen zijn.

Om deze verschillen in kaart te brengen is een aantal proeven uitgevoerd in een calibratiekamer gevuld met zand. Tijdens de preparatie van de monsters is de dichtheid van het zand en de korrelverdeling gevarieerd. In elke proef zijn een horizontale en een of meer verticale sonderingen uitgevoerd in hetzelfde monster. Van deze metingen zijn de conusweerstand en de schachtwrijving op de diepte van de horizontale sondering met elkaar vergeleken.

Het blijkt dat de verhouding van de horizontale gedeeld door de verticale conusweerstand afhangt van de relatieve dichtheid van het zand. Bij hoge of lage relatieve dichtheden is deze verhouding ongeveer 1. Voor gemiddelde dichtheden worden waarden rond de 1,2 gevonden. De korrelverdeling van het zand lijkt nauwelijks invloed op deze verhouding te hebben.

De verhouding van de horizontale gedeeld door de verticale schachtwrijving hangt daarentegen nauwelijks van de dichtheid van het zand af, maar juist sterk van de korrelverdeling. Afhankelijk van het soort zand zijn verhoudingen tussen 0,65 en 1,3 gevonden. Een duidelijke afhankelijkheid van bijvoorbeeld de karakteristieke korreldiameter is echter niet gevonden. Het blijft hierdoor ook voornamelijk onduidelijk hoe deze verhouding in andere grondsoorten ligt.

De verschillen tussen horizontaal en verticaal sonderen zijn tevens onderzocht met een aantal schaalproeven, welke de kwalitatieve verschillen in de bezwijkmechanismen en spanningsverdelingen rond de conus laten zien. Ook is een eenvoudig lineair-elastisch model opgesteld dat rekening houdt met de niet-uniforme spanningsverdeling rond de conus. Dit model voorspelt voor normaal geconsolideerde grond dat de horizontale consusweerstand groter is dan de verticale, hetgeen overeenkomt met de metingen.

Behalve de conusweerstand en de schachtwrijving is het ook mogelijk om de waterspanning rond de conus te meten. Hiervoor wordt een piezoconus gebruikt. In slecht doorlatende grondsoorten kan hiermee de wateroverspanning die door het sonderen is opgewekt, gemeten worden. In zandgronden is over het algemeen de doorlatendheid zo hoog is dat deze wateroverspanning is gedissipeerd voordat de waterspanningsmeter arriveert.

Indien echter de sondeersnelheid sterk vergroot wordt, zou het mogelijk zijn de wateroverspanningen ook in doorlatend materiaal te meten, voordat deze dissiperen. In losgepakte contractante materialen kan dan een wateroverspanning verwacht worden, terwijl in dichtgepakte dilatante materialen een wateronderspanning optreedt. Indien deze waterover- danwel onderspanning gedetecteerd kan worden, kan met behulp van een hoge-snelheids-piezosondering de dichtheid van een zandpakket bepaald worden. De dichtheid van het zand is een indicatie voor de verwekingsgevoeligheid van het materiaal.

Om dit te testen is in een calibratiekamer een aantal hoge-snelheids-piezosonderingen uitgevoerd bij verschillende dichtheden. De wateroverspanningen die hierbij optreden zijn gemeten door de conus alsook door een tweetal waterspanningsmeters in het zandpakket. Deze metingen laten zien dat de variatie in de metingen zeer groot is. Alhoewel significante wateronderspanningen alleen in dichtgepakt materiaal gemeten worden, worden wateroverspanningen in zowel los- als dichtgepakt zand gemeten, en kan de gemeten waterspanning sterk fluctueren.

Door het ontbreken van een duidelijke relatie tussen de dichtheid van het zand en de gemeten wateroverspanning kan de dichtheid van het zand niet bepaald worden met een hoge-snelheidspiezosondering. Ter bepaling van de verwekingsgevoeligheid dienen daarom vooralsnog de bestaande correlaties met de conusweerstand gebruikt te worden.

W. Broere: Tunnel Face Stability & New CPT Applications. Delft University Press, 2001

Dank ook voor mijn vriendin, die ik al twee jaar mis.
Door haar weet ik nu eindelijk wat een depressie is.

Lebbis en Janssen: Overdrijf

Nawoord

In de afgelopen jaren heb ik, zoals iemand het eens uitdrukte, alle mogelijke zijwegen van een duidelijk afgebakend pad bewandeld op weg naar een minder duidelijk afgebakend eindproduct. Om steeds verder en verder te dolen en schijnbaar nooit het einddoel voor ogen te hebben. En nu is er dan dit boekje, waarin van al die omzwervingen weinig terug te vinden is. Ik ben zeker niet de enige die verbaasd is.

Van deze gelegenheid wil ik gebruik maken om een aantal mensen die ik de afgelopen jaren tegen ben gekomen, toch nog even te bedanken. In de eerste plaats mijn promotoren, Frits en Bandi. Bandi heeft er op onnavolgbare wijze voor gezorgd dat, ondanks alle stress die eigen is aan een promotieonderzoek, ik dit werk in relatief ontspannen sfeer heb kunnen uitvoeren. Daarnaast heeft hij, als hoogleraar ondergronds bouwen, jarenlang mensen van uiteenlopende disciplines bijeen gebracht. Voor het vinden van nieuwe zijwegen om te bewandelen is dat van groot belang geweest. Samen met Frits, in zijn dubbelfunctie als dagelijks begeleider, heb ik de afgelopen tijd de ins en outs van het promotietraject leren kennen. Behalve voor zijn steun daarin, moet ik hem bedanken voor de vele inhoudelijke discussies die wij gevoerd hebben, de grote mate van vrijheid die hij mij geboden heeft en het gestelde vertrouwen.

Op het lab heb ik een groot aantal collega's en studenten leren kennen, zien komen en vertrekken. Een man was al die jaren een constante factor op het lab, en verdient bijzonder veel dank. Joop, Meneer van Leeuwen als je hem op stang wilde jagen, stond altijd klaar om te helpen. En zonder die hulp zouden veel van de proeven die ik uitgevoerd heb, nooit zo snel van vaag idee tot werkende opstelling verworpen zijn. Hij is nu, welverdiend, met pensioen. Ik blijf nog even, maar het lab zonder Joop zal nooit meer hetzelfde zijn.

En dan een andere constante factor, mijn kamergenoot Arjen. Hem moet ik natuurlijk in de eerste plaats danken voor het in stand houden van de fabel dat wij niet met elkaar praten, maar alleen emailen. En de felle discussies over een verscheidenheid aan onderwerpen, waarbij maar al te vaak duidelijk werd dat je in de geotechniek een probleem op veel verschillende manieren kunt benaderen, en op nog veel meer, uiteindelijk dezelfde, manieren.

De koffiepauzes van Geotechniek zijn berucht, waarschijnlijk doordat ze zo publiek zijn en enorm lang kunnen duren. Soms zijn het meer werkbeprekingen of technische discussies en op andere momenten puzzelmarathons. Soms vormen ze ook gewoon een rustpunt in de dag. Voor de koffiepauzes, en de verdere ondersteuning al die jaren, dank aan Arnold, Astra, Paola, Han, Ab, Bob, Ad, Henderikus en alle anderen op het lab. Tussen de koffiepauzes door rest er nog net tijd om te gaan lunchen, en ervaringen uit te wisselen over het wel en wee van een promovendus. Andre, Sandra, Ingrid, Marc, Ernst, Bart, Joost, ik hoop dat we nog regelmatig samen zullen lunchen. En niet te vergeten Marja, bedankt voor een altijd luisterend oor.

De schare studenten/collega's/kennissen/vrienden die ik de afgelopen jaren in het werkveld heb leren kennen is schier eindeloos. Sommigen ben ik tegen gekomen tijdens hun afstuderen, weer anderen bij de verschillende boorprojecten of tijdens de ontspannen bijeenkomsten van Jong en Fris. Van hen wil ik in het bijzonder Annemarije, Jacco, Sallo, Richard, Sander, Yvo,

Fabrice, Benno, Koen, Sisira, Werner, Wouter, Predrag, Klaas-Jan, Arjan, Adam, Jurjen, Almer en Gerard bedanken voor hun vriendschap en/of de geboden ondersteuning in de afgelopen jaren. En wie van mening is dat zijn naam in dit rijtje ontbreekt: je bent op de paginascheiding weggevallen.

Tussen mijn werk in Delft en mijn dabbling in astrophysics door heb ik altijd tijd gevonden voor de broodnodige ontspanning, daarin bijgestaan door een uitgebreide vriendenkring. Sommigen van hen zijn hierboven reeds met name genoemd. Anjali, Boris en Matijs hebben zich altijd bereid getoond de theorie van het harde-bollen-gas nog eens uit te testen of een bezoek aan Kriterion te brengen, ook als daar geen bezienswaardigheid draaide. Mathijs en de andere heren van de RPG spelgroep zijn nooit te kwaad om mij en zichzelf een uitlaatklep te bieden voor een overschot aan creatieve energie. Hetzelfde kan, met enige overlap, gezegd worden van de leden van het Geofictief Interactie Project Metaphoor.

Dan rest mij nog mijn ouders te bedanken voor de ondersteuning gedurende al die jaren. En tenslotte, gewoonweg voor het blond zijn, en het gevraagd en ongevraagd met raad en daad terzijde staan, Jetske en Femke, bedankt.

Amsterdam, 4 juli 2001

‘Etiam mihi,’ dixit neglectim Cristophorus Robinus, ‘duo sunt nomina.’
‘Ecce tibi, quod demonstrandum erat,’ dixit Porcellus.

A.A. Milnei: WINNIE ILLE PU (translated to Latin by A. Lenard)

Appendix A

Basic Equations of Groundwater Flow

In the following paragraphs a brief overview of the main equations of the theory of groundwater flow will be given, focussed on the applications made in this thesis. For a more extensive overview one is referred to a basic textbook on the subject, e.g. Verruijt [166] or Strack [157].

Darcy's law for three-dimensional flow through isotropic porous media is

$$q_i = -k \partial_i \varphi \quad (\text{A.1})$$

with the head φ given by

$$\varphi = z + \frac{P}{\rho g} \quad (\text{A.2})$$

Mass balance of the flow through an element $\Delta x \Delta y \Delta z$ for steady-state flow requires that

$$\partial_i q_i = 0 \quad (\text{A.3})$$

Using (A.1) for constant k in (A.3) leads to the basic equation of steady flow (Laplace's equation)

$$\nabla^2 \varphi = 0 \quad (\text{A.4})$$

In a semi-confined aquifer it can be expected that horizontal flow will dominate and only small amounts of water will enter or leave the aquifer through the confining layers above and below it. In an aquifer of constant thickness H (see figure A.1) the amount of water percolating through the upper aquitard is

$$k_1 \frac{\varphi - \varphi_1}{d_1} \Delta x \Delta y \quad (\text{A.5})$$

and similarly for the lower aquitard. From continuity and (A.1) it follows that

$$kH (\partial_x^2 \varphi + \partial_y^2 \varphi) - \frac{\varphi - \varphi_1}{\tilde{c}_1} - \frac{\varphi - \varphi_2}{\tilde{c}_2} = 0 \quad (\text{A.6})$$

where $\tilde{c}_i = d_i/k_i$ are the hydraulic resistances of the confining layers.

For a situation where the aquifer does not change in the y -direction and the bottom layer is impermeable, as sketched in figure A.2, (A.6) reduces to

$$\frac{d^2 \varphi}{dx^2} - \frac{\varphi - \varphi_1}{\lambda^2} = 0 \quad (\text{A.7})$$

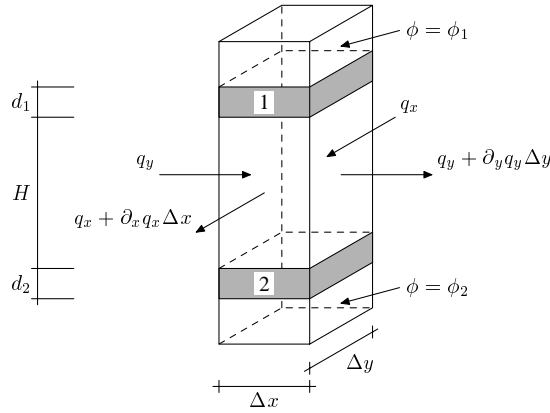


Figure A.1: Continuity in element of confined aquifer

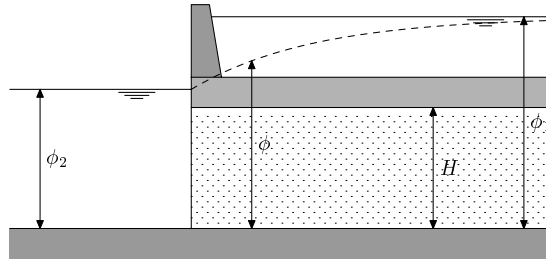


Figure A.2: Rectilinear semi-confined aquifer

where $\lambda = \sqrt{kH\bar{c}}$ is the leakage factor. This differential equation has the general solution

$$\varphi - \varphi_1 = A e^{x/\lambda} + B e^{-x/\lambda} \tag{A.8}$$

with A and B depending on boundary conditions. For the situation in figure A.2 the boundary conditions are

$$\begin{aligned} x \rightarrow \infty & \quad \varphi \rightarrow \varphi_1 \\ x = 0 & \quad \varphi = \varphi_2 \end{aligned} \tag{A.9}$$

It follows that $A = 0$ and $B = \varphi_2 - \varphi_1$ and the solution becomes

$$\varphi = \varphi_1 + (\varphi_2 - \varphi_1) e^{-x/\lambda}. \tag{A.10}$$

A.1 Semi-confined System of Aquifers

For a system of several aquifers, separated by aquitards, the same basic equations hold [157]. The aquifers are numbered $i = 1, 2, \dots, n$, with 1 the uppermost aquifer, φ_i the piezometric head

in each aquifer, k_i the permeability and H_i the layer thickness. The aquitard above layer i has conductivity \tilde{c}_i and the specific discharge q_i through this aquitard is

$$q_i = \frac{\Phi_i - \Phi_{i-1}}{\tilde{c}_i} = \frac{\Phi_i - \Phi_0}{\tilde{c}_i} - \frac{\Phi_{i-1} - \Phi_0}{\tilde{c}_{i+1}} \quad (\text{A.11})$$

with Φ_0 the constant head above the top layer.

The potential for layer i is

$$\Phi_i = k_i H_i (\varphi_i - \Phi_0) \quad (\text{A.12})$$

Introducing $a_{i,j} = 1/(k_i H_i \tilde{c}_j)$ the differential equation for each layer is given by

$$\nabla^2 \Phi_i = q_i - q_{i+1} = -a_{i-1,i} \Phi_{i-1} + (a_{i,i} + a_{i,i+1}) \Phi_i - a_{i+1,i+1} \Phi_{i+1} \quad (\text{A.13})$$

where due to boundary conditions for the lowest aquifer

$$\begin{cases} a_{i,n+1} = 0 \\ a_{n+1,i} = 0 \end{cases} \quad \forall i = 1, 2, \dots, n \quad (\text{A.14})$$

For one-dimensional and axi-symmetrical problems the particular solutions satisfy the differential equation

$$\nabla^2 W(x, y, \omega) = \omega^2 W(x, y, \omega) \quad (\text{A.15})$$

and it follows that

$$\Phi_i = A_i W(x, y, \omega) \quad (\text{A.16})$$

is a suitable set of solutions to this problem. Substituting this solution in the set of differential equations for this system leads to

$$A_i \omega^2 = -a_{i-1,i} A_{i-1} + (a_{i,i} + a_{i,i+1}) A_i - a_{i+1,i+1} A_{i+1}, \quad (\text{A.17})$$

with the requirement that $A_0 = 0$ in order to include $\Phi_0 = 0$. This system of equations in terms of A_i has nontrivial solutions only if the determinant vanishes. That condition leads to an equation in terms ω^2 which has n roots ω_j^2 with accompanying constants $A_{i,j}$. As the equation for $i = 1$ has only two constants, it can be divided by $A_{1,j}$ to find the ratio $A_{2,j}/A_{1,j}$, which in turn can be used to find $A_{3,j}/A_{1,j}$ and so on. This leads to a set of constants

$$\alpha_{i,j} = A_{i,j}/A_{1,j} \quad (\text{A.18})$$

for each value of ω_j .

Now the set of particular solutions for each value of ω_j can be written as

$$\Phi_i = \sum_{j=1}^n \alpha_{i,j} A_{1,j} W(x, y, \omega_j) \quad (\text{A.19})$$

where $A_{1,j}$ is an unknown parameter. For the problem of one-dimensional flow there are two particular solutions: $e^{-\omega_j x}$ and $e^{\omega_j x}$. For this case the particular solution can be rewritten as

$$\Phi_i = \sum_{j=1}^n \alpha_{i,j} [B_j e^{\omega_j x} + C_j e^{-\omega_j x}] \quad (\text{A.20})$$

with unknown coefficients B_j and C_j , which have to be determined from boundary conditions.

For the special case of a two-aquifer system ($n = 2$), (A.17) reduces to

$$\omega_j^2 = a_{1,1} + a_{1,2} - a_{2,2}\alpha_{2,j} \quad (\text{A.21})$$

$$\alpha_{2,j}\omega_j^2 = -a_{1,2} + a_{2,2}\alpha_{2,j} \quad (\text{A.22})$$

where use has been made of the fact that $\alpha_{1,j} = 1$. Substituting the first equation in the second leads to a quadratic equation in ω_j^2 , which has solutions

$$\omega_j^2 = \frac{1}{2}(a_{1,1} + a_{1,2} + a_{2,2}) + \frac{1}{2}\sqrt{(a_{1,1} - a_{2,2})^2 + 2(a_{1,1} + a_{2,2})a_{1,2} + a_{1,2}^2} \quad (\text{A.23})$$

Using (A.21):

$$\alpha_{2,j} = \frac{a_{1,1} + a_{1,2} - \omega_j^2}{a_{2,2}} \quad (\text{A.24})$$

the set of solutions can be written as

$$\Phi_1 = A^+W(x, y, \omega_1) + A^-W(x, y, \omega_2) \quad (\text{A.25})$$

$$\Phi_2 = A^+\alpha_{2,1}W(x, y, \omega_1) + A^-\alpha_{2,2}W(x, y, \omega_2) \quad (\text{A.26})$$

For a set of two aquifers with a limited head at $x \rightarrow \infty$ only the terms $e^{-\omega_j x}$ need to be considered, so the potentials can be expressed as

$$\Phi_1 = A^+e^{-\omega_1 x} + A^-e^{-\omega_2 x} \quad (\text{A.27})$$

$$\Phi_2 = A^+\alpha_{2,1}e^{-\omega_1 x} + A^-\alpha_{2,2}e^{-\omega_2 x} \quad (\text{A.28})$$

and if the head for both layers at $x = 0$ is equal to $\Delta\phi$, the constants can be found as

$$A^\pm = \pm \frac{a_{1,1} + a_{1,2} - 3a_{2,2} \pm \sqrt{(a_{1,1} - a_{2,2})^2 + 2(a_{1,1} + a_{2,2})a_{1,2} + a_{1,2}^2}}{2\sqrt{(a_{1,1} - a_{2,2})^2 + 2(a_{1,1} + a_{2,2})a_{1,2} + a_{1,2}^2}} \Delta\phi \quad (\text{A.29})$$

completing the potential in the aquifers.

A.2 Transient Flow

The above relations hold for steady-state flow. If transient flow is considered, the differential equation changes to include a time-derivate of the potential. Using the same definitions as above,

$$\Phi = kH(\phi - \phi_0) \quad (\text{A.30})$$

the regular form of the differential equation for transient flow in a confined aquifer, or the linearized form of the differential equation for transient flow in an unconfined aquifer is [157]

$$\nabla^2\Phi = \frac{S_s}{k}\partial_t\Phi \quad (\text{A.31})$$

with S_s the coefficient of specific storage, $S_s = \rho g(m_v + n\beta)$. In case of transient flow in a semi-confined aquifer, a further term is added, proportional to the head. Then the entire differential equation becomes

$$\nabla^2 \Phi = a^2 \phi + c^2 \partial_t \Phi \quad (\text{A.32})$$

with $a = \lambda^{-1}$ and $c^2 = S_s/k$.

Introducing a modified potential $\tilde{\Phi}$, defined by

$$\Phi = e^{-\frac{a^2}{c^2}t} \tilde{\Phi} \quad (\text{A.33})$$

the differential equation can be rewritten as

$$-e^{-\frac{a^2}{c^2}t} [\nabla^2 \tilde{\Phi} - c^2 \partial_t \tilde{\Phi}] = 0 \quad (\text{A.34})$$

and the problem is reduced to solving the diffusion equation or a confined transient flow problem.

In this form the differential equation can be readily used to investigate the time span needed for an aquifer with given excess pressure distribution to return to equilibrium, i.e. $\Phi = 0$. If at $t = 0$ the head in the aquifer is equal to the one-dimensional static solution, $\Phi = e^{-ax}$ for $x > 0$, then also the initial condition

$$\tilde{\Phi}(x, 0) = e^{-ax} \quad (\text{A.35})$$

holds for obvious reasons. Given the boundary conditions that $q = 0$ at $x = 0$ and $\Phi = 0$ for $x \rightarrow \infty$ at all times, the modified potential can be found from Fourier integrals [99] as

$$\tilde{\Phi} = \frac{1}{\sqrt{\pi}} \int_{-\infty}^{-\frac{xc}{2\sqrt{t}}} e^{a(x+\frac{z}{c}\sqrt{t})} e^{-z^2} dz + \frac{1}{\sqrt{\pi}} \int_{-\frac{xc}{2\sqrt{t}}}^{\infty} e^{-a(x+\frac{z}{c}\sqrt{t})} e^{-z^2} dz \quad (\text{A.36})$$

or, simplifying the solution by using the complementary error-function $\text{erfc}(x)$, the potential in the aquifer is given by

$$\Phi = \frac{1}{2} \left[\text{erfc} \left(-\frac{xc}{2\sqrt{t}} + \frac{a}{c} \sqrt{t} \right) e^{-ax} + \text{erfc} \left(\frac{xc}{2\sqrt{t}} + \frac{a}{c} \sqrt{t} \right) e^{ax} \right] \quad (\text{A.37})$$

From the same Fourier integrals, the time-dependent response of the system to a sudden inflow $q\delta(x)$ at $t = 0$ can be found. Integration over time can yield the response to a continuous inflow $q(t)$ as a superposition of delta-function inflows. The response of a system with initial head $\Phi = 0$ and $\Phi = 0$ for $x \rightarrow \infty$ to a continuous inflow q at $x = 0$ for $t > 0$ is [49]

$$\Phi = \frac{q}{4a} \left[\text{erfc} \left(\frac{xc}{2\sqrt{t}} + \frac{a}{c} \sqrt{t} \right) e^{ax} - \text{erfc} \left(\frac{xc}{2\sqrt{t}} - \frac{a}{c} \sqrt{t} \right) e^{-ax} \right] \quad (\text{A.38})$$

Note the similarity between (A.37) and (A.38).

“I’ve got two names,” said Christopher Robin carelessly.

“Well, there you are, that proves it,” said Piglet.

A.A. Milne: Winnie-The-Pooh

Appendix B

Basic Equations of Elasticity

Given a polar coordinate system defined in figure B.1, with stresses σ_{ij} and displacements u_i , the equations of equilibrium in radial and tangential directions are

$$\frac{\partial \sigma_{rr}}{\partial r} + \frac{1}{r} \frac{\partial \sigma_{r\theta}}{\partial \theta} + \frac{\sigma_{rr} - \sigma_{\theta\theta}}{r} = 0 \quad (\text{B.1})$$

$$\frac{\partial \sigma_{r\theta}}{\partial r} + \frac{1}{r} \frac{\partial \sigma_{\theta\theta}}{\partial \theta} + 2 \frac{\sigma_{r\theta}}{r} = 0 \quad (\text{B.2})$$

The deformations in radial and tangential directions are defined as

$$\epsilon_{rr} = \frac{\partial u_r}{\partial r} \quad (\text{B.3})$$

$$\epsilon_{\theta\theta} = \frac{u_r}{r} + \frac{1}{r} \frac{\partial u_\theta}{\partial \theta} \quad (\text{B.4})$$

$$\epsilon_{r\theta} = \frac{1}{2} \left(\frac{\partial u_\theta}{\partial r} + \frac{1}{r} \frac{\partial u_r}{\partial \theta} - \frac{u_\theta}{r} \right) \quad (\text{B.5})$$

and the volume strain as

$$e = \epsilon_{rr} + \epsilon_{\theta\theta} = \frac{\partial u_r}{\partial r} + \frac{u_r}{r} + \frac{1}{r} \frac{\partial u_\theta}{\partial \theta} \quad (\text{B.6})$$

The stresses can now be expressed as

$$\sigma_{rr} = \mu((m-1)e + 2\epsilon_{rr}) \quad (\text{B.7})$$

$$\sigma_{\theta\theta} = \mu((m-1)e + 2\epsilon_{\theta\theta}) \quad (\text{B.8})$$

$$\sigma_{r\theta} = 2\mu\epsilon_{r\theta} \quad (\text{B.9})$$

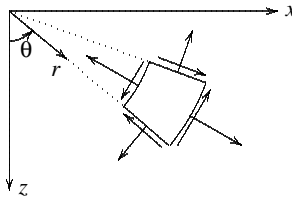


Figure B.1: Element in polar coordinates

Here m is defined as

$$m = \frac{\lambda + \mu}{\mu} \quad (\text{B.10})$$

with λ and μ the Lamé constants,

$$\lambda = \frac{\nu E}{(1 + \nu)(1 - 2\nu)} \quad (\text{B.11})$$

$$\mu = \frac{E}{2(1 - \nu)} \quad (\text{B.12})$$

The equilibrium equations (B.1) and (B.2) can now be expressed as

$$(m + 1) \left[\frac{\partial^2 u_r}{\partial r^2} + \frac{1}{r} \frac{\partial u_r}{\partial r} - \frac{u_r}{r^2} \right] + \frac{1}{r^2} \frac{\partial^2 u_r}{\partial \theta^2} + \frac{m}{r} \frac{\partial^2 u_\theta}{\partial r \partial \theta} - \frac{m + 2}{r^2} \frac{\partial u_\theta}{\partial \theta} = 0 \quad (\text{B.13})$$

$$\frac{m + 1}{r^2} \frac{\partial^2 u_\theta}{\partial \theta^2} + \frac{m}{r} \frac{\partial^2 u_r}{\partial r \partial \theta} + \frac{m + 2}{r^2} \frac{\partial u_r}{\partial \theta} + \frac{\partial^2 u_\theta}{\partial r^2} + \frac{1}{r} \frac{\partial u_\theta}{\partial r} - \frac{u_\theta}{r^2} = 0 \quad (\text{B.14})$$

According to Timoshenko [163] a general class of solutions can be constructed,

$$u_r^{(k)} = r^n \cos k\theta \quad (\text{B.15})$$

$$u_\theta^{(k)} = \alpha r^n \sin k\theta \quad (\text{B.16})$$

where, for given k , α and n are determined by substitution of (B.15) and (B.16) in (B.13) and (B.14). This leads to

$$n = \pm(k + 1) \quad \vee \quad n = \pm(k - 1) \quad (\text{B.17})$$

as possible values for n , and α given by

$$\alpha = \frac{(m + 1)(n^2 - 1) - k^2}{k(m + 2 - mn)} \quad (\text{B.18})$$

From these equations the general solutions for $k = 0$ and $k = 2$ can be derived.

For the case $k = 0$, the possible values for n and α are

$$n = 1 \quad : \quad \alpha = 0 \quad (\text{B.19})$$

$$n = -1 \quad : \quad \alpha = 0 \quad (\text{B.20})$$

which leads to the general solution for the case $k = 0$

$$u_r^{(0)} = A^{(0)} r + \frac{B^{(0)}}{r} \quad (\text{B.21})$$

$$u_\theta^{(0)} = 0 \quad (\text{B.22})$$

This in turn leads to strain components

$$\varepsilon_{rr}^{(0)} = A^{(0)} - \frac{B^{(0)}}{r^2} \quad (\text{B.23})$$

$$\varepsilon_{\theta\theta}^{(0)} = A^{(0)} + \frac{B^{(0)}}{r^2} \quad (\text{B.24})$$

$$\varepsilon_{r\theta}^{(0)} = 0 \quad (\text{B.25})$$

and volume strain

$$e^{(0)} = 2A^{(0)} \tag{B.26}$$

The stresses are then given by

$$\sigma_{rr}^{(0)} = 2\mu \left[mA^{(0)} - \frac{B^{(0)}}{r^2} \right] \tag{B.27}$$

$$\sigma_{\theta\theta}^{(0)} = 2\mu \left[mA^{(0)} + \frac{B^{(0)}}{r^2} \right] \tag{B.28}$$

$$\sigma_{r\theta}^{(0)} = 0 \tag{B.29}$$

For the case $k = 2$ (B.17) leads to four different values of n and α

$$n = 1 \quad : \quad \alpha = -1 \tag{B.30}$$

$$n = -1 \quad : \quad \alpha = -\frac{1}{m+1} \tag{B.31}$$

$$n = 3 \quad : \quad \alpha = -\frac{2m+1}{m-1} \tag{B.32}$$

$$n = -3 \quad : \quad \alpha = 1 \tag{B.33}$$

The general solution for the case $k = 2$ is now expressed with a slightly different definition for $C^{(2)}$ as

$$u_r^{(2)} = \left[A^{(2)}r + \frac{B^{(2)}}{r} + \frac{m-1}{3}C^{(2)}r^3 + \frac{D^{(2)}}{r^3} \right] \cos 2\theta \tag{B.34}$$

$$u_\theta^{(2)} = \left[-A^{(2)}r - \frac{B^{(2)}}{(m+1)r} - \frac{2m+1}{3}C^{(2)}r^3 + \frac{D^{(2)}}{r^3} \right] \sin 2\theta \tag{B.35}$$

The strain components and volume strain are

$$\epsilon_{rr}^{(2)} = \left[A^{(2)} - \frac{B^{(2)}}{r^2} + (m-1)C^{(2)}r^2 - 3\frac{D^{(2)}}{r^4} \right] \cos 2\theta \tag{B.36}$$

$$\epsilon_{\theta\theta}^{(2)} = \left[-A^{(2)} + \frac{m-1}{m+1}\frac{B^{(2)}}{r^2} + (-m-1)C^{(2)}r^2 + 3\frac{D^{(2)}}{r^4} \right] \cos 2\theta \tag{B.37}$$

$$\epsilon_{r\theta}^{(2)} = \left[-A^{(2)} - \frac{m}{m+1}\frac{B^{(2)}}{r^2} - mC^{(2)}r^2 - 3\frac{D^{(2)}}{r^4} \right] \sin 2\theta \tag{B.38}$$

$$e^{(2)} = \left[-\frac{2}{m+1}\frac{B^{(2)}}{r^2} - 2C^{(2)}r^2 \right] \cos 2\theta \tag{B.39}$$

and the stresses are

$$\sigma_{rr}^{(2)} = \left[2A^{(2)} - 4\frac{m}{m+1}\frac{B^{(2)}}{r^2} - 6\frac{D^{(2)}}{r^4} \right] \mu \cos 2\theta \quad (\text{B.40})$$

$$\sigma_{\theta\theta}^{(2)} = \left[-2A^{(2)} - 4mC^{(2)}r^2 + 6\frac{D^{(2)}}{r^4} \right] \mu \cos 2\theta \quad (\text{B.41})$$

$$\sigma_{r\theta}^{(2)} = \left[-2A^{(2)} - \frac{2m}{m+1}\frac{B^{(2)}}{r^2} - 2mC^{(2)}r^2 - 6\frac{D^{(2)}}{r^4} \right] \mu \sin 2\theta \quad (\text{B.42})$$